SYNTHESIS AND CHARACTERIZATION OF LOW-SPIN D6 POLYPYRIDYL COMPLEXES: MANIPULATION OF EXCITED-STATE ELECTRONIC STRUCTURE THROUGH LIGAND DESIGN

By

Jonathan Taylor Yarranton

A DISSERTATION

Submitted to
Michigan State University
in partial fulfillment of the requirements
for the degree of

Chemistry – Doctor of Philosophy

2023

ABSTRACT

Iron(II) polypyridyl chromophores are among one of the most promising earth-abundant alternatives to ruthenium-based complexes in the realms of photo-redox catalysis and solar energy harvesting. The biggest hurdle to their implementation is the sub-150 fs metal-to-ligand charge transfer (MLCT) excited-state lifetime which limits their implementation in diffusion-limited processes. The main way in which researchers have approached this problem is by attempting to invert the ligand-field (LF) and MLCT manifolds by increasing the donor ability of the ligands employed. To better understand the destabilizing nature of the ligands employed, a series of Co(III) complexes were synthesized as an isoelectronic stand-in for Fe(II) to measure the LF transitions of various polypyridyl ligands as well as the first carbene ligand coordinated to Fe(II) to determine the relevant ligand-field parameters and assess the splitting observed. These results indicate that polypyridyl complexes do not impose a strong enough LF to destabilize them above the MLCT. To that end, we synthesized a series of simple bis pyridinium-based polypyridyl ligands with increased sigma-donor ability compared to the widely used carbene systems, achieving a MLCT lifetime of 18 ps, a 2-fold increase from the first reported tetra-carbene system. A final thrust was to better understand the unique MLCT manifold of $[Fe(dcpp)_2]^{2+}$ (where dcpp is 2,6-di(2-carboxypyridyl)pyridine) using symmetric π-substitutions. With this method, we were able to synthetically deconvolute the MLCT spectrum and selectively enhance different transitions based upon the substitution pattern. The computational insights gleaned can now guide new promising ligands in this family of complexes.

This dissertation is dedicated to my Mom and Dad and to all those that have always believed in me.

ACKNOWLEDGEMENTS

First, I would like to thank my advisor, Jim, for his unwavering support and understanding throughout my graduate career at MSU, giving me a project that I've enjoyed exploring, allowing me the ability to freely explore new chemistries, and has pushed me to become the chemist I am today. I would also like to thank my guidance committee for their advice throughout my project. Dr. Richard Staples has had to deal with too many of my "bad" crystals to count and has never let me forget that I should always be looking at the end goal of my Ph.D. Thank you to Dr. Dan Holmes for his expertise in collecting my difficult data. A big thanks to Bob Rasico for always being available for every emergency that came our way.

Thank you to my McCusker group members past and present who trained me when I started and for being scientific sounding boards when I'm stumped on my project. I appreciate Atanu, Bekah, and Hayden for proofreading my dissertation. Thank you to Atanu for collecting ultrafast TA on my complexes.

I would like to thank my family for their unwavering support and constant encouragement during this time. Without your consistent support none of this would have been possible.

Finally, I would like to thank my partner, Mario, for his understanding and patience these past years and always believing in me and my abilities.

TABLE OF CONTENTS

CHAPTER 1: DIFFICULTIES IN THE UTILIZATION OF IRON(II) CHROMOPHORES IN LIGHT-INDUCED CHARGE SEPARATED PROCESSES

1.1 Introduction

Global energy consumption continues to increase each year, with a vast majority of the energy being produced derived from fossil fuels. However, there has been a large push towards renewable energy sources within the United States and across the world, with the main one being solar.[1] Sunlight is an abundant and almost inexhaustible energy source. The amount of energy the Sun delivers to Earth in 1 hour is equivalent to the amount of energy humans consume annually, and a full year of irradiation delivers over 1.2×10^5 TW, well surpassing any production or consumption of energy utilized by the human civilization.[2] Given the overwhelming pressures put on the planet by CO_2 emissions from the combustion of fossil fuels, the necessity to develop and improve carbon-neutral energy is of the utmost importance, with sunlight being the best candidate. As chemists, we look to nature for inspiration, and the conversion of solar energy into fuel is all around us, in the form of photosynthesis. This process allows for the absorption of a photon of light by chlorophyll, creating a transmembrane potential, to create new chemical bonds in the form of glucose for the plant to use as food, fuel.[3] Using these fundamental steps in photosynthesis, chemists have sought to use light-induced charge-separation to drive organic transformations as well as to capture solar energy.

Transition metal chromophores are well suited to exploring the fundamentals and applications of charge-separated excited-states, which typically have strong absorptions in the visible region of the electromagnetic spectrum. Upon absorption of a photon these molecules can create a charge-separated state, either a metal-to-ligand or ligand-to-metal charge transfer (MLCT or LMCT) excited state. A general transition metal chromophore containing polypyridyl ligands is

shown in Figure 1.1. Upon that absorption of a photon, the molecule populates an MLCT excited state, whereby the metal center is formally oxidized and the polypyridyl ligand is reduced. The molecule, now in this excited state, is able to access reactivity not present in the ground state. The metal can now act as an oxidant or the ligand as a reductant allowing for new electron transfer processes. To manipulate this dual reactivity, the optical and redox properties of these chromophores can be easily tuned by judicious choice of ligand scaffold allowing for the tailoring of the chromophore for differing applications, be it electron-transfer to a semiconductor substrate or to/from organic substrates for photocatalysis.

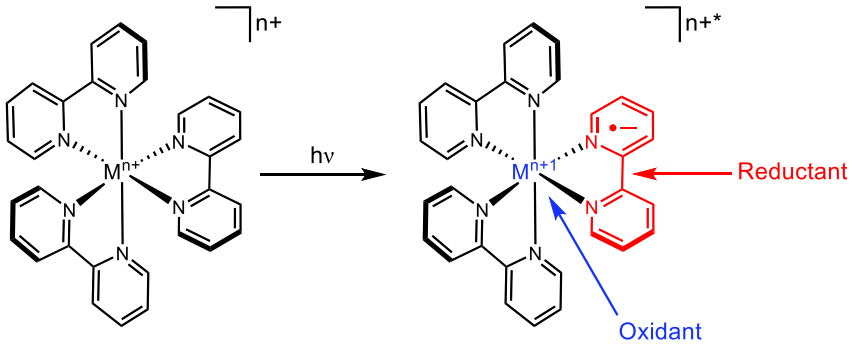

Figure 1.1. Scheme showing the metal-to-ligand-charge transfer (MLCT) of a generic transition-metal polypyridyl chromophore.

The typical metals that come to mind when thinking of solar energy conversion or photocatalysis are ruthenium and iridium, second- and third-row transition metals. The most widely and well-studied chromophores of these metals are $[Ru(bpy)_3]^{2+}$ and $Ir(ppy)_3$ (where bpy = 2,2′-bipyridine and ppy = 2-phenylpyridine). These complexes possesses a low-spin d^6 electron configuration which, upon absorption of a photon of visible light, creates a long-lived and emissive ^{3}MLCT state.[4–7] As second- and third-row metals they intrinsically possess a higher ligand-field (LF) strength than the first-row congeners. This allows for the destabilization of the metal-centered

LF excited states making them inaccessible during excited-state evolution. This destabilization creates a scenario in which the lowest-energy excited state for these complexes is predominantly ^{3}MLCT in character and exhibit lifetimes on the order of microseconds as shown in Figure 1.2.[8,9]

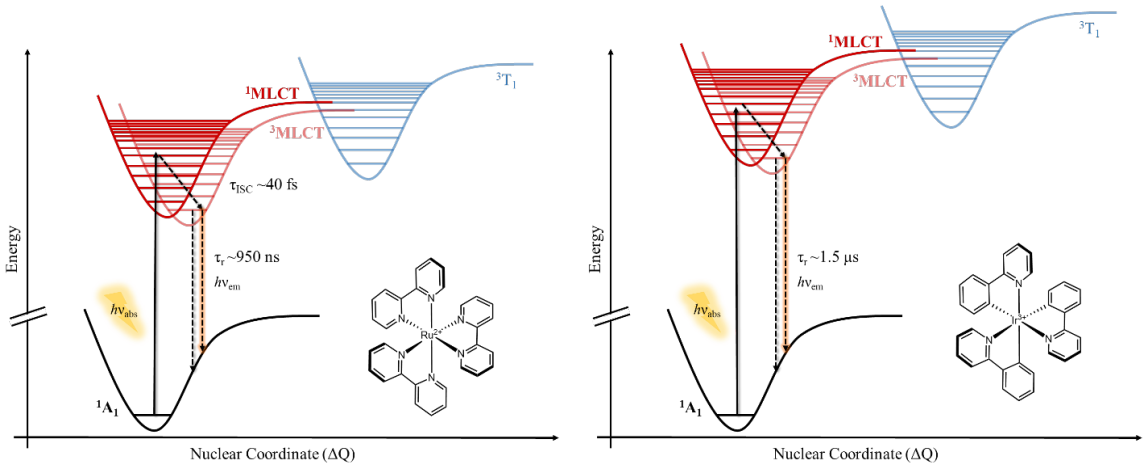

Figure 1.2. Potential energy surface diagrams and photocycles of $[Ru(bpy)_3]^{2+}$ (left) and $[Ir(ppy)_3]$ (right) with their average respective emission time constants from literature in fluid solution.

These long lived excited states coupled with the tunability of the ground- and redox-active states along with the optical properties has made them amenable for use in various light-capture applications including solar energy conversion[10–12] and photoredox catalysis by which increasingly complex organic building blocks can be synthesized.[13–16]

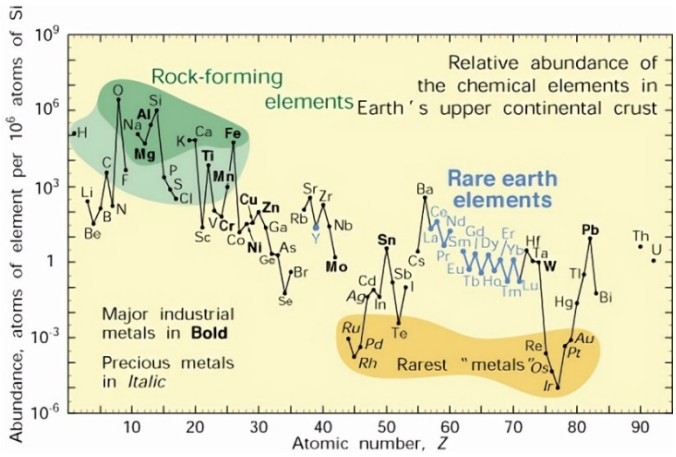

Figure 1.3. Relative abundance of the chemical elements in Earth's upper continental from reference 17.

Though the above metals work markedly well in those applications, a problem begins to emerge when the light absorbing application becomes materials-intensive. In that case, it now becomes restrictive in the use of these rare and expensive metals (Figure 1.3)[17] and cheaper more abundant alternatives would be more favorable. The first-row transition metals on the other hand have orders of magnitude higher natural crustal abundance, than the second- and third-row metals. With sights set on utilization of these first-row metals in place of the heavier elements currently used, there has been a very rapid expansion in the research space towards their implementation.[18]

Though the abundance of the first-row transition metals is attractive there are fundamental barriers to their use in many of the applications where ruthenium and iridium have found their footholds. Unlike the second- and third-row metals, the first-row metals are subject to the primogenic effect.[19,20] This effect is present in all elements for the first occurrence of an angular moment value, *l*. For the first transition series, where n=3 and *l*=2, this causes the radial extension of the *d*-orbitals to contract closer to the nucleus due to the absence of a radial node. This in turn causes a reduction in the overlap between the ligand-based orbitals and the metal 3*d*-orbitals leading to an effective decrease in ligand-field splitting, Δ_O or 10Dq, compared to the second- and

third-row metals.[20] This decreased splitting causes a stabilization of the LF states compared to the late transition series, changing the nature of the lowest-energy excited state from MLCT in nature to LF. This typically provides effective deactivation pathways from the charge-transfer states that are known to undergo electron-transfer to the fairly isolated and shorter-lived metal-centered LF states, thus hampering their use in light-induced electron transfer processes.

Though this may sound as if the first-row may be less likely to be able to be used in the applications dominated by ruthenium and iridium, there has been considerable and extremely promising work to that effect. One of the most explored early transition elements is Cu(I). Polypyridyl complexes of this element absorb visible light and populate a CT state. Due to Cu(I) being a d^{10} metal, the possibility of deactivation through low-lying LF states is not possible creating a long-lived MLCT. This has garnered its use in dye sensitized solar cells (DSSCs) and photoredox catalysis.[21–23] Moving from pure polypyridyl complexes, there have been exciting results in the use of polydentate isocyanide ligands on Mn(I) and Cr(0).[24–26] These ions possess a d^6 electron configuration and in these new ligand scaffolds have shown emissive MLCT states with lifetimes on the order of ~1 ns and ~6 ns, respectively, at room temperature.[25,27] There has also been considerable work in leveraging not just the MLCT but also the LF states of transition metal complexes for participation in bimolecular electron-transfer processes.[28–31]

Another attractive earth-abundant metal that has been investigated is Fe(II). When placed in a sufficiently strong LF, the d^6 ion takes on a low-spin configuration ($^1A_1$, t_{2g}^6) making it a great comparison to the valence isoelectronic second-row congener, Ru(II).[32] Apart from both possessing the same $^1A_1$ ground-state it is well known that the photophysics of these complexes differ greatly. Comparing $[Fe(bpy)_3]^{2+}$ and $[Ru(bpy)_3]^{2+}$, it was observed in 1980 by Creutz *et al.* that upon photoexcitation of both complexes into the MLCT manifold, a positive signal was only

observed in transient absorption measurements for $[Ru(bpy)_3]^{2+}$, corresponding to the formation of the bipyridine anion radical ($bpy^{-\bullet}$).[33] For $[Fe(bpy)_3]^{2+}$, a negative bleach signal was observed corresponding to the unity formation of a LF state in less than 10 ps due to the absence of the $bpy^{-\bullet}$ signature.[33] Since this observation and the advent of laser systems with sub-picosecond pulses, the entire photocycle of $[Fe(bpy)_3]^{2+}$ has been studied in great detail.

Similar to $[Ru(bpy)_3]^{2+}$, $[Fe(bpy)_3]^{2+}$ also absorbs strongly in the visible spectrum and upon absorption of light excites into a ^{1}MLCT manifold which then undergoes ultrafast intersystem crossing, sub 30 fs, into a ^{3}MLCT state.[34,35] From here, the photophysics of the two complexes begin to diverge. Unlike $[Ru(bpy)_3]^{2+}$ with the lowest-energy excited state being a ^{3}MLCT, the intrinsic LF strength of $[Fe(bpy)_3]^{2+}$ is substantially lower with the LF states now below the MLCT state Figure 1.4.[36,37] Due to the large density of states, deactivation from the ^{1,3}MLCT manifold to the lowest-energy excited state, $^5T_2$, occurs within 150 fs.[38–41] During this deactivation, an intermediate ^{3}T state is sampled but not populated as shown by the Gaffney group.[42] The ground-state is then fully recovered with ~1 ns from the $^5T_2$ ($t_{2g}^4 e_g^2$) LF state.[41,43] Over the years there have been many attempts to disrupt this photocycle and prolong the ^{3}MLCT lifetime to create an instance where Fe(II) behaves like Ru(II) through: addition of steric bulk, an increased octahedral coordination environment, and changing denticity of the ligator.[44–47] Unfortunately, these attempts, while creating interesting new complexes, have had little effect on the deactivation of the ^{3}MLCT.

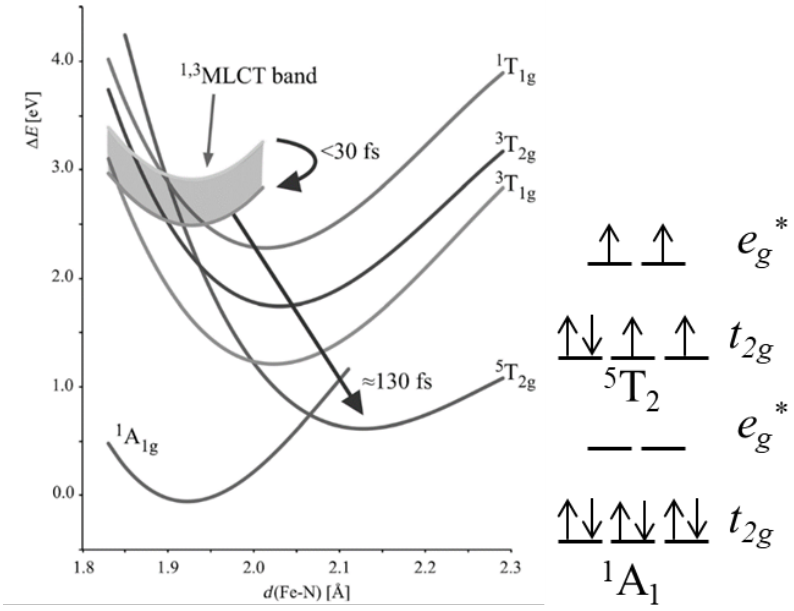

Figure 1.4. Calculated energetics and ordering of the ligand-field states of $[Fe(bpy)_3]^{2+}$ from reference 38 and the 1-electron picture of the low-spin and high-spin electron configurations.

The prohibitively short lifetime of the ^{3}MLCT of Fe(II) polypyridyl chromophores has impacted their use in many applications that require charge separation, especially in the case of bimolecular reactivity. Considering that the lifetimes of these chromophores are < 200 fs in the charge-separated state and the timescale for diffusion is typically on the order of nanoseconds it would require the extension of the lifetime of the MLCT state by orders of magnitude to be able to compete with ruthenium-based complexes. It has been shown that despite this short lifetime select iron-based chromophores are able to inject electrons into a TiO_2 substrate in use in DSSCs, though with an extremely low efficiency.[48] This low efficiency is again still associated with the short lifetime of the MLCT state.[49,50] Other avenues have sought to use the LF excited-states, typically thought not viable, instead of the MLCT for the use in photocatalysis with promising results as these states typically persist on the order of nanoseconds.[28,51,52] The main hurdle to this approach is the fairly isolated metal-center, for it to engage in electron-transfer, difficulty in tuning

the LF energetics to match with the organic substrates being used, and the small potential stored in these states.[53] As the $^5T_2$ is S = 2 and the ground-state is $^1A_1$, S = 0, this transition is not emissive precluding easily measuring the stored potential in these states across complexes as well.

In order to increase the ease of selection of iron-based chromophores for an application, the ^{3}MLCT lifetime must be increased. There are two approaches that can be envisioned for the extension of the charge-transfer state lifetime: a kinetic approach and an energetic approach. In essence, the kinetic approach seeks to constrain the geometric distortions that facilitate the ultrafast deactivation from the ^{3}MLCT (changes to the nuclear coordinate) whereas the energetic approach seeks to manipulate the energetic ordering of states so that excited-state landscape more closely resembles that of the second- and third-row congeners. Our group has recently shown that by encapsulating the Fe(II) ion inside a bipyridyl cage (Figure 1.5) that has been capped with Cu(I)-imines, the MLCT lifetime can be increased 20-fold to 2.6 ps.[54] Knowing that the deactivation from the MLCT to the $^5T_2$ is accompanied by a 0.2 Å elongation of the Fe-N bond lengths this became a molecular motion to target.[55,56] This new cage structure effectively constrains the expansion of the first-coordination sphere (Fe-N bonds) that is associated with formation of the $^5T_2$ state thereby slowing its population. This shows promise in leveraging the kinetic approach for MLCT lifetime extension.

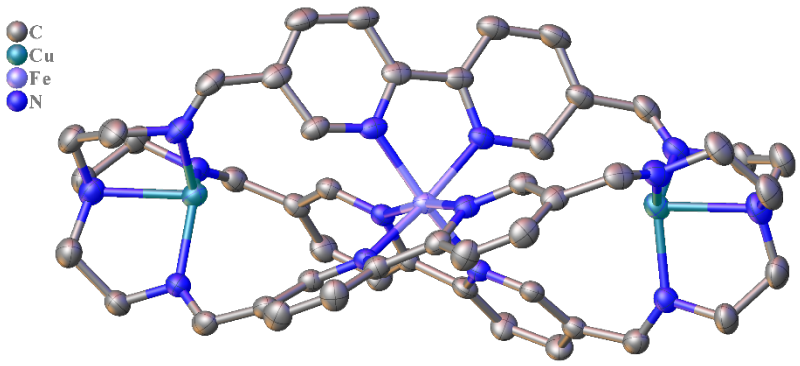

Figure 1.5. Crystal Structure of bipyridyl iron cage with anions and hydrogens removed for clarity. Thermal ellipsoids are presented at a 50% probability.

The energetic approach has been much more widely applied. Groups across the world have been attempting to tackle this research question with the main focus being the destabilization of the LF states with strong-field ligands to produce a ^{3}MLCT lowest-energy excited state. Our group initially pursued this approach utilizing a nearly perfectly octahedral complex, $[Fe(dcpp)_2]^{2+}$ (where dcpp is bis(2,6-di(2-carboxypyridyl)pyridine) based upon the work of Schramm *et al.* (Figure 1.6a).[46,57] The complex exhibited an extremely low energy MLCT transition, but the nearly perfect octahedral geometry about the Fe(II) center increased the rate of ground state recovery leading to a shorter lifetime for the MLCT and $^5T_2$ state, 76 fs and 280 ps, respectively. These dynamics and their analysis are discussed in great detail in the dissertation of Dr. Monica Carey.[58] The use of strong carbon-donors has been pioneered by Wärnmark and coworkers (Figure 1.6b). Through their use of six strongly σ-donating carbenes they have been able to achieve a complex with the lowest-energy excited state being ^{3}MLCT in character and a lifetime of 528 ps.[59] In a similar vein, the use of cyclometallation has also been explored, but with less appreciable increases in lifetime than to the carbene approach.[60] Another avenue pursued towards MLCT extension has been called HOMO-inversion (highest occupied molecular orbital). This approach was originally posited by the Jakubikova group whereby allowing the mixing of the metal *d*π-orbitals with the

filled *p*-orbitals of the ligand could create a situation in which the HOMO of the complex is no longer metal-based but ligand-based allowing for a panchromatic iron complex that could exhibit more favorable photophysical properties.[61] Taking inspiration from this computational study, Bruan *et al*. were able to successfully synthesize a new Fe(II) quinolinyl amido phenanthridine complex (Figure 1.6c) with this strategy where the complex exhibits panchromatic absorption as well as a record breaking MLCT lifetime of 2.5 ns.[62] In this complex, they attribute the long lifetime not to complete HOMO-inversion, but to an energetic match between the iron *d*π-orbitals and ligand π-system leading to intimate mixing with the lone pair on the amido moiety. The energetic approach therefore shows quite a promising method for prolonging the MLCT lifetime of iron-based chromophores.

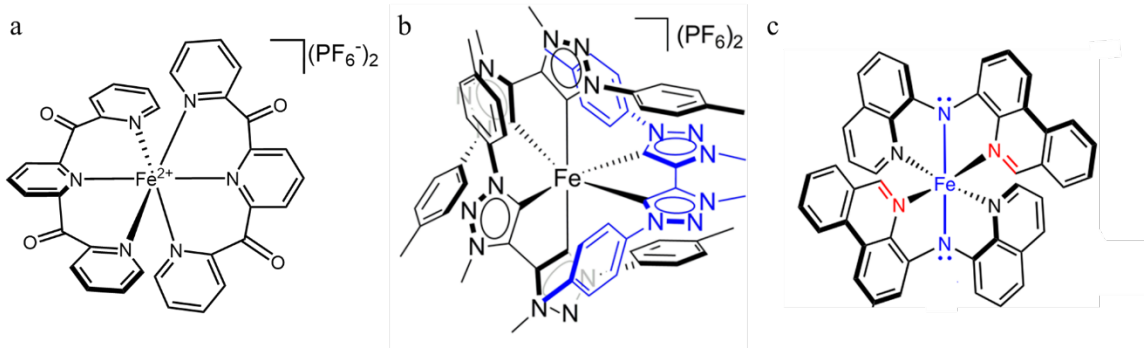

Figure 1.6. Drawings of (a) Octahedral Fe(II) complex(b) Wärnmark and coworkers' hexacarbene Fe(II) complex and (c) The Herbert group's panchromatic Fe(II) complex exhibiting HOMO-inversion.

With all the advances that have been made in the synthesis and understanding of Fe(II) chromophores with extended ^{3}MLCT lifetimes, there have been large steps towards using Fe(II) in applications that have always been dominated by Ru(II) and Ir(III). Though there is still work to be done, we are closer now than when the first glimpse of the ultrafast dynamics of iron were

observed in 1980. This is in thanks to the ability to modify the energetic landscape of these chromophores through judicious ligand design.

1.2 Contents of Dissertation

Chapter 2 first summarizes the findings of our 2022 *Journal of the American Chemical Society* report[63] on the use of electronic absorption spectroscopy of Co(III) polypyridyl complexes and the observation of ligand-field bands to build a spectrochemical series to better understand the LF energetics of Co(III) and to translate those findings to Fe(II) polypyridyl complexes. Chapter 3 continues the theme of understanding electronic structure through ligand design, but now focuses on the MLCT manifold of an Fe(II) complex previously synthesized by our group, $[Fe(dcpp)_2]^{2+}$,[46] and deconvolving the manifold through synthetic design via aromatic substitutions, understanding the unique structure through computational methods, and extending those findings towards achieving longer MLCT lifetimes. Chapter 4 attempts to build upon the insights gleaned from our groups 2021 report in the *Journal of the American Chemical Society* using a modular approach to carbenes.[64] Therein we were able to maintain the intense and low energy MLCT transition of polypyridyl ligands while inducing a strong LF through the of use acylic alkylamino carbenes. My work continues this by investigating new ligand motifs and incorporating new and stronger σ-donors to further destabilize the metal-centered states. Chapter 5 is a culmination of insights gained from each chapter towards future directions for the individual projects expanded on previously.

REFERENCES

(1) International Energy Agency. *World Energy Outlook, Executive Summary*; 2023.

(2) Crabtree, G. W.; Lewis, N. S. Solar Energy Conversion. *Phys. Today* **2007**, *60* (3), 37–42. DOI: 10.1063/1.2718755.

(3) Dogutan, D. K.; Nocera, D. G. Artificial Photosynthesis at Efficiencies Greatly Exceeding That of Natural Photosynthesis. *Acc. Chem. Res.* **2019**, *52* (11), 3143–3148. DOI: 10.1021/acs.accounts.9b00380.

(4) Juris, A.; Balzani, V.; Barigelletti, F.; Campagna, S.; Belser, P.; von Zelewsky, A. Ru(II) Polypyridine Complexes: Photophysics, Photochemistry, Electrochemistry, and Chemiluminescence. *Coord. Chem. Rev.* **1988**, *84*, 85–277. DOI: 10.1016/0010-8545(88)80032-8.

(5) Campagna, S.; Puntoriero, F.; Nastasi, F.; Bergamini, G.; Balzani, V. Photochemistry and Photophysics of Coordination Compounds: Ruthenium. In *Photochemistry and Photophysics of Coordination Compounds I*; Springer Berlin Heidelberg: Berlin, Heidelberg, 2007; Vol. 280, pp 117–214. DOI: 10.1007/128_2007_133.

(6) Hofbeck, T.; Yersin, H. The Triplet State of *Fac* -Ir(Ppy)$_3$. *Inorg. Chem.* **2010**, *49* (20), 9290–9299. DOI: 10.1021/ic100872w.

(7) Koide, Y.; Takahashi, S.; Vacha, M. Simultaneous Two-Photon Excited Fluorescence and One-Photon Excited Phosphorescence from Single Molecules of an Organometallic Complex Ir(Ppy)$_3$. *J. Am. Chem. Soc.* **2006**, *128* (34), 10990–10991. DOI: 10.1021/ja0616635.

(8) Damrauer, N. H.; McCusker, J. K. Ultrafast Dynamics in the Metal-to-Ligand Charge Transfer Excited-State Evolution of [Ru(4,4′-Diphenyl-2,2′-Bipyridine)$_3$]$^{2+}$. *J. Phys. Chem. A* **1999**, *103* (42), 8440–8446. DOI: 10.1021/jp9927754.

(9) Ladouceur, S.; Swanick, K. N.; Gallagher-Duval, S.; Ding, Z.; Zysman-Colman, E. Strongly Blue Luminescent Cationic Iridium(III) Complexes with an Electron-Rich Ancillary Ligand: Evaluation of Their Optoelectronic and Electrochemiluminescence Properties. *Eur. J. Inorg. Chem.* **2013**, 5329–5343. DOI: 10.1002/ejic.201300849.

(10) O'Regan, B.; Grätzel, M. A Low-Cost, High-Efficiency Solar Cell Based on Dye-Sensitized Colloidal TiO_2 Films. *Nature* **1991**, *353*, 737–740. DOI: 10.1038/353737a0.

(11) Aghazada, S.; Gao, P.; Yella, A.; Marotta, G.; Moehl, T.; Teuscher, J.; Moser, J.-E.; De Angelis, F.; Grätzel, M.; Nazeeruddin, M. K. Ligand Engineering for the Efficient Dye-Sensitized Solar Cells with Ruthenium Sensitizers and Cobalt Electrolytes. *Inorg. Chem.* **2016**, *55* (13), 6653–6659. DOI: 10.1021/acs.inorgchem.6b00842.

(12) Sinopoli, A.; Wood, C. J.; Gibson, E. A.; Elliott, P. I. P. New Cyclometalated Iridium(III) Dye Chromophore Complexes for p-Type Dye-Sensitised Solar Cells. *Dyes and Pigments* **2017**, *140*, 269–277. DOI: 10.1016/j.dyepig.2017.01.011.

(13) Sakai, H. A.; MacMillan, D. W. C. Nontraditional Fragment Couplings of Alcohols and Carboxylic Acids: C(sp^3)–C(sp^3) Cross-Coupling via Radical Sorting. *J. Am. Chem. Soc.* **2022**, *144* (14), 6185–6192. DOI: 10.1021/jacs.2c02062.

(14) Shaw, M. H.; Twilton, J.; MacMillan, D. W. C. Photoredox Catalysis in Organic Chemistry. *J. Org. Chem.* **2016**, *81* (16), 6898–6926. DOI: 10.1021/acs.joc.6b01449.

(15) Teegardin, K.; Day, J. I.; Chan, J.; Weaver, J. Advances in Photocatalysis: A Microreview of Visible Light Mediated Ruthenium and Iridium Catalyzed Organic Transformations. *Org. Process. Res. Dev.* **2016**, *20* (7), 1156–1163. DOI: 10.1021/acs.oprd.6b00101.

(16) Chan, A. Y.; Perry, I. B.; Bissonnette, N. B.; Buksh, B. F.; Edwards, G. A.; Frye, L. I.; Garry, O. L.; Lavagnino, M. N.; Li, B. X.; Liang, Y.; Mao, E.; Millet, A.; Oakley, J. V.; Reed, N. L.; Sakai, H. A.; Seath, C. P.; MacMillan, D. W. C. Metallaphotoredox: The Merger of Photoredox and Transition Metal Catalysis. *Chem. Rev.* **2022**, *122* (2), 1485–1542. DOI: 10.1021/acs.chemrev.1c00383.

(17) United States Geological Survey. *Rare Earth Elements-Critical Resources for High Technology*. Rare Earth Elements—Critical Resources for High Technology (accessed 2023-09-12).

(18) Wenger, O. S. Photoactive Complexes with Earth-Abundant Metals. *J. Am. Chem. Soc.* **2018**, *140* (42), 13522–13533. DOI: 10.1021/jacs.8b08822.

(19) Pyykko, P. Relativistic Effects in Structural Chemistry. *Chem. Rev.* **1988**, *88* (3), 563–594. DOI: 10.1021/cr00085a006.

(20) McCusker, J. K. Electronic Structure in the Transition Metal Block and Its Implications for Light Harvesting. *Science* **2019**, *363* (6426), 484–488. DOI: 10.1126/science.aav9104.

(21) Alonso-Vante, N.; Nierengarten, J.-F.; Sauvage, J.-P. Spectral Sensitization of Large-Band-Gap Semiconductors (Thin Films and Ceramics) by a Carboxylated Bis(1,10-Phenanthroline)Copper(I) Complex. *J. Chem. Soc., Dalton Trans.* **1994**, No. 11, 1649. DOI: 10.1039/dt9940001649.

(22) Housecroft, C. E.; Constable, E. C. The Emergence of Copper(I)-Based Dye Sensitized Solar Cells. *Chem. Soc. Rev.* **2015**, *44* (23), 8386–8398. DOI: 10.1039/C5CS00215J.

(23) Hossain, A.; Bhattacharyya, A.; Reiser, O. Copper's Rapid Ascent in Visible-Light Photoredox Catalysis. *Science* **2019**, *364* (eaav9713). DOI: 10.1126/science.aav9713.

(24) Büldt, L. A.; Guo, X.; Prescimone, A.; Oliver Wenger, and S.; Büldt, L. A.; Guo, D.; Prescimone, D.; enger, D. Photoredox Catalysis A Molybdenum(0) Isocyanide Analogue of

Ru(2,2′-Bipyridine)$_3^{2+}$: A Strong Reductant for Photoredox Catalysis. **2016**, *55*, 1247–11250. DOI: 10.1002/ange.201605571.

(25) Herr, P.; Kerzig, C.; Larsen, C. B.; Häussinger, D.; Wenger, O. S. Manganese(I) Complexes with Metal-to-Ligand Charge Transfer Luminescence and Photoreactivity. *Nat. Chem.* **2021**, *13* (10), 956–962. DOI: 10.1038/s41557-021-00744-9.

(26) Büldt, L. A.; Guo, X.; Vogel, R.; Prescimone, A.; Wenger, O. S. A Tris(Diisocyanide)Chromium(0) Complex Is a Luminescent Analog of Fe(2,2′-Bipyridine)$_3^{2+}$. *J. Am. Chem. Soc.* **2017**, *139* (2), 985–992. DOI: 10.1021/jacs.6b11803.

(27) Wegeberg, C.; Häussinger, D.; Wenger, O. S. Pyrene-Decoration of a Chromium(0) Tris(Diisocyanide) Enhances Excited State Delocalization: A Strategy to Improve the Photoluminescence of 3d^6 Metal Complexes. *J. Am. Chem. Soc.* **2021**, *143* (38), 15800–15811. DOI: 10.1021/jacs.1c07345.

(28) Woodhouse, M. D.; McCusker, J. K. Mechanistic Origin of Photoredox Catalysis Involving Iron(II) Polypyridyl Chromophores. *J. Am. Chem. Soc.* **2020**, *142* (38), 16229–16233. DOI: 10.1021/jacs.0c08389.

(29) Dorn, M.; East, N. R.; Förster, C.; Kitzmann, W. R.; Moll, J.; Reichenauer, F.; Reuter, T.; Stein, L.; Heinze, K. D-d and Charge Transfer Photochemistry of 3d Metal Complexes. In *Comprehensive Inorganic Chemistry III*; Reedijk, J., Poeppelmeier, K. R., Eds.; Elsevier, 2023; pp 707–788. DOI: 10.1016/B978-0-12-823144-9.00063-7.

(30) Chan, A. Y.; Ghosh, A.; Yarranton, J. T.; Twilton, J.; Jin, J.; Arias-Rotondo, D. M.; Sakai, H. A.; McCusker, J. K.; MacMillan, D. W. C. Exploiting the Marcus Inverted Region for First-Row Transition Metal-Based Photoredox Catalysis. *Accepted to Science* **2023**.

(31) Alowakennu, M. M.; Ghosh, A.; McCusker, J. K. Direct Evidence for Excited Ligand Field State-Based Oxidative Photoredox Chemistry of a Cobalt(III) Polypyridyl Photosensitizer. *J Am Chem Soc* **2023**, *145* (38), 20786–20791. DOI: 10.1021/jacs.3c09374.

(32) Wenger, O. S. Is Iron the New Ruthenium? *Chem. Euro. J.* **2019**, *25* (24), 6043–6052. DOI: 10.1002/chem.201806148.

(33) Creutz, C.; Chou, M.; Netzel, T. L.; Okumura, M.; Sutin, N. Lifetimes, Spectra, and Quenching of the Excited States of Polypyridine Complexes of Iron(II), Ruthenium(II), and Osmium(II). *J. Am. Chem. Soc.* **1980**, *102* (4), 1309–1319. DOI: 10.1021/ja00524a014.

(34) Cannizzo, A.; van Mourik, F.; Gawelda, W.; Zgrablic, G.; Bressler, C.; Chergui, M. Broadband Femtosecond Fluorescence Spectroscopy of [Ru(Bpy)$_3$]$^{2+}$. *Angew. Chem. Int. Ed.* **2006**, *45* (19), 3174–3176. DOI: 10.1002/anie.200600125.

(35) Gawelda, W.; Cannizzo, A.; Pham, V.-T.; van Mourik, F.; Bressler, C.; Chergui, M. Ultrafast Nonadiabatic Dynamics of [Fe^{II}(Bpy)$_3$]$^{2+}$ in Solution. *J. Am. Chem. Soc.* **2007**, *129* (26), 8199–8206. DOI: 10.1021/ja070454x.

(36) de Graaf, C.; Sousa, C. Study of the Light-Induced Spin Crossover Process of the $[Fe^{II}(Bpy)_3]^{2+}$ Complex. *Chem. Euro. J.* **2010**, *16* (15), 4550–4556. DOI: 10.1002/chem.200903423.

(37) Graaf, C. De; Sousa, C. On the Role of the Metal-to-ligand Charge Transfer States in the Light-induced Spin Crossover in $Fe^{II}(Bpy)_3$. *Int. J. Quantum Chem.* **2011**, *111* (13), 3385–3393. DOI: 10.1002/qua.22991.

(38) Sousa, C.; De Graaf, C.; Rudavskyi, A.; Broer, R.; Tatchen, J.; Etinski, M.; Marian, C. M. Ultrafast Deactivation Mechanism of the Excited Singlet in the Light-Induced Spin Crossover of $[Fe(2,2'\text{-Bipyridine})_3]^{2+}$. *Chem. Euro. J.* **2013**, *19* (51), 17541–17551. DOI: 10.1002/chem.201302992.

(39) Auböck, G.; Chergui, M. Sub-50-Fs Photoinduced Spin Crossover in $[Fe(Bpy)_3]^{2+}$. *Nat. Chem.* **2015**, *7* (8), 629–633. DOI: 10.1038/nchem.2305.

(40) Smeigh, A. L.; Creelman, M.; Mathies, R. A.; McCusker, J. K. Femtosecond Time-Resolved Optical and Raman Spectroscopy of Photoinduced Spin Crossover: Temporal Resolution of Low-to-High Spin Optical Switching. *J. Am. Chem. Soc.* **2008**, *130* (43), 14105–14107. DOI: 10.1021/ja805949s.

(41) McCusker, J. K.; Walda, K. N.; Dunn, R. C.; Simon, J. D.; Magde, D.; Hendrickson, D. N. Subpicosecond $^1MLCT \rightarrow {}^5T_2$ Intersystem Crossing of Low-Spin Polypyridyl Ferrous Complexes. *J. Am. Chem. Soc.* **1993**, *115* (1), 298–307. DOI: 10.1021/ja00054a043.

(42) Zhang, W.; Alonso-Mori, R.; Bergmann, U.; Bressler, C.; Chollet, M.; Galler, A.; Gawelda, W.; Hadt, R. G.; Hartsock, R. W.; Kroll, T.; Kjær, K. S.; Kubiek, K.; Lemke, H. T.; Liang, H. W.; Meyer, D. A.; Nielsen, M. M.; Purser, C.; Robinson, J. S.; Solomon, E. I.; Sun, Z.; Sokaras, D.; Van Driel, T. B.; Vankó, G.; Weng, T. C.; Zhu, D.; Gaffney, K. J. Tracking Excited-State Charge and Spin Dynamics in Iron Coordination Complexes. *Nature* **2014**, *509* (7500), 345–348. DOI: 10.1038/nature13252.

(43) Carey, M. C.; Adelman, S. L.; Mccusker, J. K. Insights into the Excited State Dynamics of Fe(II) Polypyridyl Complexes from Variable-Temperature Ultrafast Spectroscopy. *Chem. Sci.* **2019**, *10*, 134-144. DOI: 10.1039/c8sc04025g.

(44) Shepard, S. G.; Fatur, S. M.; Rappé, A. K.; Damrauer, N. H. Highly Strained Iron(II) Polypyridines: Exploiting the Quintet Manifold To Extend the Lifetime of MLCT Excited States. *J. Am. Chem. Soc.* **2016**, *138* (9), 2949–2952. DOI: 10.1021/jacs.5b13524.

(45) Fatur, S. M.; Shepard, S. G.; Higgins, R. F.; Shores, M. P.; Damrauer, N. H. A Synthetically Tunable System To Control MLCT Excited-State Lifetimes and Spin States in Iron(II) Polypyridines. *J. Am. Chem. Soc.* **2017**, *139* (12), 4493–4505. DOI: 10.1021/jacs.7b00700.

(46) Jamula, L. L.; Brown, A. M.; Guo, D.; McCusker, J. K. Synthesis and Characterization of a High-Symmetry Ferrous Polypyridyl Complex: Approaching the $^5T_2/^3T_1$ Crossing Point for FeII. *Inorg. Chem.* **2014**, *53* (1), 15–17. DOI: 10.1021/ic402407k.

(47) Jamula, L. L. Exploring Design Strategies to Tune the Electronic Structure and Ultrafast Dynamics of Iron(II) Polypyridyl Chromophores. Ph. D., Michigan State University, East Lansing, 2013.

(48) Ferrere, S.; Gregg, B. A. Photosensitization of TiO_2 by [Fe(II)(2,2′-Bipyridine-4,4′-Dicarboxylic Acid)$_2$(CN)$_2$]: Band Selective Electron Injection from Ultra-Short-Lived Excited States. *J. Am. Chem. Soc.* **1998**, *120* (4), 843–844. DOI: 10.1021/ja973504e.

(49) Tachibana, Y.; Moser, J. E.; Grätzel, M.; Klug, D. R.; Durrant, J. R.; Hannappel, T.; Burfeindt, B.; Storck, W.; Willig, F.; Schilt, A. A. *Photosensitization of TiO_2 by [Fe^{II}(2,2'-Bipyridine-4,4'-Dicarboxylic Acid)$_2$(CN)$_2$]: Band Selective Electron Injection from Ultra-Short-Lived Excited States*; 1993; Vol. 115.

(50) Tichnell, C. R.; Miller, J. N.; Liu, C.; Mukherjee, S.; Jakubikova, E.; Mccusker, J. K. Influence of Electrolyte Composition on Ultrafast Interfacial Electron Transfer in Fe-Sensitized TiO2-Based Solar Cells. *J. Phys. Chem. C* **2020**, *124* (3), 1794–1811. DOI: 10.1021/ACS.JPCC.9B09404.

(51) Gualandi, A.; Marchini, M.; Mengozzi, L.; Natali, M.; Lucarini, M.; Ceroni, P.; Cozzi, P. G. Organocatalytic Enantioselective Alkylation of Aldehydes with [Fe(Bpy)$_3$]Br$_2$ Catalyst and Visible Light. *ACS Catal.* **2015**, *5* (10), 5927–5931. DOI: 10.1021/acscatal.5b01573.

(52) Parisien-Collette, S.; Hernandez-Perez, A. C.; Collins, S. K. Photochemical Synthesis of Carbazoles Using an [Fe(Phen)$_3$](NTf$_2$)$_2$/O$_2$ Catalyst System: Catalysis toward Sustainability. *Org. Lett.* **2016**, *18* (19), 4994–4997. DOI: 10.1021/acs.orglett.6b02456.

(53) Ashley, D. C.; Jakubikova, E. Tuning the Redox Potentials and Ligand Field Strength of Fe(II) Polypyridines: The Dual π-Donor and π-Acceptor Character of Bipyridine. *Inorg. Chem.* **2018**, *57* (16), 9907–9917. DOI: 10.1021/acs.inorgchem.8b01002.

(54) Paulus, B. C.; Adelman, S. L.; Jamula, L. L.; McCusker, J. K. Leveraging Excited-State Coherence for Synthetic Control of Ultrafast Dynamics. *Nature* **2020**, *582* (7811), 214–218. DOI: 10.1038/s41586-020-2353-2.

(55) Gawelda, W.; Pham, V.-T.; Benfatto, M.; Zaushitsyn, Y.; Kaiser, M.; Grolimund, D.; Johnson, S. L.; Abela, R.; Hauser, A.; Bressler, C.; Chergui, M. Structural Determination of a Short-Lived Excited Iron(II) Complex by Picosecond X-Ray Absorption Spectroscopy. *Phys. Rev. Lett.* **2007**, *98* (5), 057401. DOI: 10.1103/PhysRevLett.98.057401.

(56) Jiang, Y.; Liu, L. C.; Sarracini, A.; Krawczyk, K. M.; Wentzell, J. S.; Lu, C.; Field, R. L.; Matar, S. F.; Gawelda, W.; Müller-Werkmeister, H. M.; Miller, R. J. D. Direct Observation of Nuclear Reorganization Driven by Ultrafast Spin Transitions. *Nat. Commun.* **2020**, *11* (1). DOI: 10.1038/s41467-020-15187-y.

(57) Schramm, F.; Meded, V.; Fliegl, H.; Fink, K.; Fuhr, O.; Qu, Z.; Klopper, W.; Finn, S.; Keyes, T. E.; Ruben, M. Expanding the Coordination Cage: A Ruthenium(II)−Polypyridine Complex Exhibiting High Quantum Yields under Ambient Conditions. *Inorg. Chem.* **2009**, *48* (13), 5677–5684. DOI: 10.1021/ic802040v.

(58) Carey, M. C. Achieving a Long-Lived Charge-Seperated Fe(II) Chromophore: Insights into the Role of Reorganization Energy on the Ultrafast Photophysical Processes of D6 Polypyridyl Complexes, Michigan State University, East Lansing, 2018.

(59) Chábera, P.; Kjaer, K. S.; Prakash, O.; Honarfar, A.; Liu, Y.; Fredin, L. A.; Harlang, T. C. B.; Lidin, S.; Uhlig, J.; Sundström, V.; Lomoth, R.; Persson, P.; Wärnmark, K. FeII Hexa N-Heterocyclic Carbene Complex with a 528 Ps Metal-To-Ligand Charge-Transfer Excited-State Lifetime. *J. Phys. Chem. Lett.* **2018**, *9* (3), 459–463. DOI: 10.1021/acs.jpclett.7b02962.

(60) Steube, J.; Burkhardt, L.; Päpcke, A.; Moll, J.; Zimmer, P.; Schoch, R.; Wölper, C.; Heinze, K.; Lochbrunner, S.; Bauer, M. Excited-State Kinetics of an Air-Stable Cyclometalated Iron(II) Complex. *Chem. Euro. J.* **2019**, *25* (51), 11826–11830. DOI: 10.1002/chem.201902488.

(61) Mukherjee, S.; Torres, D. E.; Jakubikova, E. HOMO Inversion as a Strategy for Improving the Light-Absorption Properties of Fe(II) Chromophores. *Chem. Sci.* **2017**, *8* (12), 8115–8126. DOI: 10.1039/c7sc02926h.

(62) Braun, J. D.; Lozada, I. B.; Kolodziej, C.; Burda, C.; Newman, K. M. E.; van Lierop, J.; Davis, R. L.; Herbert, D. E. Iron(II) Coordination Complexes with Panchromatic Absorption and Nanosecond Charge-Transfer Excited State Lifetimes. *Nat. Chem.* **2019**, *11* (12), 1144–1150. DOI: 10.1038/s41557-019-0357-z.

(63) Yarranton, J. T.; McCusker, J. K. Ligand-Field Spectroscopy of Co(III) Complexes and the Development of a Spectrochemical Series for Low-Spin d^6 Charge-Transfer Chromophores. *J. Am. Chem. Soc.* **2022**, *144* (27), 12488–12500. DOI: 10.1021/jacs.2c04945.

(64) Paulus, B. C.; Nielsen, K. C.; Tichnell, C. R.; Carey, M. C.; McCusker, J. K. A Modular Approach to Light Capture and Synthetic Tuning of the Excited-State Properties of Fe(II)-Based Chromophores. *J. Am. Chem. Soc.* **2021**, *143* (21), 8086–8098. DOI: 10.1021/jacs.1c02451.

CHAPTER 2: LIGAND-FIELD SPECTROSCOPY OF Co(III) COMPLEXES AND THE DEVELOPMENT OF A SPECTROCHEMICAL SERIES FOR LOW-SPIN d^6 CHARGE-TRANSFER CHROMOPHORES

2.1 Introduction

The photophysical properties of first-row metal complexes have experienced renewed interest over the past several years due to the emergent recognition of the value of earth-abundant alternatives to the more commonly employed second- and third-row transition metal-based chromophores for a variety of photolytic applications.[1–3] Many of these applications focus on electron transfer processes, where the absorbed light results in the formation of an excited state that can facilitate the oxidation or reduction of substrates ranging from semiconductors in the case of photovoltaics (e.g., dye-sensitized solar cells)[4,5] to organic molecules in the rapidly expanding field of photoredox catalysis.[6] Although there are circumstances in which ligand-field excited states can engage in electron transfer chemistry,[7–9] charge-transfer excited states are more predisposed toward this type of chemistry due to the fact that light absorption directly results in the creation of chemical potential in the form of a charge-separated species. While the absorptive properties of many first-row metal complexes are dominated by intense charge-transfer bands in much the same way as their second- and third-row congeners, the relative energies of their charge-transfer and ligand-field-state manifolds are such that ultrafast conversion from the former to the latter outpaces the desired charge transfer-based chemistry. The origin of this situation can be linked to the primogenic effect,[10] resulting in weaker metal-ligand interactions in the first transition series relative to other regions of the transition block and impacts a host of physical and photophysical properties, including the propensity toward photo-induced electron transfer.

Identification of the nature of this problem has spurred considerable research activity into finding ways around this situation in order to create new classes of first-row chromophores whose photophysical properties resemble compounds like $[Ru(bpy)_3]^{2+}$ and $Ir(ppy)_3$. The most successful approaches have exploited the strong σ-donating characteristics of carbene and isocyanide ligands. The pioneering example was published by Wärnmark and co-workers in 2013,[11] but this has since been followed by and expanded upon through work from a number of groups including Wenger,[12] Heinze,[13] Bauer,[14,15] Herbert,[16,17] and Gros[18,19] to name a few. A less well-developed but potentially promising approach of exploiting information from quantum coherence was recently demonstrated by us,[20] but for both of these research threads the problem ultimately distills down to synthetic design. Proper synthetic design in turn relies on an understanding of the key parameters that are needed to create an electronic structure in a first-row metal complex that mimics what is easily realized in the second and third transition series.

The success achieved with ligand motifs such as N-heterocyclic carbenes derives from the strong ligand field that these sorts of molecules present to the metal ion. The energetics of charge-transfer states are more closely aligned with redox potentials (e.g., the oxidation potential of the metal and reduction potential of the ligand for metal-to-ligand charge-transfer states), so approaches that target ligand-field strength rely on destabilizing the ligand-field excited states such that the CT state(s) are the lowest energy excited states of the system. Recent work from our group suggests that these two factors can be independently controlled,[21] but a significant challenge for achieving this energetic inversion stems from an inability to know in advance the ligand-field strength required to achieve the desired result. The problem is compounded by the fact that experimentally assessing ligand-field strengths is difficult if not impossible in most first-row systems of interest. For example, the spectrum of $[Fe(bpy)_3]^{2+}$ shown in Figure 2.1 is dominated

in the mid-visible by an intense feature assigned as a $^1A_1 \rightarrow {}^1$MLCT transition(s). The molar absorptivity of this band is on the order of 10,000 M^{-1} cm^{-1} – exactly what one wants from the perspective of light capture – but its large oscillator strength simultaneously prevents an evaluation of the ligand-field strength associated with 2,2'-bipyridine because the (much weaker) d-d transitions that inform on ligand-field strength are buried under the MLCT envelope. This is a conundrum that one is faced with across the first transition series, i.e., ligands that facilitate the realization of intense absorption cross-sections for light harvesting are at the same time obscuring certain features necessary to assess their ability to leverage that stored chemical potential.

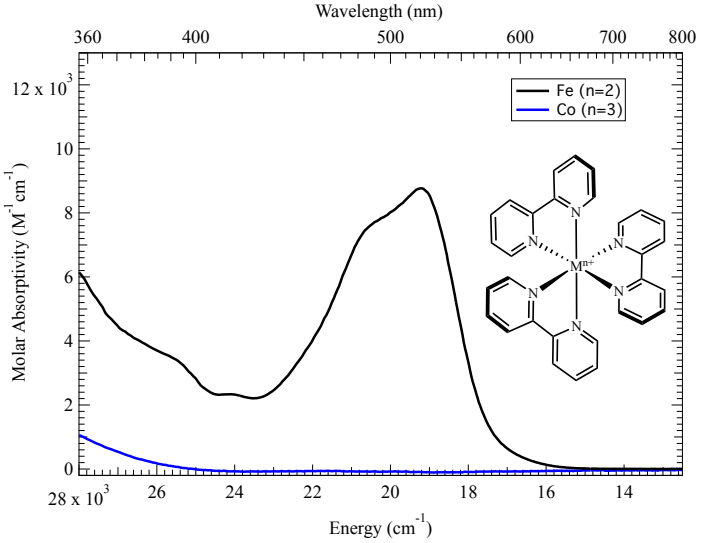

Figure 2.1. Electronic absorption spectra of $[Fe(bpy)_3](PF_6)_2$ (black) and $[Co(bpy)_3](PF_6)_2$ (blue) in CH_3CN. The plots reveal the significant difference in the optical characteristics of these isoelectronic species due to the change in character of the charge-transfer band from the MLCT in the case of Fe(II) to the LMCT in the case of Co(III).

The question of how to gauge ligand-field strength with an eye toward application-driven synthetic design is not new. Indeed, this issue was studied extensively in the area of spin-crossover chemistry, where the goal was to design systems whose ligand-field strength was comparable to the spin-pairing energy such that variations in temperature could drive interconversion between

the low-spin and high-spin forms of a given compound.[22,23] A successful approach along these lines in the case of Fe(II) spin-crossover systems was to examine isoelectronic Co(III) analogs.[24] The change in character of the charge-transfer band from MLCT in the case of Fe(II) to LMCT for Co(III) contributes to a dramatic blue-shift of this absorption feature into the near-ultraviolet (Figure 2.1, blue line), thereby allowing the lower intensity d-d bands in the visible region of the spectrum to be revealed.

In this report, we have used this same approach to create a strategy for developing what amounts to a spectrochemical series for charge-transfer complexes of six-coordinate d^6 first-row metal complexes. Specifically, the synthesis and spectroscopic characterization of a range of Co(III) complexes has allowed us to determine all of the relevant ligand-field parameters that define these ligand systems; the observation of spin-forbidden bands has furthermore provided the necessary information to specify values not just for 10 Dq – the ligand field-splitting parameter – but also independent values for other terms relevant to excited-state electronic structure. To our knowledge, these results provide the first experimental insights into the relative ligand-field strengths of commonly used ligands to effect light absorption by transition metal-based charge-transfer states and, we believe, will contribute to the realization of a roadmap for synthetic design of photofunctional chromophores based on first-row transition metal ions.

2.2 Experimental

2.2.1 Synthesis

General. All reaction and spectroscopic solvents were obtained from Sigma Aldrich Chemical Co. and used without further purification unless otherwise stated. Dry THF, MeCN, and DCM were obtained from a Solvtek solvent drying system. 2,2′-bipyridine (bpy), 4,4′-dimethyl-2,2′-bipyridine (4,4'-dmb), 5,5′-dimethyl-2,2′-bipyridine (5,5'-dmb), and 4,4′-di(tert-butyl)-2,2′-

bipyridine (dtb), 4,4'-dimethoxy-2,2′-bipyridine (OMe_2bpy) were obtained from Oakwood Chemicals. 2,2′:6′,2″-terpyridine (tpy) and elemental bromine were obtained from Sigma Aldrich. 4,4′-dibromo-2,2′-bipyridine (Br_2bpy) was obtained from Ambeed. $Co(ClO_4)_2•6H_2O$ and anhydrous $CoBr_2$ were obtained from Alfa Aesar. $CoCl_2•6H_2O$ was obtained from Spectrum Chemical. $NOPF_6$ was obtained from Acros Organics. NMR spectra were collected in the Max T. Rogers NMR Facility of Michigan State University on an Agilent 500 MHz spectrometer; spectra were referenced internally to the residual solvent peak. Elemental analyses were performed by Midwest Micro Labs. 4,4'-diethylester-2,2′-bipyridine (deeb),[25,26] 4,4′-dichloro-2,2′-bipyridine (Cl-bpy),[27] 3,3′-(pyridine-2,6-diyl)bis(1-methyl-1*H*-3-imidazolium) hexafluorophosphate ($[B^{Me}ImPyH](PF_6)_2$),[28] $[Co(NH_3)_6]Cl_3$,[29] $[Co(en)_3]Cl_3$,[30] $[Co(bpy)_3](PF_6)_3$,[31] $[Co(4,4'\text{-}dmb)_3](PF_6)_3$,[32] $[Co(5,5'\text{-}dmb)_3](PF_6)_3$,[32] $[Co(phen)_3](PF_6)_3$,[31] $[Co(dtb)_3](PF_6)_3$,[31] $[Co(terpy)_2](PF_6)_3$,[33] $[Co(Cl\text{-}bpy)_3](PF_6)_3$,[34] and $[Co(OMe\text{-}bpy)_3](PF_6)_3$[35] were all prepared by literature methods.

tris-(4,4'-diethylester-2,2'-bipyiridine)cobalt(II) hexafluorophosphate, ($[Co(deeb)_3](ClO_4)_2$). ***Care should be taken as metal perchlorates are potentially explosive.*** An amount of 0.400 g of deeb (1.3 mmol, 3.3 eq) was dissolved in 30 mL of $CHCl_3$. A solution of 0.147 g of $Co(ClO_4)_2•6H_2O$ (0.40 mmol, 1.0 eq) in 15 mL of acetone was added dropwise producing an orange solution. The solution was stirred overnight at room temperature; during the course of the reaction a precipitate formed. The reaction mixture was filtered and washed with $CHCl_3$ and diethyl ether. The yellow solid was dried under vacuum. The complex was used without further purification. Yield: 0.329 g (72%).

tris-(4,4'-diethylester-2,2'-bipyiridine)cobalt(III) hexafluorophosphate ($[Co(deeb)_3](PF_6)_3$). An amount of 0.300 g of $[Co(deeb)_3](ClO_4)_2$ (0.26 mmol, 1.0 eq) were dissolved in 20 mL of dry

CH_2Cl_2 and 53 mg of solid $NOPF_6$ (0.31 mmol, 1.2 eq) were added. The reaction stirred vigorously under N_2 for 2 h. The dark solution slowly became cloudy with a yellow precipitate. The dichrloromethane was evaporated and the complex was dissolved in minimal MeCN and excess NH_4PF_6 was added and it stirred for 30 min. Diethyl ether was added to crash out a pale yellow solid. It was filtered and washed with H_2O, EtOH, and diethyl ether and dried under vacuum. It was recrystallized by slow diffusion of diethyl ether into an acetonitrile/ethanol solution.. Yield: 0.253 g (70%). Anal. Calcd. (Found) for $C_{48}H_{48}CoF_{18}N_6O_{12}P_3$: C, 41.43 (40.98); H, 3.47 (3.52); N 6.03 (5.76). ^{1}H NMR (500 MHz, acetone-d_6): δ 9.66 (d, *J*=1.9 Hz, 2H), 8.25 (dd, *J*=6.1, 1.9 Hz, 2H), 8.16 (d, *J*=6.0 Hz, 2H), 4.48 (q, *J*= 7.2 Hz, 4H), 1.36 (t, *J*=6.9 Hz, 6H).

Tris(4,4′-dipyrrolidinyl-2,2′-bipyridine)cobalt(III) hexafluorophosphate ([Co(pyrro-bpy)$_3$](PF$_6$)$_3$). Starting from $[Co(Cl\text{-}bpy)_3](PF_6)_3$, 0.266 g (0.230 mmol, 1.00 eq) were suspended in 30 mL of dry still methanol and 300 µL of pyrrolidine (3.6 mmol, 16 eq) were added. The solution instantly changed colors from yellow to red-orange and the solution was heated overnight under N_2. Once at reflux, 1-2 mL of MeCN were added to aid solubilization. The solution was cooled to room temperature and 0.371 g of NH_4PF_6 (2.30 mmol, 10.0 eq) were added and stirred for 30 min. The solvent was removed and the residue was suspended in 50 mL of water and vacuum filtered. The orange solid was washed with H_2O (6 x 30 mL) and diethyl ether until a powder formed. The solid was dried under vacuum. It was recrystallized by slow diffusion of diethyl ether into an acetone/methanol solution. Yield: 0.221 g (70%). Anal. Calcd. (Found) for $C_{54}H_{66}CoF_{18}N_{12}P_3$: C, 47.10 (47.15); H, 4.83 (4.61); N 12.21 (11.81). ^{1}H NMR (500 MHz, acetone-d_6): δ 7.8 (d, *J*=2.8 Hz, 2H), 6.98 (d, *J*=7.1 Hz, 2H), 6.80 (dd, *J*=7.2, 2.8 Hz, 2H), 3.62 (m, 4H), 3.47 (m, 4H), 2.09 (m, 8H).

Tris(4,4′-dibromo-2,2′-bipyridine)cobalt(II) hexafluorophosphate, ([Co(Br$_2$bpy)$_3$](PF$_6$)$_2$). To a round-bottom flask containing 60 mL of CH_3CN was added 977 mg of Br_2bpy (3.0 mmol, 3.0 equiv.). A 15 mL aqueous solution of 238 mg of $CoCl_2$•$6H_2O$ (1.0 mmol, 1.0 equiv.) was added slowly to the suspension, affording an orange mixture. The suspension was heated to 70 ºC for 1 hour after which an orange solution formed. A saturated aqueous solution of KPF_6 was added to the hot solution causing precipitation of a pale solid. The solid was filtered and washed with H_2O (3 x 20 mL), MeOH (3 x 20 mL), and Et_2O. The complex was crystallized by slow diffusion of Et_2O into a saturated CH_3CN solution of the complex. The complex was used in the next step without further purification. Yield: 1.006 g (78%). ^{1}H NMR (CD_3CN, 500 MHz): δ = 90.51 (s), 81.20 (s), 42.62 (s).

Tris(4,4′-dibromo-2,2′-bipyridine)cobalt(III) hexafluorophosphate, ([Co(Br$_2$bpy)$_3$](PF$_6$)$_3$). In a round-bottom flask 1.000 g of [Co(Br$_2$bpy)$_3$](PF$_6$)$_2$ (0.77 mmol, 1 equiv.) was suspended in 10 mL of H_2O. To this, 10 mL of H_2O saturated with 8 drops of Br_2 were added. The bright orange suspension stirred for 18 hours at room temperature shielded from light. To the suspension was added 1.255 g of NH_4PF_6 (7.7 mmol, 10 equiv.) and it stirred for 30 minutes. The solid was filtered and washed with H_2O, MeOH, and Et_2O to afford a pale yellow solid. The solid was recrystallized twice by diffusion of Et_2O into a saturated CH_3CN solution affording X-ray quality single crystals. Yield: 1.050 g (95%). Anal. Calcd. (Found) for $C_{30}H_{18}N_6Br_6CoF_{18}P_3$: C, 25.10 (25.13); H, 1.26 (1.45); N, 5.85 (5.98). ^{1}H NMR (CD_3CN, 500 MHz): 8.90 (d, *J* = 2.2 Hz, 6H), 7.95 (dd, *J* = 6.4, 2.2 Hz, 6H), 7.11 (d, *J* = 6.4 Hz, 6H).

bis(2,6-di(3-methylimidazol-1-ylidene)pyridine)cobalt(III) hexafluorophosphate, ([Co(B^{Me}ImPy)$_2$](PF$_6$)$_3$). The complex was synthesized using a modified literature procedure.[15] To a suspension of 2.00 g [B^{Me}ImPy](PF$_6$)$_2$ (3.76 mmol, 2.00 eq) in 100 mL of dry THF, 1.322 g

of LiHMDS (7.90 mmol, 4.20 eq) in 20 mL of dry THF was added dropwise at -78ºC under nitrogen. The suspension stirred for 1 hour at this temperature affording a clear red-orange solution. A solution of 0.411 g of anhydrous $CoBr_2$ (1.88 mmol, 1.00 eq) in 40 mL dry THF was added dropwise over 10 minutes at -78ºC and stirred for an additional 2 hours at this temperature. The reaction warmed to room temperature overnight affording a dark green solution. The dark solution was saturated with air for 45 minutes to effect oxidization of Co(II) to Co(III), affording a light brown suspension. The solvent was removed *in vacuo* and the crude was dissolved in acetone and the solution was filtered to remove any insoluble material. The filtrate was concentrated slightly and a saturated solution of $KPF_{6(aq)}$ was added to precipitate the complex. The solid was filtered and washed with water and diethyl ether. The crude was recrystallized twice by slow diffusion of diethyl ether into acetonitrile, columned twice on Sephadex LH-20 with 70% acetone/H_2O, and recrystallized again by slow diffusion of diethyl ether into an acetonitrile solution. Yield: 0.652 g (37%). Anal. Calcd. (Found) for $C_{26}H_{26}CoF_{18}N_{10}P_3$: C, 32.12 (32.01); H, 2.69 (2.83); N, 14.40 (14.14). ^{1}H NMR (500 MHz, acetone-d_6): δ 8.61 (t, J= 8.3 Hz, 2H), 8.61 (d, J= 2.1 Hz, 4H), 8.47 (d, J= 8.3 Hz, 4H), 7.58 (d, J= 2.1 Hz, 4H), 3.09 (s, 12H).

2.2.2 Physical Characterization

Electronic Absorption Spectroscopy. All electronic absorption spectra were acquired on a double beam Perkin-Elmer Lambda 1050 spectrophotometer. Spin-allowed transitions were measured in matched 1 cm-pathlength quartz cells at a concentration of ~6 mM, whereas spin-forbidden transitions were measured in a 10 cm-pathlength quartz cell at concentrations of ~20 mM; for the latter, divergence of the light beam through the longer pathlength cell necessitated a manual subtraction of the solvent blank. Spectra for hexafluorophosphate salts were measured in spectroscopic grade CH_3CN, whereas the chloride salts of $[Co(en)_3]^{3+}$ and $[Co(NH_3)_6]^{3+}$ were

measured in spectroscopic grade H_2O. Gaussian deconvolution was performed on each spectrum using IgorPro to accurately determine transition energies and molar absorptivities.

X-Ray Crystallography. Crystals of appropriate size were selected and mounted on a nylon loop with paratone oil on a XtaLAB Synergy, Dualflex, HyPix diffractometer. The crystals were kept at a steady T = 100.0(2) K during data collection. The structures were solved with the ShelXT[36] solution program using intrinsic phasing and by using Olex2 1.3[37] as the graphical interface. The model was refined with ShelXL 2018/3[38] using full matrix least squares minimization on $\boldsymbol{F^2}$.

One crystal, $[Co(deeb)_3](PF_6)_3$, was collected using a Bruker CCD (charge coupled device) based diffractometer equipped with an Oxford Cryostream low-temperature apparatus operating at 173 K. The total number of images was based on results from the program COSMO[39] where redundancy was expected to be 4.0 and completeness of 100% out to 0.83 Å. Cell parameters were retrieved using APEX II[40] software and refined using SAINT on all observed reflections. Data reduction was performed using the SAINT software[41] which corrects for Lp. Scaling and absorption corrections were applied using SADABS[42] multi-scan technique, supplied by George Sheldrick. The solution and refinement were carried out using the same programs as the previous crystals.

2.3 Results and Discussion

The goal of this study was an evaluation of the ligand-field strength of ligands that are commonly employed to create charge-transfer absorption features in first-row, d^6 metal complexes. The challenge lies in the combined influence of the relative intensities of charge-transfer versus ligand-field transitions and their spectral overlap, obfuscating any meaningful experimental assessment of ligand-field strength in this class of chromophores. As indicated above, our approach takes inspiration from work in the 1970s and 1980s on spin-crossover complexes, in which

isoelectronic Co(III) complexes were used as surrogates for the Fe(II) compounds of interest.[24] Whereas the visible spectra of most Fe(II) complexes containing aromatic ligands are dominated by metal-to-ligand charge-transfer (MLCT) transitions, the ligand-to-metal charge-transfer (LMCT) nature of transitions for Co(III) coupled with the increased potentials associated with reduction of Co(III) and oxidation of the aromatic ligands results in a substantial shift of the LMCT feature(s) to higher energy; in most cases, these bands now appear in the near-ultraviolet. This essentially opens up the visible region of the spectrum to where the much lower intensity ligand-field absorptions are now readily observable. This is illustrated in Figure 2.2 which shows the ground-state absorption spectrum of $[Co(bpy)_3]^{3+}$ acquired in CH_3CN solution. The red edge of the LMCT band, whose maximum is at 319 nm in the ultraviolet, can be seen tailing into the blue region of the spectrum. A pronounced shoulder evident on the low-energy portion of this band is easily resolved upon Gaussian deconvolution of the spectrum as a broad feature centered near 460 nm; it's molar absorptivity of ~60 M^{-1} cm^{-1} is consistent with an assignment as a spin-allowed, Laporte-forbidden d-d band.

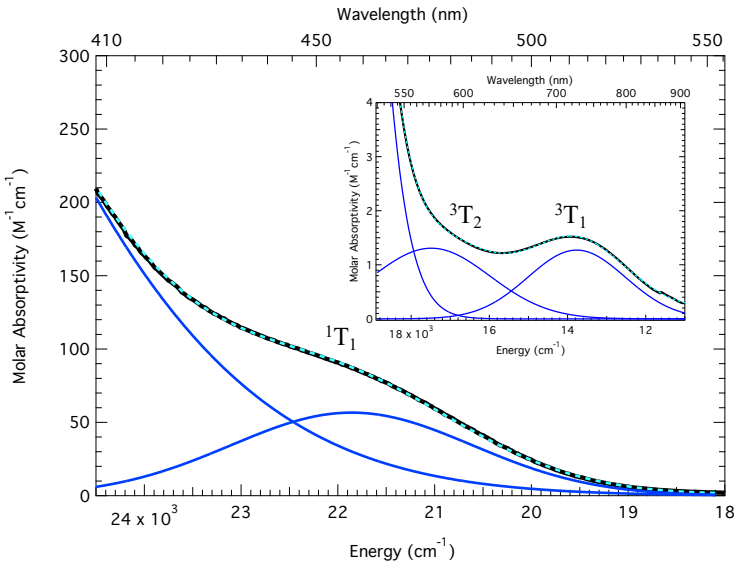

Figure 2.2. Electronic absorption spectrum of $[Co(bpy)_3](PF_6)_2$ in CH_3CN solution, highlighting the ligand-field transitions in the visible region. The blue solid lines show the result of Gaussian deconvolution of the spectrum using the minimum number of components required to fit the experimental spectrum. In the inset is plotted the spectrum obtained at $\lambda > 550$ nm obtained at a higher solute concentration in a 10 cm pathlength cell. The measured molar absorptivities of ca. 1 $M^{-1}cm^{-1}$ indicates that these are spin-forbidden.

Substantially increasing the concentration of the solution and employing 10 cm pathlength optical cells allowed us to further observe one extremely weak but cleanly resolved absorption feature red of 700 nm, as well as a small inflection at higher energy that appears as a shoulder on the low-energy tail of the spin-allowed d-d band (Figure 2.2, inset). Gaussian deconvolution revealed two broad absorption bands centered at 720 nm and 575 nm, each with molar absorptivities of ~1 M^{-1} cm^{-1} suggesting spin-forbidden origins for both transitions. The intensities and relative proximities of these three features thus allow for straightforward assignments of $^1A_1 \rightarrow {}^3T_1$, $^1A_1 \rightarrow {}^3T_2$, and $^1A_1 \rightarrow {}^1T_1$ for the bands at 730 nm, 575 nm, and 460 nm, respectively.

With these assignments it now becomes possible to determine values for 10 Dq and the Racah B and C parameters, which will serve to define the energetics of the entire excited ligand field-state manifold of the compound. As a reminder, these three parameters have their origins in

formalisms first developed by Bethe[43] and expanded upon by many researchers over the years but most significantly by Condon and Shortley,[44] Racah,[45] Jørgensen,[46] Ballhausen,[47] Griffith,[48] and, of course, Tanabe and Sugano.[49,50] A perturbative treatment of electronic structure in the transition block can start from either an infinitely strong field, in which interelectronic repulsions are neglected and a hydrogen-like, one-electron picture can be invoked, or an infinitely weak field in which the dominant influence of electron-electron repulsion leads to a breakdown of the one-electron picture and the need to employ multielectronic terms states for describing electronic structure. Most molecules lie somewhere between these two extremes, but the more ionic nature of bonding in the first transition series (relative to the second- and third-row) places these systems closer to the free-ion limit even in cases where the strength of the ligand field is sufficient to yield a low-spin ground state. Accordingly, primary consideration of electron-electron repulsion and the use of multielectronic term states is the lens through which the electronic structures of such compounds - including the Co(III) complexes we are considering herein - must be viewed.

Following the excellent discussion of this topic by Schmidtke,[51] parameterization of the electron-electron repulsion terms breaks the problem up into a series of integrals that are grouped together according to the approach outlined by Condon and Shortley.[44] In the limit of spherical symmetry (i.e., free ion), the analysis reduces to a set of integrals describing the radial part of the orbital wavefunction ($R_a(r)$) having the general form

$$F^k = \int_0^\infty \left[\int_0^{r_2} R_a^2(r_1) \frac{r_1^k}{r_2^{k+1}} r_1^2 dr_1 + \int_{r_2}^\infty R_a^2(r_1) \frac{r_2^k}{r_2^{k+1}} r_1^2 dr_1 \right] R_c^2(r_2) r_2^2 dr \qquad (2.1)$$

where symmetry restrictions limit the non-vanishing terms to even values of k (i.e., 0, 2, 4, etc.); the magnitudes of the integrals decrease with increasing k (so, $F^0 > F^2 > F^4$, etc.) with only the first three terms being relevant for a d orbital-based configuration. For numerical convenience, new terms F_k are usually introduced wherein

$$F_2 = \frac{1}{49} F^2 \quad (2.2a)$$

and

$$F_4 = \frac{1}{441} F^4 \quad (2.2b)$$

A more widely familiar (and arguably more useful) formalism was introduced by Racah who defined three terms based on the Condon-Shortley parameters as shown in eq 3:

$$A = F_0 - 49\,F_4 \quad (2.3a)$$

$$B = F_2 - 5\,F_4 \quad (2.3b)$$

$$C = 35\,F_4 \quad (2.3c)$$

Since electron-electron repulsion integrals must be positive in terms of their magnitude (i.e., electron-electron repulsions are destabilizing interactions), it follows from eqs 2.3a and 2.3b that

$$F_0 > 49\,F_4 \quad (2.4a)$$

$$F_2 > 5\,F_4 \quad (2.4b)$$

and, in general,

$$C > B \quad (2.4c)$$

The A term is common to all term state energy expressions of a given configuration and therefore cancels when assessing energy differences between states (e.g., a spectroscopic transition): given this, the utility of the Racah parameters lies in the fact that transitions between states corresponding to the highest value of S for a given configuration will only be a function of B, which greatly simplifies the analysis of absorption spectra in the weak-field limit.

Integrals of the form in eq 2.1 are rarely solved in practice, rather, the formalisms represented by eqs 2.2 and 2.3 are used to empirically fit experimentally measured absorption spectra. There are two approaches that can be pursued: 1) full-matrix diagonalization of the determinant representing the multielectronic term states of, in the case of Co(III), the d^6

configuration using an operator of the appropriate field symmetry (e.g., O_h), or 2) approximating this determinant by using only the diagonal terms. The latter amounts to assuming an infinitely strong ligand field with a solution that corresponds to solving a series a linearly independent equations based on the expressions derived by Tanabe and Sugano;[49,50] for the four transitions of a d^6 ion in O symmetry we will be considering herein, these are:

$$\Delta E\ (^1T_2 - {}^1A_1) = 10Dq + 16B - C \quad (2.5a)$$

$$\Delta E\ (^1T_1 - {}^1A_1) = 10Dq - C \quad (2.5b)$$

$$\Delta E\ (^3T_2 - {}^1A_1) = 10Dq + 8B - 3C \quad (2.5c)$$

$$\Delta E\ (^3T_1 - {}^1A_1) = 10Dq - 3C \quad (2.5d)$$

Following this second, more commonly employed approach, the assignments of the bands for $[Co(bpy)_3]^{3+}$ corresponding to eqs 2.5b through 2.5d affords values of 25,860 cm^{-1}, 440 cm^{-1}, and 4050 cm^{-1} for 10Dq, B, and C, respectively. Full-matrix diagonalization, which allows for mixing among the various term states, is most conveniently done using Bendix's program, LIGFIELD.[52] The corresponding values obtained for $[Co(bpy)_3]^{3+}$ using this approach are 24,490 cm^{-1}, 520 cm^{-1}, and 3880 cm^{-1}. The similarity between the two results indicates that the degree of off-diagonal mixing involving the three lowest-energy excited states of $[Co(bpy)_3]^{3+}$ is relatively low. A Tanabe-Sugano diagram specific for $[Co(bpy)_3]^{3+}$ based on our spectroscopic data and full-matrix diagonalization analysis is shown in Figure 2.3.

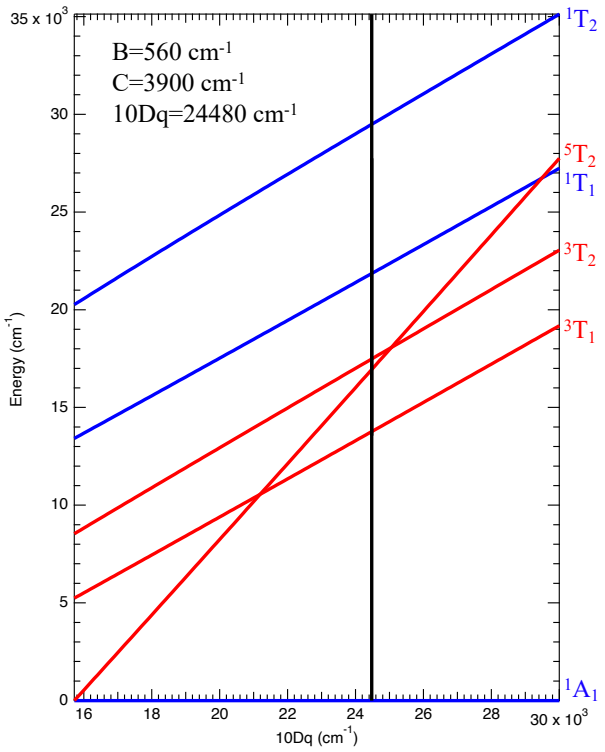

Figure 2.3. Tanabe-Sugano diagram for a d^6 O symmetry metal complex. The black dashed line corresponds to the position for $[Co(bpy)_3]^{3+}$ based on the experimentally determined values of 10 Dq, Racah B, and Racah C parameters shown in the inset.

A more detailed understanding of what these parameters tell us concerning the ligand-field strength of 2,2'-bipyridine - and more importantly what factors are critical in terms of ligand design for modulating the ligand-field strength - can be achieved by examining a series of compounds in which systematic changes in the composition of the ligand are correlated with changes in the ligand-field strength as gauged from their optical properties. We therefore undertook the synthesis of a series of Co(III) complexes consisting of (a) polypyridyl ligands with various substituents at the *para* and *meta* positions of the pyridine rings, representing differing types of perturbations (e.g., σ donating, π accepting, etc.), (b) carbene-based ligands, reflecting current trends in research on Fe(II)-based chromophores through the use of strongly σ-donating ligands, and (c) several

"classic" Co(III) coordination complexes (e.g., $[Co(NH_3)_6]^{3+}$) in order to provide a baseline for comparisons across the series (Figure 2.4).

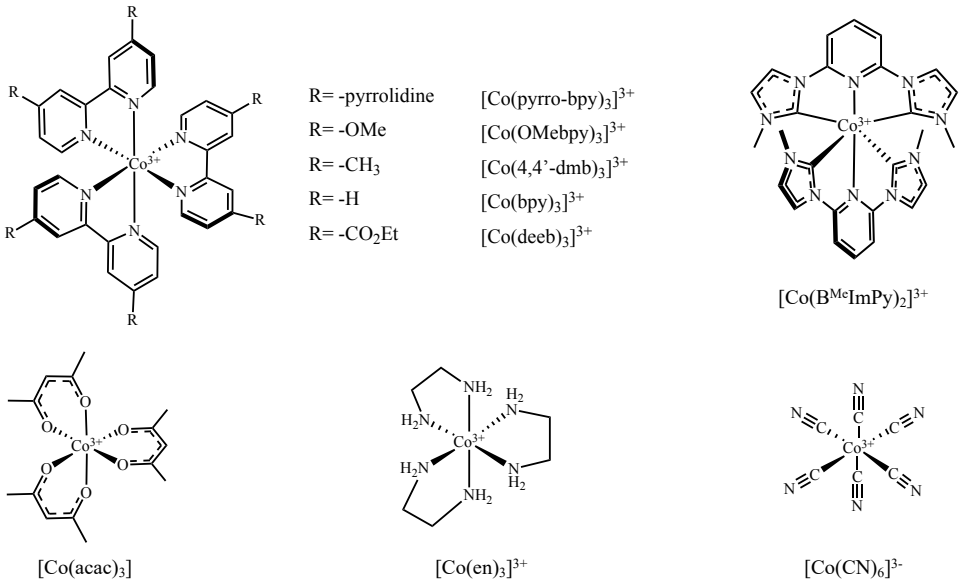

Figure 2.4. Drawings of several of the compounds prepared for the creation of a spectrochemical series of low-spin, six-coordinate, Co(III) complexes.

2.3.1 Synthesis and Structures of $[Co(deeb)_3](PF_6)_3$, $[Co(pyrro\text{-}bpy)_3](PF_6)_3$, and $[Co(B^{Me}ImPy)_2](PF_6)_3$

Many of the compounds we prepared for this expanded assessment of the optical properties of Co(III) complexes are well known in the literature, but three of the compounds are new. In the case of $[Co(deeb)_3](PF_6)_3$, literature methods were used for the preparation of the ethyl ester ligand which was then coordinated to cobalt(II) in a mixed solvent system of $CHCl_3$ and acetone; due to the lability of cobalt(II) and the weaker coordination of electron deficient bipyridyl ligands, this solvent system was chosen in order to minimize the formation of stable solvent species. Under these conditions, $[Co(deeb)_3](ClO_4)_2$ begins to precipitate as the reaction proceeds toward completion, leaving behind unreacted ligand in solution and allowing for facile isolation of the

metal complex. The compound is surprisingly soluble in CH_2Cl_2, so oxidation of $[Co(deeb)_3]^{2+}$ was achieved by addition of $NOPF_6$ to the solution. As oxidation proceeds, $[Co(deeb)_3]^{3+}$ precipitates from CH_2Cl_2 as a mixed ClO_4^-/PF_6^- salt which can be fully converted to the desired PF_6^- salt using an aqueous saturated solution of KPF_6.

The synthesis of $[Co(pyrro\text{-}bpy)_3]^{2+}$ has been previously reported but we were unable to find any reference to the Co(III) form. The Co(II) complex was originally synthesized using the pre-formed pyrro-bpy ligand and complexing to Co(II), however, we developed an alternate route for the formation of the Co(III) complex due to concerns about side reactions associated with the pyrrolidinyl nitrogen during oxidation from Co(II) to Co(III). We therefore prepared $[Co(4,4'\text{-}Cl_2\text{-}bpy)_3]^{3+}$ as a starting point. The Co(III) center activates the 4 and 4′ positions on the bpy backbone for substitution by the pyrrolidine as evidenced by the immediate color change from yellow to orange upon addition of the pyrrolidine to a methanolic solution of the $[Co(4,4'\text{-}Cl_2\text{-}bpy)_3]^{3+}$. Due to the formation of HCl in the substitution reaction, a slight excess of pyrrolidine was used to ensure that all the pyrrolidinyl nitrogen atoms were deprotonated in the isolated complex.

The synthesis of $[Co(B^{Me}ImPy)_2](PF_6)_3$ started with deprotonation of the carbene ligand using LiHMDS at low temperature. Addition of anhydrous $CoBr_2$ initiated the formation of the desired Co(II) complex, which manifested as a dark green solution as the reaction mixture was slowly warmed to room temperature. Due to the strong σ-donation from the carbene, the complex was easily oxidized to Co(III) by simply bubbling air into the solution, whereupon the dark green solution slowly changed to a light brown and began to precipitate as the oxidation proceeded. The overall reaction was not as clean as for the other two compounds, as purification required two initial recrystallizations to remove a dark, slightly tacky material which then allowed for better separation on a Sephadex LH-20 size-exclusion column. Two bands – the first dark yellow in color

and the second also yellow but less intense – moved closely together on the column. The first eluent contained the desired compound but also contained unidentified impurities, while the second contained a more highly purified form of the compound. Recrystallization of the material obtained from this second band afforded the analytically pure material for use in our studies.

The structures of the cations of all three of these compounds are unremarkable, with metal-ligand bond distances and angles about the primary coordination sphere consistent with low-spin Co(III). Additional details of the structures, refinement, and drawings of the cations for all three complexes can be found in the appendix.

2.3.2 π-Donors v. π-Acceptors and their Net Influence in the First Transition Series

The molecules contained in our series of 14 compounds were chosen to span a reasonably wide range of substituents from strongly π donating in the case of 4,4′-dipyrrolidinyl-2,2′-bipyridine (pyrro-bpy) to π acids such as 4,4′-diethylester-2,2′-bipyridine (deeb), as well as ligands devoid of π interactions (e.g., NH_3 and ethylenediamine). Extremes in s donating and π accepting character were also included in the cases of $[Co(B^{Me}ImPy)_2]^{3+}$ and $[Co(CN)_6]^{3+}$, respectively, as a means for comparison. We acquired absorption spectra for the entire series and analyzed them following the same protocol outlined above for $[Co(bpy)_3]^{3+}$. The ligand-field parameters obtained from both diagonal and full-matrix analyses of the deconvolved spectra are collected in Tables 1 and 2, respectively; the experimental spectra and Tanabe-Sugano diagrams constructed for each compound based on these parameters can be found in the Appendix. In two of these cases – $[Co(terpy)_2]^{3+}$ and $[Co(B^{Me}ImPy)_2]^{3+}$ - the overlapping nature of the absorption features prevented us from assigning with confidence the minimum number of three ligand-field bands needed to specify values for 10 Dq and the Racah B and C parameters. Inspection of eq 2.5 reveals that the $^1A_1 \rightarrow {}^3T_1$ and $^1A_1 \rightarrow {}^1T_1$ transitions do not depend on the Racah B parameter, so we were able to

focus on these two transitions in $[Co(terpy)_2]^{3+}$ and $[Co(B^{Me}ImPy)_2]^{3+}$ to afford quantitative values for 10 Dq and Racah C for these compounds.

Table 2.1. Ligand-field Transition Energies and Parameters for Co(III) Complexes in CH_3CN Solution Calculated Using Diagonal Expressions[a]

Complex	$^3T_1$	$^3T_2$	$^1T_1$	$^1T_2$	10Dq	*B*	**β**[b]	*C*	*C/B*
$[Co(acac)_3]$[c]	9450	12550	16880	23010	20600	390	0.36	3720	9.6
$[Co(pyrro\text{-}bpy)_3](PF_6)_3$	13010	16240	20100		23650	400	0.37	3550	8.8
$[Co(NH_3)_6]Cl_3$[d]	13640	17440	21050	29500	24760	475	0.44	3710	7.8
$[Co(phen)_3](PF_6)_3$	13950	17070	21430		25170	390	0.36	3740	9.6
$[Co(dtb)_3](PF_6)_3$	14540	17080	21650		25200	320	0.29	3550	11.2
$[Co(en)_3]Cl_3$[d]	13920	17300	21460	29590	25230	420	0.39	3770	8.9
[Co(Br2bpy)3](PF6)3	14430	18170	21670		25340	480	0.44	3670	7.6
$[Co(5,5'\text{-}dmb)_3](PF_6)_3$	14420	17390	21820		25510	370	0.34	3700	9.9
$[Co(OMe\text{-}bpy)_3](PF_6)_3$	13650	17220	21580		25550	450	0.41	3970	8.9
$[Co(4,4'\text{-}dmb)_3](PF_6)_3$	14600	17750	21960		25640	390	0.36	3680	9.4
$[Co(bpy)_3](PF_6)_3$	13770	17490	21860		25900	470	0.43	4050	8.7
$[Co(deeb)_3](PF_6)_3$	14910	18220	22170		25800	410	0.38	3630	8.8
$[Co(terpy)_2](PF_6)_3$	15558		23017		26747			3730	
$[Co(B^{Me}ImPy)_2](PF_6)_3$	19938		26830		30270			3450	
$K_3[Co(CN)_6]$[d,e]	25470		31830	39240	35010	460	0.43	3180	6.9

[a]All values reported in cm^{-1}. [b]Calculated using eq 2.6 with a value of $B_0 = 1080\ cm^{-1}$. [c]Spectrum recorded in $CHCl_3$ solution. [d]Spectrum recorded in H_2O. [e]Transition energies taken from references 53 and 54.

Inspection of the data in Table 2.1 and Table 2.2 reveals a fairly narrow spread in the magnitude of ligand-field splitting (i.e., 10 Dq) despite the substantial change in the nature of the substituents on the aromatic ligands. Excluding the carbene-based $B^{Me}ImPy$ complex and

$[Co(CN)_6]^{3-}$, there is only a ~3,000 cm^{-1} range covered by this series of low-spin complexes based on the diagonal terms (Table 2.1); this spread is attenuated to slightly more than 2,000 cm^{-1} for the full-matrix analysis (Table 2.2). This observation, coupled with the fact that compounds such as $[Co(NH_3)_6]^{3+}$ and $[Co(en)_3]^{3+}$ lie in the middle of the series in terms of the magnitude of 10 Dq, suggests that π bonding plays a relatively minor role (at least in terms of absolute contributions) in determining the ligand-field strength presented by polypyridyl ligands of this type to Co(III). Qualitatively this is to be expected given the more ionic nature of the bonding in complexes of the first transition series as compared to their second- and third-row congeners, but the overall lack of sensitivity of 10 Dq to the specific changes introduced into the ligand backbone across this series was surprising.

Table 2.2. Ligand-Field Transition Energies and Parameters for Co(III) Complexes in CH_3CN Solution Calculated from Full Diagonalization Analysis[a]

Complex	10Dq	*B*	**β**	*C*	*C/B*
$[Co(acac)_3]$	19210	480	0.44	3590	7.5
$[Co(pyrro\text{-}bpy)_3](PF_6)_3$	22440	480	0.45	3430	7.1
$[Co(NH_3)_6]Cl_3$	23430	580	0.53	3550	6.2
$[Co(phen)_3](PF_6)_3$	23940	460	0.43	3630	7.9
$[Co(en)_3]Cl_3$	23950	500	0.46	3640	7.3
$[Co(dtb)_3](PF_6)_3$	24130	370	0.34	3480	9.5
$[Co(OMe\text{-}bpy)_3](PF_6)_3$	24170	530	0.50	3830	7.2
$[Co(5,5'\text{-}dmb)_3](PF_6)_3$	24330	430	0.40	3600	8.3
[Co(Br2bpy)3](PF6)3	24040	580	0.54	3515	6.1
$[Co(4,4'\text{-}dmb)_3](PF_6)_3$	24450	460	0.43	3570	7.8
$[Co(bpy)_3](PF_6)_3$	24480	560	0.52	3900	7.0
$[Co(deeb)_3](PF_6)_3$	24620	490	0.45	3520	7.2
$K_3[Co(CN)_6]$	34160	510	0.47	3080	6.1

[a]All values reported in cm^{-1}.

More surprising than the limited range of ligand-field splitting was the apparent nature of the π interactions that are present. To understand the effect we believe is operative, one needs to consider several aspects of the electronic properties of the ligands that are relevant for determining d-orbital splitting in these compounds. As mentioned above, we interpret the range of 10 Dq accessible across the series of complexes we've prepared as an indication of a minor role for π bonding in an absolute sense. That stated, inspection of trends within the series of compounds does reveal an influence from π-based interactions in terms of their relative energetics. Consider first what would be expected in the absence of any π interactions. Although there are several factors that influence the magnitude of ligand-field splitting due to s bonding, the d-orbital splitting should roughly correlate with the basicity of the donor atoms (i.e., the stronger the base, the larger the ligand-field splitting). The strength of pyridyl-based ligands acting as Lewis bases to a metal center can be gauged from their pK_b values (or, more conveniently, the pK_a values of the corresponding bipyridinium salts). Table 2.3 lists pK_a values of the hydrochloride salts of several of the ligands used in our study.[55] Not surprisingly, the strongest acid is 4,4′-diethylester-2,2′-bipyridinium chloride, where the electron withdrawing characteristics of the ester groups attenuates the donor ability of the nitrogen atoms by more than an order of magnitude relative to 2,2'-bipyridine. Introduction of CH_3 groups (i.e., 5,5′- and 4,4′-dimethyl) increases the ligand's basicity relative to the unsubstituted ligand, as might be expected given their electron donating properties. At the other end of the spectrum is 1,10-phenanthroline. While a more challenging comparison due to structural differences as compared to the bpy derivatives, it is nevertheless roughly two orders of magnitude more basic than deeb. If π interactions were irrelevant, the expectation would be that measured values of 10 Dq for Co(III) complexes comprised of this subset of compounds should follow a qualitatively predictable trend from largest (phen) to smallest (deeb). Inspection of Table 2.1 and

Table 2.2 reveal that this is the exact opposite trend of what is measured for 10 Dq across this series. While the correlation is not quantitatively robust, $[Co(deeb)_3]^{3+}$ exhibits the largest value of 10 Dq for this series, while $[Co(phen)_3]^{3+}$ exhibits the smallest. Again, the variations are not large, but π interactions between the ligand and metal are clearly sufficient to modulate the ligand-field splitting of these compounds in a manner that opposes the predicted trend based on σ interactions alone.

Table 2.3. p*K*a Values of Selected Polypyridyl Ligands[a]

Ligand	pK_a	pK_a^L-pK_a^{bpy}
phen	4.53	0.91
4,4'-dmb	4.40	0.78
5,5'-dmb	3.97	0.35
bpy	3.62	0
deeb	2.45	-1.17

[a]From reference 55.

To identify the nature of the π-effect, we first consider the compound with the smallest ligand-field splitting, $[Co(pyrro\text{-}bpy)_3]^{3+}$. The lone pair associated with the ternary nitrogen of the pyrrolidine ring coupled with its location at the 4 and 4′ positions of bipyridine makes this substituent an effective π-donor to the ligand, which means that pyrro-bpy is expected to be more electron rich than the unsubstituted form of the ligand as a result. The question is whether this makes pyrro-bpy a stronger π-donor to Co(III) or a weaker π-acceptor. The same argument applies to $[Co(deeb)_3]^{3+}$, i.e., does the more electron deficient nature of deeb make it a better π-acceptor or a weaker π-donor? Either of these scenarios would result in shifts of the t_{2g} orbitals of the metal center in the appropriate direction to rationalize the changes in 10 Dq that are experimentally

observed. This question is difficult to answer in isolation - something akin to asking if an answer of 4 is achieved from the sum of 3 and 1 or 6 and -2 – but is important from the point-of-view of ligand design. Should we view polypyridyl ligands bound to first-row metals as net π donors or net π acceptors in terms of their influence on the electronic structure of the resulting metal complex?

We believe the answer to this question can be found in the data presented in Table 2.1, specifically in the parameters derived for $[Co(terpy)_2]^{3+}$. To understand this, consider first the electronic structure of $[Ru(terpy)_2]^{2+}$. This compound, which has been well studied by many groups in a variety of contexts over the years,[53–57] represents an outlier when it comes to the photophysics of Ru(II) polypyridyls in terms of the surprisingly short lifetime of its lowest-lying ^{3}MLCT excited state. In contrast to $[Ru(bpy)_3]^{2+}$, whose ^{3}MLCT state persists for ~1 ms in deoxygenated solution at room temperature, the corresponding lifetime for $[Ru(terpy)_2]^{2+}$ is ~250 ps.[58] This dramatically reduced lifetime relative to $[Ru(bpy)_3]^{2+}$ has been attributed to thermal accessibility of the lowest energy $^3T_1$ ligand-field state from the charge-transfer manifold, resulting in a significantly larger value for the rate constant for non-radiative decay (k_{nr}) for the ^{3}MLCT state.[59,60] Apart from the consequences of this as it pertains to the excited-state properties of $[Ru(terpy)_2]^{2+}$ (e.g., significantly attenuated emission, limited utility for biomolecular photoredox chemistry, etc.), the difference in photophysical behavior indicates that terpy presents a much weaker ligand field to Ru(II) than bpy. The reason for this is believed to be associated with the structural constraints endemic to the terpy ligand as evidenced by acute N-Ru-N bond angles of ca. 80˚ and 165˚ for *cis* and *trans*, respectively, resulting in relatively poor metal-ligand overlap affecting both σ-donation from the nitrogen atoms and π-backbonding from the metal into the π* orbital(s) of the ligand.[61]

In contrast, the data we have acquired on $[Co(bpy)_3]^{3+}$ and $[Co(terpy)_2]^{3+}$ exhibits the exact opposite relationship from what is inferred for their Ru(II) analogs. While the absorption spectrum of $[Co(terpy)_2]^{3+}$ does not allow for detection of the three transitions needed to independently assess the Racah B and C parameters, we were able to quantify that the broadest measure of ligand-field strength – 10 Dq – is approximately 1,000 cm^{-1} larger for $[Co(terpy)_2]^{3+}$ than $[Co(bpy)_3]^{3+}$. The steric constraints associated with terpy binding to Co(III) are very similar to that for Ru(II) (Table 2.4), so the same attenuation in metal-ligand interactions due to distortions from octahedral geometry identified for $[Ru(terpy)_2]^{2+}$ should be operative for $[Co(terpy)_2]^{3+}$. But, rather than leading to a reduction in ligand-field strength relative to bpy as is seen for Ru(II), the net result in the case of Co(III) is an increase in that same parameter. These observations lead us to the conclusion that terpy must be acting as a net π donor to Co(III): only in this circumstance can one rationalize how an attenuation in a metal-ligand interaction can lead to a larger ligand-field strength.

Table 2.4. Comparison of Structural Parameters for $[Ru(terpy)_2]^{2+}$ and $[Co(terpy)_2]^{3+}$

	Average				
Complex	M-N_{axial} (Å)	M-$N_{eq.}$ (Å)	N_{axial}-M-N_{axial}(º)	$N_{eq.}$-M-$N_{eq.}$(º)	$N_{eq.}$-M-N_{axial} (º)
$[Ru(terpy)_2]^{2+}$[a]	1.968	2.074	178.04	157.77	78.9
$[Co(terpy)_2]^{3+}$[b]	1.856	1.943	178.41	165.55	82.8
Difference (Ru-Co)	0.112	0.131	-0.37	-7.78	-3.9

[a]From reference 65. [b]From reference 33.

Indeed, we believe that net donation is the primary mode of π interactions between Co(III) and all of the polypyridyl-based ligands being considered herein; the variation in 10 Dq across the different substituents noted above is therefore not associated with changes in the π accepting nature

of the ligand but rather due to modulations in their ability to act as a base. The likely origin of this effect – and by extension the reason for the reversal in behavior between metal polypyridyl complexes of the first and second transition series – is the shift in energy of the t_{2g}-symmetry d orbitals as a function of charge and principal quantum number. Both the filled π and unfilled π* orbitals of the polypyridyl ligands are of the appropriate symmetry to interact with, in the case of a low-spin d^6 ion, the filled t_{2g} orbitals of the metal center. Whether a ligand like 2,2′-bipyridine acts as a net π donor or π acceptor in a given compound will therefore reflect a balance of interactions that depend largely on the energy of the metal-based t_{2g} orbitals relative to these ligand-based π and π* orbitals. For the two metal ions being compared here, the higher valence orbital ionization energy of Co(III) as compared to Ru(II) indicates that the d-orbitals of Co(III) are significantly lower in energy, which we believe results in a more favorable energetic match with the filled π orbitals of the polypyridyl ligands and trends in 10 Dq that are consistent with net π donation. This picture inverts for Ru(II) due to the increase in principal quantum number coupled with the decrease in ionic charge, increasing in the energy of the d orbitals to where the d-π* gap becomes the dominant interaction. It should be noted that the idea of considering polypyridyl ligands like bpy as net π-donors to first-row metals was previously suggested by Jakubikova and co-workers based on their computational studies of Fe(II) complexes.[62] Although our measurements were carried out on Co(III) complexes, we nevertheless view our results as experimental support for their conclusions.

2.3.3 Trends in the Racah B and Racah C Parameters

The most challenging aspect in analyzing the data on the series of compounds we have prepared and characterized is the significance (if any) of variations in the Racah B and C parameters listed in Table 2.1 and Table 2.2. As mentioned previously, these two parameters correspond to the linear

combinations of electron-electron repulsion integrals indicated in eq 2.3. These parameters were originally defined in this manner primarily to simplify spectral analyses in the weak-field limit, but researchers have since tried to ascribe a deeper physical significance to the numerical values obtained. These efforts have largely focused on the B parameter, in large part because reliable data on the C parameter is relatively scarce due to the experimental challenges associated with measuring spin-forbidden transitions. The B values of a given transition metal complex are typically compared to the corresponding values for the free ion, B_0, in the form of a ratio defined as

$$\beta = \frac{B}{B_0} \tag{2.6}$$

The B value for a compound is almost invariably smaller than B_0; since B is defined in terms of electron-electron repulsion integrals, the value of β has served as a qualitative assessment of the degree of covalency in the metal-ligand bonding interaction (the idea being increased covalency leads to greater delocalization of the d orbitals and therefore a reduction in the magnitude of electron-electron repulsion within the d-orbital manifold). Inspection of Table 2.1 and Table 2.2 reveal that the experimental values for B for all of the compounds studied is significantly attenuated as compared to the free-ion value of 1080 cm^{-1} for Co(III), but there is no obvious correlation across the series with the notable exception that the two compounds devoid of π interactions – $[Co(NH_3)_6]^{3+}$ and $[Co(en)_3]^{3+}$ - do exhibit the largest values of B relative to the other members of the series. One could therefore speculate that this supports at least qualitatively the notion of B reflecting the extent of d-orbital interaction with the ligands, with the two σ-only complexes being the most ionic (i.e., possessing the largest value of β). That stated, we believe that a more detailed analysis of these data (including the physical significance of variations in the

C parameter) would require an extensive theoretical effort that is well beyond the scope of the present study.

2.3.4 Insights into the Ligand-field Strength for Iron(II)

The broader goal of this study was to develop the means to assess ligand-field strengths in cases for which the requisite transitions are obscured by more intense absorption features (e.g., Fe(II) charge-transfer complexes). One way to achieve this is to find a few Fe(II) complexes wherein at least one ligand-field transitions could be observed, then set up a correlation with the optical properties of the corresponding Co(III) complex. Although this approach would not be expected to be robust, it could still offer an approximation for the ligand-field strength of the Fe(II) complex where none would otherwise be available. We acquired an electronic absorption spectrum of $[Fe(bpy)_3]^{2+}$ using the same approach as was done for the Co(III) complexes and were able to identify a reasonably well-defined feature centered at ~830 nm which we assign as the $^1A_1 \rightarrow {}^3T_1$ absorption (Figure 2.5). This is consistent with the assignment of Palmer and Piper in their analysis of the single-crystal absorption spectrum of $[Fe(bpy)_3]Cl_2$.[63] The corresponding transition for $[Co(bpy)_3]^{3+}$ sits at 730 nm, a value that allows us to infer a substantial decrease in 10 Dq upon replacement of Co(III) for Fe(II), as expected due to the decreased charge on the iron ion. With only one ligand-field band is observed for $[Fe(bpy)_3]^{2+}$ one cannot quantify its ligand-field parameters in the same way we were able to for $[Co(bpy)_3]^{3+}$, however, we can approximate the positions of the $^3T_2$ and $^1T_1$ absorptions of $[Fe(bpy)_3]^{2+}$ based on their observed locations in $[Co(bpy)_3]^{3+}$. The expressions in eqs 2.3b – 2.5d specify the energies for ground-state absorption to the $^1T_1$, $^3T_2$, and $^3T_1$ states, respectively, of a d^6 ion. If we take the ratio of the $^3T_2$ and $^3T_1$ transition energies of $[Co(bpy)_3]^{3+}$ (i.e., $E(^3T_2)/E(^3T_1)$) as well as that of the $^1T_1$ and $^3T_1$ states ($E(^1T_1)/E(^3T_1)$), average them, then reference them to the observed $^1A_1 \rightarrow {}^3T_1$ absorption of

$[Fe(bpy)_3]^{2+}$, we can obtain approximate locations of the $^1A_1 \rightarrow {}^3T_2$ and $^1A_1 \rightarrow {}^1T_1$ absorptions for $[Fe(bpy)_3]^{2+}$ and use those values to estimate a value of 10 Dq for $[Fe(bpy)_3]^{2+}$ of ~21,000 cm^{-1}.[64] The data therefore indicate that replacing Co(III) with Fe(II) in the same ligand-field environment leads to a reduction in the magnitude of 10 Dq on the order of ~3000 cm^{-1}. While we concede that a comparison between two compounds does not provide the basis for a robust correlation, we believe that information on the absorptive properties of a ligand system of interest bound to Co(III) does allow one to make a reasonable approximation of the ligand-field strength of the corresponding Fe(II) complex that would otherwise be exceedingly difficult to obtain.

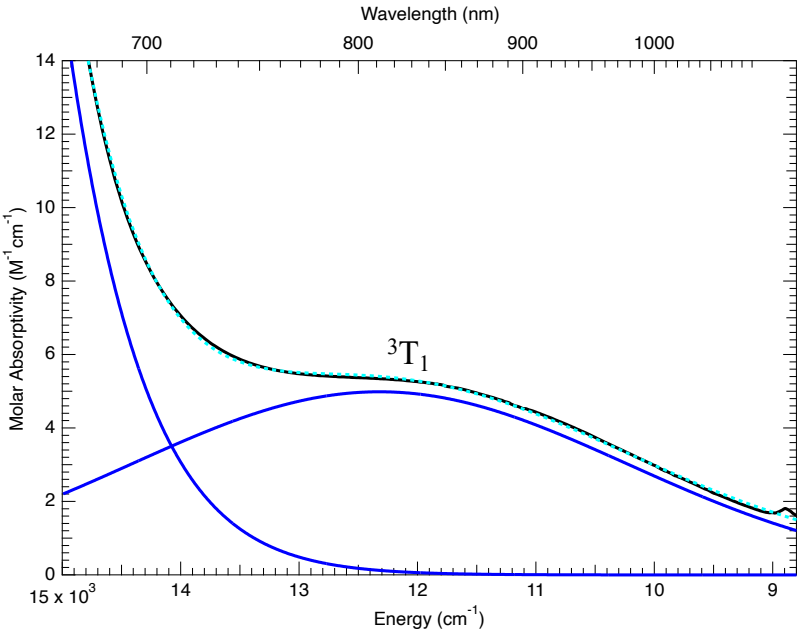

Figure 2.5. Near-IR electronic absorption spectrum of $[Fe(bpy)_3]^{2+}$ in CH_3CN solution obtained in a 10 cm pathlength cell at high concentration. The low extinction coefficient for the band centered at 830 nm is consistent with a spin-forbidden transition and is assigned as the $^1A_1 \rightarrow {}^3T_1$ absorption.

Given the limited amount of information we have on Fe(II) analogs, it's difficult to experimentally address the question of whether polypyridyl ligands behave as net π donors or net π acceptors when bound to Fe(II) as we did with Co(III). That stated, following the reasoning discussed above, the

higher energy associated with the d orbitals of Fe(II) relative to Co(III) suggests that these competing effects are likely close to offsetting each other in Fe(II). This would be consistent with results we have previously reported on ground-state recovery dynamics following photoexcitation of $[Fe(bpy)_3]^{2+}$ and $[Fe(4,4'\text{-dmb})_3]^{2+}$, where a modest ~35 cm^{-1} increase in the barrier associated with ground-state recovery for the latter suggested a slightly weaker ligand field associated with 4,4'-dmb as compared to bpy.

2.4 Concluding Remarks

The synthesis and electronic absorption spectroscopy of a series of Co(III) complexes have been carried out in an effort to assess the field strength presented by ligands that are commonly used to create strong charge transfer-based absorption cross-sections in transition metal complexes. The intensity of these bands coupled with their spectral location typically renders the observation of the ligand-field transitions necessary to make such an assessment difficult if not impossible for most chromophores of the first transition series. This is particularly true in the case of the d^6 configuration, complexes whose photophysical properties are of considerable interest for applications involving photo-induced electron transfer chemistry. The significant blue-shift in the LMCT transition(s) of Co(III) complexes provided the mechanism by which the underlying ligand-field transitions could be observed and quantified. A detailed analysis of both spin-allowed and spin-forbidden d-d absorptions allowed for a quantitative measure of the ligand-field splitting parameter – 10 Dq – as well as the Racah B and C terms that together provide a complete description of the energies of the multielectronic states that comprise the excited-state electronic manifold of the compounds. It was found that the ligand-field strength imposed on Co(III) by polypyridyl ligands is ca. 25,000 cm^{-1}, a value that can be tuned by ± ~1,500 cm^{-1} via substituent changes on the periphery of the aromatic residues. An unexpected outcome of this analysis was

the observation that, while dominated by σ-based interactions between the lone pairs on the ligating nitrogen atoms and the metal center, ligands of this class behave as net π donors to the metal. This stands in contrast to their net π accepting character when bound to ions from second and third transition series and represents an important conceptual shift for how to think about metal-ligand interactions for the purposes of ligand design. Results obtained on a carbene-based complex further established experimentally the ability of these strong, σ-donating ligands to destabilize ligand-field excited states, thereby enhancing the utility of charge-transfer states for photochemical transformations. We believe that this approach of using Co(III) as a surrogate for ions such as Fe(II) will prove to be a useful tool if one is seeking to manipulate the relative energetics of ligand-field and charge-transfer excited states to modulate photoredox activity of these earth-abundant compounds through targeted synthetic design.

REFERENCES

(1) Wenger, O. S. Is Iron the New Ruthenium? *Chem. Euro. J.* **2019**, *25* (24), 6043–6052. DOI: 10.1002/chem.201806148.

(2) Wegeberg, C.; Wenger, O. S. Luminescent First-Row Transition Metal Complexes. *JACS Au* **2021**. DOI: 10.1021/jacsau.1c00353.

(3) Glaser, F.; Kerzig, C.; Wenger, O. S. Multi-Photon Excitation in Photoredox Catalysis: Concepts, Applications, Methods. *Angew. Chem. Int. Ed.* **2020**, *59* (26), 10266–10284. DOI: 10.1002/anie.201915762.

(4) Nazeeruddin, Md. K.; Zakeeruddin, S. M.; Humphry-Baker, R.; Jirousek, M.; Liska, P.; Vlachopoulos, N.; Shklover, V.; Fischer, C.-H.; Grätzel, M. Acid−Base Equilibria of (2,2‘-Bipyridyl-4,4‘-Dicarboxylic Acid)Ruthenium(II) Complexes and the Effect of Protonation on Charge-Transfer Sensitization of Nanocrystalline Titania. *Inorg. Chem.* **1999**, *38* (26), 6298–6305. DOI: 10.1021/ic990916a.

(5) Kreitner, C.; Mengel, A. K. C.; Lee, T. K.; Cho, W.; Char, K.; Kang, Y. S.; Heinze, K. Strongly Coupled Cyclometalated Ruthenium Triarylamine Chromophores as Sensitizers for DSSCs. *Chem Eur. J.* **2016**, *22* (26), 8915–8928. DOI: 10.1002/chem.201601001.

(6) Chan, A. Y.; Perry, I. B.; Bissonnette, N. B.; Buksh, B. F.; Edwards, G. A.; Frye, L. I.; Garry, O. L.; Lavagnino, M. N.; Li, B. X.; Liang, Y.; Mao, E.; Millet, A.; Oakley, J. v; Reed, N. L.; Sakai, H. A.; Seath, C. P.; MacMillan, D. W. C. Metallaphotoredox: The Merger of Photoredox and Transition Metal Catalysis. *Chem. Rev.* **2022**, *122* (2), 1485–1542. DOI: 10.1021/acs.chemrev.1c00383.

(7) Woodhouse, M. D.; McCusker, J. K. Mechanistic Origin of Photoredox Catalysis Involving Iron(II) Polypyridyl Chromophores. *J. Am. Chem. Soc.* **2020**, *142* (38), 16229–16233. DOI: 10.1021/jacs.0c08389.

(8) Gualandi, A.; Marchini, M.; Mengozzi, L.; Natali, M.; Lucarini, M.; Ceroni, P.; Cozzi, P. G. Organocatalytic Enantioselective Alkylation of Aldehydes with $[Fe(Bpy)_3]Br_2$ Catalyst and Visible Light. *ACS. Catal.* **2015**, *5* (10), 5927–5931. DOI: 10.1021/acscatal.5b01573.

(9) Parisien-Collette, S.; Hernandez-Perez, A. C.; Collins, S. K. Photochemical Synthesis of Carbazoles Using an $[Fe(Phen)_3](NTf_2)_2/O_2$ Catalyst System: Catalysis toward Sustainability. *Org. Lett.* **2016**, *18* (19), 4994–4997. DOI: 10.1021/acs.orglett.6b02456.

(10) McCusker, J. K. Electronic Structure in the Transition Metal Block and Its Implications for Light Harvesting. *Science* **2019**, *363* (6426), 484–488. DOI: 10.1126/science.aav9104.

(11) Liu, Y.; Harlang, T.; Canton, S. E.; Chábera, P.; Suárez-Alcántara, K.; Fleckhaus, A.; Vithanage, D. a; Göransson, E.; Corani, A.; Lomoth, R.; Sundström, V.; Wärnmark, K. Towards Longer-Lived Metal-to-Ligand Charge Transfer States of Iron(II) Complexes: An N-Heterocyclic Carbene Approach. *Chem. Commun.* **2013**, *49* (57), 6412. DOI: 10.1039/c3cc43833c.

(12) Herr, P.; Glaser, F.; Büldt, L. A.; Larsen, C. B.; Wenger, O. S. Long-Lived, Strongly Emissive, and Highly Reducing Excited States in Mo(0) Complexes with Chelating Isocyanides. *J. Am. Chem. Soc.* **2019**, *141* (36), 14394–14402. DOI: 10.1021/jacs.9b07373.

(13) Reuter, T.; Kruse, A.; Schoch, R.; Lochbrunner, S.; Bauer, M.; Heinze, K. Higher MLCT Lifetime of Carbene Iron(II) Complexes by Chelate Ring Expansion. *Chem. Commun.* **2021**, *57* (61), 7541–7544. DOI: 10.1039/d1cc02173g.

(14) Steube, J.; Burkhardt, L.; Päpcke, A.; Moll, J.; Zimmer, P.; Schoch, R.; Wölper, C.; Heinze, K.; Lochbrunner, S.; Bauer, M. Excited-State Kinetics of an Air-Stable Cyclometallated Iron(II) Complex. *Chem. Euro. J.* **2019**, *25* (51), 11826–11830. DOI: 10.1002/chem.201902488.

(15) Vukadinovic, Y.; Burkhardt, L.; Päpcke, A.; Miletic, A.; Fritsch, L.; Altenburger, B.; Schoch, R.; Neuba, A.; Lochbrunner, S.; Bauer, M. When Donors Turn into Acceptors: Ground and Excited State Properties of Fe II Complexes with Amine-Substituted Tridentate Bis-Imidazole-2-Ylidene Pyridine Ligands. *Inorg. Chem.* **2020**, *59* (13), 8762–8774. DOI: 10.1021/acs.inorgchem.0c00393.

(16) Braun, J. D.; Lozada, I. B.; Herbert, D. E. In Pursuit of Panchromatic Absorption in Metal Coordination Complexes: Experimental Delineation of the HOMO Inversion Model Using Pseudo-Octahedral Complexes of Diarylamido Ligands. *Inorg. Chem.* **2020**, acs.inorgchem.0c02973. DOI: 10.1021/acs.inorgchem.0c02973.

(17) Braun, J. D.; Lozada, I. B.; Kolodziej, C.; Burda, C.; Newman, K. M. E.; van Lierop, J.; Davis, R. L.; Herbert, D. E. Iron(II) Coordination Complexes with Panchromatic Absorption and Nanosecond Charge-Transfer Excited State Lifetimes. *Nat. Chem.* **2019**, *11* (12), 1144–1150. DOI: 10.1038/s41557-019-0357-z.

(18) Magra, K.; Francés-Monerris, A.; Cebrián, C.; Monari, A.; Haacke, S.; Gros, P. C. Bidentate Pyridyl-NHC Ligands: Synthesis, Ground and Excited State Properties of Their Iron(II) Complexes and the Role of the Fac/Mer Isomerism. *Eur. J. Inorg. Chem*. **2022**, *2022* (7). DOI: 10.1002/ejic.202100818.

(19) Liu, L.; Duchanois, T.; Etienne, T.; Monari, A.; Beley, M.; Assfeld, X.; Haacke, S.; Gros, P. C. A New Record Excited State ^{3}MLCT Lifetime for Metalorganic Iron(II) Complexes. *Phys. Chem. Chem. Phys.* **2016**, *18* (18), 12550–12556. DOI: 10.1039/C6CP01418F.

(20) Paulus, B. C.; Adelman, S. L.; Jamula, L. L.; McCusker, J. K. Leveraging Excited-State Coherence for Synthetic Control of Ultrafast Dynamics. *Nature* **2020**, *582* (7811), 214–218. DOI: 10.1038/s41586-020-2353-2.

(21) Paulus, B. C.; Nielsen, K. C.; Tichnell, C. R.; Carey, M. C.; McCusker, J. K. A Modular Approach to Light Capture and Synthetic Tuning of the Excited-State Properties of Fe(II)-Based Chromophores. *J. Am. Chem. Soc.* **2021**, *143* (21), 8086–8098. DOI: 10.1021/jacs.1c02451.

(22) Hauser, A. Reversibility of Light-Induced Excited Spin State Trapping in the $Fe(Ptz)_6(BF_4)_2$, and the $Zn_{1-x}Fe_x(Ptz)_6(BF_4)_2$ Spin-Crossover Systems. *Chem. Phys. Lett.* **1986**, *124* (6), 543–548. DOI: 10.1016/0009-2614(86)85073-4.

(23) Hauser, A. Intersystem Crossing in the $[Fe(Ptz)_6](BF_4)_2$ Spin Crossover System (Ptz=1-propyltetrazole). *J. Chem. Phys.* **1991**, *94* (4), 2741–2748. DOI: 10.1063/1.459851.

(24) Klaeui, W.; Eberspach, W.; Guetlich, P. Spin-Crossover Cobalt(III) Complexes: Steric and Electronic Control of Spin State. *Inorg. Chem.* **1987**, *26* (24), 3977–3982. DOI: 10.1021/ic00271a004.

(25) Oki, A. R.; Morgan, R. J. An Efficient Preparation of 4,4′-Dicarboxy-2,2′-Bipyridine. *Synth. Commun.* **1995**, *25* (24), 4093–4097. DOI: 10.1080/00397919508011487.

(26) Worl, L. A.; Duesing, R.; Chen, P.; Ciana, L. Della; Meyer, T. J. Photophysical Properties of Polypyridyl Carbonyl Complexes of Rhenium(I). *J. Chem. Soc., Dalton Trans.* **1991**, No. S, 849–858. DOI: 10.1039/DT9910000849.

(27) Tancini, F.; Wu, Y.-L.; Schweizer, W. B.; Gisselbrecht, J.-P.; Boudon, C.; Jarowski, P. D.; Beels, M. T.; Biaggio, I.; Diederich, F. 1,1-Dicyano-4-[4-(Diethylamino)Phenyl]Buta-1,3-Dienes: Structure-Property Relationships. *European J Org Chem* **2012**, *2012* (14), 2756–2765. DOI: 10.1002/ejoc.201200111.

(28) Peris, E.; Mata, J.; Loch, J. A.; Crabtree, R. H. A Pd Complex of a Tridentate Pincer CNC Bis-Carbene Ligand as a Robust Homogenous Heck Catalyst. *Chem. Commun.* **2001**, No. 2, 201–202. DOI: 10.1039/b008038l.

(29) Bjerrum, J.; McReynolds, J. P.; Oppegard, A. L.; Parry, R. W. Hexamminecobalt(III) Salts. In *Inorganic Syntheses*; 1946; Vol. 2, pp 216–221.

(30) Work, J. B.; McReynolds, J. P. Tris(Ethylenediamine)Cobalt(III) Chloride. In *Inorganic Syntheses*; Fernelius, W. C., Ed.; 1946; Vol. 2, pp 221–222. DOI: 10.1002/9780470132333.ch70.

(31) Bella, F.; Vlachopoulos, N.; Nonomura, K.; Zakeeruddin, S. M.; Grätzel, M.; Gerbaldi, C.; Hagfeldt, A. Direct Light-Induced Polymerization of Cobalt-Based Redox Shuttles: An Ultrafast Way towards Stable Dye-Sensitized Solar Cells. *Chem. Commun.* **2015**, *51* (91), 16308–16311. DOI: 10.1039/C5CC05533D.

(32) Panja, A. Mononuclear Cobalt(III) and Iron(II) Complexes with Diimine Ligands: Synthesis, Structure, DNA Binding and Cleavage Activities, and Oxidation of 2-Aminophenol. *Polyhedron* **2012**, *43* (1), 22–30. DOI: 10.1016/j.poly.2012.05.041.

(33) Constable, E. C.; Harris, K.; Housecroft, C. E.; Neuburger, M.; Zampese, J. a. Turning $\{M(Tpy)_2\}^{n+}$ Embraces and CH···π Interactions on and off in Homoleptic Cobalt(II) and Cobalt(III) Bis(2,2′:6′,2″-Terpyridine) Complexes. *CrystEngComm* **2010**, *12* (10), 2949. DOI: 10.1039/c002834g.

(34) Burschka, J.; Kessler, F.; Baranoff, E.; Nazeeruddin, M. K.; Graetzel, M. Metal Complexes for Use as Dopants and Other Uses. WO 2012/114316 A1, 2012.

(35) Wong, K. W.; Wong, M. C. COBALT-POLYPYRIDYL COMPLEX FOR TREATMENT OF CANCER , A PHARMACEUTICAL COMPOSITION AND A KIT COMPRISING IT. US 2018/0050044 A1, 2018.

(36) Sheldrick, G. M. SHELXT – Integrated Space-Group and Crystal-Structure Determination. *Acta Crystallogr. A* **2015**, *71* (1), 3–8. DOI: 10.1107/S2053273314026370.

(37) Dolomanov, O. v.; Bourhis, L. J.; Gildea, R. J.; Howard, J. A. K.; Puschmann, H. OLEX2 : A Complete Structure Solution, Refinement and Analysis Program. *J. Appl. Crystallogr.* **2009**, *42* (2), 339–341. DOI: 10.1107/S0021889808042726.

(38) Sheldrick, G. M. Crystal Structure Refinement with SHELXL. *Acta Crystallogr. C* **2015**, *71* (1), 3–8. DOI: 10.1107/S2053229614024218.

(39) COSMO. Software for the CCD Detector Systems for Determining Data Collection Parameters. Bruker Analytical X-ray Systems: Madison, WI 2009.

(40) V2010.11-3, A. Software for the CCD Detector System. Bruker Analytical X-ray Systems: Madison, WI 2010.

(41) V7.68A, S. Software for the Integration of CCD Detector System. Bruker Analytical X-ray Systems: Madison, WI 2010.

(42) Blessing, R. H. An Empirical Correction for Absorption Anisotropy. *Acta Crystallogr. A* **1995**, *51* (1), 33–38. DOI: 10.1107/S0108767394005726.

(43) Bethe, H. Termaufspaltung in Kristallen. *Ann. Phys.* **1929**, *395* (2), 133–208. DOI: 10.1002/andp.19293950202.

(44) Condon, E. U.; Shortley, G. H. The Theory of Complex Spectra II. *Phys. Rev.* **1931**, *37* (9), 1025–1043. DOI: 10.1103/PhysRev.37.1025.

(45) Racah, G. Theory of Complex Spectra. II. *Phys. Rev.* **1942**, *62* (9–10), 438–462. DOI: 10.1103/PhysRev.62.438.

(46) Jørgensen, Chr. K. Studies of Absorption Spectra VIII. Three and More d-Electrons in Cubic Crystal Fields. *Acta Chem. Scand.* **1955**, *9*, 116–121. DOI: 10.3891/acta.chem.scand.09-0116.

(47) Ballhausen, C. J. *Introduction to Ligand Field Theory*; McGraw-Hill Book Company, Inc., 1962.

(48) Griffith, J. S.; Orgel, L. E. Ligand-Field Theory. *Quarterly Reviews, Chemical Society* **1957**, *11* (4), 381–393. DOI: 10.1039/qr9571100381.

(49) Tanabe, Y.; Sugano, S. On the Absorption Spectra of Complex Ions. I. *J. Physical Soc. Japan* **1954**, *9* (5), 753–766. DOI: 10.1143/JPSJ.9.753.

(50) Tanabe, Y.; Sugano, S. On the Absorption Spectra of Complex Ions II. *J. Physical Soc. Japan* **1954**, *9* (5), 766–779. DOI: 10.1143/JPSJ.9.766.

(51) Schmidtke, H.-H. *The Variation of Slater-Condon Parameters Fk and Racah Parameters B and C with Chemical Bonding in Transition Group Complexes*; Mingos, D. M. P., Schönherr, T., Eds.; Springer: Berlin, Heidelberg, 2004. DOI: 10.1007/b11303.

(52) Bendix, J. LIGFIELD. Copenhagen, Denmark.

(53) Stone, M. L.; Crosby, G. A. Charge-Transfer Luminescence from Ruthenium(II) Complexes Containing Tridentate Ligands. *Chem. Phys. Lett.* **1981**, *79* (1), 169–173. DOI: 10.1016/0009-2614(81)85312-2.

(54) Young, R. C.; Nagle, J. K.; Meyer, T. J.; Whitten, D. G. Electron Transfer Quenching of Nonemitting Excited States of Ru(TPP)$(Py)_2$ and Ru$(Trpy)_2^{2+}$. *J. Am. Chem. Soc.* **1978**, *100* (15), 4773–4778.

(55) Kirchhoff, J. R.; McMillin, D. R.; Marnot, P. A.; Sauvage, J. P. Photochemistry and Photophysics of Bis(Terpyridyl) Complexes of Ru(II) in Fluid Solution. Evidence for the Formation of an H_2-Diphenylterpyridine Complex. *J. Am. Chem. Soc.* **1985**, *107* (5), 1138–1141. DOI: 10.1021/ja00291a009.

(56) Vallett, P. J.; Damrauer, N. H. Experimental and Computational Exploration of Ground and Excited State Properties of Highly Strained Ruthenium Terpyridine Complexes. *J. Phys. Chem. A* **2013**, *117* (30), 6489–6507. DOI: 10.1021/jp404248z.

(57) Lin, C.-T.; Böttcher, W.; Chou, M.; Creutz, C.; Sutin, N. Mechanism of the Quenching of the Emission of Substituted Polypyridineruthenium(II) Complexes by Iron(III), Chromium(III), and Europium(III) Ions. *J. Am. Chem. Soc.* **1976**, *98* (21), 6536–6544. DOI: 10.1021/ja00437a020.

(58) Winkler, J. R.; Netzel, T. L.; Creutz, C.; Sutin, N. Direct Observation of Metal-to-Ligand Charge-Transfer (MLCT) Excited States of Pentaammineruthenium(II) Complexes. *J. Am. Chem. Soc.* **1987**, *109* (8), 2381–2392. DOI: 10.1021/ja00242a023.

(59) Hewitt, J. T.; Vallett, P. J.; Damrauer, N. H. Dynamics of the ^{3}MLCT in Ru(II) Terpyridyl Complexes Probed by Ultrafast Spectroscopy: Evidence of Excited-State Equilibration and Interligand Electron Transfer. *J. Phys. Chem. A* **2012**, *116* (47), 11536–11547. DOI: 10.1021/jp308091t.

(60) Amini, A.; Harriman, A.; Mayeux, A. The Triplet Excited State of Ruthenium(II) Bis(2,2':6',2″-Terpyridine): Comparison between Experiment and Theory. *Phys. Chem. Chem. Phys.* **2004**, *6* (6), 1157–1164. DOI: 10.1039/b313526h.

(61) Islam, A.; Ikeda, N.; Yoshimura, A.; Ohno, T. Nonradiative Transition of Phosphorescent Charge-Transfer States of Ruthenium(II)-to-2,2′-Biquinoline and Ruthenium(II)-to-2,2′:6′,2″-Terpyridine in the Solid State. *Inorg. Chem.* **1998**, *37* (12), 3093–3098. DOI: 10.1021/ic9702429.

(62) Ashley, D. C.; Jakubikova, E. Tuning the Redox Potentials and Ligand Field Strength of Fe(II) Polypyridines: The Dual π-Donor and π-Acceptor Character of Bipyridine. *Inorg. Chem.* **2018**, *57* (16), 9907–9917. DOI: 10.1021/acs.inorgchem.8b01002.

(63) Palmer, R. A.; Piper, T. S. 2,2'-Bipyridine Complexes. I. Polarized Crystal Spectra of Tris (2,2'-Bipyridine)Copper(II), -Nickel(II), -Cobalt(II), -Iron(II), and -Ruthenium(II). *Inorg. Chem.* **1966**, *5* (5), 864–878. DOI: 10.1021/ic50039a034.

(64) Using the Average Energy Ratios of the Co(III) Series, $E(^3T_2)/E(^3T_1)$ = 1.24 and $E(^1T_1)/E(^3T_1)$ = 1.53, the $^3T_2$ Transitions Is Calculated at 15310 cm^{-1} and the $^1T_1$ Is Calculated at 18890 cm^{-1}.

APPENDIX 2.A. LIGAND-FIELD SPECTRA, TANABE-SUGANO DIAGRAMS, NMR SPECTRA, AND CRYSTALLOGRAPHIC DATA

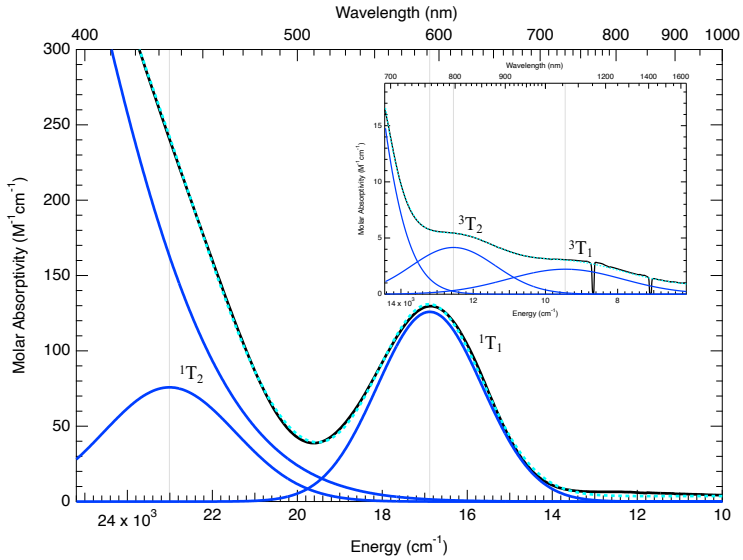

Figure 2.6. Deconvolved UV-Vis spectrum of $[Co(acac)_3]$ in $CHCl_3$. The dips in the low energy absorption spectrum are due to poor baseline correction due to $CHCl_3$ overtones and difficulty in baseline correcting with 10 cm quartz cells.

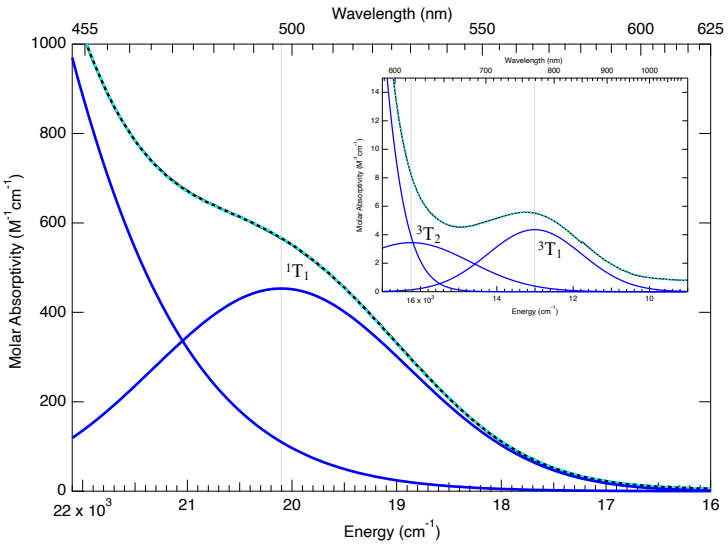

Figure 2.7. Deconvolved UV-Vis spectrum of $[Co(pyro\text{-}bpy)_3](PF_6)_3$ in MeCN.

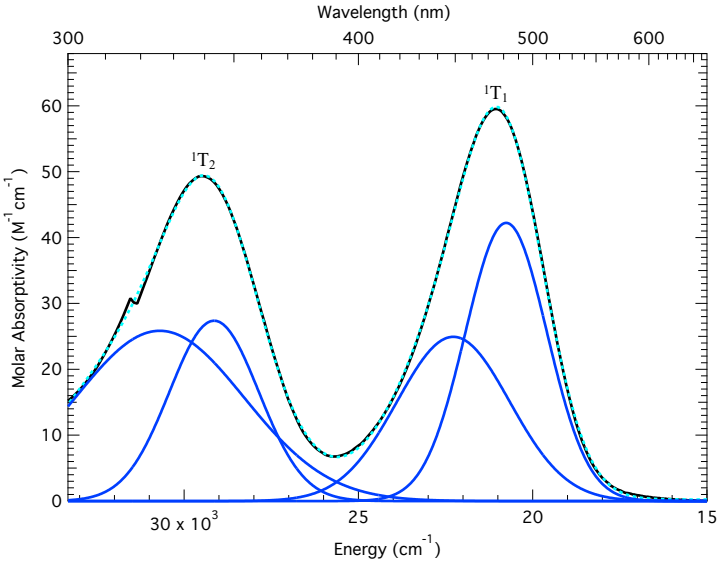

Figure 2.8. Deconvolved high energy UV-Vis spectrum of $[Co(NH_3)_6]Cl_3$ in H_2O. The splitting of the $^1T_1$ and $^1T_2$ bands can be observed due to descending in symmetry as the ammine ligands interact with the solvent through intermolecular hydrogen bonding.

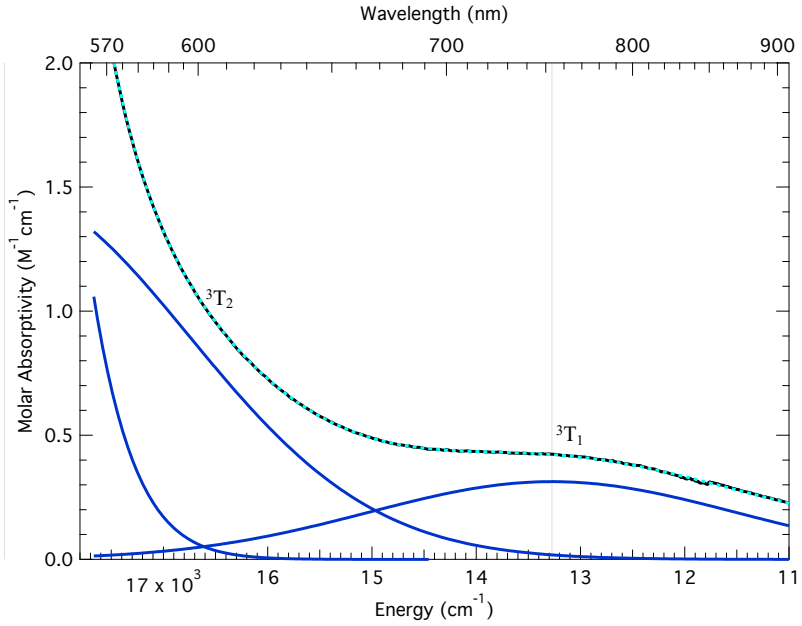

Figure 2.9. Deconvolved low energy UV-Vis spectrum of $[Co(NH_3)_6]Cl_3$ in H_2O.

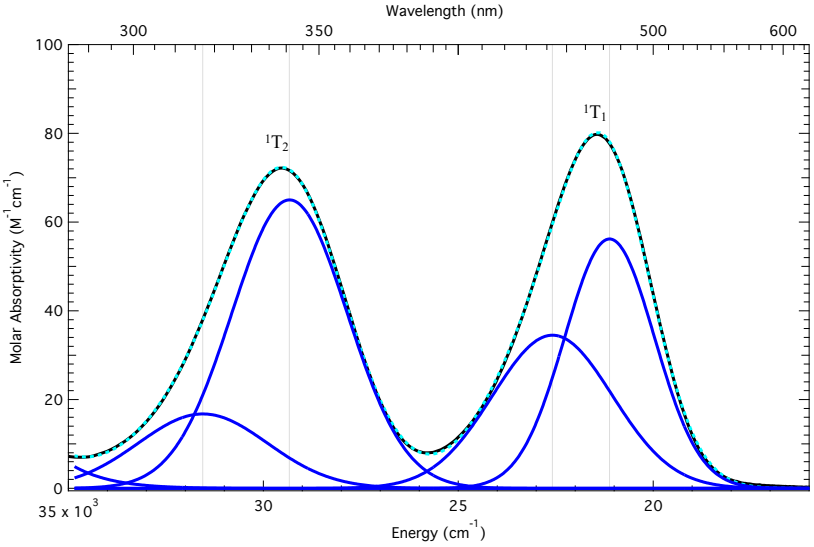

Figure 2.10. Deconvolved high energy UV-Vis spectrum of $[Co(en)_3]Cl_3$ in H_2O. The splitting of the $^1T_1$ and $^1T_2$ bands can be observed due to descending in symmetry as the ammine ligands interact with the solvent through intermolecular hydrogen bonding.

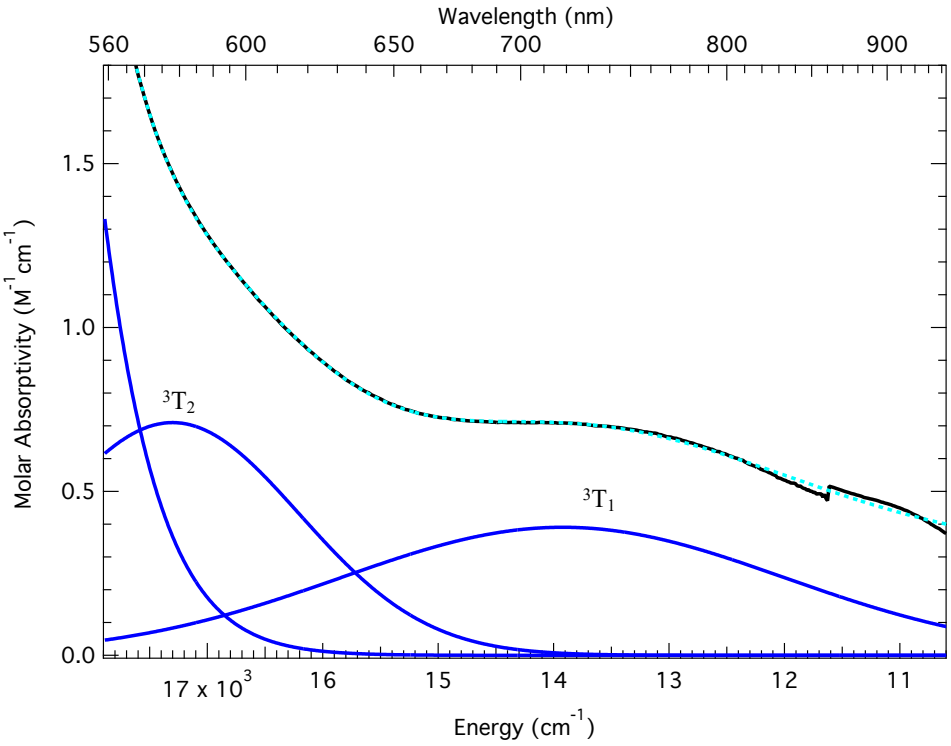

Figure 2.11. Deconvolved low energy UV-Vis spectrum of $[Co(en)_3]Cl_3$ in H_2O.

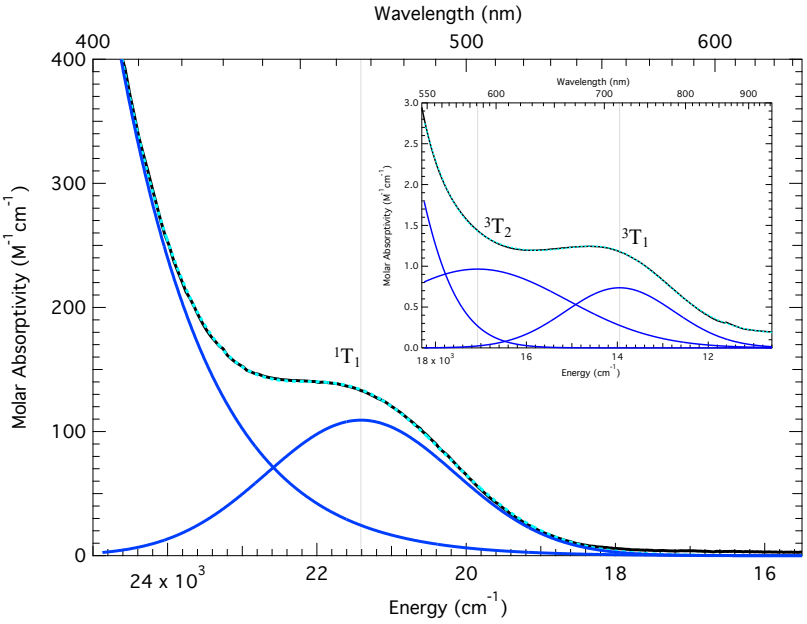

Figure 2.12. Deconvolved UV-Vis spectrum of $[Co(phen)_3](PF_6)_3$ in MeCN.

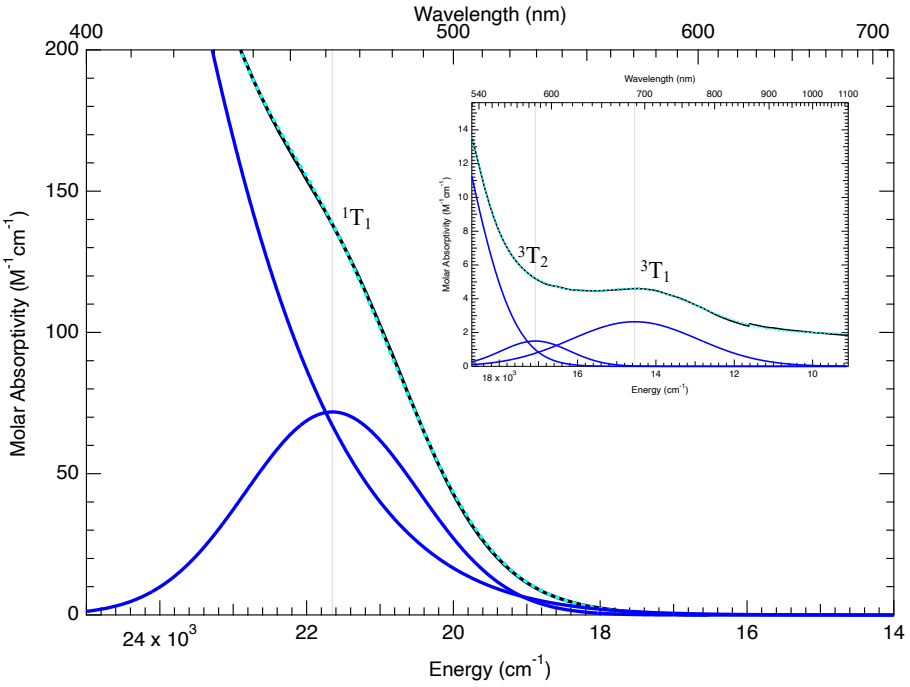

Figure 2.13. Deconvolved UV-Vis spectrum of $[Co(dtb)_3](PF_6)_3$ in MeCN.

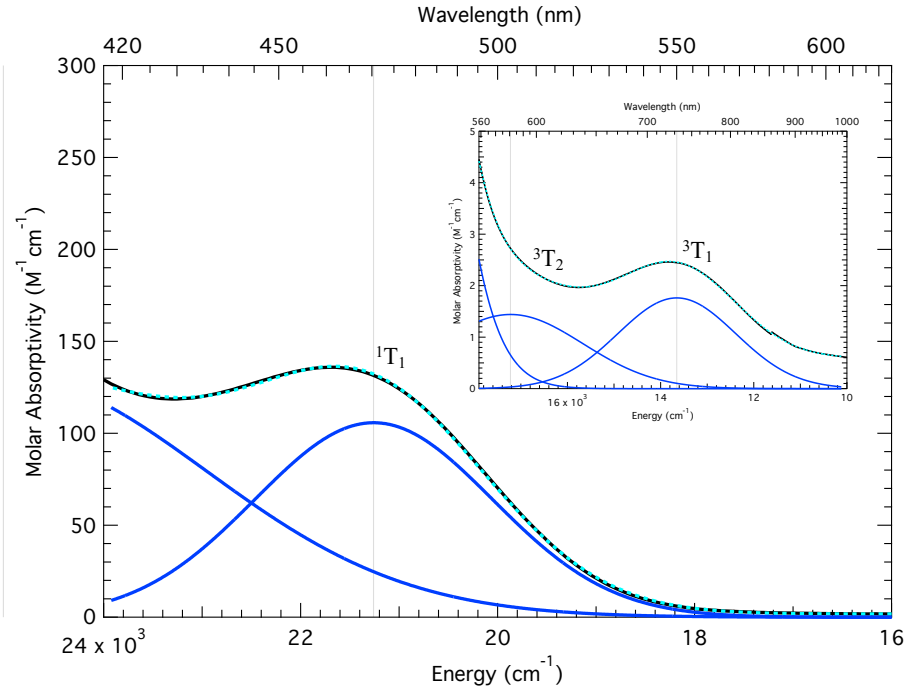

Figure 2.14. Deconvolved UV-Vis spectrum of $[Co(OMe\text{-}bpy)_3](PF_6)_3$ in MeCN.

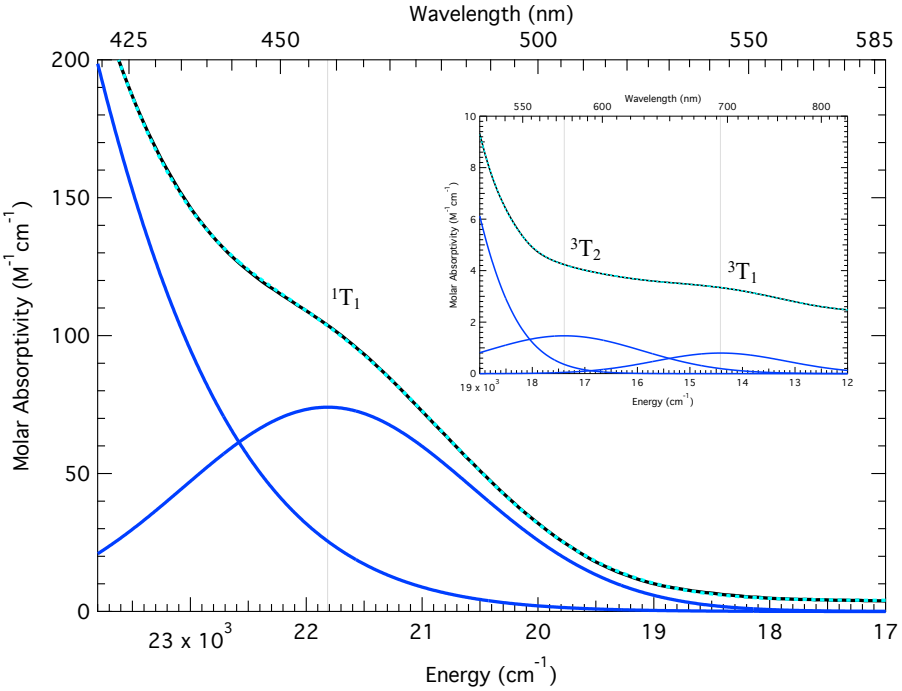

Figure 2.15. Deconvolved UV-Vis spectrum of $[Co(5,5'\text{-dmb})_3](PF_6)_3$ in MeCN.

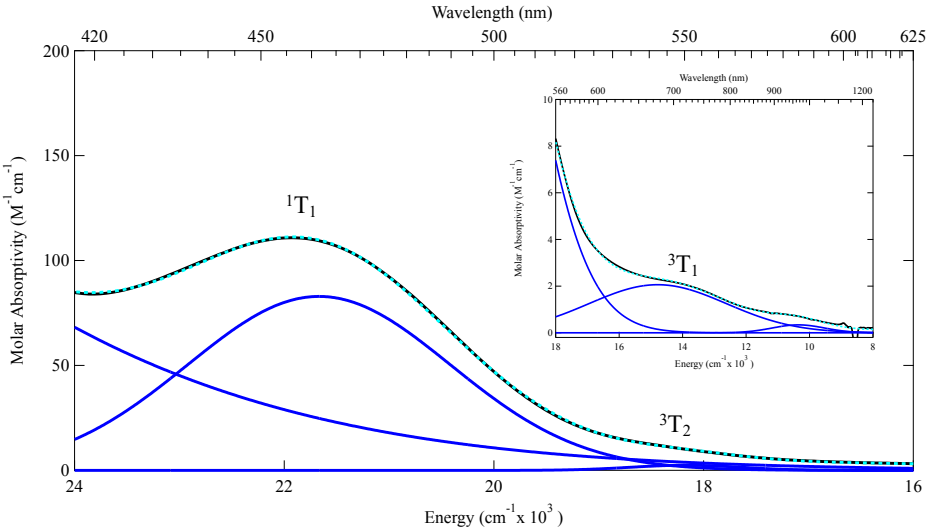

Figure 2.16. Deconvolved UV-Vis spectrum of $[Co(Br_2bpy)_3](PF_6)_2$ in MeCN.

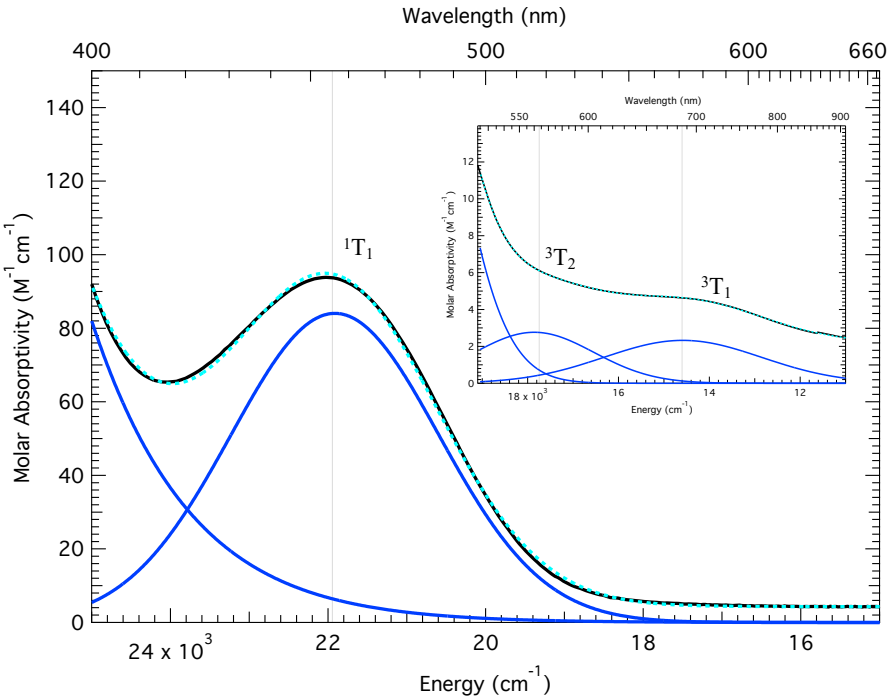

Figure 2.17. Deconvolved UV-Vis spectrum of $[Co(4,4'\text{-dmb})_3](PF_6)_3$ in MeCN.

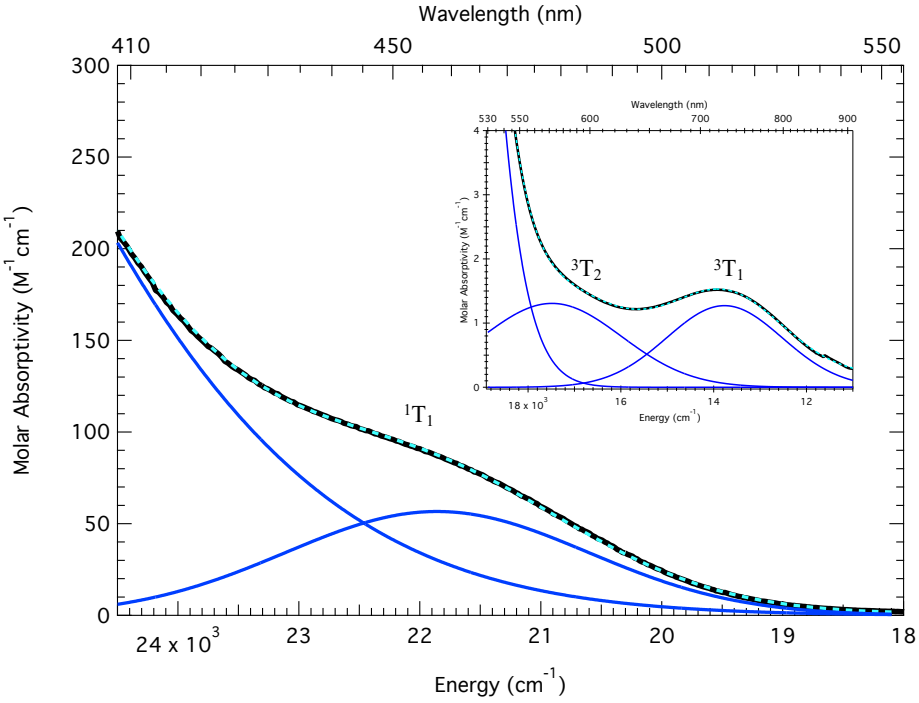

Figure 2.18. Deconvolved UV-Vis spectrum of $[Co(bpy)_3](PF_6)_3$ in MeCN.

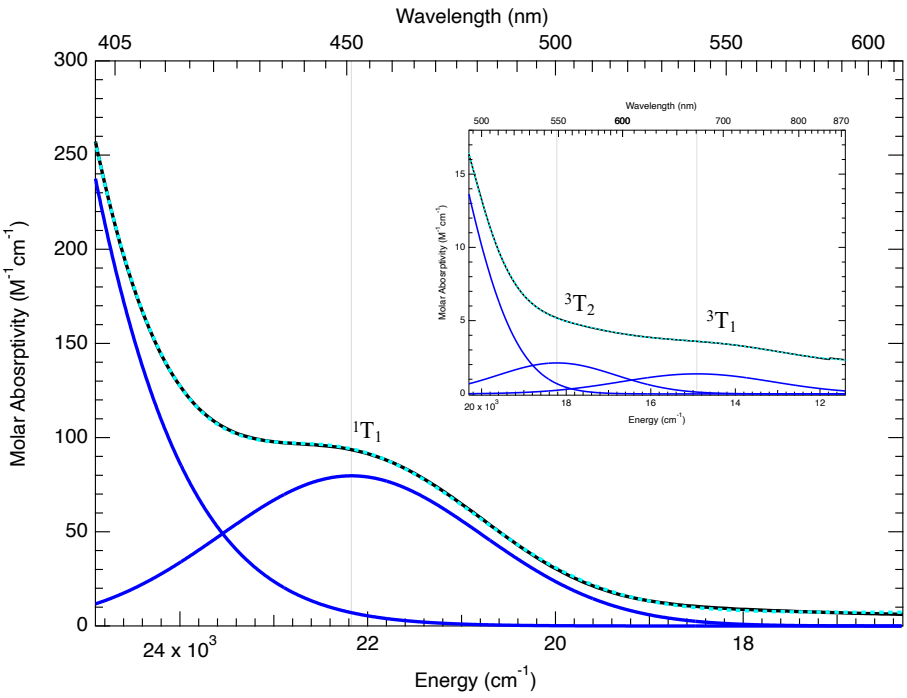

Figure 2.19 Deconvolved UV-Vis spectrum of $[Co(deeb)_3](PF_6)_3$ in MeCN.

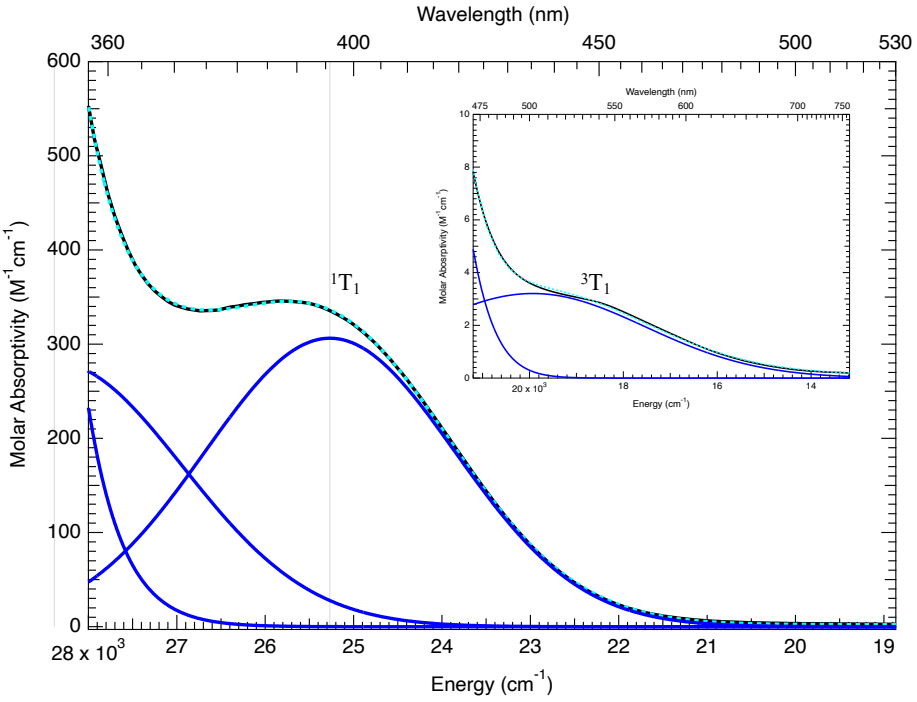

Figure 2.20. Deconvolved UV-Vis spectrum of $[Co(B^{Me}ImPy)_2](PF_6)_3$ in MeCN.

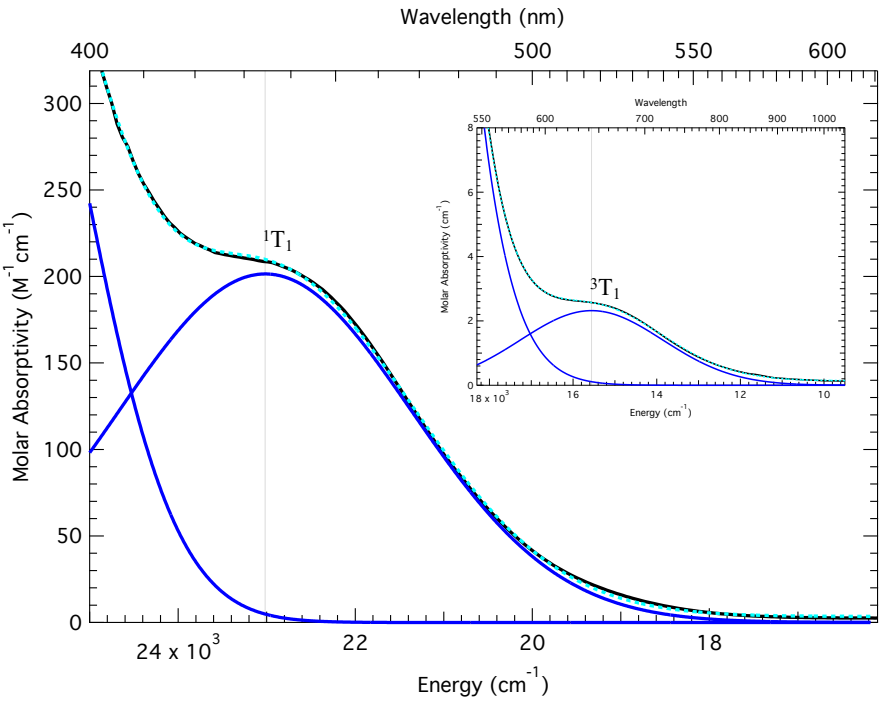

Figure 2.21. Deconvolved UV-Vis spectrum of $[Co(terpy)_2](PF_6)_3$ in MeCN.

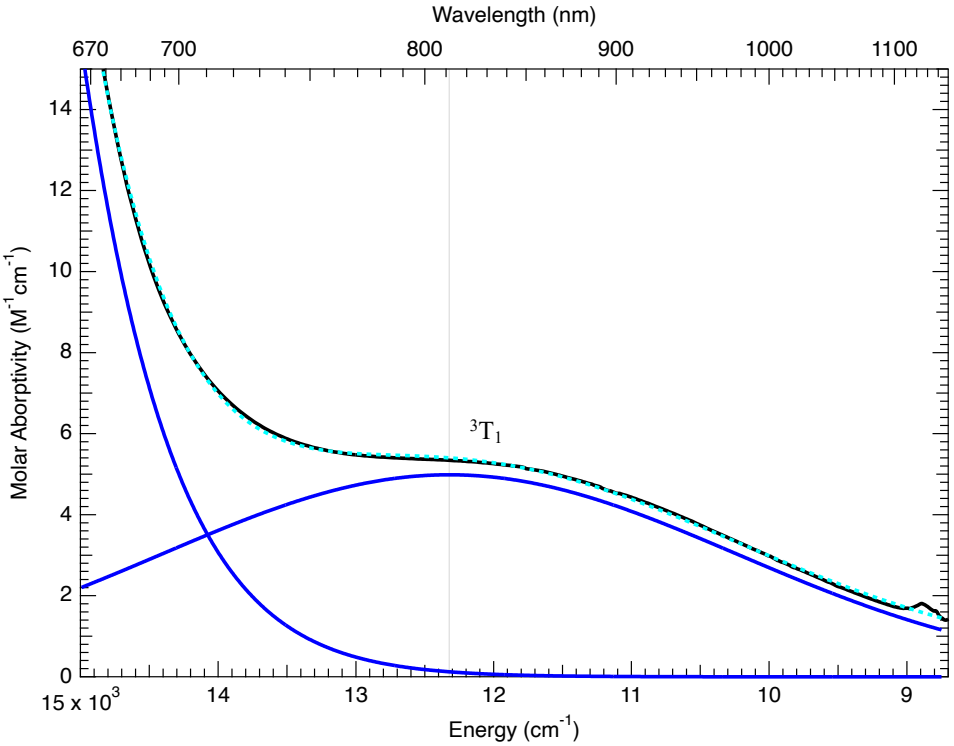

Figure 2.22. Deconvolved UV-Vis spectrum of $[Fe(bpy)_3](PF_6)_2$ in MeCN.

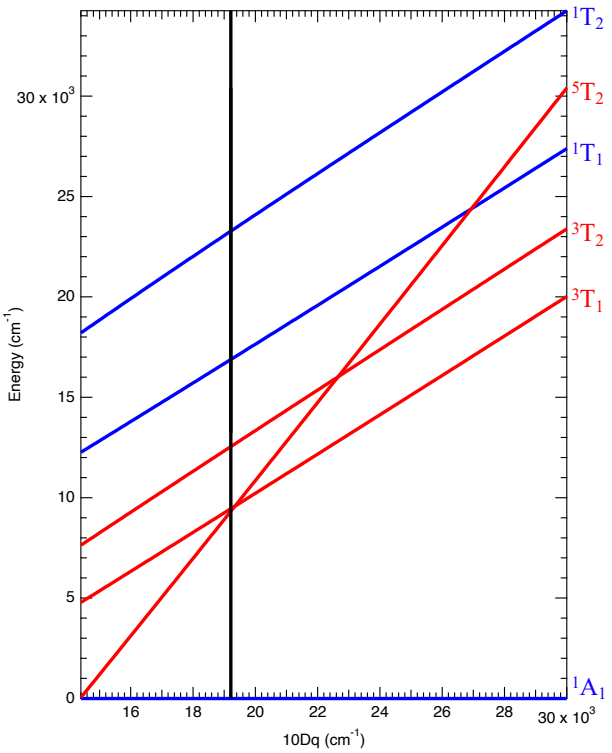

Figure 2.23. Tanabe-Sugano Diagram of $[Co(acac)_3]$. B = 480 cm^{-1}, C = 3590 cm^{-1}, 10Dq = 19210 cm^{-1}.

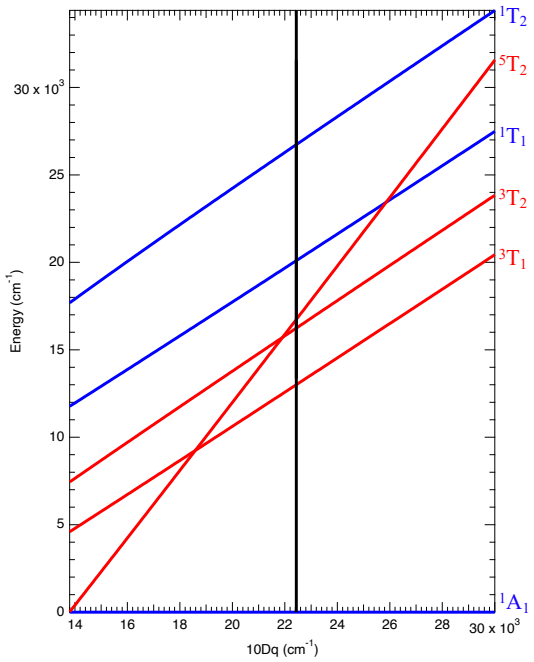

Figure 2.24. Tanabe-Sugano Diagram of $[Co(pyrro\text{-}bpy)_3](PF_6)_3$. B = 480 cm^{-1}, C = 3430 cm^{-1}, 10Dq = 22440 cm^{-1}.

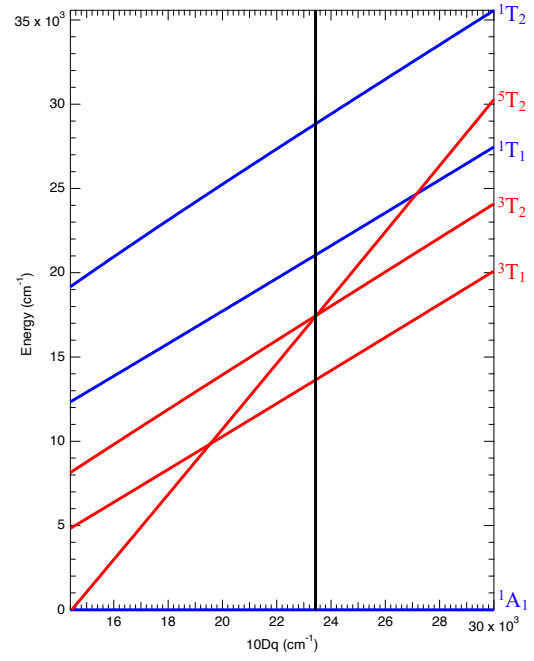

Figure 2.25. Tanabe-Sugano Diagram of $[Co(NH_3)_6]Cl_3$. B = 580 cm^{-1}, C = 3550 cm^{-1}, 10Dq = 23430 cm^{-1}.

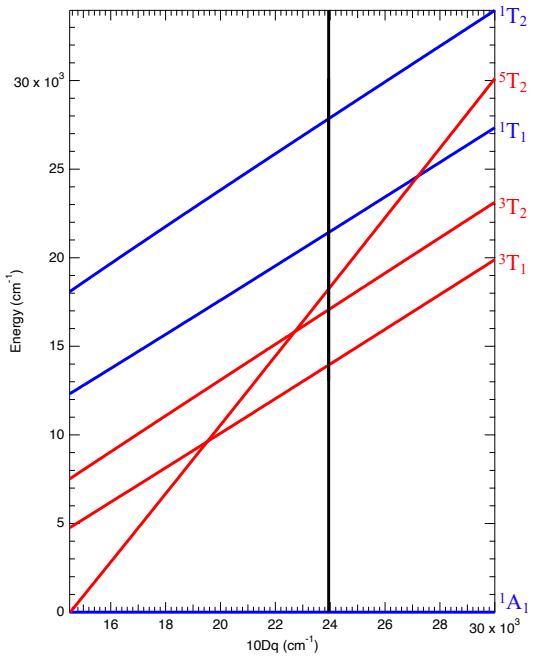

Figure 2.26. Tanabe-Sugano Diagram of $[Co(phen)_3](PF_6)_3$. B = 460 cm^{-1}, C = 3630 cm^{-1}, 10Dq = 23940 cm^{-1}.

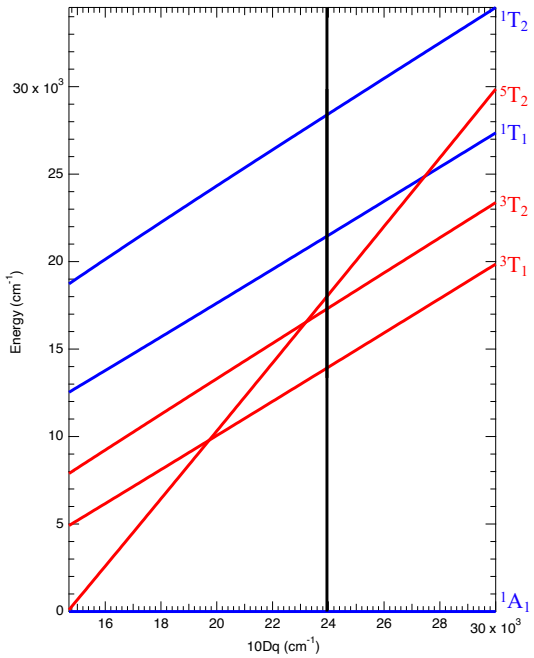

Figure 2.27. Tanabe-Sugano Diagram of $[Co(en)_3]Cl_3$. B = 500 cm^{-1}, C = 3640 cm^{-1}, 10Dq = 23950 cm^{-1}.

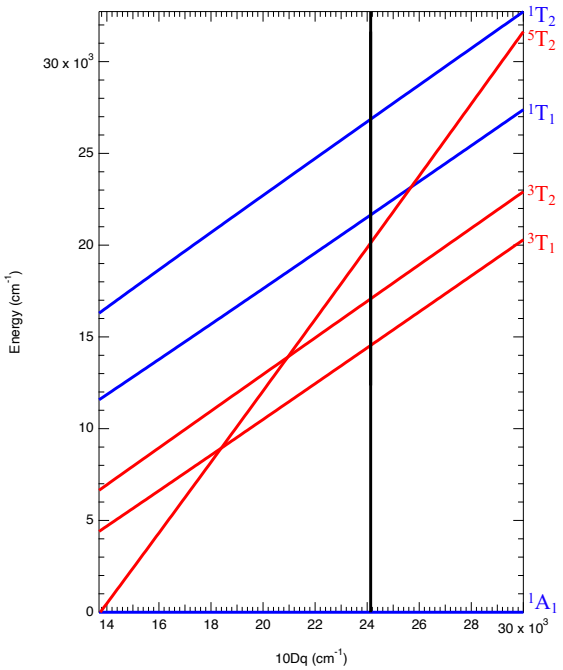

Figure 2.28. Tanabe-Sugano Diagram of $[Co(dtb)_3](PF_6)_3$. B = 370 cm^{-1}, C = 3480 cm^{-1}, and 10Dq = 24130 cm^{-1}.

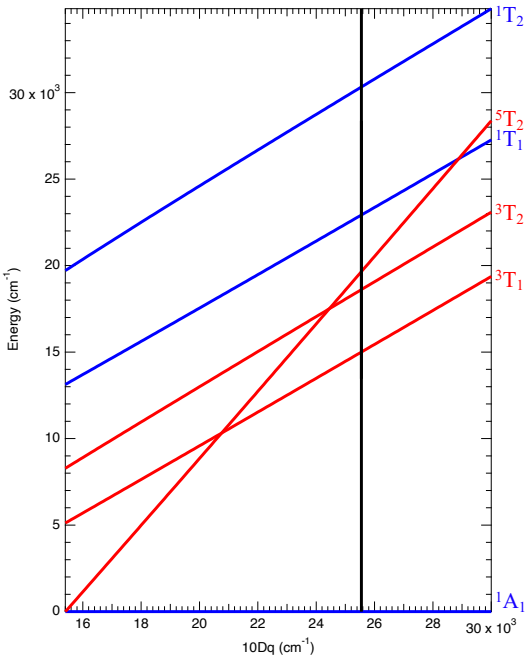

Figure 2.29. Tanabe-Sugano Diagram of $[Co(OMe\text{-}bpy)_3](PF_6)_3$. B = 530 cm^{-1}, C = 3830 cm^{-1}, 10Dq = 24170 cm^{-1}.

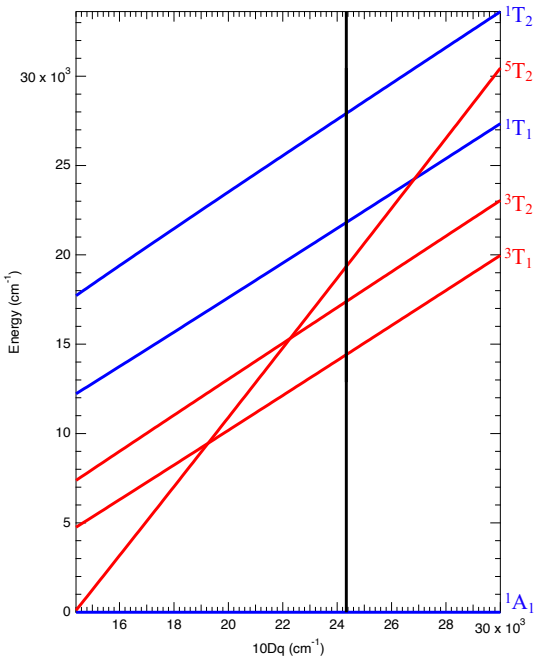

Figure 2.30. Tanabe-Sugano Diagram of $[Co(5,5'\text{-dmb})_3](PF_6)_3$. B = 430 cm^{-1}, C = 3600 cm^{-1}, 10Dq = 24330 cm^{-1}.

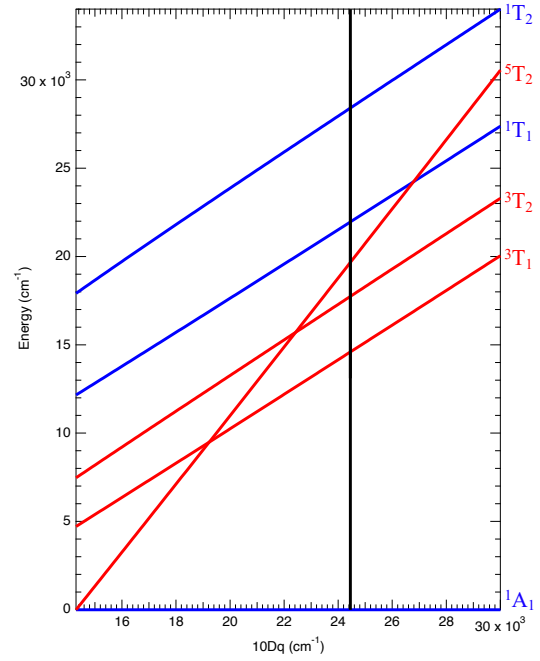

Figure 2.31. Tanabe-Sugano Diagram of $[Co(4,4'\text{-dmb})_3](PF_6)_3$. B = 460 cm^{-1}, C = 3570 cm^{-1}, 10Dq = 24450 cm^{-1}.

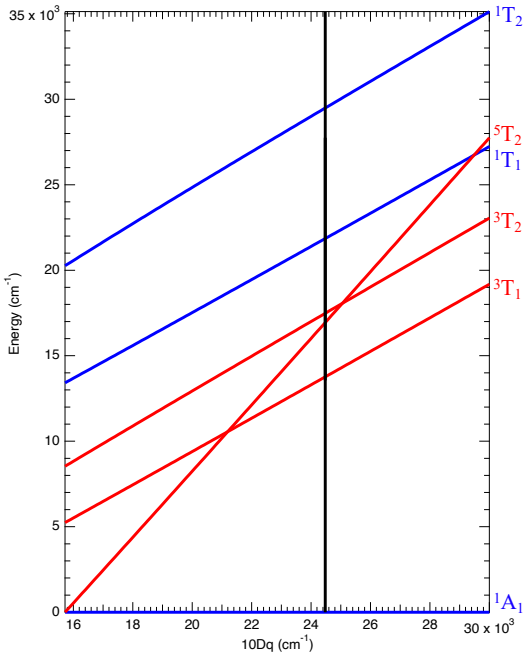

Figure 2.32. Tanabe-Sugano Diagram of $[Co(bpy)_3](PF_6)_3$. B = 560 cm^{-1}, C = 3900 cm^{-1}, 10Dq = 24480 cm^{-1}.

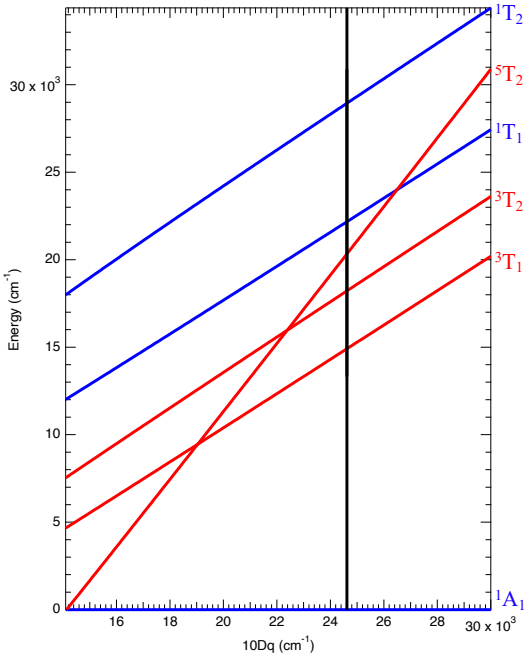

Figure 2.33. Tanabe-Sugano Diagram of $[Co(deeb)_3](PF_6)_3$. B = 490 cm^{-1}, C = 3520 cm^{-1}, 10Dq = 24620 cm^{-1}.

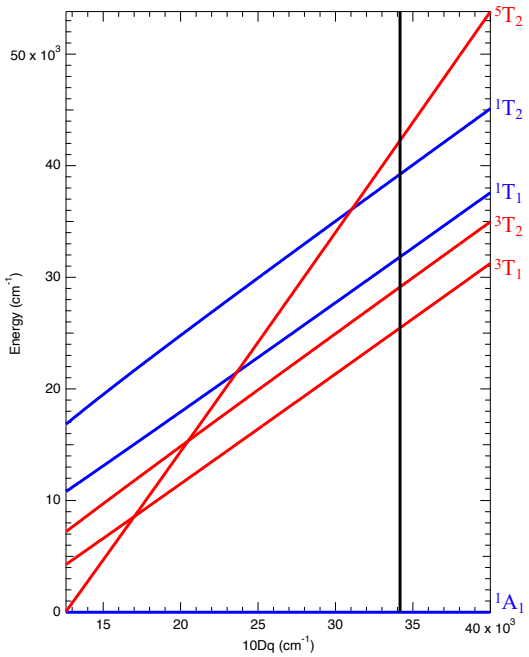

Figure 2.34. Tanabe-Sugano Diagram of $K_3[Co(CN)_6]$. B = 510 cm^{-1}, C = 3080 cm^{-1}, 10Dq = 34160 cm^{-1}.

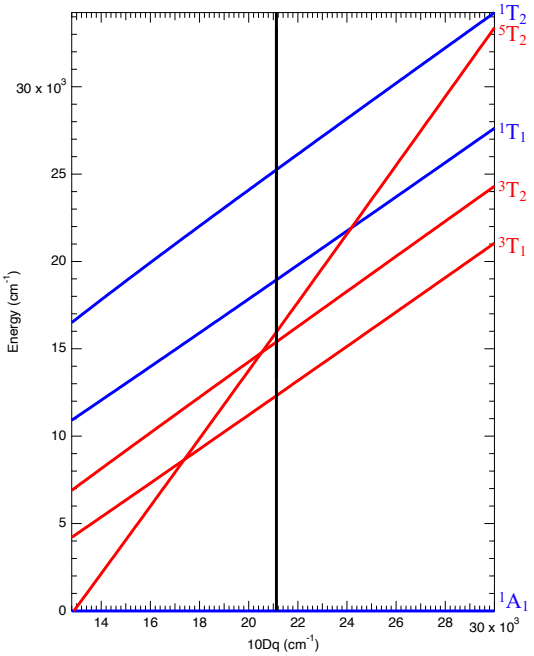

Figure 2.35. Tanabe-Sugano Diagram of $[Fe(bpy)_3](PF_6)_2$. B = 460 cm^{-1}, C = 3200 cm^{-1}, 10Dq = 21120 cm^{-1}.

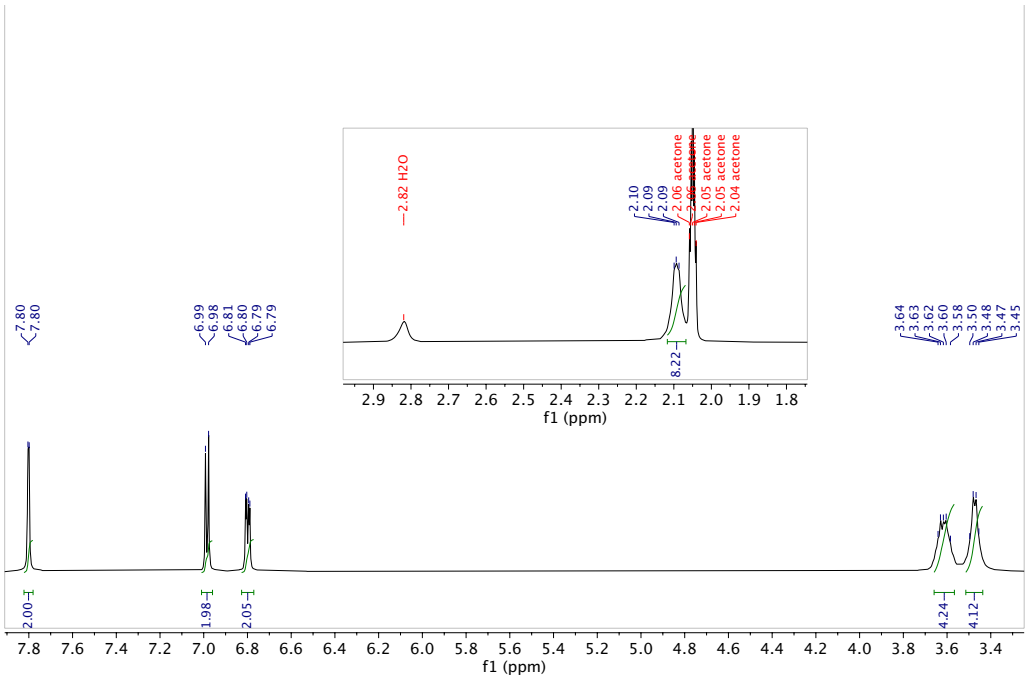

Figure 2.36. ^{1}H NMR of $[Co(pyrro\text{-}bpy)_3](PF_6)_3$ in acetone-d_6.

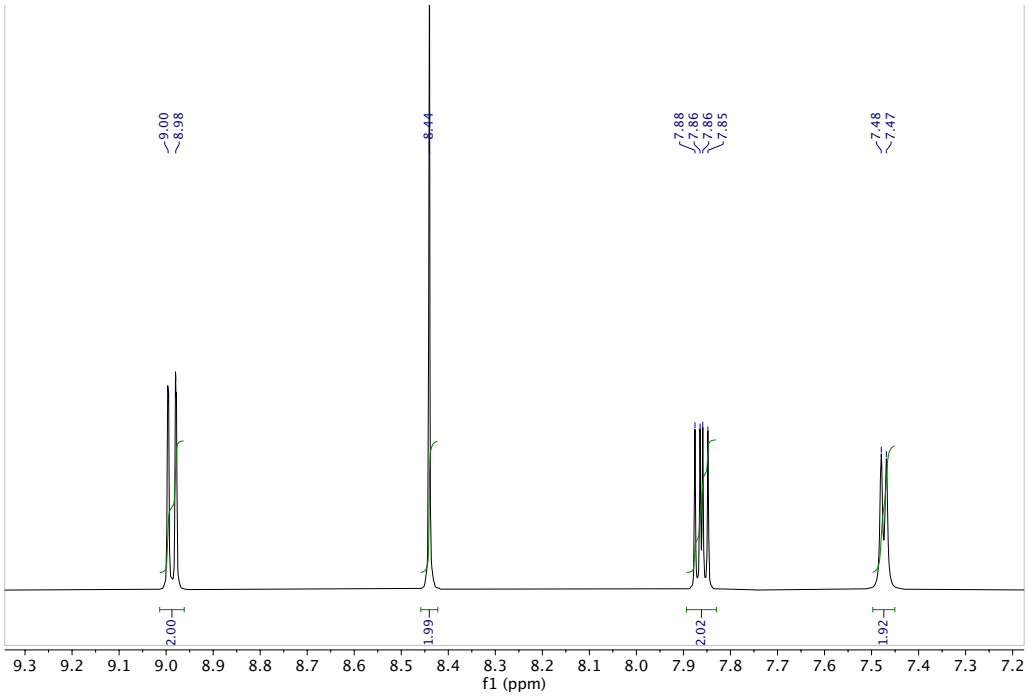

Figure 2.37. ^{1}H NMR of $[Co(phen)_3](PF_6)_3$ in CD_3CN.

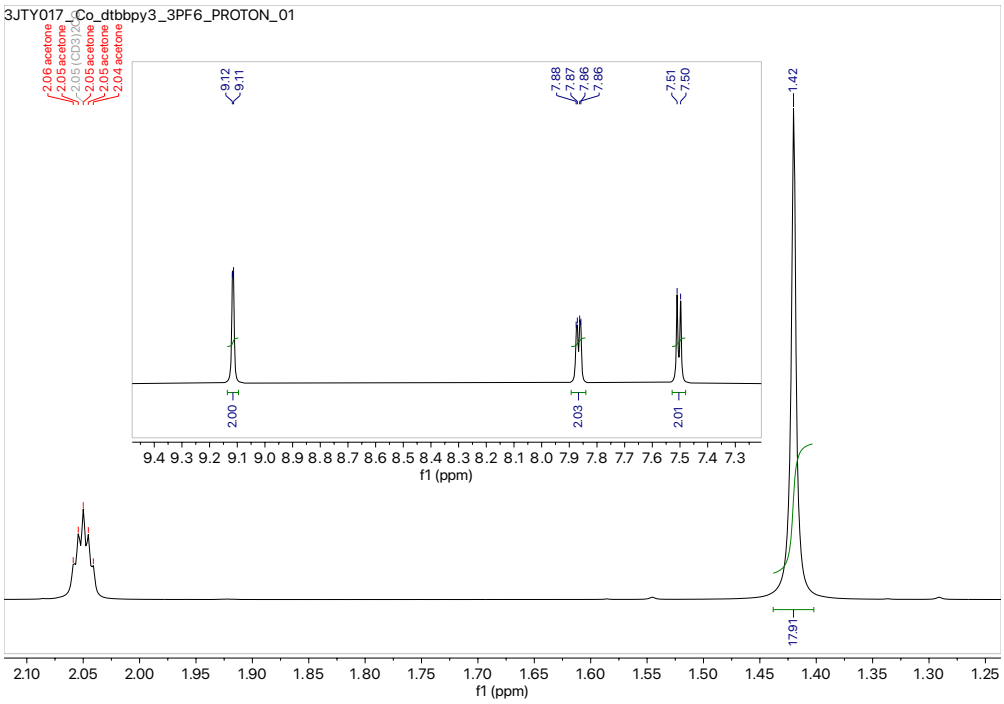

Figure 2.38. ^{1}H NMR of $[Co(dtb)_3](PF_6)_3$ in acetone-d_6.

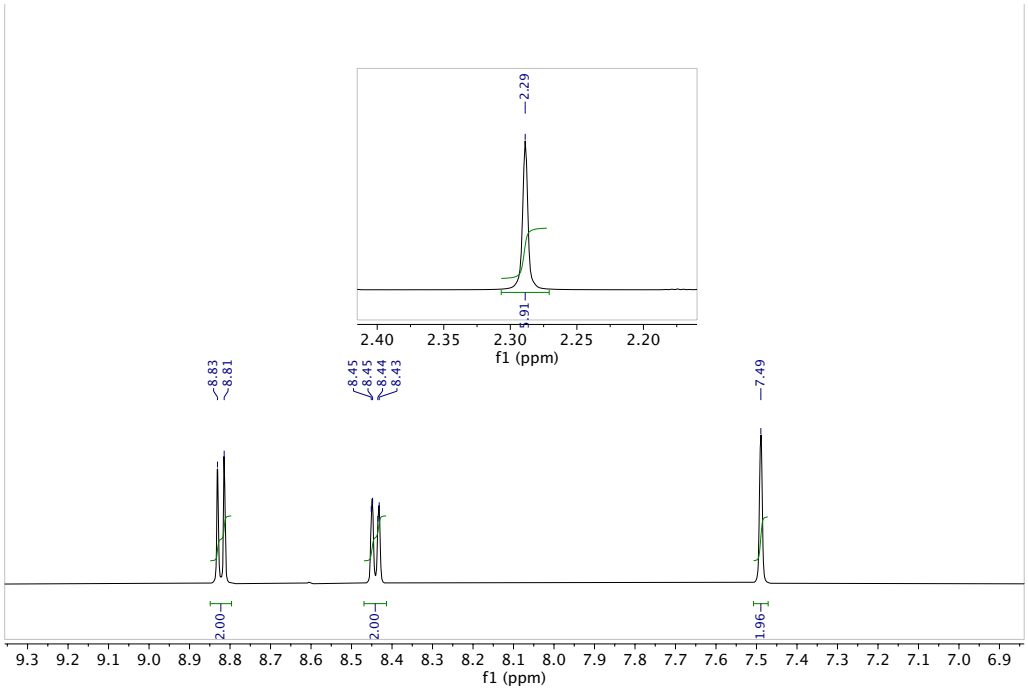

Figure 2.39. ^{1}H NMR of $[Co(5,5'\text{-dmb})_3](PF_6)_3$ in acetone-d_6.

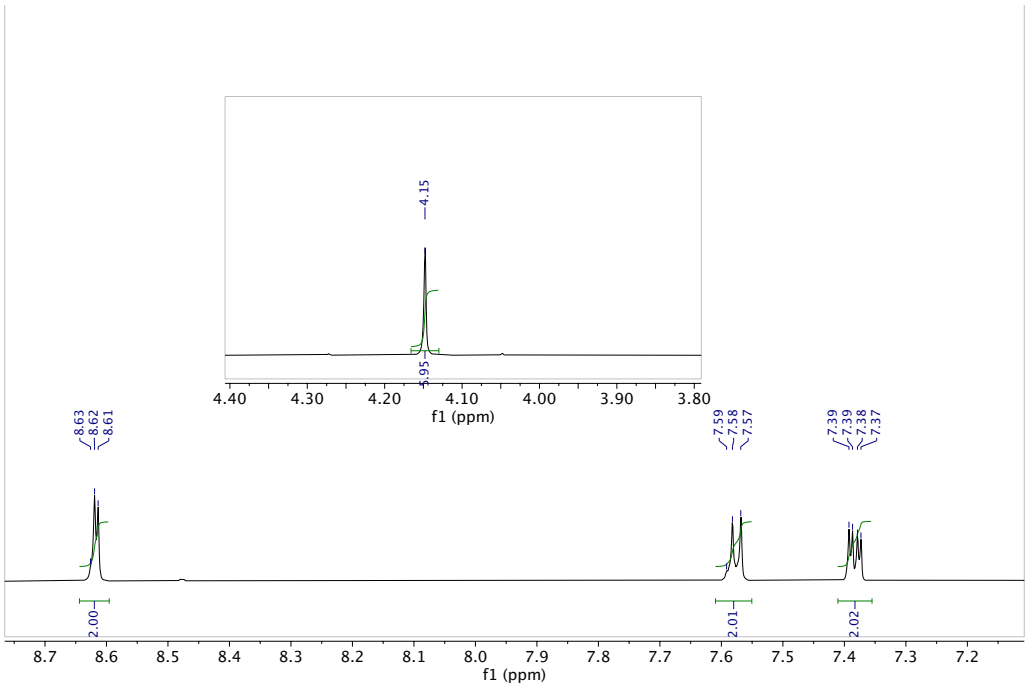

Figure 2.40. ^{1}H NMR of $[Co(OMe\text{-}bpy)_3](PF_6)_3$ in acetone-d_6.

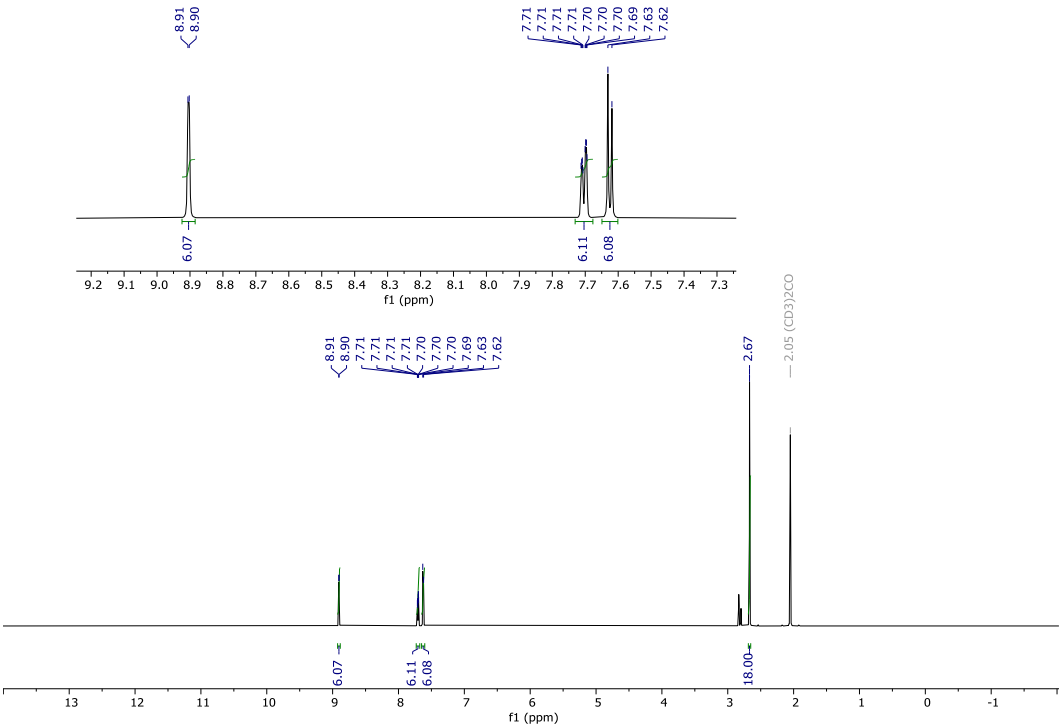

Figure 2.41. ^{1}H NMR of $[Co(4,4'\text{-}dmb)_3](PF_6)_3$ in acetone-d_6.

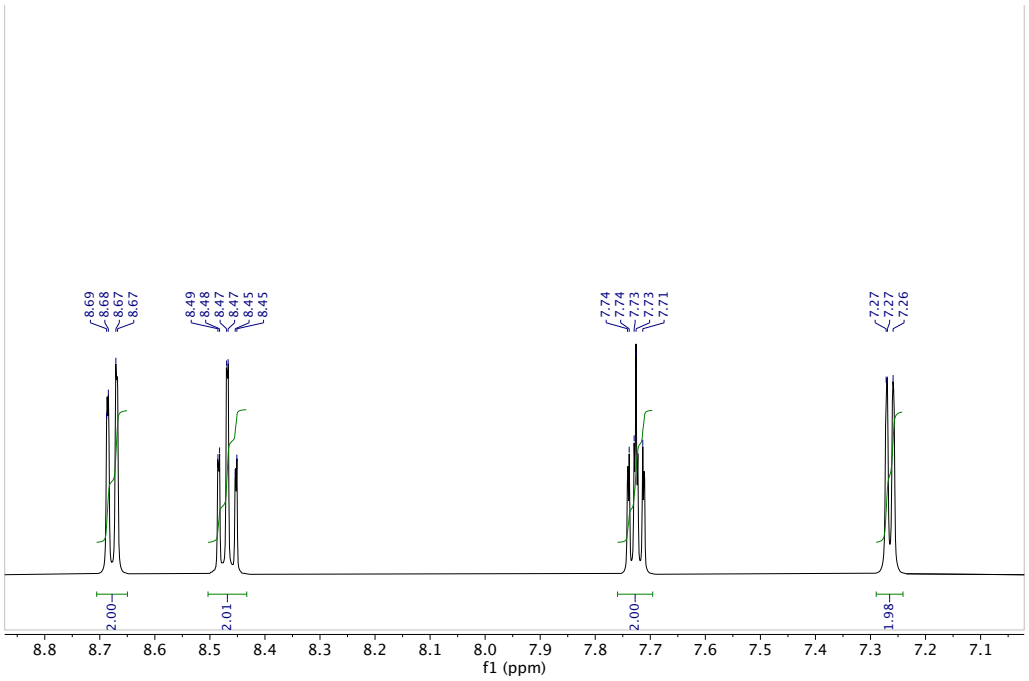

Figure 2.42. ^{1}H NMR of $[Co(bpy)_3](PF_6)_3$ in CD_3CN.

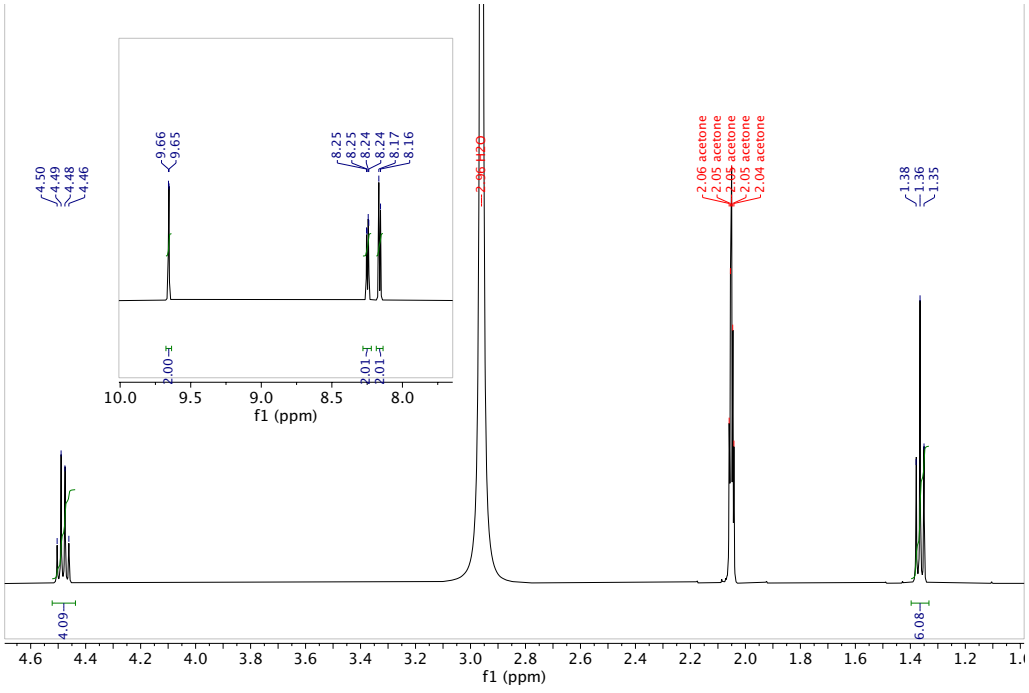

Figure 2.43. ^{1}H NMR of $[Co(deeb)_3](PF_6)_3$ in acetone-d_6.

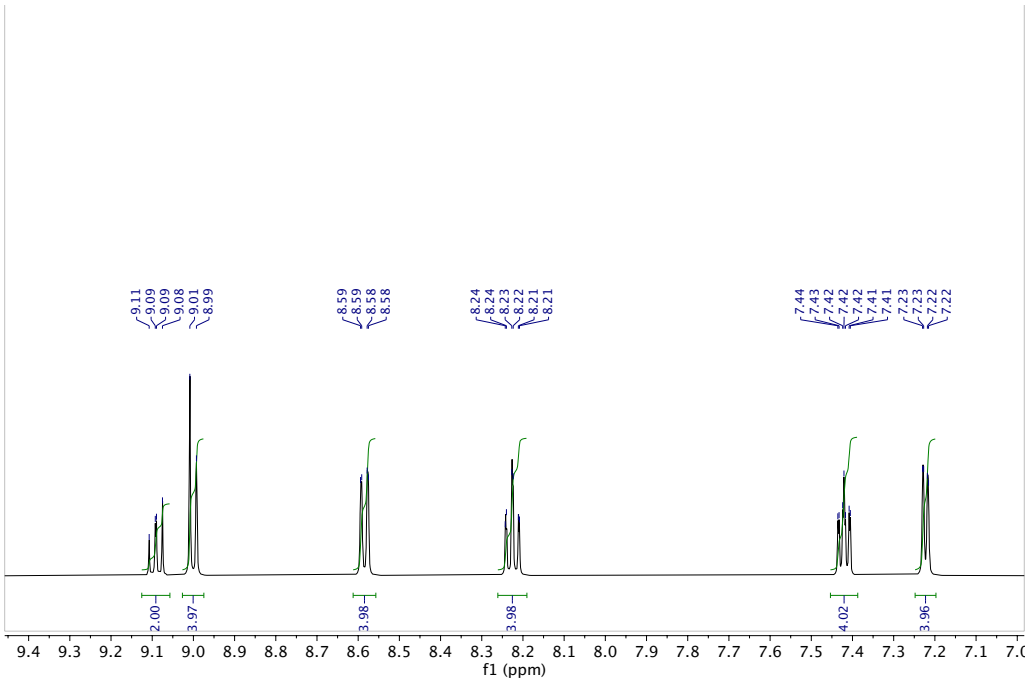

Figure 2.44. ^{1}H NMR of $[Co(tpy)_2](PF_6)_3$ in CD_3CN.

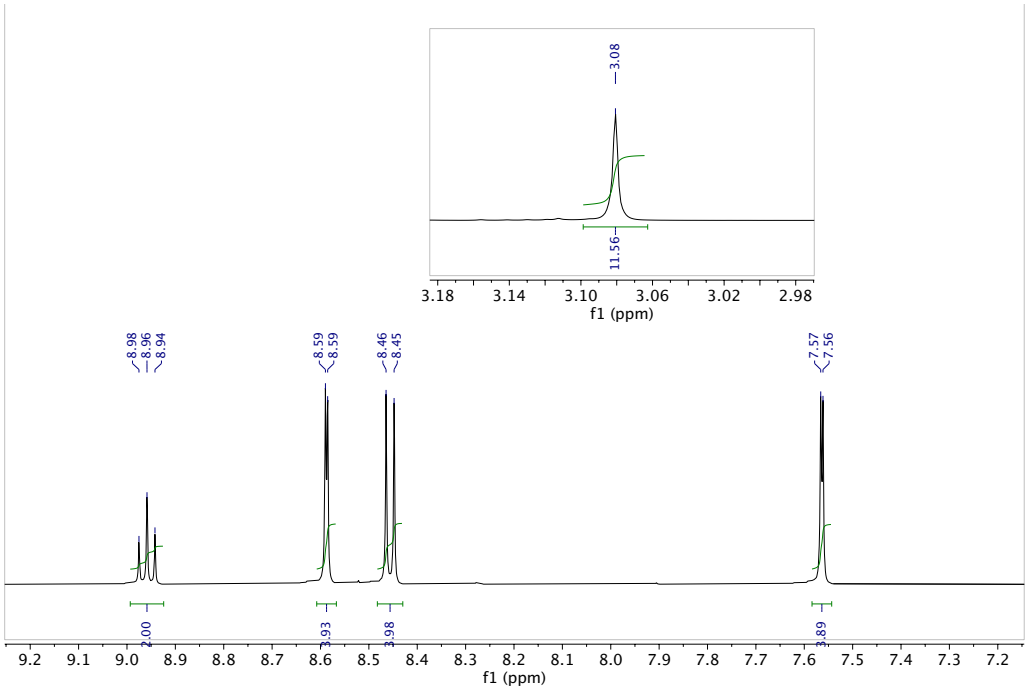

Figure 2.45. ^{1}H NMR of $[Co(B^{Me}ImPy)_2](PF_6)_3$ in acetone-d_6.

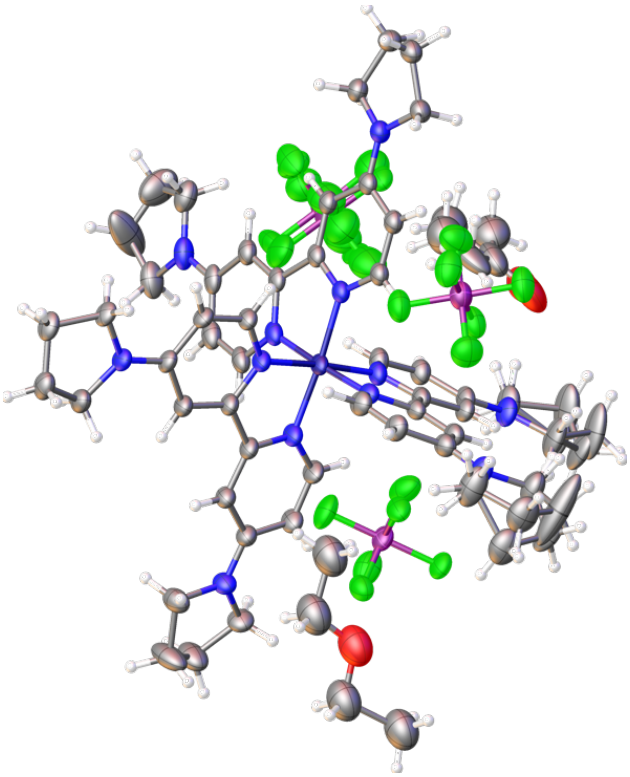

Figure 2.46. Single-crystal X-ray structure of $[Co(pyrro\text{-}bpy)_3](PF_6)_3$.

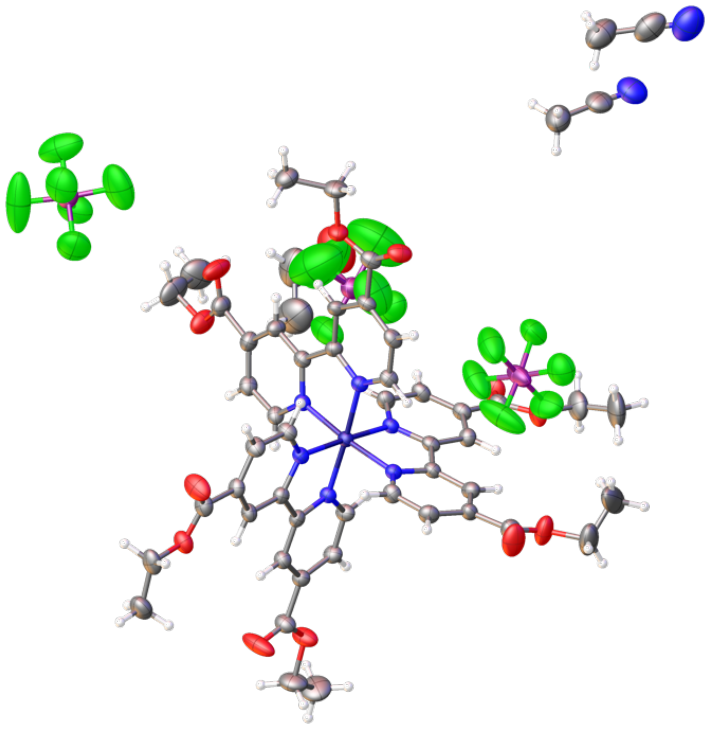

Figure 2.47. Single-crystal X-ray structure of $[Co(deeb)_3](PF_6)_3$.

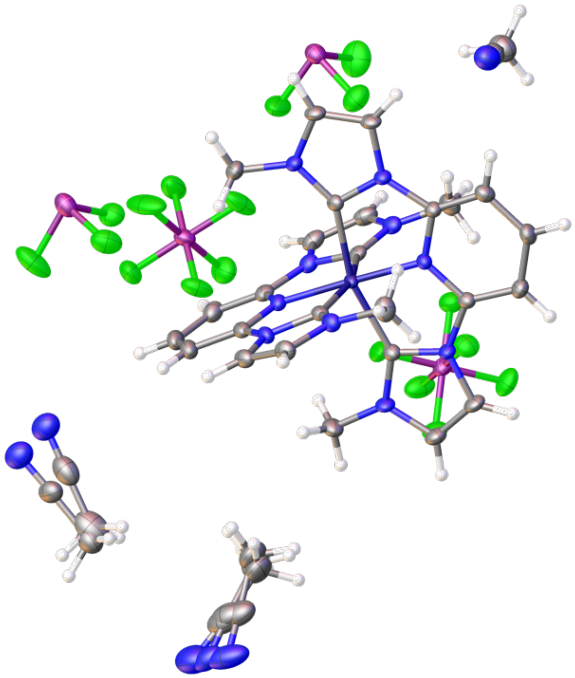

Figure 2.48. Single-crystal X-ray structure of $[Co(B^{Me}ImPy)_2](PF_6)_3$.

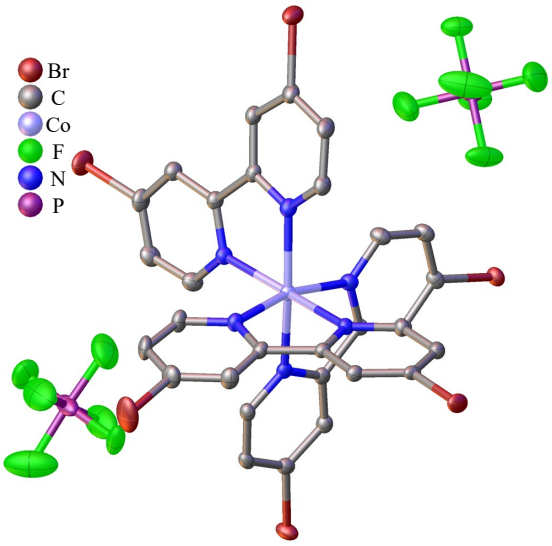

Figure 2.49. Single-crystal X-ray structure of $[Co(Br_2bpy)_3](PF_6)_2$.

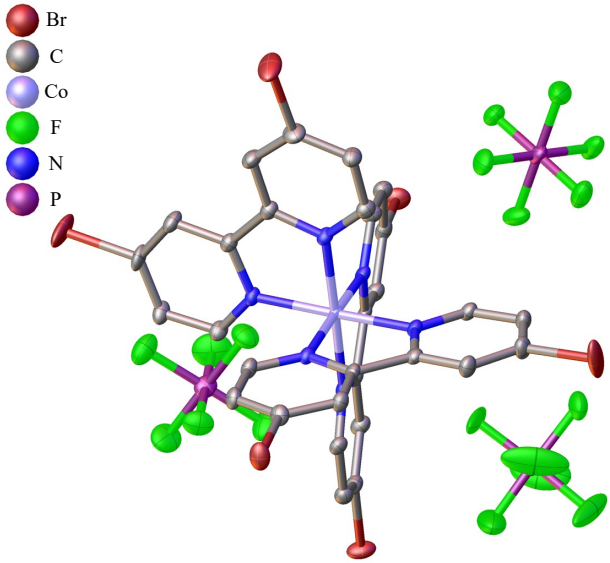

Figure 2.50. Single-crystal X-ray structure of $[Co(Br_2bpy)_3](PF_6)_3$.

Table 2.5. Crystal Data and Structure Refinement

Identification code	[Co(pyrrobpy)$_3$][PF$_6$]$_3$•(CH$_3$)$_2$CO.0.7Et$_2$O	[Co(deeb)$_3$][PF$_6$]$_3$•2CH$_3$CN.EtOH	[Co(B^{Me}ImPy)$_2$][PF$_6$]$_3$•3CH$_3$CN	5JTY204	5JTY198_CoIIIBr2bpyPF6
Empirical formula	$C_{59.8}H_{70}CoF_{18}N_{12}O_{1.7}P_3$	$C_{54}H_{60}CoF_{18}N_8O_{13}P_3$	$C_{32}H_{35}CoF_{18}N_{13}P_3$	$C_{34}H_{24}Br_6CoF_{12}N_8P_2$	$C_{36.4}H_{29.75}Br_6CoF_{18.38}N_{8.88}O_{0.8}P_3$
Formula weight	1486.99	1519.18	1095.57	1372.94	1585.66
Temperature/K	100.00(10)	173.02	100.02(11)	100.00(10)	100.00(10)
Crystal system	triclinic	monoclinic	monoclinic	triclinic	triclinic
Space group	P-1	$P2_1/c$	C2/c	P-1	P-1
a/Å	13.25924(11)	10.2402(3)	19.2943(3)	11.21483(10)	10.65870(10)
b/Å	14.62477(13)	28.3157(8)	14.2346(2)	12.48286(13)	13.50600(10)
c/Å	17.74343(13)	22.1229(6)	31.6092(4)	16.64253(18)	18.7551(2)
α/°	76.8477(7)	90	90	96.8018(9)	82.2290(10)
β/°	85.7019(6)	92.568(2)	95.9340(10)	106.7672(9)	81.2030(10)
γ/°	85.2909(7)	90	90	98.1133(8)	80.5970(10)
Volume/Å^3	3333.51(5)	6408.3(3)	8634.8(2)	2177.11(4)	2615.43(4)
Z	2	4	8	2	2
ρ_{calc}g/cm^3	1.481	1.575	1.685	2.094	2.013
μ/mm^{-1}	3.601	3.883	5.295	11.060	9.793
F(000)	1539	3103	4416	1318.0	1529.0
Crystal size/mm^3	0.371 × 0.146 × 0.074	0.301 × 0.217 × 0.074	0.519 × 0.314 × 0.176	0.154 × 0.113 × 0.072	0.259 × 0.201 × 0.136
Radiation	Cu Kα (λ = 1.54184)	CuKα (λ = 1.54178)	Cu Kα (λ = 1.54184)	Cu Kα (λ = 1.54184)	Cu Kα (λ = 1.54184)
2Θ range for data collection/°	5.124 to 154.592	5.072 to 140.416	5.622 to 154.734	5.626 to 154.324	4.798 to 154.454
Index ranges	-16 ≤ h ≤ 16, -18 ≤ k ≤ 17, -22 ≤ l ≤ 18	-12 ≤ h ≤ 12, -34 ≤ k ≤ 34, -26 ≤ l ≤ 26	-23 ≤ h ≤ 13, -17 ≤ k ≤ 17, -39 ≤ l ≤ 40	-14 ≤ h ≤ 12, -15 ≤ k ≤ 15, -20 ≤ l ≤ 20	-11 ≤ h ≤ 13, -17 ≤ k ≤ 17, -22 ≤ l ≤ 23
Reflections collected	75332	51812	29808	49002	60299
Independent reflections	13341 [R_{int} = 0.0321, R_{sigma} = 0.0211]	12152 [R_{int} = 0.1020, R_{sigma} = 0.0777]	8762 [R_{int} = 0.0580, R_{sigma} = 0.0379]	8703 [R_{int} = 0.0370, R_{sigma} = 0.0244]	10531 [R_{int} = 0.0413, R_{sigma} = 0.0264]
Data/restraints/parameters	13341/52/943	12152/9/882	8762/243/661	8703/7/597	10531/52/718
Goodness-of-fit on F^2	1.028	1.035	1.064	1.056	1.032
Final R indexes [I>=2σ (I)]	R_1 = 0.0687, wR_2 = 0.1857	R_1 = 0.0766, wR_2 = 0.2059	R_1 = 0.0565, wR_2 = 0.1473	R_1 = 0.0385, wR_2 = 0.0924	R_1 = 0.0455, wR_2 = 0.1116
Final R indexes [all data]	R_1 = 0.0760, wR_2 = 0.1920	R_1 = 0.1175, wR_2 = 0.2353	R_1 = 0.0597, wR_2 = 0.1499	R_1 = 0.0409, wR_2 = 0.0937	R_1 = 0.0479, wR_2 = 0.1131
Largest diff. peak/hole / e Å^{-3}	1.21/-0.85	0.72/-0.63	0.91/-1.15	1.96/-1.76	1.73/-1.85

APPENDIX 2.B. USING LIGFIELD FOR THE CALCULATION OF LIGAND-FIELD PARAMETERS

In order to use LIGFIELD you must install the program DOSBox, a DOS emulator, on to your PC or Mac. This program is available for free on the internet. For PCs DOSBox should be placed on the C: drive along with the folder containing the executables for LIGFIELD. For Mac, it is recommended that the LIGFIELD folder is placed inside the folder for DOSBox on the Desktop. This allows for ease in execution and mounting of the appropriate drive. The initial loading of LIGFIELD and the syntax used in DOSBox is different for PC and Mac, so the initial section will be split between Mac and PC start-up. Note that when using DOSBox all directories are case-sensitive, i.e. **Desktop** and **desktop** are not equivalent.

2.B.1. Running DOSBox on Mac

Once DOSBox has opened a screen will be displayed as shown below in Figure 2.51. The initial drive mounted is the Z-Drive, which is a virtual drive within DOSBox. A new drive must be mounted that contains the files on the hard drive. This is done by typing *mount C ~/Desktop* (if the folder containing LIGFIELD is on the Desktop). If successful text will appear as shown in Figure 2.51. The new drive is then accessed by typing *c:* which should switch to the new drive with the main folder being the Desktop. Navigate to the LIGFIELD folder and execute the program by typing *LIGFIELD* and hitting enter. LIGFIELD should now be running and ready for calculations.

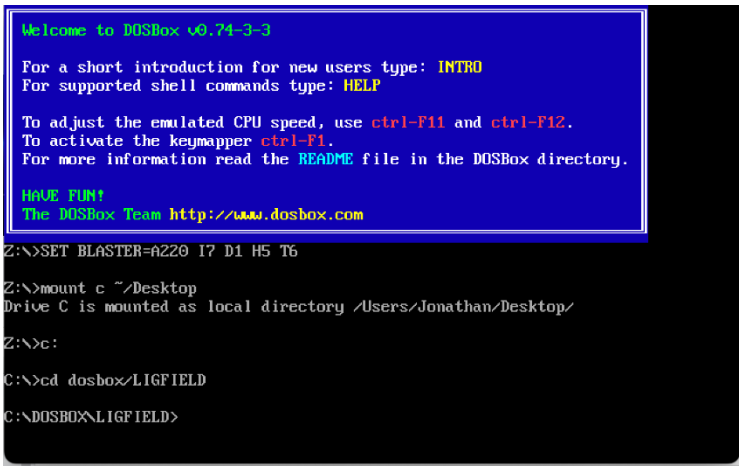

Figure 2.51. DOSBox startup screen and mounting commands for Mac operating system.

2.B.2. Running DOSBox on PC

Once DOSBox is open the drive containing LIGFIELD must be mounted. If place directly on the C: drive, mounting the drive and opening LIGFIELD is shown in Figure 2.52.

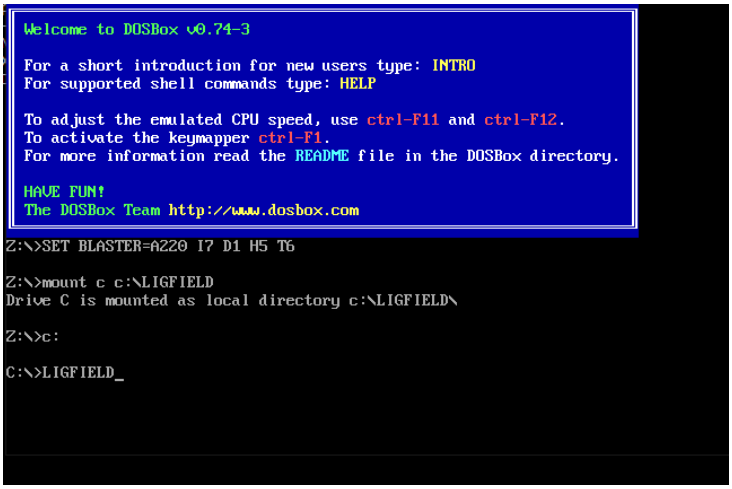

Figure 2.52. DOSBox starting screen and mounting commands to mount LIGFIELD as the local directory and execute LIGFIELD on a PC.

2.B.3. Ligand-Field Calculations using LIGFIELD

Initial Setup

The first thing that must be done is changing the input and output directories for the program which is done in the **Options→Program options**. They need to be set to the correct path corresponding to where the LIGFIELD program is located. For both PC and Mac users, if DOSBox and LIGFIELD were placed in the locations suggested the input and output directory paths should be:

Mac

Input directory: C:\DOSBOX\LIGFIELD\INPUT

Output directory: C:\DOSBOX\LIGFIELD\OUTPUT

PC

Input directory: C:\INPUT

Output directory: C:\OUTPUT

Once the directory paths have been set the program is ready to begin calculations. If the path is invalid the program will create a popup and ask to redefine the path.

1. The first step is to create the matrices for the calculations. This is done by navigating to **Setup→Generate matrices.** A dialog will appear asking for the name of the output file that will be generated (Figure 2.53a). The only requirement for the name is that it must be **less than 7 characters**. If longer, the program will not be able to read in the file. In the new screen you are able to pick the *p*-, *d*- or *f*-electron count that the calculation will be for, the free-ion term states that will be included in the calculation (it is recommended to include all states if doing a ligand-field analysis), the function basis, which should be *SLJMJ* (though the choice of basis no longer matters after step 3), the type of ligand field analysis to use, either *Angular Overlap*

Model (AOM) or *O>D4>D2* (for normal ligand-field analysis). For most calculations, these are the only selections that are required. The selections for a full d^6 ligand-field analysis are shown in Figure 2.53b. Note, for Mac users, "End" is fn+right arrow.

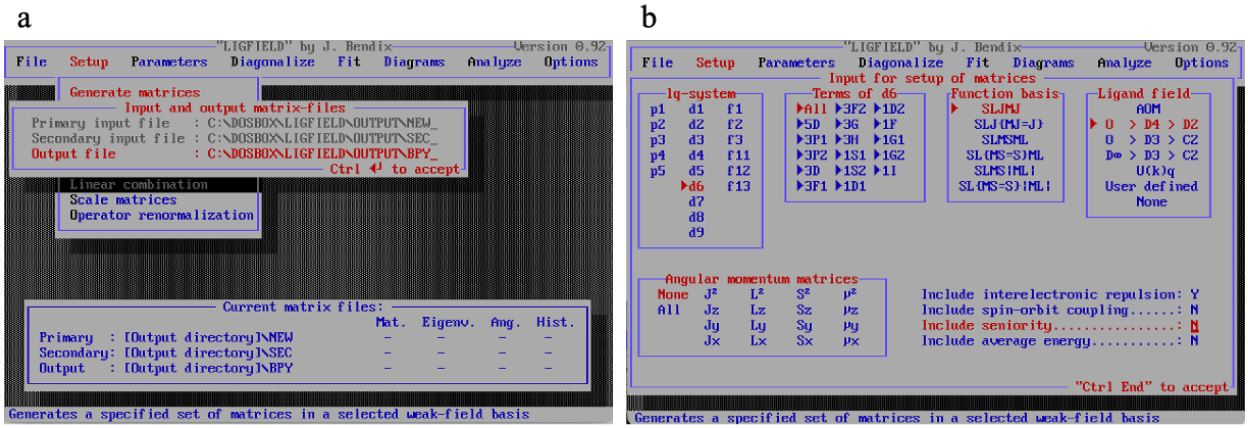

Figure 2.53. (a) Initial matrix file creation dialog with output file naming (b) Matrix file creation screen with selections for a full d^6 analysis without the incorporation of spin-orbit coupling.

2. After creation of the matrix file, the initial parameters (in cm^{-1}) for the calculations need to be entered by navigating to the **Parameters** tab. After accepting the input file that was created in the previous step the initial ligand-field parameters calculated from the diagonal expressions will be entered in the next dialog with *Delta(Oh)* corresponding to Δ_O or 10Dq, and Racah *B* and Racah *C*, the Racah interelectronic repulsion terms (Figure 2.54).

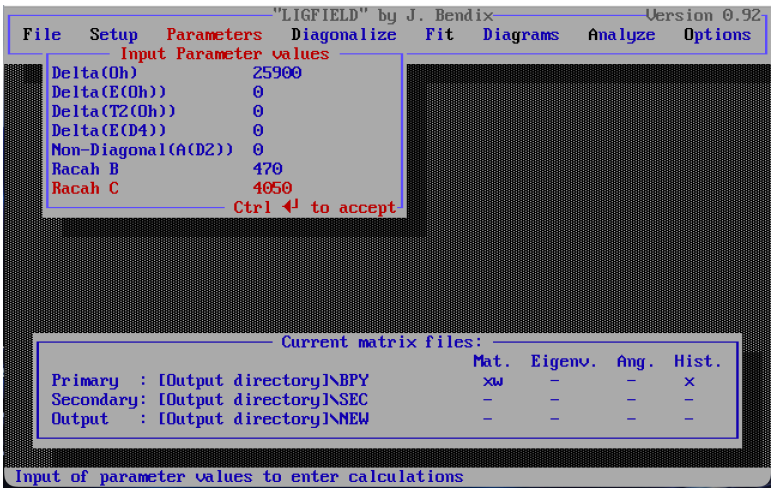

Figure 2.54. Example initial parameters input dialog for ligand-field analysis using the diagonal expression values calculated for $[Co(bpy)_3]^{3+}$ in cm^{-1}.

3. After inputting the initial parameters, the matrix file needs to first be rediagonalized and then diagonalized, contrary to the naming of the operations.[a] To do this, navigate to **Diagonalize→Rediagonalize.** This will bring up a new dialog. The input file should be the matrix file with the parameters from the previous step and now a new output file will be created. To keep track of file contents a convention that may be useful is to name the output file the same name as the input, but with an "R" on the end of the name for rediagonalized as shown in Figure 2.55. The program will then prompt to confirm the initial parameters used before performing the transformation. After the operation has completed the transformed matrix file will then be diagonalized.

[a]During the diagonalization, function numbers are generated for each term-state and these function numbers are required for the fitting procedure. Sometimes during rediagonalization the function numbers may switch to different terms therefore the function number for a term-state may be incorrect when continuing to the fitting procedure.

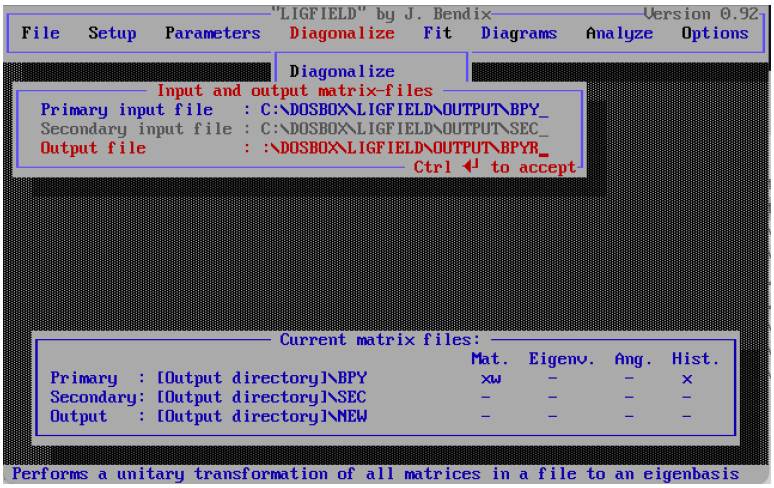

Figure 2.55. Rediagonalization dialog with the input file being the initially generated matrix file and the output file to be named for the rediagonalization file.

4. Select **Diagonalize** from the drop-down menu and confirm the input file, which should be the output file from the previous step. The parameters will be confirmed again, and a new screen will be shown. The diagonalization screen gives many options for how to treat the matrix file. For a normal analysis in an idealized O_h complex the selections are shown in Figure 2.56. Sorting the eigenvalues by ascending will sort from lowest energy to highest energy. The eigenvectors from the diagonalization should be selected in addition to the spin multiplicity for each eigenvalue that is being calculated. The list of "Groups to use" allows for the selection of various holohedral point groups (rotational only) and double groups. If assuming an octahedral splitting, then the selection of O is necessary but lower symmetry groups can be used if needed. A final option is available is for LIGFIELD to calculate the orbital populations for each electronic state but requires more time for the calculation to finish. After the calculation has finished, "In a textfile" should be selected to view the results as the other selections do not allow one to save the output externally.

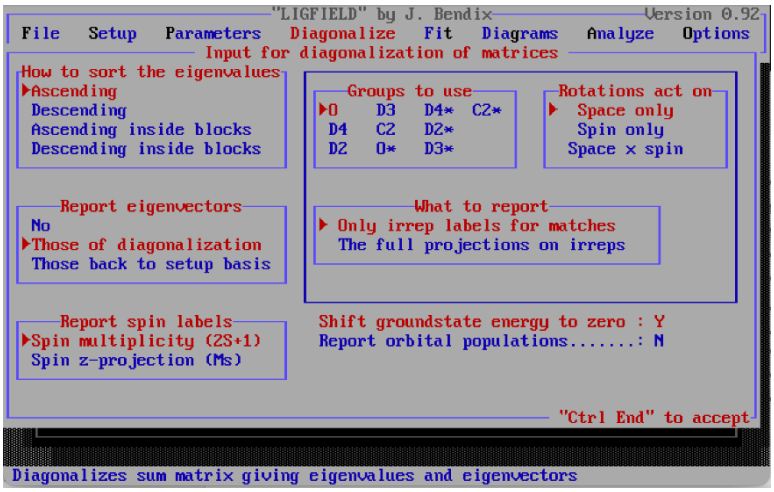

Figure 2.56. Diagonalization dialog with selections for a typical analysis in an octahedral ligand-field.

The output file now contains the function numbers, the energy, spin, and symmetry of the calculated eigenfunctions (Figure 2.57) based upon the initial parameters used in step 2. The relevant information from this file for the analysis are the function numbers. As shown in Figure 2.57, the ground-state $^1A_1$ term-state is Function 161 and the next group of terms correspond to the $^3T_1$ term-state. For the analysis, the function number of the ground-state and each observed ligand-field band is required. Only the first function number for each grouping of terms is needed. As the $^3T_1$ state is 9-fold degenerate, only Function 128 is needed, and the other 8 functions can be ignored.

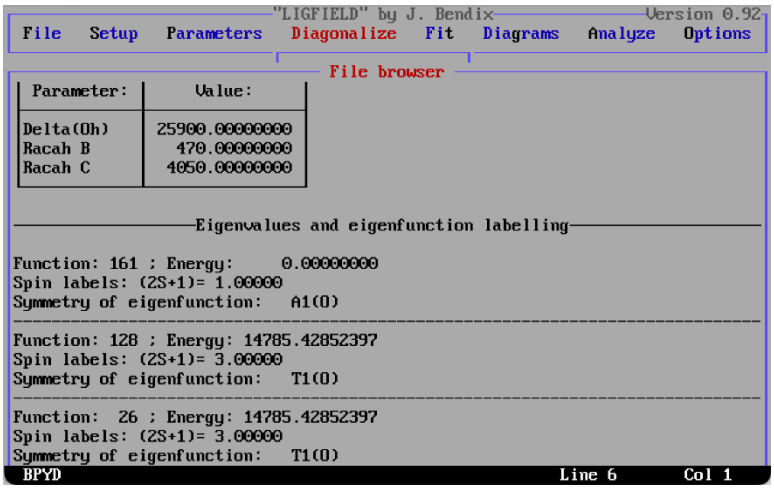

Figure 2.57. Output file after diagonalization with the functions, energies, and term state symbols in an octahedral field.

5. With the function numbers in-hand the ligand-field parameters can now be fit. Navigate to **Fit→Fit parameters** and name the output file for the fitting (appending an "F" to the file name may be helpful) and confirm the ligand-field parameters again. A new window will appear and will need to be modified to resemble Figure 2.58a. Observations from *Keyboard* means that the function numbers and energies will be entered manually on the next screen and the *Unit Matrix* will weight all the transitions equally in the calculation of the ligand-field parameters. The method of fitting by default is a nonlinear regression using the Leuwenberg-Marquardt algorithm. The next screen is where the function numbers and energies are input from step 4 (Figure 2.58b). The "From Function" will be the ground-state and the "To Function" will be the ligand-field excited state that was observed. In this example there are 3 observed transitions corresponding to $^1A_1 \rightarrow {}^3T_1$, $^1A_1 \rightarrow {}^3T_2$, and $^1A_1 \rightarrow {}^1T_1$, respectively.

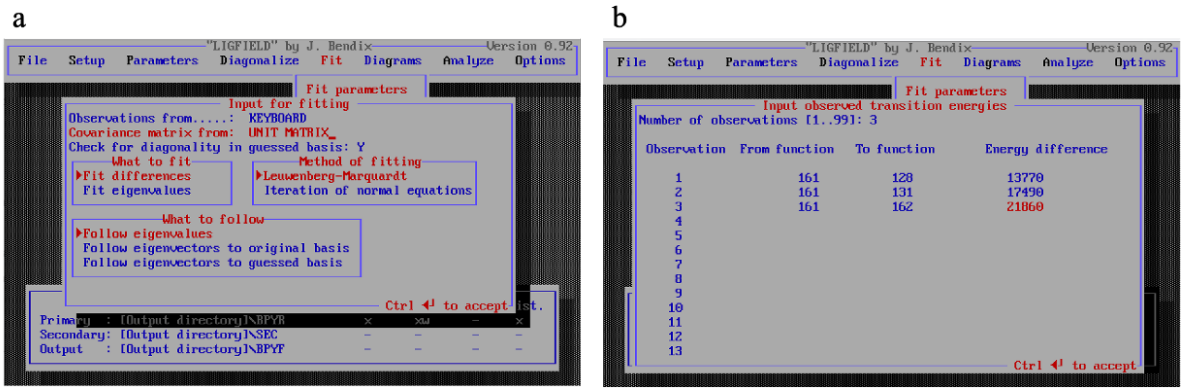

Figure 2.58. (a) Fitting procedure dialog with correct input for observations and covariance matrix (b) Input screen for the term-state function numbers and the observed experimental energies of the transitions for $[Co(bpy)_3]^{3+}$.

After accepting the transitions, a new screen will appear asking what parameters LIGFIELD should refine against. In this example the parameters refined are 10Dq, Racah *B*, and Racah *C*. (Figure 2.59a). Accepting these will then begin the non-linear fitting procedure (Figure 2.59b). The fitting will continue indefinitely unless stopped by the user when an acceptable "last change" or chi-squared value is obtained. When the iterations have been finished a pop-up will appear, and the data should be saved as a text file similarly as in step 4. With the fitting done and file saved, the ligand-field parameters using a full d^n analysis has been completed. During the fitting procedure if "control+r" is pressed, LIGFIELD will also rediagonalize the matrix using the new parameters from the fit allowing for the calculation of the energies of all the ligand-field states. These new state energies can be calculated by repeating step 4.

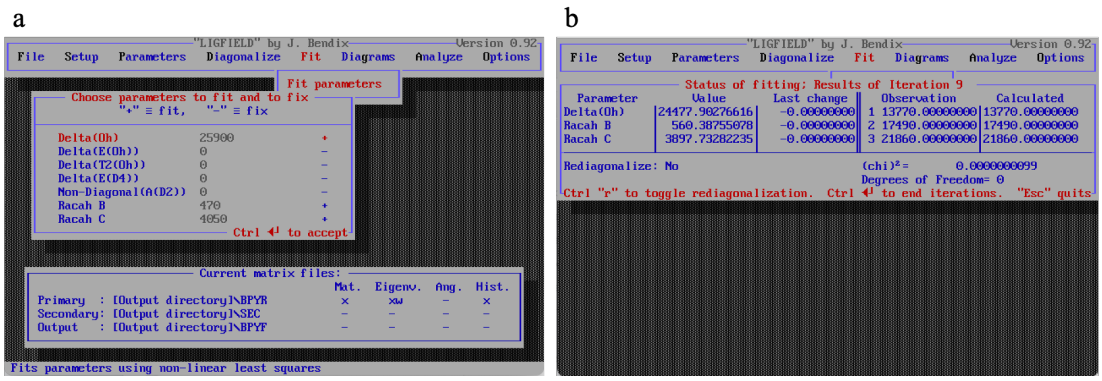

Figure 2.59. (a) Choice of parameters for the fitting procedure with "+" meaning the parameter will be used for fitting and "-" being held constant (b) Non-linear fitting procedure after 9 iterations with the ligand-field parameters successfully being fit to the experimentally observed transition energies.

APPENDIX 2.C. CREATION OF STRONG FIELD TANABE-SUGANO DIAGRAMS USING DTANSUG

Once the ligand-field parameters have been calculated using the method in Appendix 2.B, a Tanabe-Sugano diagram for any *d*-configuration can be constructed in the strong-field limit using the program, DTANSUG, created by Prof. Joshua Telser. This compiled Fortran program is run in Terminal for Macs and in the Command Prompt for PCs.

To start the program, one must navigate to the directory, via Terminal or the Command Prompt, in which it is saved. Once in the directory, execution of the program is called for by typing *./dtansug.out* and hitting enter.

1. Enter the file name for the output file and select the *d*-configuration for which to carry-out the analysis.
2. Select if the analysis will be down in an assumed octahedral (O) or tetragonal (T) field.
3. The next option allows for the selection of which parameter should be varied for the calculation. One can either keep the Racah *B* and *C* parameters constant and vary 10Dq, a typical Tanabe-Sugano diagram, or Racah *C* and 10Dq can be kept constant and the value of Racah *B* is varied.
4. The value of Racah *B* is selected using either the free-ion value or the value obtained from an alternative ligand-field analysis.
5. The value of Racah *C* is selected using either the free-ion value or the value obtained from an alternative ligand-field analysis.
6. The final parameters entered are the starting and ending value of Dq. Note, this is Dq **not** 10Dq. The initial and final values can be any numbers except negative. A typical range to use is 0-3000 cm^{-1}. By starting at 0 cm^{-1} it can be helpful when analyzing the output file to determine

the term-states to choose. The step size for the analysis needs to be chosen as well. If the step size is too small, too many data points created, the program will terminate with an error. This can be remedied by either choosing larger steps or selecting a smaller range of Dq values to loop over.

7. Three additional questions are asked after step 6 regarding additional information about the analysis to be included in the output file. The important prompt to answer "yes" to is the second prompt, "*Do you want to print out the wavefunction coefficients?*". By answering yes to this prompt, the analysis will display the coefficients for each multi-electronic term state selected as well as the purity of each state as a function of the ligand-field splitting. The initial setup and selections chosen for $[Co(bpy)_3]^{3+}$ are shown in Figure 2.60 below.

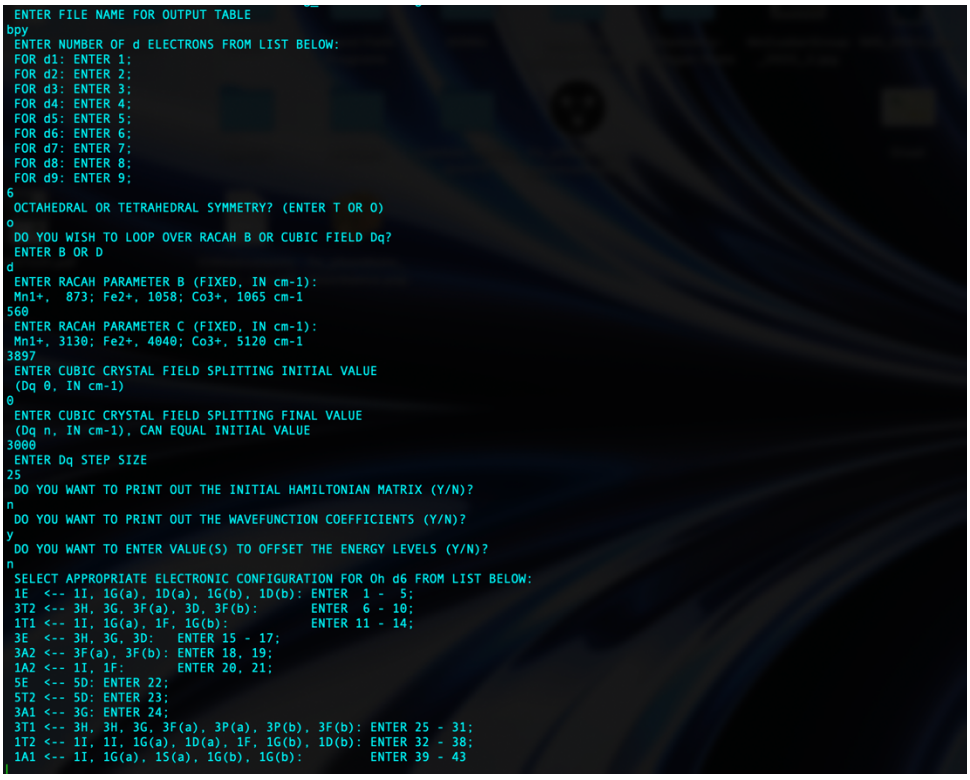

Figure 2.60. Example initial setup of DTANSUG for an octahedral low-spin d^6 transition metal that loops over Dq and prints the wavefunction coefficients for the states of interest.

8. All that is left now is to select which multi-electronic term states will be included in the calculation. The number corresponds to the free-ion term state that gives rise to the ligand-field term state. From the example in Figure 2.60, to print the energies of the $^1A_1$ ground state *39* would be selected as the ^1I free-ion term gives rise to the $^1A_1$ ground state within the strong-field limit of the d^6 electron configuration. Select each term the analysis should be carried out on individually, responding with "*y*" to perform another calculation, until all the relevant states have been calculated. After responding "*n*" to "*Do you want to start all over?*" a text file will be created in the same directory as where DTANSUG is stored containing the analysis requested.
9. The output file will have two sections for each term-state selected: Energetics and the wavefunction coefficients. The energetics will have 3 columns for each configuration: Dq[b], Energy (0^{th}), and Energy (Exact). Following this section, the wavefunction coefficients section will have multiple columns, each corresponding to a configuration, and the amount of mixing of other configurations into that term-state as a function of Dq, effectively allowing for the determination of the purity of the states being observed.
10. For most systems that will be analyzed, the configuration number in the output file with the lowest energy will either be the ground-state or the exited-state configuration that we are interested in for the analysis. Looking at the first few configurations (Figure 2.61a) for the $^1A_1$ state, the first configuration, $i = 39$, is the lowest in energy and therefore is the correct choice for the ground-state of a low-spin d^6 metal. One can also look at the wavefunction coefficients

[b]DTANSUG uses the hole-formalism for ease of calculating the relevant energetics from the diagonalization of the Tanabe-Sugano matrices. Therefore, Dq will be negative for all *d*-electron configurations over d^5, as switching between d^n and d^{10-n} only entails switching the sign of Dq on the diagonal of the matrix, and all term-states displayed must be read using the hole-formalism, i.e. $^1A_1$ $(e_g)^4$ for d^4 corresponds to the $(t_{2g})^6(e_g)^0$ configuration for d^6.

(Figure 2.61b) and see that for $i = 39$ the electron configuration e^4, corresponding to t_2^6 using the hole-formalism, is the highest purity as a function of Dq and is therefore the correct choice.

a

CONFIG i=39 Dq	ENERGY (0th)	ENERGY (EXACT)
-0.00000E+00	0.5840900E+05	0.3442100E+05
-0.25000E+02	0.5880900E+05	0.3420448E+05
-0.50000E+02	0.5920900E+05	0.3393791E+05
-0.75000E+02	0.5960900E+05	0.3362562E+05
-0.10000E+03	0.6000900E+05	0.3327403E+05
-0.12500E+03	0.6040900E+05	0.3288998E+05
-0.15000E+03	0.6080900E+05	0.3247963E+05
-0.17500E+03	0.6120900E+05	0.3204804E+05
-0.20000E+03	0.6160900E+05	0.3159922E+05
-0.22500E+03	0.6200900E+05	0.3113628E+05
-0.25000E+03	0.6240900E+05	0.3066161E+05
-0.27500E+03	0.6280900E+05	0.3017708E+05

CONFIG i=40 Dq	ENERGY (0th)	ENERGY (EXACT)
-0.00000E+00	0.4282100E+05	0.3674893E+05
-0.25000E+02	0.4297100E+05	0.3656846E+05
-0.50000E+02	0.4312100E+05	0.3641054E+05
-0.75000E+02	0.4327100E+05	0.3627410E+05
-0.10000E+03	0.4342100E+05	0.3615563E+05
-0.12500E+03	0.4357100E+05	0.3605083E+05
-0.15000E+03	0.4372100E+05	0.3595573E+05
-0.17500E+03	0.4387100E+05	0.3586717E+05
-0.20000E+03	0.4402100E+05	0.3578278E+05
-0.22500E+03	0.4417100E+05	0.3570090E+05
-0.25000E+03	0.4432100E+05	0.3562036E+05
-0.27500E+03	0.4447100E+05	0.3554038E+05

CONFIG i=41 Dq	ENERGY (0th)	ENERGY (EXACT)
-0.00000E+00	0.7014600E+05	0.4045228E+05
-0.25000E+02	0.7004600E+05	0.4046327E+05
-0.50000E+02	0.6994600E+05	0.4049430E+05
-0.75000E+02	0.6984600E+05	0.4054262E+05
-0.10000E+03	0.6974600E+05	0.4060584E+05
-0.12500E+03	0.6964600E+05	0.4068188E+05
-0.15000E+03	0.6954600E+05	0.4076894E+05
-0.17500E+03	0.6944600E+05	0.4086549E+05
-0.20000E+03	0.6934600E+05	0.4097022E+05
-0.22500E+03	0.6924600E+05	0.4108199E+05
-0.25000E+03	0.6914600E+05	0.4119985E+05
-0.27500E+03	0.6904600E+05	0.4132295E+05

b

Dq (cm-1)	cij^2, j= 39,...,43 i= 39 1A1 t4	(1I) 1A1 t3{2E}e	(1Ga) 1A1 t2{1A1}e2{1A1}	(1Sa) 1A1 t2{1E}e2{1E}	(1Gb) 1A1 e4
-.0000E+00	0.10389610	0.05194805	0.20779221	0.32467532	0.31168831
-.2500E+02	0.09004724	0.02905107	0.21606393	0.27626031	0.38857746
-.5000E+02	0.07696457	0.01409359	0.21861538	0.22553934	0.46478712
-.7500E+02	0.06533992	0.00565102	0.21610779	0.17854911	0.53435216
-.1000E+03	0.05548591	0.00163474	0.21002678	0.13870142	0.59415115
-.1250E+03	0.04736736	0.00018882	0.20190841	0.10678877	0.64374664
-.1500E+03	0.04075997	0.00003928	0.19291997	0.08205446	0.68422632
-.1750E+03	0.03538740	0.00044229	0.18380132	0.06318640	0.71718260
-.2000E+03	0.03099352	0.00101126	0.17496365	0.04886960	0.74416197
-.2250E+03	0.02736699	0.00156599	0.16660684	0.03799649	0.76646369
-.2500E+03	0.02434235	0.00203470	0.15880788	0.02970322	0.78511186
-.2750E+03	0.02179294	0.00239840	0.15157724	0.02333978	0.80089164
-.3000E+03	0.01962240	0.00266169	0.14489189	0.01842461	0.81439942
-.3250E+03	0.01775724	0.00283815	0.13871372	0.01460256	0.82608834
-.3500E+03	0.01614100	0.00294345	0.13299948	0.01161135	0.83630472
-.3750E+03	0.01472987	0.00299242	0.12770589	0.00925632	0.84531550
-.4000E+03	0.01348950	0.00299788	0.12279209	0.00739208	0.85332845
-.4250E+03	0.01239266	0.00297044	0.11822066	0.00590923	0.86050701
-.4500E+03	0.01141750	0.00291864	0.11395798	0.00472479	0.86698109
-.4750E+03	0.01054632	0.00284925	0.10997405	0.00377537	0.87285500
-.5000E+03	0.00976466	0.00276755	0.10624230	0.00301216	0.87821333
-.5250E+03	0.00906055	0.00267765	0.10273919	0.00239729	0.88312532
-.5500E+03	0.00842403	0.00258268	0.09944392	0.00190121	0.88764816
-.5750E+03	0.00784676	0.00248504	0.09633806	0.00150069	0.89182946
-.6000E+03	0.00732164	0.00238654	0.09340529	0.00117735	0.89570918
-.6250E+03	0.00684267	0.00228855	0.09063108	0.00091658	0.89932112
-.6500E+03	0.00640469	0.00219204	0.08800252	0.00070672	0.90269404
-.6750E+03	0.00600324	0.00209775	0.08550806	0.00053838	0.90585257
-.7000E+03	0.00563449	0.00200619	0.08313737	0.00040398	0.90881797

Figure 2.61. (a) Three configurations giving rise to the $^1A_1$ term-state with the lowest energy configuration highlighted in green (b) Wavefunction coefficients for configuration 39, showing parentage of the state coming from the e^4 (t_2^6) electron configuration.

11. Once the lowest energy configuration for each multi-electronic term state is found it is only a matter of plotting the differences between the ground-state and each excited-state. The easiest way to do this is to copy the three columns for each configuration of interest and paste them individually into separate text files. Then importing these text files into Excel, only importing the **Exact Energy** for each configuration and the values of **Dq** for one configuration. The sign of Dq must be switched for d-electron counts **greater** than d^5 but is correct for d^5 and less, but all values will need to be multiplied by 10 to match 10Dq that is typically displayed.
12. Once all the data columns have been imported and the energy differences taken, the resulting data can be plotted in any plotting software. The resulting plot will resemble a Tanabe-Sugano

diagram for the strong-field side. The x-axis will need to be adjusted to a value of 10Dq such that the exited state energies are above the ground state, e.g. non-negative.

APPENDIX 2.D. DERIVATION OF LIGAND-FIELD DIAGONAL EXPRESSIONS FROM TANABE-SUGANO ENERGY MATRICES

Though the diagonal expressions used to calculate ligand-field parameters are found throughout literature, at times it is easier to derive the expressions from the matrices originally created by Tanabe and Sugano directly instead of having to search through the literature. This appendix will give a short walkthrough of the steps needed to derive the expressions needed as well as discuss how to convert between a d^n energy matrix to a d^{10-n} energy matrix utilizing the hole-formalism.

The following examples will involve using the d^4 electron configuration in a cubic field as the starting point to discuss the d^6 configuration that is typically seen in our group, as well as derive the diagonal expression for the $^1A_1 \rightarrow {}^1T_1$ transition.

a

$^1A_1$ (a^1S, b^1S, a^1G, b^1G, ^1I)					
t_{2g}^4	$-16Dq + 10C$	$-12\sqrt{2}B$	$\sqrt{2}(4B + 2C)$	$2\sqrt{2}B$	0
$t_{2g}^3(\,^2E)e_g^1$		$-6Dq + 6C$	$-12B$	$-6B$	0
$t_{2g}^2(^1A_1)e_g^2(^1A_1)$			$4Dq + 14B + 11C$	$20B$	$\sqrt{6}(2B + C)$
$t_{2g}^2(\,^1E)e_g^2(\,^1E)$				$4Dq - 3B + 6C$	$2\sqrt{6}B$
e_g^4					$24Dq - 16B + 8C$

b

$^1T_1$ (^1F, a^1G, b^1G, ^1I)				
$t_{2g}^4(^2T_1)e_g^1$	$-6Dq - 3b + 6C$	$5\sqrt{3}B$	$3B$	$\sqrt{6}B$
$t_{2g}^3(\,^2T_2)e_g^1$		$-6Dq - 3B + 8C$	$-5\sqrt{3}B$	$\sqrt{2}(B + C)$
$t_{2g}^2(^1T_2)e_g^2(^1E)$			$4Dq - 3B + 6C$	$-\sqrt{6}B$
$t_{2g}^1e_g^3$				$14Dq - 16B + 7C$

Figure 2.62. (a) The excited-state $^1A_1$ energy matrix for the d^4 electron configuration (b) the excited-state $^1T_1$ energy matrix for the d^4 electron configuration in a cubic field.

In the d^4 electron configuration, both the $^1A_1$ and $^1T_1$ are spin-forbidden excited-states, whereas for low-spin d^6 metals, the $^1A_1$ is now the ground-state and the $^1T_1$ is the first spin-allowed ligand-field excited state. The d^4 energy matrices for these configurations are shown in Figure 2.62. It is important to note that the parameter, Dq, only appears in the diagonal elements of each matrix. Before converting the d^4 matrices to the d^6 matrices, it is important to know how the value of Dq for each diagonal element is determined.

Using a simple *d*-orbital picture in an octahedral field, we know this gives rise to two sets of orbitals, the triply degenerate t_{2g} set and the doubly degenerate e_g^* set which are barycentered at -4Dq and +6Dq, respectively (Figure 2.63). With this information in-hand, it is now a straightforward process to calculate the values of Dq for any element in the matrix with the prior knowledge of the electron configuration that gives rise to that element. Each electron contained in the e_g^* set will contribute +6Dq to that configuration, while each electron in the t_{2g} set will contribute -4Dq. Referencing to Figure 2.62a, the t_{2g}^4 configuration of the $^1A_1$ multi-electronic term state has a value of -16Dq on the diagonal. This derives from the four electrons in the t_{2g} set with each electron contributing -4Dq, $\left(4e_{t2g}^-\right) * (-4\mathrm{Dq}) = -16\mathrm{Dq}$. Extending this to the second configuration in the $^1A_1$ energy matrix, $t_{2g}^3 e_g^1$, the three t_{2g} electrons will contribute -4Dq each and the one e_g^* electron will contribute +6Dq, $\left(3e_{t2g}^-\right) * (-4\mathrm{Dq}) + \left(1e_{eg}^-\right) * (+6\mathrm{Dq}) = -6\mathrm{Dq}$. With this simple method, the value of Dq can be calculated for each diagonal element.

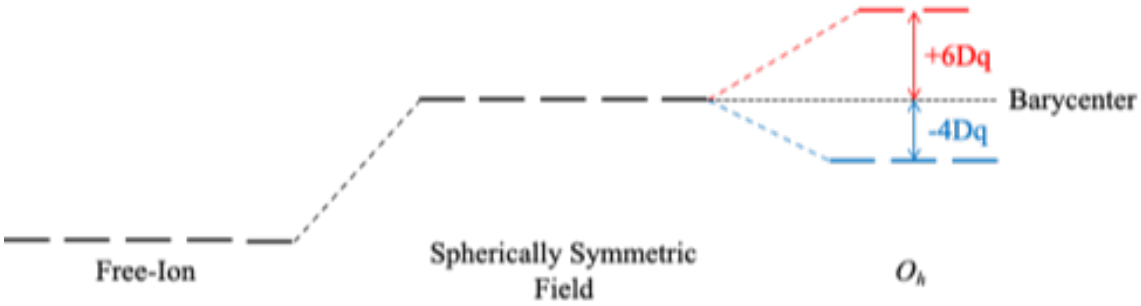

Figure 2.63. Energetics of the d-orbital manifold as a free-ion, in a spherically symmetric field, and with six point charges in a cubic octahedral field showing the displacement of the orbital sets from the barycenter.

Transitioning to a d^6 electron count from d^4, the same matrices are used as the two electron configurations are related by 10-n. To convert the d^4 matrix to d^6, all that is required is to change the sign of Dq on the diagonal for each element. The validity of this approach can be shown by using the hole-formalism. Counting the "holes" in each orbital set converts to populated electrons in the corresponding 10-n electron configuration. This approach is shown using the $^1A_1$ matrix from Figure 2.62a to give the corresponding d^6 configurations shown Figure 2.64a. From these, one can see that the last configuration, t_{2g}^6, corresponds to the ground-state electron configuration for a low-spin d^6 metal and would give a value of -24Dq, and is the expression needed for the analysis. The same treatment will be used on the configurations giving rise to the $^1T_1$ term state (Figure 2.64b). The values of *B* and *C* remain unchanged in this treatment. Using the expressions for the configurations of interest and ensuring that the sign of Dq has been switched for d^6, the diagonal expression for the energy of $^1A_1 \rightarrow {}^1T_1$ transition can be derived (Figure 2.64c). Though this example worked only with two of the energy matrices for the d^4 configuration and one ligand-field transition, this can be extended to any *d*-configuration as well as any ligand-field transition of interest.

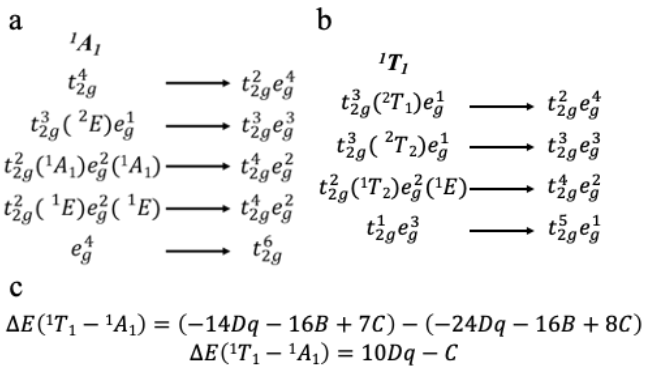

Figure 2.64. Using the hole-formalism (a) Conversion of the $^1A_1$ d^4 configurations to the corresponding d^6 (b) Conversion of the $^1T_1$ d^4 configurations to the corresponding d^6 (c) Derivation of the diagonal expression for the energy of the $^1A_1 \rightarrow {}^1T_1$ transition energy.

CHAPTER 3: SYNTHETIC DECONVOLUTION OF THE CHARGE-TRANSFER MANIFOLD OF $[FE(DCPP)_2]^{2+}$: EFFECTS OF DELOCALIZATON ON MLCT CHARACTER.

3.1 Introduction

As discussed in chapter 1, our group originally set out to synthesize an Fe(II) chromophore with a highly symmetric coordination environment such that we could collapse the ligand-field manifold and slow the deactivation from the charge-transfer excited state in order to prolong its lifetime. The complex, $[Fe(dcpp)_2]^{2+}$ (where dcpp is 2,6-di(2-carboxypyridyl)pyridine), was synthesized and its ground- and excited-state properties, and the underlying electronic structure have been subsequently studied in-depth.[1–4] Though succeeding in the synthesis of a nearly perfect octahedral complex, $[Fe(dcpp)2]^{2+}$ showed faster excited-state decay dynamics, contrary to expectation, possessing a ground-state recovery lifetime of 280 ps and an MLCT lifetime of 76 fs,[1,2] a ground-state recovery lifetime approximately 4-times shorter than that of $[Fe(bpy)_3]^{2+}$ (where bpy is 2,2′-bipyridine).[5] An in-depth analysis of this behavior can be found in the dissertation of Dr. Monica Carey and is outside the scope of the present work.[6] Seeing as the MLCT lifetime was shortened with this new complex, various ways to attempt to extend it were envisioned while maintaining the almost ideal octahedral coordination environment.

To that end, inspiration was taken from the ruthenium literature in which by appending various aromatic substituents to the backbone of bpy and terpyridyl systems, an increase in the MLCT lifetime was observed.[7–9] This is due in part to the delocalization of the wavefunction in the charge-transfer state. By extending the wavefunction, one can imagine decoupling of the metal and ligand during the MLCT excitation extending the lifetime. Though this route did not have the effect that we had originally set out to accomplish with the extension of charge-transfer lifetimes,

we were now able to begin to dissect the MLCT manifold as a function of substitution of $[Fe(dcpp)_2]^{2+}$ using synthetic and computational chemistry.

3.2 Experimental

3.2.1 Synthesis

General. All reaction and spectroscopic solvents were obtained from Sigma Aldrich Chemical Co. and used without further purification unless otherwise stated. Dry THF, MeCN, and DCM were obtained from a Solvtek solvent drying system using neutral alumina. Unless otherwise noted, all reactions were conducted either using standard Schlenk techniques or in an inert atmosphere glove box (nitrogen-filled, Vacuum Atmospheres). Chelidamic acid monohydrate (CAH), KPF_6, and Phenylboronic acid ($PhB(OH)_2$) were obtained from TCI Chemicals. $Fe(BF_4)_2 \bullet 6H_2O$, 1.6 M n-BuLi, acetyl chloride, and $Pd(dppf)Cl_2 \bullet DCM$, were obtained from Sigma Aldrich Chemical Co. 2-Bromopyridine was obtained from Sigma Aldrich Chemical Co. and was distilled from KOH and activated carbon under reduced pressure before use and stored over KOH pellets. Sodium Iodide was obtained from Fischer Scientific. 4-Iodo-2-chloropyridine (4-I-2ClPy) was obtained from Oakwood Chemicals. *p*-Tolylboronic acid (*p*-$TolB(OH)_2$) was obtained from Matrix Scientific. 4-Bromo-2,6-lutidine was obtained from Combi-Blocks. 4-pyridylboronic acid pinacol ester (4-PyBPin) was obtained from Boron Molecular. Potassium dichromate ($K_2Cr_2O_7$) and triphenylphosphine (PPh_3) were obtained from Alfa Aesar. NMR spectra were collected in the Max T. Rogers NMR Facility of Michigan State University on an Agilent 500 MHz spectrometer or a Bruker 500 MHz spectrometer; spectra were referenced internally to the residual solvent peak of $CDCl_3$, CD_3CN, DMSO-d_6, or $(CD_3)_2CO$ which were obtained from Cambridge Isotopes. Elemental analyses were obtained through the analytical facilities at Michigan State University on samples that had been ground in a vial and stored under vacuum overnight prior to analysis. Diethyl

4-chloro-chelidimate (Cl-DEP)[10], diethyl 4-iodo-chelidimate (I-DEP),[11] diethyl 4-(4-cyanophenyl)-2,6-pyridine dicarboxylate,[12] 4-phenyl-2-chloropyridine,[13] 2,6-dimethyl-4,4′-bipyridine,[14] dcpp,[1] and $[Fe(dcpp)_2](PF_6)_2$[1,15] were all prepared by literature methods.

2-iodo-4-phenylpyridine. To a flame dried flask was added 1.000 g of 2-chloro-4-phenylpyridine (5.27 mmol, 1.0 eq), 7.904 g of NaI (52.7 mmol, 10 eq), and 9 mL of MeCN. This stirred for 30 minutes protected from light under N_2. To this yellow suspension, 0.75 mL of acetyl chloride (10.55 mmol, 2.0 eq) were added dropwise affording a bright orange suspension. The reaction was heated to reflux protected from light and tracked by NMR. After 24 hours, consumption of the starting material was complete. A 10% K_2CO_3 solution was added until the reaction was basic by pH paper. Excess saturated $Na_2S_2O_{3(aq)}$ solution was added as well. The cloudy suspension was transferred to a separatory funnel and 50 mL of DCM was added and the layers separated. The aqueous layer was extracted with DCM (3 x 25 mL). The organic layers were all combined and dried over Na_2SO_4, filtered, and evaporated to afford a brown oil. The crude was purified on silica with 10:1 hexanes/EtOAc to give a white solid. Yield: 1.206 g, 81%. ^{1}H NMR (500 MHz, $CDCl_3$): δ 8.40 (d, J = 5.3 Hz, 1H), 7.95 (d, J = 1.7 Hz, 1H) 7.62-7.56 (m, 2H) 7.53-7.45 (m, 4H).

Diethyl 4-phenyl-2,6-pyridine dicarboxylate (Ph-DEP). In a glove box, 1.500 g of I-DEP (4.3 mmol, 1.0 eq), 0.681 g of phenylboronic acid (5.6 mmol, 1.3 eq), 1.781 g of Cs_2CO_3 (5.5 mmol, 1.3 eq), 177 mg of Pd(dppf)Cl_2•DCM (0.21 mmol, 5mol%), and 9 mL of dry 1,4-dioxane were combined. The reaction was heated to 80ºC under N_2 and was followed by TLC. After 18 hours it was cooled to room temperature and the dioxane was removed. The red residue was taken into 100 mL of EtOAc. The organic layer was washed with H_2O (2 x 50 mL) and brine (60 mL). The EtOAc layer was dried over $MgSO_4$, filtered, and evaporated. The crude product can either be purified by column chromatography on silica with 30% EtOAc/hexanes or recrystallized from hot EtOH and

placed in the freezer. Yield: 1.097g, 85%. ^{1}H NMR (500 MHz, $CDCl_3$): δ 8.52 (s, 2H), 7.79-7.73 (m, 2H), 7.58-7.47 (m, 3H), 4.52 (q, *J* = 7.1 Hz, 4H), 1.48 (t, *J* = 7.1 Hz, 6H).

Diethyl 4-(*p*-tolyl)-2,6-pyridine dicarboxylate (*p*Tol-DEP). This compound was synthesized with a variation of a literature procedure.[4,16] In a glove box, 2.227 g of I-DEP (6.4 mmol, 1.0 eq), 1.128 g of *p*-tolylboronic acid (8.3 mmol, 1.3 eq), 2.645 g of Cs_2CO_3 (8.3 mmol, 1.3 eq), 265 mg of Pd(dppf)Cl_2•DCM (0.31 mmol, 5mol%), and 12 mL of dry 1,4-dioxane were combined. The reaction was heated to 80ºC under N_2 and was followed by TLC. After 36 hours it was cooled to room temperature and the dioxane was removed. The red residue was taken into 100 mL of EtOAc. The organic layer was washed with H_2O (2 x 50 mL) and brine (60 mL). The EtOAc layer was dried over $MgSO_4$, filtered, and evaporated. The crude was columned on silica with 2% EtOAc in DCM and then recrystallized from EtOH and adding hexanes until cloudy and placing in the freezer to yield light pink needles. Yield: 1.213 g, 61%. ^{1}H NMR (500 MHz, $CDCl_3$): δ 8.50 (s, 2H), 7.67 (d, *J* = 8.0 Hz, 2H), 7.34 (d, *J* = 7.9 Hz, 2H), 4.52 (q, *J* = 7.1 Hz, 4H), 2.44 (s, 3H), 1.48 (t, *J* = 7.1 Hz, 6H).

4,4′-bipyridine-2,6-dicarboxylic acid. This compound was synthesized using a modification of literature procedure.[17] To a round bottom flask was added 2.000 g of 2,6-dimethyl-4,4′-bipyridine (10.86 mmol, 1.0 eq) and 25 mL of 98% H_2SO_4. The suspension was stirred until complete dissolution of the ligand. To this was added 12.774 g of $K_2Cr_2O_7$ (43.4 mmol, 4.0 eq) in small portions so that the temperature of the reaction was maintained between 70-80ºC over the course of 1.5 hours. After complete addition the green solution was allowed to cool to room temperature and was then poured over 300 mL of ice. The green suspension was filtered to afford a yellow powder which was washed with copious amounts of water, acetone, and diethyl ether. It was dried under vacuum overnight with P_2O_5 to yield a light seafoam powder. Yield: 1.772 g, 67%. ^{1}H NMR

(500 MHz, DMSO-d_6): δ 13.60 (broad singlet, 1H), 8.76 (dd, J = 5.6, 2.9 Hz, 2H), 8.55 (s, 2H), 7.95 (dd, J = 5.6, 2.9 Hz, 2H).

Diethyl 4,4′-bipyridine-2,6-dicarboxylate (4-Py-DEP). This compound was synthesized using a modification of a literature procedure.[18] In a flame-dried round bottom flask was added 1.700 g of 4,4′-bipyridine-2,6-dicarboxylic acid (7.0 mmol, 1.0 eq) and 30 mL of $SOCl_2$. The green suspension was brought to reflux with a $CaCl_2$ drying tube for 24 hours. The light green suspension was cooled to room temperature and the excess $SOCl_2$ was distilled under vacuum. The green residue was suspended in anhydrous DCM and was added slowly to 100 mL of anhydrous EtOH at 0ºC and was allowed to stir for 1 hour at room temperature. The reaction was brought to reflux for 30 hours during which a yellow solution was afforded. It was cooled to room temperature and a saturated $NaHCO_{3(aq)}$ solution was added until the pH was basic. It was extracted with DCM (3 x 50 mL). The combined organics were dried over $MgSO_4$, filtered, and evaporated to yield a light peach colored powder. Yield: 1.370 g, 66%. ^{1}H NMR (500 MHz, $CDCl_3$): δ 8.83-8.78 (m, 2H), 8.53 (s, 2H), 7.68-7.63 (m, 2H), 4.53 (q, J = 7.1 Hz, 4H), 1.48 (t, J = 7.1 Hz, 6H).

2,6-di(2-carboxypyridyl)-4-phenylpyridine (dcpPhp). This compound was prepared analogously as dcpp with modification of the published procedure.[1] In a flame dried flask were added 0.35 mL of 2-bromopyridine (3.7 mmol, 2.2 eq) and 50 mL of anhydrous THF. This solution was cooled to -78ºC and 2.3 mL of 1.6 M n-BuLi (3.7 mmol, 2.2 eq) were added dropwise over 20 min. After completion of the addition the yellow solution stirred for an additional 15 min at -78ºC. A 20 mL THF solution containing 0.502 g of diethyl 4-phenyl-2,6-pyridine dicarboxylate (1.7 mmol, 1.0 eq) was added dropwise via a 22G cannula over 40 minutes. The reaction changed from yellow to orange. After the addition the reaction stirred for an additional 30 minutes before being quenched by the addition of 4 mL of methanol. The reaction was allowed to warm to room

temperature and stir overnight. The THF was evaporated, and the residue was taken into 40 mL of 10% HCl. The aqueous layer was extracted with 20 mL of DCM. The acidic layer was basified with 5 M NaOH. This was extracted with DCM (4 x 30 mL). The combined organics were dried over $MgSO_4$, filtered and evaporated. Yield: 313 mg, 52%. ^{1}H NMR (500 MHz, $CDCl_3$) δ 8.77 (dt, *J* = 4.8, 1.3 Hz, 2H), 8.53 (s, 2H), 8.22 (dd, *J* = 7.8, 1.1 Hz, 2H), 7.84 – 7.77 (m, 4H), 7.59 – 7.51 (m, 3H), 7.47 (ddd, *J* = 7.8, 4.7, 1.2 Hz, 2H).

2,6-di(2-carboxypyridyl)-4-(4-cyanophenyl)pyridine (dcpCNPhp). In a flame-dried round bottom flask was added 0.27 mL of 2-bromopyridine (2.8 mmol, 2.2 eq), and it was cooled to 0ºC. To this was added 2.2 mL of 1.3 M ^{i}PrMgCl•LiCl (2.8 mmol, 2.2 eq) dropwise over 20 minutes. The yellow solution warmed to room temperature and stirred for 1 hour. It was then cooled to -78ºC and a solution of 412 mg of diethyl 4-(4-cyanophenyl)-2,6-pyridine dicarboxylate (1.3 mmol, 1.0 eq) in 20 mL of THF was added dropwise over 30 minutes. The brown suspension turned bright red immediately. The red suspension was allowed to warm to room temperature and stir overnight. To this was added 3 mL of saturated $NH_4Cl_{(aq)}$ and the deep red solution turned purple. It stirred for 3 hours. The THF was evaporated, and the purple residue was taken into 30 mL of 10% HCl. The aqueous layer was extracted with DCM (1 x 10 mL). The acidic layer was then basified with 5 M NaOH and was extracted with DCM (3 x 50 mL). The combined organics were dried over $MgSO_4$, filtered, and evaporated to afford a light-yellow powder. It was further purified on silica with 4% EtOH/DCM. Yield: 300 mg, 61%. ^{1}H NMR (500 MHz, $CDCl_3$) δ 8.77 (ddd, *J* = 4.8, 1.7, 0.9 Hz, 2H), 8.50 (s, 2H), 8.24 (dt, *J* = 7.8, 1.1 Hz, 2H), 7.93 – 7.89 (m, 2H), 7.89 – 7.80 (m, 4H), 7.49 (ddd, *J* = 7.6, 4.7, 1.2 Hz, 2H).

2,6-di(2-carboxy-4-phenylpyridyl)pyridine (dcPhpp). This compound was prepared analogously as dcpp with modification of the published procedure.[1] In a flame-dried round bottom

flask was added 1.000 g of 2-iodo-phenylpyridine (3.6 mmol, 2.2 eq) and 25 mL of THF. This was cooled to -78ºC and 2.2 mL of 1.6 M n-BuLi (3.6 mmol, 2.2 eq) were added over 35 minutes. The solution instantly turned red. It stirred for an additional 10 minutes. A 10 mL THF solution containing 0.361 g of diethyl picolinate (1.6 mmol, 1.0 eq) was added dropwise to the red solution via a 22G cannula over 40 minutes. The reaction stirred for 2 hours at -78ºC. The red solution slowly darkened to brown. 3 mL of MeOH were added at -78ºC and the reaction was allowed to warm to room temperature and stir overnight. The reaction was concentrated to ~5 mL and 50 mL of 10% HCl and 15 mL of hexanes were added. The acidic layer was washed with 30 mL of DCM. The acidic layer was basified with 5 M NaOH and was extracted with DCM (3 x 50 mL). The combined organics were dried over MgSO4, filtered, and evaporated to yield an orange oil. Upon sonication with diethyl ether the oil solidified into a pale orange powder. Yield: 230 mg, 33%. ^{1}H NMR (500 MHz, $CDCl_3$) δ 8.49 (d, J = 5.0 Hz, 2H), 8.38 (s, 2H), 8.36 – 8.32 (m, 2H), 8.16 (t, J = 7.8 Hz, 1H), 7.55 – 7.42 (m, 12H).

2,6-di(2-carboxy-4-phenylpyridyl)-4-*p*-tolypyridine (dcPhpTp). This compound was prepared analogously as dcpp with modification of the published procedure.[1] To a 100 mL round bottom flask was added 600 mg of 2-iodo-4-phenylpyridine (2.1 mmol, 2.2 eq) and 40 mL of dry THF. The solution was cooled to -78ºC and 1.34 mL of 1.6 M n-BuLi (2.1 mmol. 2.2 eq) were added dropwise over 20 minutes affording a bright red-orange solution. This stirred for an additional 10 minutes. A 20 mL THF solution containing 304 mg of *p*Tol-DEP (0.97 mmol, 1 eq) were added dropwise over 1 hour via a 22G cannula. The purple solution stirred for an additional 1 hour at -78ºC before being quenched with 3 mL of MeOH. The reaction was allowed to warm to room temperature and stir overnight. The resulting brown solution was evaporated, and the crude residue was purified on silica gel with 20% EtOAc/DCM eluting as the 2nd band. The combined fractions

were then dissolved in minimal EtOAc and hexanes was added until cloudy to precipitate a pale orange solid. Yield: 150 mg, 30%. ^{1}H NMR (500 MHz, $CDCl_3$) δ 8.59 (s, 2H), 8.47 (d, J = 5.1 Hz, 2H), 8.35 (d, J = 1.9 Hz, 2H), 7.74 (d, J = 8.2 Hz, 2H), 7.54 – 7.41 (m, 12H), 7.37 (d, J = 8.1 Hz, 2H), 2.46 (s, 3H).

2,6-di(2-carboxypyridyl)-4-(4-pyridyl)pyridine (pyper). This compound was prepared analogously as dcpp with modification of the published procedure.[1] In a flame dried flask were added 0.7 mL of 2-bromopyridine (7.3 mmol, 2.2 eq) and 40 mL of anhydrous THF. This solution was cooled to -78ºC and 4.6 mL of 1.6 M n-BuLi (7.3 mmol, 2.2 eq) were added dropwise over 30 min. After completion of the addition the yellow solution stirred for an additional 15 min at -78ºC. An 80 mL THF solution containing 1.000 g of diethyl 4,4′-bipyridine-2,6-dicarboxylate (3.3 mmol, 1.0 eq) was added dropwise via a 22G cannula over 40 minutes. The reaction changed from yellow to orange. After the addition the reaction stirred for an additional 2 hours before being quenched by the addition of 3 mL of methanol. The reaction was allowed to warm to room temperature and stir overnight. The reaction was concentrated by ~75% and 100 mL of 10% HCl were added in addition to 50 mL of hexanes to help promote separation. The aqueous layer was extracted with 20 mL of DCM. The acidic layer was basified with 5 M NaOH. This was extracted with DCM (3 x 50 mL). The combined organics were dried over $MgSO_4$, filtered and evaporated. The beige residue was recrystallized from minimal EtOAc and adding hexanes until cloudy and placed in the freezer overnight. Yield: 313 mg, 52%. ^{1}H NMR (500 MHz, $CDCl_3$) δ 8.82 (d, J = 6.0 Hz, 2H), 8.77 (d, J = 5.2 Hz, 2H), 8.53 (s, 2H), 8.23 (s, 2H), 7.83 (td, J = 7.8, 1.8 Hz, 2H), 7.69 (d, J = 5.9 Hz, 2H), 7.48 (dd, J = 4.8, 2.9 Hz, 2H).

$[Fe(dcpPhp)_2](PF_6)_2$. In an N_2 purged flask, 61 mg of dcpPhp (0.17 mmol, 2.3 eq) were dissolved in 5 mL of dry still MeCN. To this was added 24 mg of $Fe(BF_4)_2$•$6H_2O$ (0.07 mmol, 1.0 eq). The

yellow solution turned dark blue instantly. It was heated to 65ºC for 24 hours. The reaction was then cooled to room temperature and the solvent removed *in vacuo*. The crude reaction was columned on silica eluting with 9:1 MeCN/$KNO_{3(aq)}$. The collected fractions were combined and concentrated and saturated $KPF_{6(aq)}$ was added to precipitate a dark blue solid. The solid was filtered and washed with H_2O and diethyl ether. Yield: 30 mg, 38%. ^{1}H NMR (500 MHz, acetone-d_6) δ 8.76 (s, 4H), 8.37 (td, *J* = 7.6, 1.4 Hz, 4H), 8.21 (dd, *J* = 7.9, 1.5 Hz, 14H), 8.17 – 8.11 (m, 8H), 7.71 – 7.64 (m, 6H), 7.50 (ddd, *J* = 7.6, 5.8, 1.6 Hz, 4H). ^{13}C NMR (126 MHz, CD_3CN) δ 181.59, 161.82, 159.93, 159.78, 153.89, 141.87, 135.00, 132.88, 130.85, 130.05, 129.14, 129.03, 128.67. Elemental Analysis: Calc'd (%): C, 51.32; H, 2.81; N, 7.81. Found: C, 51.65; H, 2.65; N, 7.35.

[Fe(dcPhpp)$_2$](PF$_6$)$_2$. In an N_2 purged flask, 96 mg of dcPhpp (0.21 mmol, 2.3 eq) were suspended in 5 mL of dry still MeCN. To this was added 30 mg of $Fe(BF_4)_2$•$6H_2O$ (0.09 mmol, 1.0 eq). The yellow solution instantly turned a dark green. It was heated to 65ºC for 24 hours. The dark solution was cooled to room temperature and concentrated slightly before diethyl ether was added to precipitate a grey/purple solid. The crude was columned on silica eluting with 7:1 MeCN/$KNO_{3(aq)}$. The collected purple fractions were combined and saturated $KPF_{6(aq)}$ was added to precipitate a purple solid. The solid was filtered and washed with H_2O and diethyl ether. Yield: 48 mg, 44%. ^{1}H NMR (500 MHz, acetone) δ 8.82 (t, *J* = 7.8 Hz, 2H), 8.54 (d, *J* = 7.8 Hz, 4H), 8.50 (d, *J* = 2.2 Hz, 4H), 8.18 (d, *J* = 6.1 Hz, 4H), 7.97 (dd, *J* = 7.1, 2.3 Hz, 8H), 7.83 (dd, *J* = 6.1, 2.2 Hz, 4H), 7.66 – 7.59 (m, 12H). ^{13}C NMR (126 MHz, CD_3CN) δ 181.39, 161.77, 160.10, 159.92, 153.20, 142.39, 135.10, 132.68, 132.13, 130.75, 128.53, 126.63, 126.27. Elemental Analysis: Calc'd (%): C, 56.69; H, 3.12; N, 6.84. Found: C, 56.82; H, 2.84; N, 6.46.

[Fe(dcPhpTp)$_2$](PF$_6$)$_2$. In an N_2 purged flask, 41 mg of dcPhpTp (0.07 mmol, 2.2 eq) were dissolved in 6 mL of dry MeCN. To this yellow solution was added 9 mg of $Fe(BF_4)_2$•$6H_2O$ and the solution turned black instantly. The reaction was gently heated to 50ºC for 18 hours and then cooled to room temperature. Upon cooling precipitation of a fine powder began. Et_2O was added to fully precipitate a dark blue solid. The solid was filtered and washed with Et_2O. The crude powder was dissolved in minimal MeCN (~25 mL) and a saturated solution of $KPF_{6(aq)}$ was added to metathesize the complex. The precipitate was filtered and washed with H_2O and Et_2O and then additionally purified on Bio-Beads S-X1 with 6:4 toluene/MeCN. Yield: 23 mg, 48%. ^{1}H NMR (500 MHz, CD_3CN) δ 8.63 (s, 4H), 8.39 (d, *J* = 2.1 Hz, 4H), 7.96 – 7.91 (m, 4H), 7.90 – 7.85 (m, 8H), 7.68 (d, *J* = 6.1 Hz, 4H), 7.66 – 7.60 (m, 16H), 7.63 – 7.57 (m, 4H), 2.45 (s, 6H). ^{13}C NMR (126 MHz, DMSO-d_6) δ 180.93, 161.08, 159.45, 159.02, 150.43, 150.35, 141.97, 133.76, 131.47, 130.72, 130.46, 129.66, 127.45, 127.31, 126.42, 124.72, 123.82, 20.97. Elemental Analysis: Calc'd (%): C, 61.38; H, 3.58; N, 5.96. Found: C, 61.76; H, 3.24; N. 5.59.

[Fe(dcpCNPhp)$_2$](PF$_6$)$_2$. In an N_2 purged flask, 96 mg of dcpCNPhp (0.21 mmol, 2.2 eq) were suspended in 5 mL of dry still MeCN. To this was added 30 mg of $Fe(BF_4)_2$•$6H_2O$ (0.09 mmol, 1.0 eq). The yellow solution instantly turned a dark green. It was heated to 65ºC for 24 hours. The dark solution was cooled to room temperature and concentrated slightly before diethyl ether was added to precipitate a grey/purple solid. The crude was columned on silica eluting with 7:1 MeCN/$KNO_{3(aq)}$. Purification on silica with 7:1 MeCN/$KNO_{3(aq)}$ followed by metatheses with saturated $KPF_{6(aq)}$ provided the intended product as a dark blue solid. Yield: 30 mg, 30% ^{1}H NMR (500 MHz, MeCN-d_3) δ 8.62 (s, 4H), 8.20 (td, *J* = 7.6, 1.4 Hz, 4H), 8.12 (d, *J* = 8.2 Hz, 4H), 8.07 (dd, *J* = 7.9, 1.6 Hz, 4H), 8.00 (d, *J* = 8.2 Hz, 4H), 7.55 (dd, *J* = 5.8, 1.3 Hz, 4H), 7.33 (ddd, *J* = 7.5, 5.7, 1.6 Hz, 4H). ^{13}C NMR (126 MHz, CD_3CN) δ 181.32, 161.83, 160.24, 159.58, 152.11,

142.00, 139.37, 134.50, 130.19, 129.58, 129.14, 118.99, 115.72.Elemental Analysis: Calc'd (%): C, 51.18; H, 2.51; N, 9.95. Found: C, 51.21; H, 2.62; N, 7.46.

$[Fe(pyper)_2](PF_6)_2$. In an N_2 purged flask was added 53 mg of pyper (0.14 mmol, 2.2 eq) and 15 mL of THF. Under positive pressure, 20 mg of $Fe(BF_4)_2 \bullet 6H_2O$ (0.06 mmol, 1.0 eq) were added and the reaction instantly turned blue. It was heated to 60°C overnight. The reaction was cooled to room temperature and filtered. The collected solid was washed with THF (3 x 15 mL) and diethyl ether. It was redissolved in minimal MeCN and treated with triethylamine to ensure the protonation state of the complex. Excess $KPF_{6(aq)}$ was added, and the blue precipitate was filtered and washed with H_2O and diethyl ether. Size exclusion chromatography on Bio-Beads S-X1with 6:4 toluene/MeCN afforded clean product. X-ray quality single crystals were grown by slow evaporation of the crude $[Fe(pyper)_2](BF_4)_2$ salt from a 6:4 toluene/MeCN solution. Yield: 22 mg, 34%. ^{1}H NMR (500 MHz, CD_3CN) δ 8.92 – 8.87 (m, 4H), 8.68 (s, 4H), 8.22 (td, *J* = 7.7, 1.3 Hz, 4H), 8.20 – 8.15 (m, 4H), 8.09 (dd, *J* = 7.9, 1.6 Hz, 4H), 7.55 (dd, *J* = 5.7, 1.4 Hz, 4H), 7.36 (ddd, *J* = 7.5, 5.7, 1.6 Hz, 4H). ^{13}C NMR (126 MHz, CD_3CN) δ 181.28, 161.84, 160.38, 159.55, 152.16, 151.54, 142.50, 142.04, 130.22, 129.54, 129.18, 122.62. Elemental Analysis: Calc'd (%): C, 49.00; H, 2.62; N, 10.39. Found: C, 48.61; H, 2.55; N, 9.28.

$[Fe(Etpyper)_2](PF_6)_4$: To a flame-dried flask was added 10 mg of $[Fe(pyper)_2](PF_6)_2$ (0.01 mmol, 1.0eq.) and 5 mL of MeCN. To the blue solution was added ~4 mg of $[Et_3O]BF_4$ (0.02 mmol, 2.0 eq). The reaction was stirred at room temperature for 40 mins and then heated to 60°C for 1 hour. The reaction was followed by electronic absorption spectroscopy. At this time, the intended complex was not isolated but spectroscopic evidence shows that it is most likely mono-alkylated product that has formed.

3.2.2 Physical Characterization

X-ray crystal structure determination. Crystals of appropriate size were selected and mounted on a nylon loop with paratone oil on a XtaLAB Synergy, Dualflex, HyPix diffractometer. The crystals were kept at a steady T = 100.0(2) K during data collection. The structures were solved with the ShelXT[19] solution program using intrinsic phasing or direct methods for twinned data and by using Olex2 1.3[20] as the graphical interface. The model was refined with ShelXL 2018/3[21] using full matrix least squares minimization on $\boldsymbol{F^2}$.

Ground-state absorption spectroscopy. All molar absorptivity measurements were collected in spectrophotometric grade acetonitrile (Sigma Aldrich) in a 1 cm quartz cuvettes on a PerkinElmer Lambda 1050 dual-beam spectrophotometer at a concentration between 10-30 μM.

Electrochemistry. Electrochemistry was performed using a CH Instruments potentiostat in a 0.1 M tetrabutylammonium hexafluorophosphate ($TBAPF_6$) acetonitrile solution with a Pt working electrode, Pt counter electrode, and a Ag wire pseudo-reference electrode in an Ar-filled glovebox. Cyclic voltammetry measurements were conducted with a 100 mV/s scan rate to determine the reversibility of redox processes and differential pulse voltammetry (DPV) was used to accurately determine $E_{1/2}$. All potentials were internally referenced to the Fc/Fc^+ redox couple. $TBAPF_6$ was purchased from Oakwood Chemical Company and recrystallized from ethanol twice before use.

3.2.3 Computational Methods

All calculations were performed with Gaussian 16[22] on the Michigan State University High Performance Computing Center servers. Calculations were performed using either B3LYP,[23] B3LYP*,[24] in which the percentage of Hartree-Fock exchange was modified, or TPSSh functionals in an integral equation formalism variant of the polarizable continuum model (IEFPCM) for

acetonitrile. Grimme's Empirical dispersion correction, D2, was employed on all functionals.[25] For geometry optimizations and frequency calculations, a split basis was used with 6-311G(d) for C, H, N, and O, and the SDD basis and pseudo-potential for Fe. The frequency calculations were examined for negative frequencies to ensure that a minimum had been found. Time-dependent DFT (TD-DFT) was performed using the previous functionals and the 6-311G(d) basis set for all atoms and requesting 40 singlet states. Molecular orbital analysis and decomposition was performed using AOMix.[26,27] Molecular orbitals were visualized using Avogadro with an isovalue of 0.02.[28,29]

3.3 Results and Discussion

3.3.1 Synthesis

The synthesis of the central phenyl and tolyl esters was successfully accomplished through a Suzuki coupling using I-DEP. Initial attempts using the typical $Pd(PPh_3)_4$ as a catalyst and DMF as solvent employing Hünig's Base led to low yields or minimal conversion.[16] A more active palladium catalyst was sought out leading to the use of $Pd(dppf)Cl_2$•DCM in 1,4-dioxane with Cs_2CO_3 as the base.[30] These reaction conditions allowed for the facile coupling of the boronic acid to I-DEP starting material as well as allowing for ease of isolation due to using a more volatile solvent (Figure 3.1).

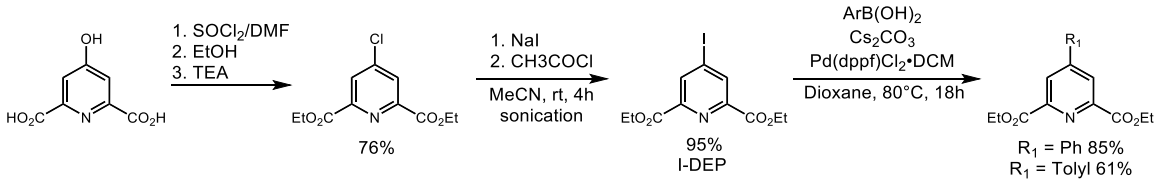

Figure 3.1. General synthetic scheme for the synthesis of phenyl and p-tolylpyridyl diethyl esters.

Attempts at synthesizing diethyl 4,4′-bipyridine-2,6-dicarboxylate did not follow the reactivity of the phenyl and tolyl esters. Initial attempts at coupling 4-pyridylboronic acid directly

to I-DEP using the coupling conditions from above led to no conversion. A coupling procedure that was shown to work for di*tert*-butyl 4-chloropyridine-2,6-dicarboxylate was attempted with the use of XPhos Pd G1 and aqueous K_3PO_4.[31] This route unfortunately led to no formation of product and only decomposition of the I-DEP due to aqueous base most likely catalyzing the hydrolysis of the ester to the carboxylic acid. An alternative route towards this precursor was sought in which a literature method for the preparation of the 4,4′-bipyridine derivative had already been established starting from 4-bromo-2,6-lutidine.[14] From this starting material, a Jones oxidation was carried out to form the dicarboxylic acid followed by synthesis of the diacyl chloride and reaction with ethanol at reflux led to the moderate yield of 4-Py-DEP (Figure 3.2).

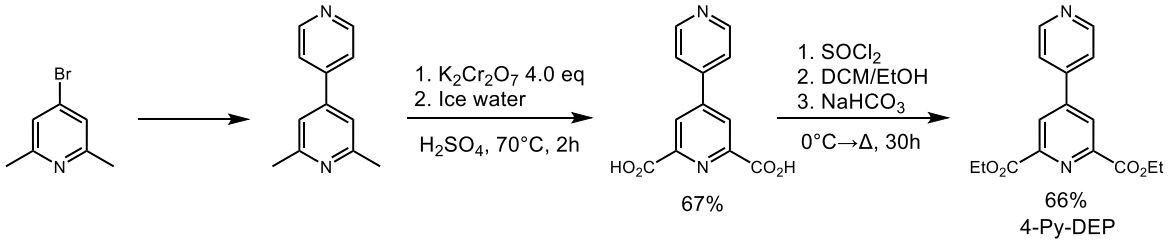

Figure 3.2. Synthetic protocol for the synthesis of diethyl 4,4′-bipyridine dicarboxylate.

The initial synthesis of 2-halo-4-phenylpyridine was first attempted starting from 2-bromo pyridine and synthesizing 2-bromo-3-iodopyridine.[32] From this intermediate, a halogen dance can be used to generate 2-bromo-4-iodopyridine. This starting material could then be used in a Kumada coupling using phenylmagnesium chloride (Figure 3.3a).[32] Though this route is an attractive pathway for the synthesis of 2-bromo-4-phenylpyridine the yield was low across the three steps. An alternative route was sought using a Suzuki coupling between 4-iodo-2-chloropyridine followed by a Finklestein halogen exchange. Similar conditions were used as the synthesis for I-DEP except the substitution required the application of heat for smooth conversion to the intended 2-iodo-4-phenylpyridine (Figure 3.3b).

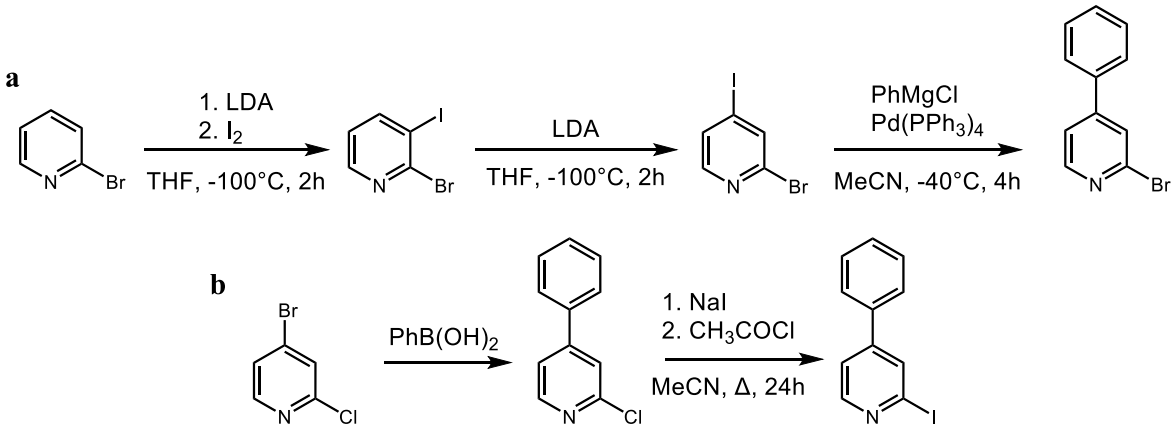

Figure 3.3. (a) Initial synthetic scheme to access 2-bromo-4-phenylpyridine through the use of a halogen dance followed by a Kumada coupling (b) Synthetic route followed for the synthesis of 2-iodo-4-phenylpyridine.

All of the derivatives of dcpp were synthesized using a modification of the original procedure, except for dcpCNPhp. The typical procedure for dcpp and its derivatives is lithiation of a halopyridine using n-BuLi at cryogenics temperatures (Figure 3.4a). This procedure tends to work well, barring any sensitive functional groups as in dcpCNPhp, which contains the nitrile moiety which is known for the reactivity of the nitrile carbon. Due to this, the lithiated pyridine was avoided because of its high nucleophilicity. An alternative route is to use a turbo Grignard, ^{i}PrMgCl•LiCl, first prepared by Knochel and coworkers.[33] The turbo Grignard allows for the facile metal-halogen exchange as seen with n-BuLi, but due to its decreased nucleophilicity, has been shown to be compatible with more sensitive functional groups and can be selective based on the reaction temperature used, which is typically -40°C or higher (Figure 3.4b).

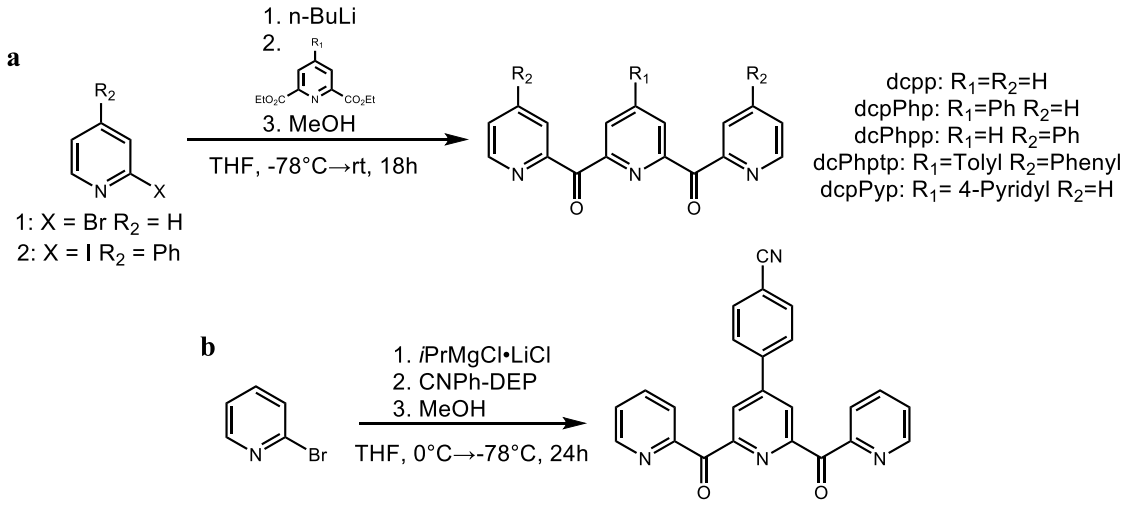

Figure 3.4. (a) General synthetic procedure for the synthesis of dcpp and aromatic derivatives (b) Synthetic scheme for the synthesis of dcpCNPhp using a turbo Grignard in place of n-BuLi due to sensitivity of nitriles.

Unlike the synthesis of $[Fe(dcpp)_2](PF_6)_2$, the complexation of the derivatives of dcpp were not as clean or high yielding. Though all the reaction mixtures were dark blue, except for dcPhpp which was purple, there were green impurities which are attributed to a monoligated complex as well as unreacted Fe(II) salts. Even with the application of heat the complexations did not progress further. These impurities could be easily removed though through column chromatography on silica with 7:1 or 9:1 $MeCN/KNO_{3(aq)}$ or size exclusion chromatography to afford clean product in low to moderate yields. The general synthesis of the complexes is shown in Figure 3.5.

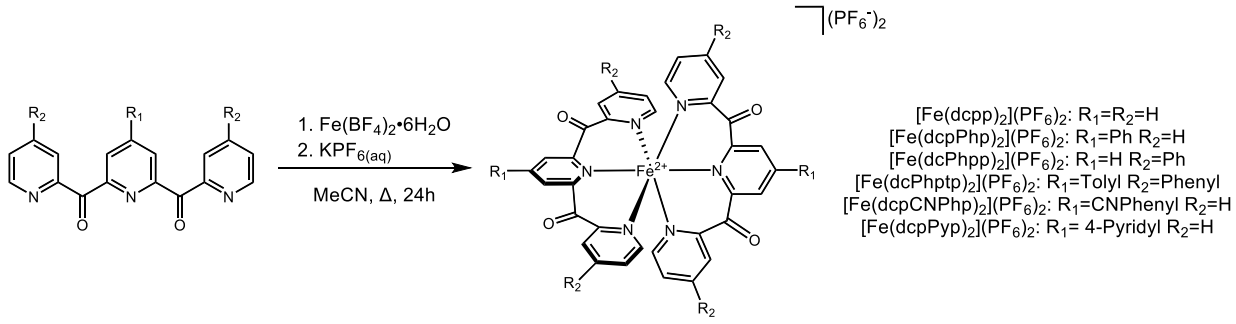

Figure 3.5. General synthetic route for the complexation of dcpp and its derivatives.

Attempts at synthesizing the "perphenylated" complex, $[Fe(dcPhpPhp)_2]^{2+}$, in which each pyridine has a phenyl substituent was precluded by solubility limitations. As the PF_6^- salt, the complex is only moderately soluble in common solvents used in photophysical measurements, i.e., acetone and acetonitrile. The metathesis to the BPh_4^- did afford increased solubility but would require all previous complexes to also be metathesized to the corresponding salts. To that end, to increase the solubility of the complex while having minimal effects on the electronic structure the ligand 2,6-di(2-carboxy-4-phenylpyridyl)-4-*p*-tolypyridine (dcPhpTp) was synthesized. The addition of the methyl group on the central ring afforded sufficient solubility as a PF_6^- salt in our commonly used solvents for purification as well as photophysical measurements. While possessing higher solubility, it still has lower solubility than the other derivatives. This was used to our benefit in the complexation, as the only moderately soluble complex, upon cooling, precipitates from the acetonitrile while leaving most impurities in solution. The product can then be metathesized and columned on Bio-Beads S-X1 to help remove excess salt from the metathesis.

The complexation of pyper to iron(II) proceeded smoothy upon switching solvents to THF. In this solvent the solubility is reduced allowing for precipitation of the intended product. The crude is then able to be filtered and washed with additional THF to remove unreacted ligand and the green impurities. The complex can then be treated with triethylamine to ensure the fully deprotonated complex and metathesized to the intended PF_6^- salt and size-exclusion chromatography was sufficient to provide clean sample for all additional studies.

An initial attempt at the synthesis of alkylated pyper, $[Fe(^{Et}pyper)_2](PF_6)_4$, was attempted using triethyloxonium as the alkylating agent. By NMR, the spectrum alludes to only mono-alkylation of the pendant pyridine and not dialkylation as was expected. This in part could be due to the decomposition of the alkylating agent as alkyloxonium salts are extremely hygroscopic and

reactive. An alternative route, instead of chemistry on the complex, would be to prepare the alkylated ligand first and then bind it to Fe(II). The worry with this particular route is that the dcpp ligand is already very electron-poor leading to poor binding to the Fe(II) center. Pulling more electron density out of the main ligand could further impede this complexation.

3.3.2 X-ray Crystallography

All complexes in the series maintained the nearly perfect octahedral geometry about the metal center with average bond lengths and angles shown in Table 3.1 for each complex that x-ray quality single crystals could be grown. The similar geometry between each complex creates an isostructural series in which we can now freely compare between complexes for the changes in electronic structure without the need to account for deviations from the parent complex's coordination environment. The overlay of the new complexes and comparison to the parent complex are shown in Figure 3.6.

Table 3.1. Comparison of Bond lengths and angles of $[Fe(dcpp)_2](PF_6)_2$ to the axial and peripheral phenyl substituted derivatives

Complex	**Average Fe-N_{ax} (Å)**	**Average Fe-N_{eq} (Å)**	**Average Cis Angle(°)**	**Average Trans Angle(°)**
$[Fe(dcpp)_2](PF_6)_2$	1.965	1.982	88.8	177.9
$[Fe(dcpPhp)_2](PF_6)_2$	1.953	1.988	90.1	177.7
$[Fe(dcPhpp)_2](BF_4)_2$	1.961	1.977	90.0	179.4

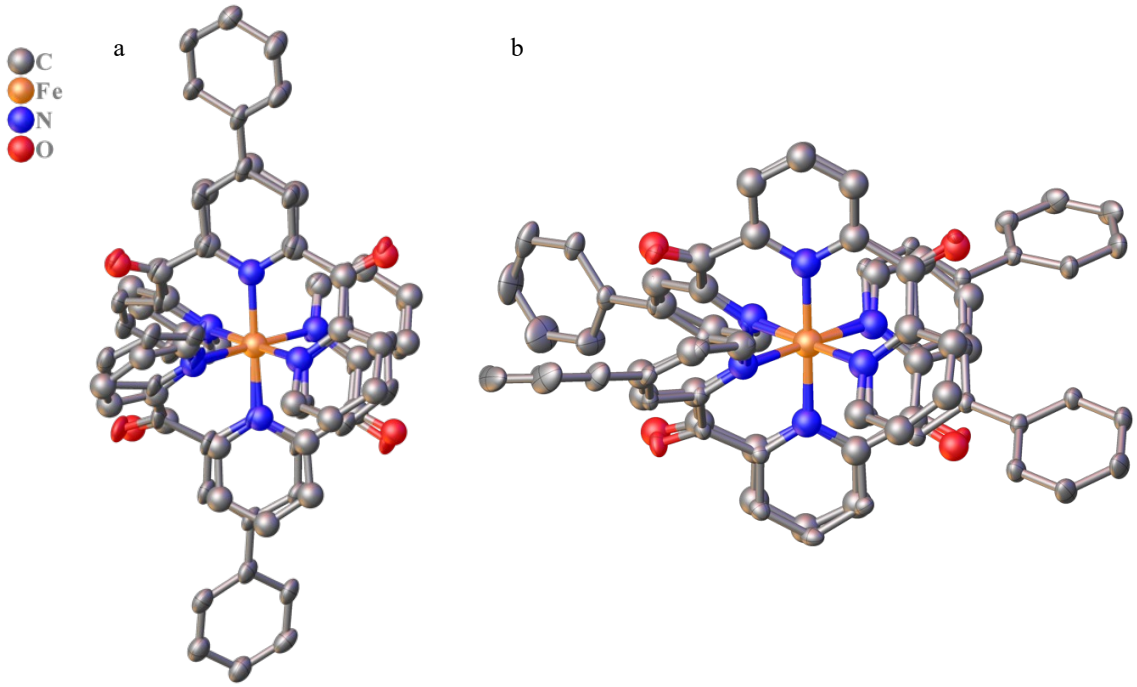

Figure 3.6. Overlay of $[Fe(dcpp)_2]^{2+}$ crystal structure with (a) The crystal structure of $[Fe(dcpPhp)_2]^{2+}$ and (b) The crystal structure of $[Fe(dcPhpp)_2]^{2+}$ showing the isostructural nature of the derivatives. Anions, solvent, and hydrogens have been removed for clarity.

$[Fe(dcPhp)_2](PF_6)_2$: The complex crystallizes in the $P2_1/c$ space group with one complex in the asymmetric unit in addition to one acetonitrile within the lattice. The crystal was twinned by 29% with component two rotated by -179.95º about the a-axis in reciprocal space.

$[Fe(dcPhpp)_2](BF_4)_2$: This complex crystallizes in $P2_1/c$ with one complex in the asymmetric unit with one acetonitrile and a disordered molecule of acetone on a symmetry site with an occupancy set to be 0.5. There is one rotationally disordered BF_4^- anion in the lattice. The occupancy of the fluorines were refined to 0.35:0.65 such that the total occupancy was unity.

$[Fe(dcpCNPhp)_2](BF_4)_2$: This derivative crystallizes in the $P2_1/c$ space group with two complexes in the asymmetric unit along with five acetonitriles and 0.5 molecules of DCM. There is one translationally disordered BF_4^- anion in the lattice and the occupancy was refined as 0.47:0.53 such that the total occupancy was unity.

[Fe(pyper)$_2$](BF$_4$)$_2$: The pyridyl-dcpp derivative crystallizes in the P2$_1$/n space group. There is one complex in the asymmetric unit cell. Attempts at crystallizing the fully deprotonated complex were unsuccessful but x-ray quality single crystals were grown from the crude reaction mixture as the BF_4^- salt from slow evaporation of a 6:4 toluene/MeCN solution. The complex crystallized as the monoprotonated ligand whereby a proton is shared between two complexes in the grown structure. This is due to trace acid present in the Fe(BF$_4$)$_2$•6H$_2$O starting material. This gives a formulation for the crystallized complex as [Fe(pyper)(Hpyper)](BF$_4$)$_3$. The quality of the data allowed for the refinement of the position of the hydrogen on the pendant pyridine. Within the asymmetric unit are three BF_4^- anions all of which are rotationally or translationally disordered. The occupancies of the anions were refined as follows: 0.71:0.29, 0.86:0.14, and 0.66:0.34, such that the total occupancy for each anion was unity. In addition to this disorder, there was appreciable solvent disorder in the lattice necessitating a solvent mask to be used. A solvent mask was calculated, and 168 electrons were found in a volume of 658 Å^3 in 2 voids per unit cell. This is consistent with the presence of 0.6 molecules of toluene and 0.5 molecules of acetonitrile per asymmetric unit which account for 164 electrons per unit cell.

3.3.3 Experimental and Computational Results

3.3.3.1 [Fe(dcpp)$_2$]$^{2+}$

The initial thrust for this research was to better understand the unique electronic structure of [Fe(dcpp)$_2$](PF$_6$)$_2$. The complex exhibits a broad and low energy metal-to-ligand charge transfer (MLCT) manifold corresponding to $^1A_1 \rightarrow {}^1$MLCT with multiple transitions present across the visible (Figure 3.7) as opposed to the most commonly studied complex, [Fe(bpy)$_3$]$^{2+}$ (where bpy is 2,2′-bipyridine), which by comparison has a narrow absorption with two main transitions.

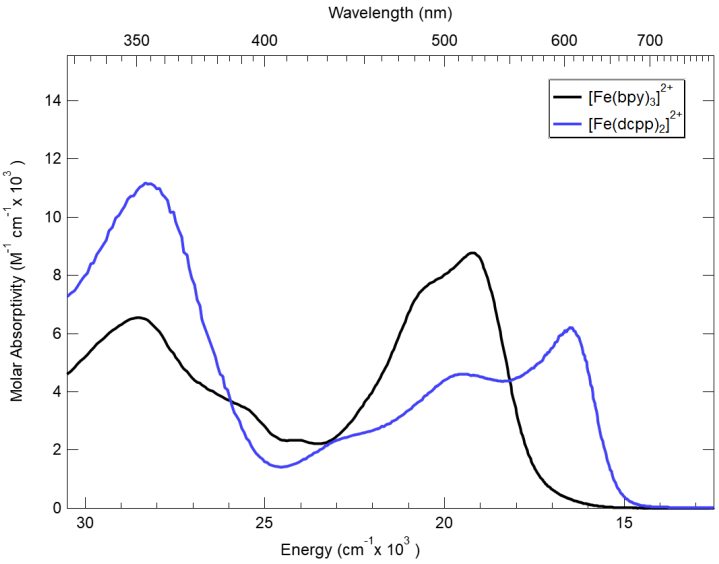

Figure 3.7. Ground-state electronic absorption spectra of $[Fe(dcpp)_2](PF_6)_2$ (blue) and $[Fe(bpy)_3](PF_6)_2$ (black) in acetonitrile.

To begin understanding the nature of these transitions for $[Fe(dcpp)_2]^{2+}$ we turned to computational chemistry for insight. The initial modeling of this complex had been done by the Jakubikova group, utilizing the widely used B3LYP functional with included empirical dispersion corrections.[3,34] This functional reproduced the crystallographic bond distances of the complex well pushing for its continued use to model this class of complexes. An aspect that had not been looked at was the ability of the functional to accurately reproduce the ground-state electronic absorption spectrum using TD-DFT. Using B3LYP+D2/SDD/6-311G(d) to optimize the ground-state geometry and then requesting TD-DFT calculations to be run with the 6-311G(d) basis set on all atoms showed a short coming for this functional formulation (Figure 3.8). Though accurate for the geometry, the energetics and the overall absorption profile dramatically differ from the experimental spectrum recorded. The hypsochromic shift of the lowest energy MLCT transition is on the order of 105 nm (0.42 eV, 3420 cm^{-1}) and shows two intense absorptions instead of the natural progression to lower molar absorptivity at shorter wavelengths. The difference between the two spectra is on the cusp of what is considered an acceptable deviation from experimental, 0.5 eV. To that end, we sought

to determine a better functional that would allow us to more accurately reproduce our experimental spectrum so that we could glean deeper insights into the excited-state properties of $[Fe(dcpp)_2]^{2+}$.

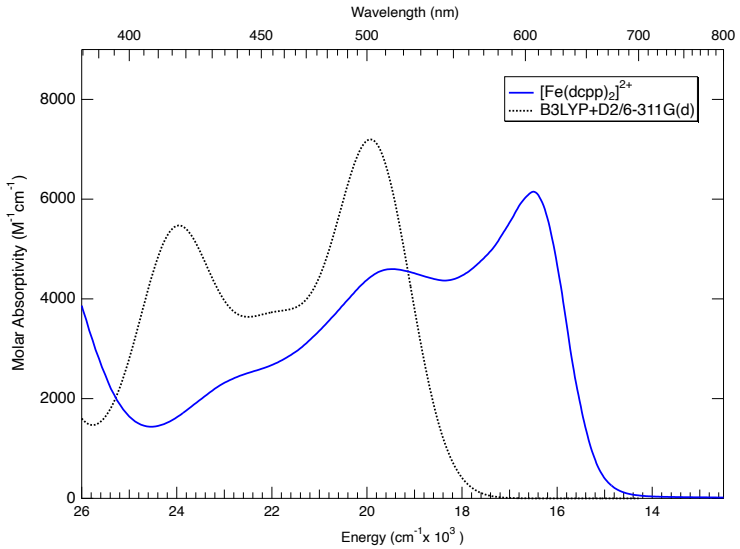

Figure 3.8. Comparison of the experimental (blue) and calculated (dashed black) ground-state electronic absorption spectrum of $[Fe(dcpp)_2]^{2+}$ in acetonitrile using the B3LYP functional with 20% Hartree-Fock Exchange and a FWHM of 900 cm^{-1}.

The first functional tested while using the SDD (Stuttfard/Dresden effective core potential) basis set and pseudopotential on iron and 6-311G(d) for all other atoms for optimization/frequency calculations and using 6-311G(d) for TD-DFT was TPSSh. This hybrid functional has been used in the modeling of other ferrous complexes with great success on reproducing geometric and energetic properties.[35] As shown in Figure 3.9a, there is a much better energetic match for the MLCT manifold that is being modeled compared to the experimental, but as with B3LYP the main features of the three transitions across the charge transfer are not as pronounced as the experimental spectrum, but are in much better agreement energetically. This difference in energetic matching as well as structure of the charge transfer begins to beg the question; what is the driving force for the dramatic bathochromic shift between these two functionals? One of the most common parameters

that is modified is the Hartree-Fock exact exchange, E_X^{HF}. Various tunings of E_X^{HF} have been proposed for octahedral Fe(II) complexes with mixings of 0%,[36] 15%,[37] and 30-50%.[38] In the case of B3LYP, the exchange is set at 20% whereas for TPSSh this value is 10%. This led us to believe that if we could use the B3LYP functional that gives satisfactory geometric agreement but modify it so that the E_X^{HF} more closely matches TPSSh we may be able to reliably match the simulated and experimental spectra. For this, 3 different percentages of Hartree-Fock exchange were used: 20% (standard), 15%, and 10% (exact exchange for TPSSh). The variations in the simulated absorption spectra versus the experimental spectrum are shown in Figure 3.9b.

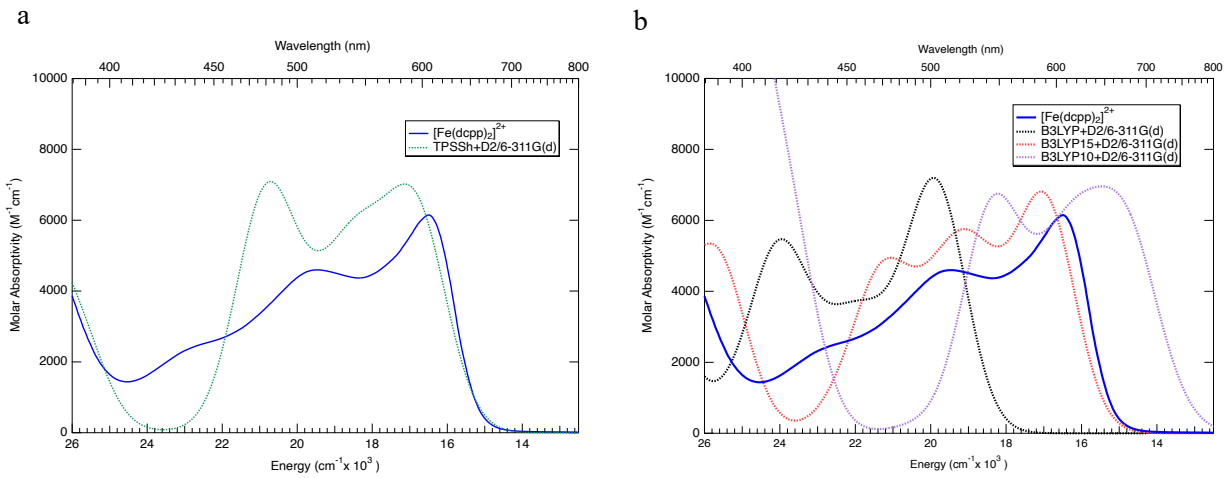

Figure 3.9. Comparison of (a) Experimental (solid blue) and calculated (green dash) spectrum of $[Fe(dcpp)_2]^{2+}$ using TPSSh+D2/6-311G(d) and (b) Experimental and calculated spectra of $[Fe(dcpp)_2]^{2+}$ using B3LYP+D2/6-311G(d) with 20% (black dash), 15% (red dash) and 10% (purple dash) Hartree-Fock Exact Exchange. All spectra are in acetonitrile and simulated spectra are modeled with a FWHM of 900 cm^{-1}.

This shows that as the percentage of exact exchange is decreased the spectrum shifts to lower energy. From this energetic variation and the overall MLCT manifold shape, the optimal percentage of exact exchange for this system is near 15% , and for our studies this is the percentage that will be used. The lowest energy charge-transfer transition is now blue-shifted by only 20 nm

(0.07 eV, 565 cm^{-1}) and the overall profile is in very good agreement with experimental, though more compressed. Shown in Figure 3.10 is the comparison of the calculated and experimental spectra using B3LYP15 including the individual transitions comprising the manifold. Inspection of the molecular orbitals involved in the transitions allows for the determination that this is indeed an MLCT manifold as known from experiment.

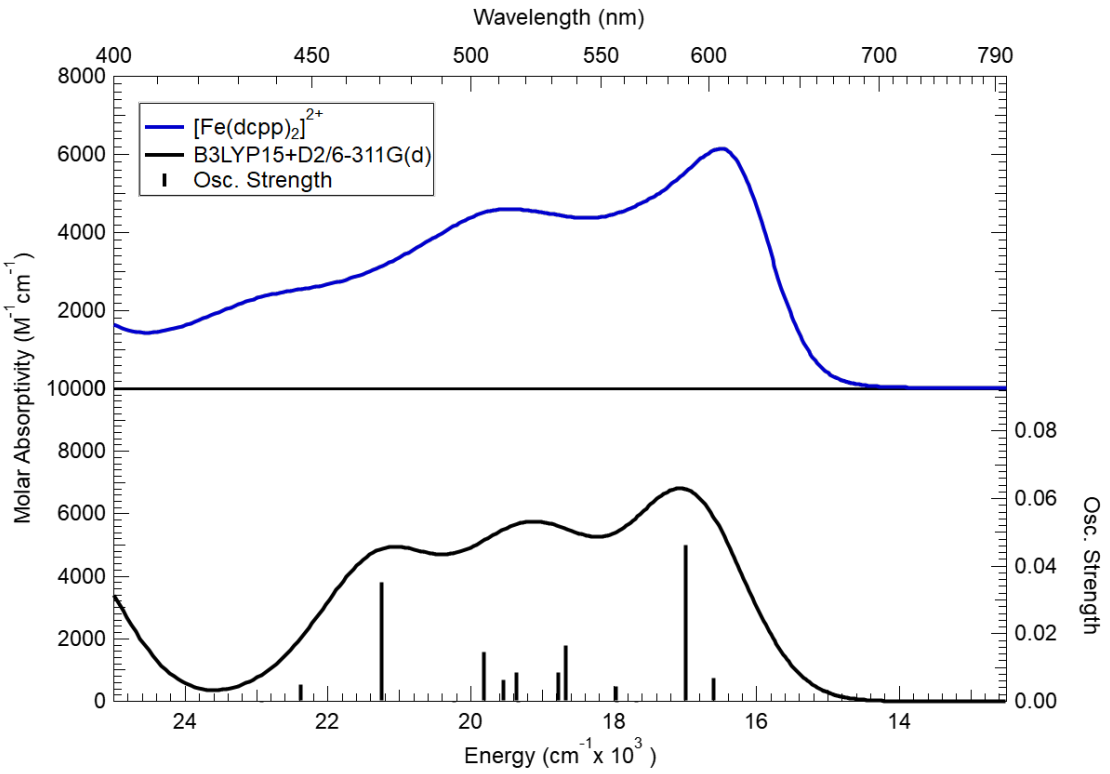

Figure 3.10. Comparison of the experimental (blue) and calculated (black) MLCT spectrum of $[Fe(dcpp)_2]^{2+}$ with individual transitions shown as black sticks on the calculated spectrum. FWHM is set to 900 cm^{-1} for the calculated spectrum.

Using the program AOMix[26] we can also quantitatively assign the nature of a transition based on percentage of molecular orbital contributions, but also begin to create a clearer picture of how these transitions manifest spatially within the molecule and what are important factors governing the nature of the charge transfer. To begin to do this, the complex of interest must be

divided into fragments such that the contributions of the individual fragments to the total molecular orbital can be analyzed. $[Fe(dcpp)_2]^{2+}$ has been divided into the fragments shown in Figure 3.11a. How to create the fragmentation schemes can be found in the AOMix manual as well as a recent publication by the Jakubikova group.[39]

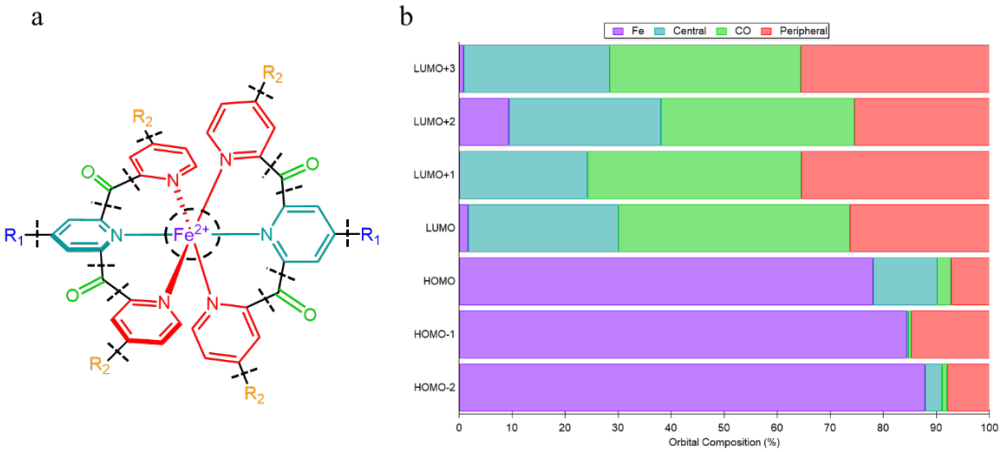

Figure 3.11. (a) Fragmentation scheme of $[Fe(dcpp)_2]^{2+}$ and its derivatives used for decomposition of molecular orbital contributions using AOMix (b) Orbital decomposition of $[Fe(dcpp)_2]^{2+}$ by AOMix and percent character of the representative fragments.

This fragmentation scheme follows what is believed to be the important features of the complex as well as what regions of the molecule are involved during the MLCT transition as determined from the orbitals involved from the initial TD-DFT analysis in Figure 3.10. The first three highest occupied molecular orbitals (HOMOs) are all shown to be high in iron character leading to the assignment of them being the metal-based t_{2g} orbitals, assuming O_h symmetry (Figure 3.11b). The unoccupied orbitals are largely ligand-based with minimal metal character. Inspection of these orbitals also shows a uniform distribution of orbital parentage suggesting a fairly symmetric excited state.

3.3.3.2 Effects of Phenyl Substitutions

We now turn our sights to the substitution of phenyl groups onto the periphery of the dcpp ligand backbone. The substitutions were made to maintain the approximate symmetry of the molecule allowing for ease of interpretation of the data. Electrochemical measurements were completed to first assess the impact of the substituents on the $Fe^{II/III}$ redox couple as well as the reduction of the ligand compared to the unsubstituted complex which are summarized in Table 3.2 and Figure 3.12.

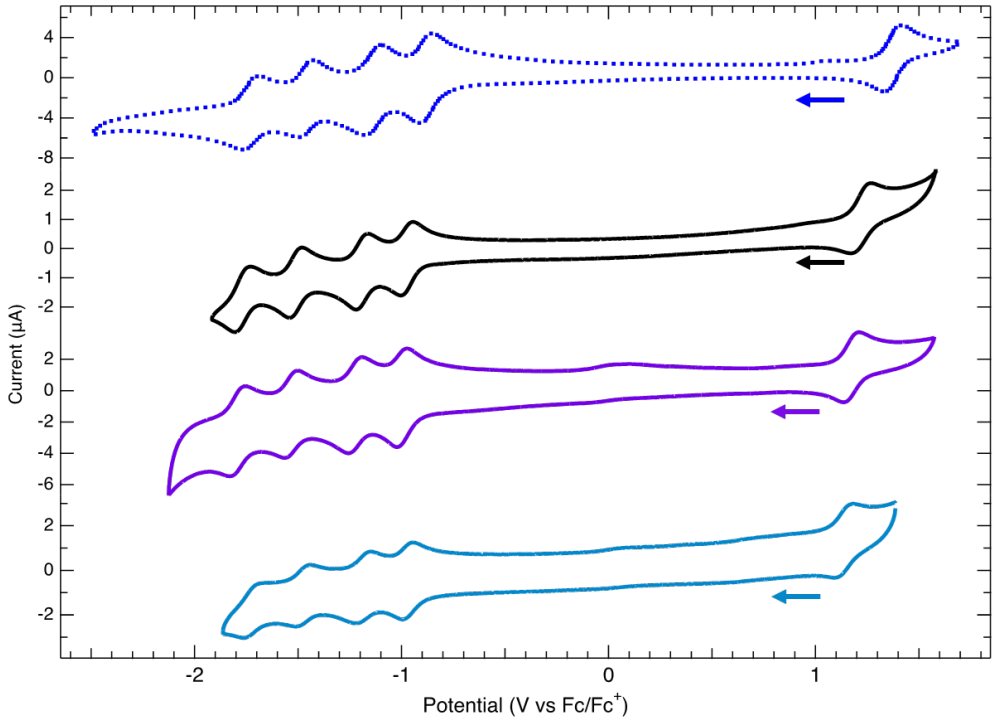

Figure 3.12. Cyclic voltammograms of $[Fe(dcpp)_2](PF_6)_2$ (blue), $[Fe(dcpPhp)_2](PF_6)_2$ (black), $[Fe(dcPhpp)_2](PF_6)_2$ (purple), and $[Fe(dcPhpTp)_2](PF_6)_2$ (turquoise) in acetonitrile solutions with 0.1 M $TBAPF_6$ as supporting electrolyte and internally referenced to the Fc/Fc^+ redox couple. Measurements were performed at 100 mV/s. Arrows indicate initial scan direction.

Table 3.2. Electrochemical data collected in acetonitrile for $[Fe(dcpp)_2](PF_6)_2$ and the phenyl substituted derivatives[a]

Complex	$E^{Ox}_{Fe^{II/III}}$	E^{Red1}_{ligand}	E^{Red2}_{ligand}	E^{Red3}_{ligand}	E^{Red4}_{ligand}
$[Fe(dcpp)_2](PF_6)_2$	1.26	-1.00	-1.24	-1.58	-1.85
$[Fe(dcpPhp)_2](PF_6)_2$	1.20	-0.96	-1.17	-1.49	-1.76
$[Fe(dcPhpp)_2](PF_6)_2$	1.16	-0.96	-1.19	-1.50	-1.76
$[Fe(dcPhpTp)_2](PF_6)_2$	1.12	-0.94	-1.15	-1.49	-1.71

[a]Potentials are internally referenced to the Fc/Fc+ redox couple. Potentials reported were determined using DPV.

The electrochemistry of these complexes is similar to that of $[Fe(dcpp)_2]^{2+}$. All complexes feature an extremely positive $Fe^{II/III}$ couple compared to well-known low-spin Fe(II) polypyridyl complexes. Of note is that as the number of aromatic substituents is increased the Fe(II) oxidation potential decreases to less positive values. This is indicative of the aromatics acting as net donors to the iron center creating a more electron-rich metal, allowing for more facile oxidation. While the iron-center follows a trend with increasing size of the π-sytem of the ligand, the reductions, however, are fairly unchanged between the three substituted complexes. While it would be expected that increased delocalization should continuously ease the potential required for the reduction of the ligand, it was put forth by Jamula and co-workers that the multiple reductions of the ligand are actually centered on the carbonyl bridge.[4] With this in mind, it would make sense that increased conjugation through the ligand would only have a modest effect on the reduction potentials after the initial substitution. As the complex is cross-conjugated, the carbonyl bridge between each ring only has communication to the pyridines to its left and right. Therefore, placing an aromatic substituent on the central or peripheral rings would have the same effect from the perspective of the carbonyl. There is a small decrease for the reduction of $[Fe(dcPhpTp)_2]^{2+}$ by approximately +20 mV which is attributed to the increased conjugation in both pyridine rings instead of only one.

With respect to the ground-state electronic absorption spectra of the complexes, it can be shown that the substitution pattern of the aromatics on the dcpp ligand backbone has a pronounced effect on the absorptive properties of these molecules (Figure 3.13). For each complex in which the substitutions occurred, either on the central, peripheral, or on all pyridines, the spectrum changes in accordance with that, exhibiting increased intensity of the MLCT manifold as well as a slight bathochromic shift. For all of the complexes, the increase in the molar absorptivity is due to the delocalization of the ground- and excited-state wavefunction. This spreading of the wavefunction leads to an increase in the transition dipole moment (t.d.m.) expectation value. The t.d.m. is dependent on the transition dipole moment operator, which for a 1-particle system is the product of the charge and the distance. The more charge moved (q) or the further it is moved (delocalized), the higher the intensity will be of the observed transition. This phenomenon has been well documented in the literature in ruthenium polypyridyl complexes.[8,40–43] Since the increased intensity of bands can be explained in general, we can now turn our focus to the individual transitions within the MLCT manifold.

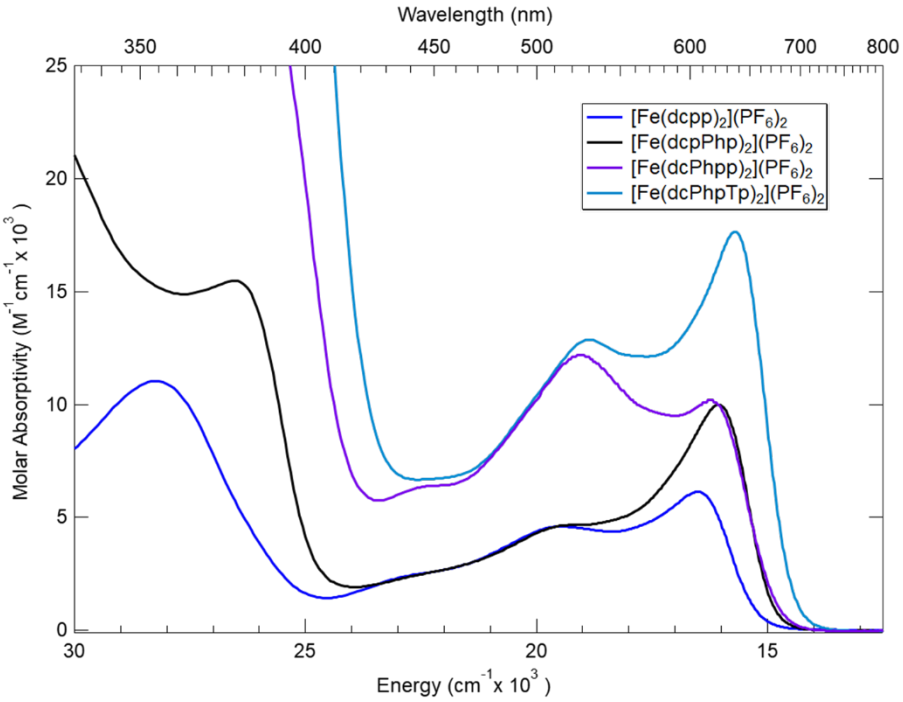

Figure 3.13. Ground-state electronic absorption spectra of $[Fe(dcpp)_2](PF_6)_2$ and its phenyl derivatives taken in MeCN.

Table 3.3. Spectroscopic data $[Fe(dcpp)_2](PF_6)_2$ and its phenyl derivatives recorded in MeCN

Complex	λ_{max}	**Molar Abs.**
	nm	$M^{-1}cm^{-1}$
$[Fe(dcpp)_2](PF_6)_2$	605	6140
$[Fe(dcpPhp)_2](PF_6)_2$	620	9990
$[Fe(dcPhpp)_2](PF_6)_2$	525	12200
$[Fe(dcPhpTp)_2](PF_6)_2$	635	17640

We can begin to deconvolve the MLCT spectrum of $[Fe(dcpp)_2]^{2+}$ using these derivatives. Looking at $[Fe(dcpPhp)_2]^{2+}$ first, from an electronegativity standpoint, it is expected that the lowest energy transition would preferentially occur towards the regions of least electron density in the ligand, the carbonyls and the central ring. This is seen for $[Fe(dcpPhp)_2]^{2+}$ in which the lowest energy absorption in the MLCT manifold shows increased intensity (Figure 3.13, black trace), leading to this transition being associated with the central pyridine. The second transition across

the manifold is left largely unchanged from the parent complex. The experimental versus the simulated spectrum can be seen in Figure 3.14a.

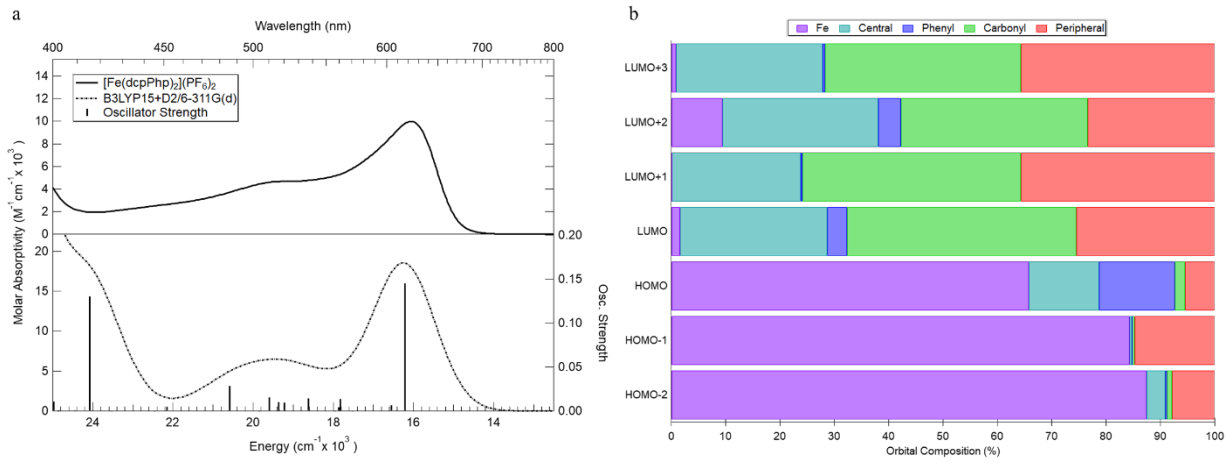

Figure 3.14. (a) (Top) Experimental MLCT spectrum of $[Fe(dcpPhp)_2](PF_6)_2$ in MeCN (Bottom) Calculated absorption spectrum (dashed) in MeCN and individual transitions (sticks) (b) Molecular orbital composition determined using AOMix.

The molecular orbital decomposition of the complex using AOMix (Figure 3.14b) shows that similar to the parent complex, the first three HOMOs of $[Fe(dcpPhp)_2]^{2+}$ are almost purely iron-based and the LUMOs become primarily ligand-based owing to the transitions being of MLCT character. The first HOMO, as compared to HOMO-1 and HOMO-2 contains an appreciable amount of central pyridine and phenyl character. The lowest energy transition in the calculated spectrum is comprised of the HOMO-LUMO transition with the rendering of those orbitals shown in Figure 3.15a. This is a pure transition with a Slater coefficient of 0.6928 with no admixture of other molecular orbitals involved. To note from this and Figure 3.14b, is that only transitions arising from a combination of HOMO, LUMO, and LUMO+2 will have any appreciable contribution from the aromatic substituent leading to the increase in the intensity of the band. Transition 13 in the spectrum at ~500 nm is only comprised of 60% of that combination owing to the decreased effect on its intensity.

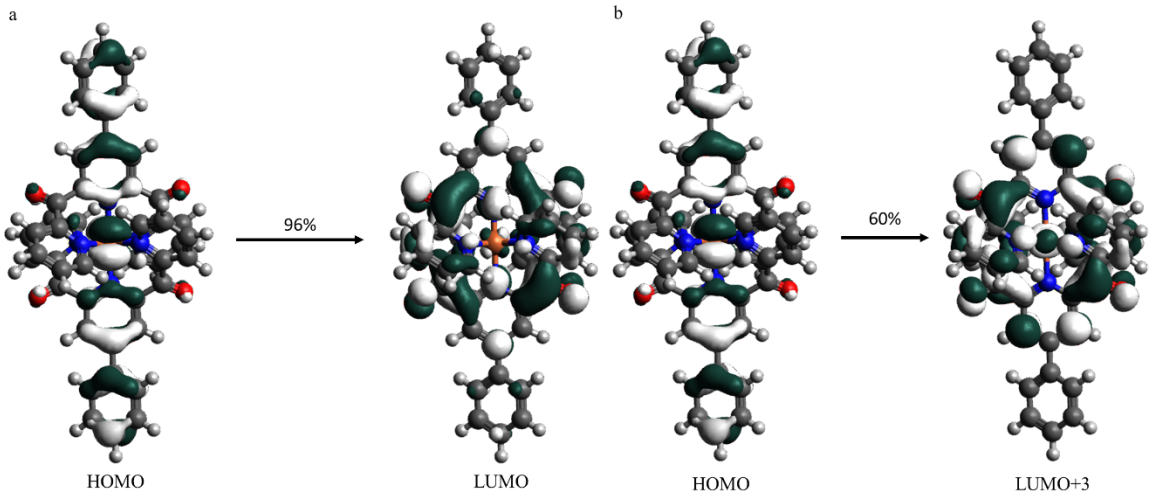

Figure 3.15. (a) Molecular orbitals of the lowest energy transition of $[Fe(dcpPhp)_2]^{2+}$ (b) Molecular orbitals with the highest Slater coefficient for transition 13. MOs are rendered at an isovalue of 0.02.

Moving towards the analysis of $[Fe(dcPhpp)_2]^{2+}$, the same analysis is used as for $[Fe(dcpPhp)_2]^{2+}$ whereby the experimental spectrum is modeled computationally, and the composition of the molecular orbitals are decomposed using AOMix. This initial analysis is shown in Figure 3.16. It is notable in this spectrum that both the lower energy side and the higher energy side of the MLCT manifold have gained intensity. Decomposition of the molecular orbitals, again, show primarily iron-based orbitals with increased contributions from the peripheral pyridine rings and the phenyl groups attached to them compared to the parent complex. Unlike in the case of $[Fe(dcpPhp)_2]^{2+}$, which only showed appreciable phenyl contributions in the HOMO, $[Fe(dcPhpp)_2]^{2+}$ maintains this in orbitals HOMO-3 through HOMO as well as in all the LUMO series shown (Figure 3.16b)

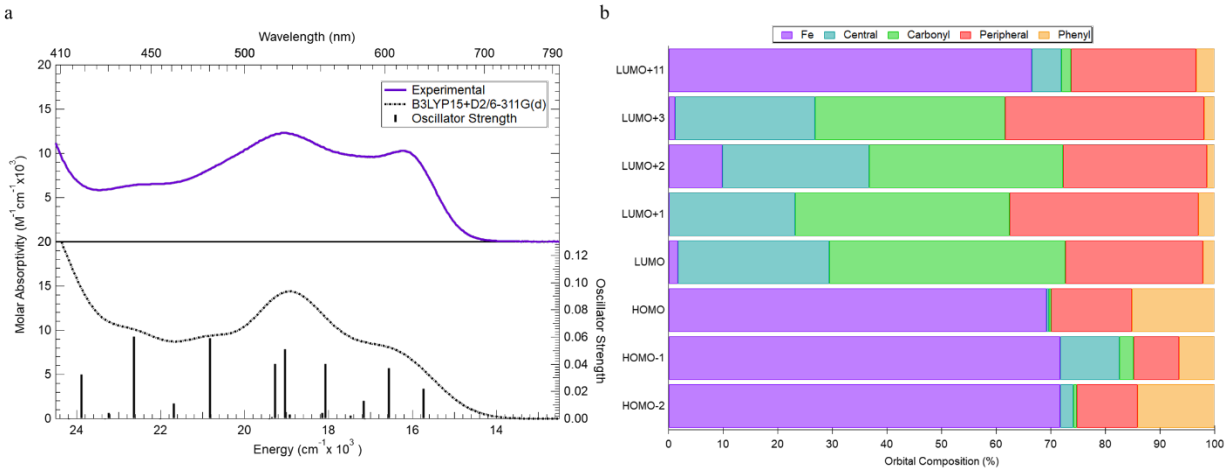

Figure 3.16. (a) (Top) Experimental MLCT spectrum of $[Fe(dcPhpp)_2](PF_6)_2$ in MeCN (Bottom) Calculated absorption spectrum (dashed) in MeCN and individual transitions (sticks) (b) Molecular orbital composition determined using AOMix.

Inspection of the HOMOs and LUMOs show that the all the transitions would be characterized as MLCT in nature. The first two transitions in the calculated spectrum correspond to transitions of HOMO→LUMO and HOMO-1→LUMO, respectively. The transitions centered around 19,000 cm^{-1} (~525 nm) in the calculated spectrum correspond to transitions of HOMO-2→LUMO+1 and a mixed transition of HOMO-1→LUMO+3 and HOMO-1→LUMO+11 with percent character of 33% and 47%, respectively (Figure 3.17).

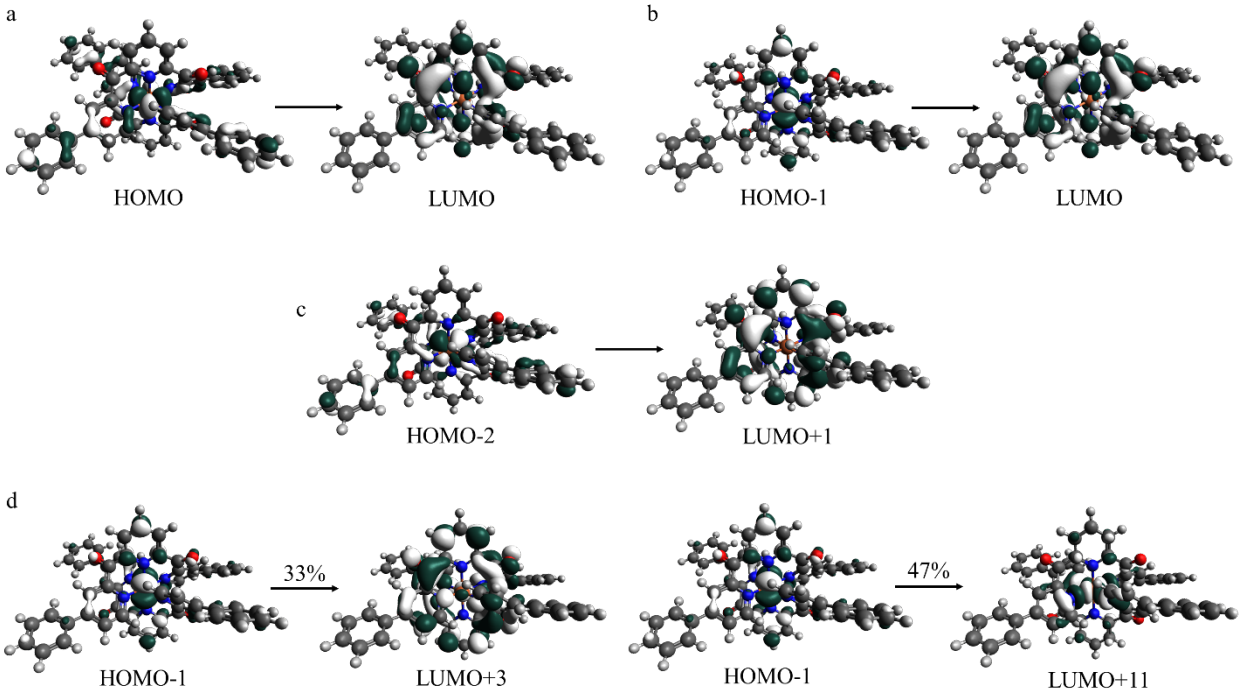

Figure 3.17. Molecular orbitals of $[Fe(dcPhpp)_2]^{2+}$ involved in (a) The lowest energy MLCT transition (b) The second lowest energy transition (c) Transition 9 at 525 nm and (d) Transition 10 at 518 nm consisting of a mixed transition set comprising of 33% and 47% from the slater coefficients, respectively.

3.3.3.3 Effects of Strongly Withdrawing Groups

Now that we know the correct functional formulation to accurately match the energetics and shape of the MLCT manifold of $[Fe(dcpp)_2]^{2+}$ and a few of its phenyl derivatives, we can now apply this protocol to predict new and interesting complexes from this family of compounds. As noted in the previous section, the vast majority of the orbital contributions and changes during the MLCT excitation occur at the carbonyl bridge and the wavefunction effectively collapsing into the main body of the ligand. Therefore, for delocalization of the excited state wavefunction to occur, there must be stronger pull from the substitutions employed on the backbone of the ligand compared to the carbonyl groups. For the wavefunction to extend further from the main ligand and allow for the benefits of delocalization on the lifetime of the MLCT, as has been seen in many 2nd-row transition metal complexes, strong electron-withdrawing groups will need to be employed as

a type of electron-sink. Three complexes were investigated synthetically and computationally towards this end: $[Fe(dcpCNPhp)_2]^{2+}$, $[Fe(pyper)_2]^{2+}$, and $[Fe(^{Me}pyper)_2]^{2+}$ (where ^{Me}pyper is the pendant *N*-alkylated methyl pyridine). This family of complexes exhibit various degrees of electron-withdrawing ability with the substitution solely on the central pyridyl-ring of dcpp. In addition to ease of synthesis these complexes also facilitate directionality in the charge-transfer which may be beneficial in future endeavors.

Table 3.4. Spectroscopic data for comparison of $[Fe(dcpCNPhp)_2](PF_6)_2$ and $[Fe(pyper)_2](PF_6)_2$ to $[Fe(dcpp)_2](PF_6)_2$ in acetonitrile

Complex	λ_{max}	Molar Abs.
	nm	$M^{-1}cm^{-1}$
$[Fe(dcpp)_2](PF_6)_2$	605	6140
$[Fe(dcpCNPhp)_2](PF_6)_2$	623	12620
$[Fe(pyper)_2](PF_6)_2$	620	9200

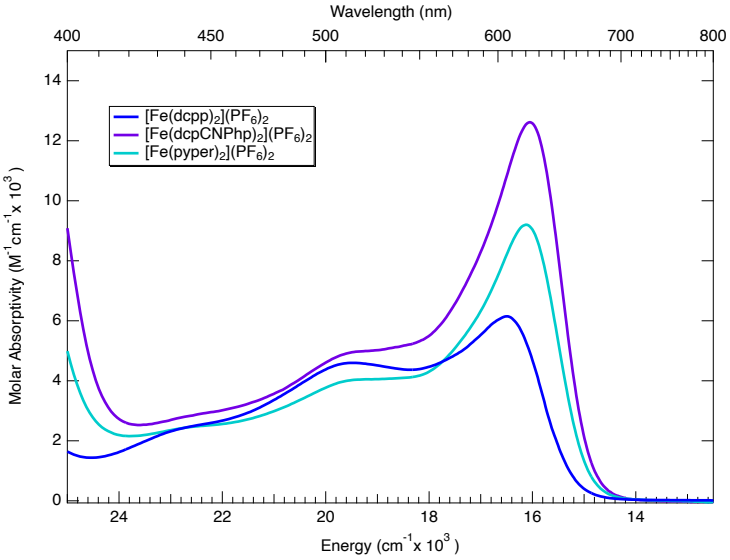

Figure 3.18. Ground-state electronic absorption spectra of $[Fe(dcpp)_2](PF_6)_2$ (dark blue), $[Fe(dcpCNPhp)_2](PF_6)_2$ (purple), and $[Fe(pyper)_2](PF_6)_2$ (teal) in acetonitrile.

The UV-Vis of $[Fe(dcpCNPhp)_2](PF_6)_2$ and $[Fe(pyper)_2](PF_6)_2$ are shown in Figure 3.19. Both complexes show an increased molar absorptivity in the MLCT manifold compared to the parent

$[Fe(dcpp)_2]^{2+}$ complex, with the most pronounced effect on the lowest energy transition as seen in the previous family of phenyl substituted complexes, $[Fe(dcpPhp)_2]^{2+}$ (Figure 3.13). The cyanophenyl complex exhibits the largest increase in molar absorptivity which is attributed to the strong electron-withdrawing nature of the substituent. It is well known that the nitrile moiety is a strong resonantly electron-withdrawing group in the cyanophenyl derivative, $[Fe(dcpCNPhp)_2]^{2+}$. This has been used in ruthenium photophysics to further prolong the lifetime of the MLCT state as well as increase the molar absorptivity of the transitions.[44,45] This complex was analyzed similarly to the other phenyl substituents in the previous sections and its orbital contributions decomposed using AOMix (Figure 3.19b). The most intense transition in the spectrum was calculated to correspond to a HOMO-LUMO excitation (Figure 3.19c). Unlike what is observed for $[Fe(dcpPhp)_2]^{2+}$ in which the central phenyl only maintains an appreciable amount of contribution in the HOMO but is lost in the LUMOs, $[Fe(dcpCNPhp)_2]^{2+}$ exhibits only a small decrease in the composition of the CNPhenyl. This is an exciting result in that by employing the nitrile functionality the wavefunction in the excited-state is beginning to delocalize further out into the ligand backbone which can potentially lead to an increase in the ^{3}MLCT lifetime. Inspection of the HOMO and LUMO Figure 3.19b and Figure 3.19c though shows that the amount of delocalization is still fairly low when compared to the contributions from the rest of the molecule, especially the carbonyl functional group which still dominates in the contributions in the excited states.

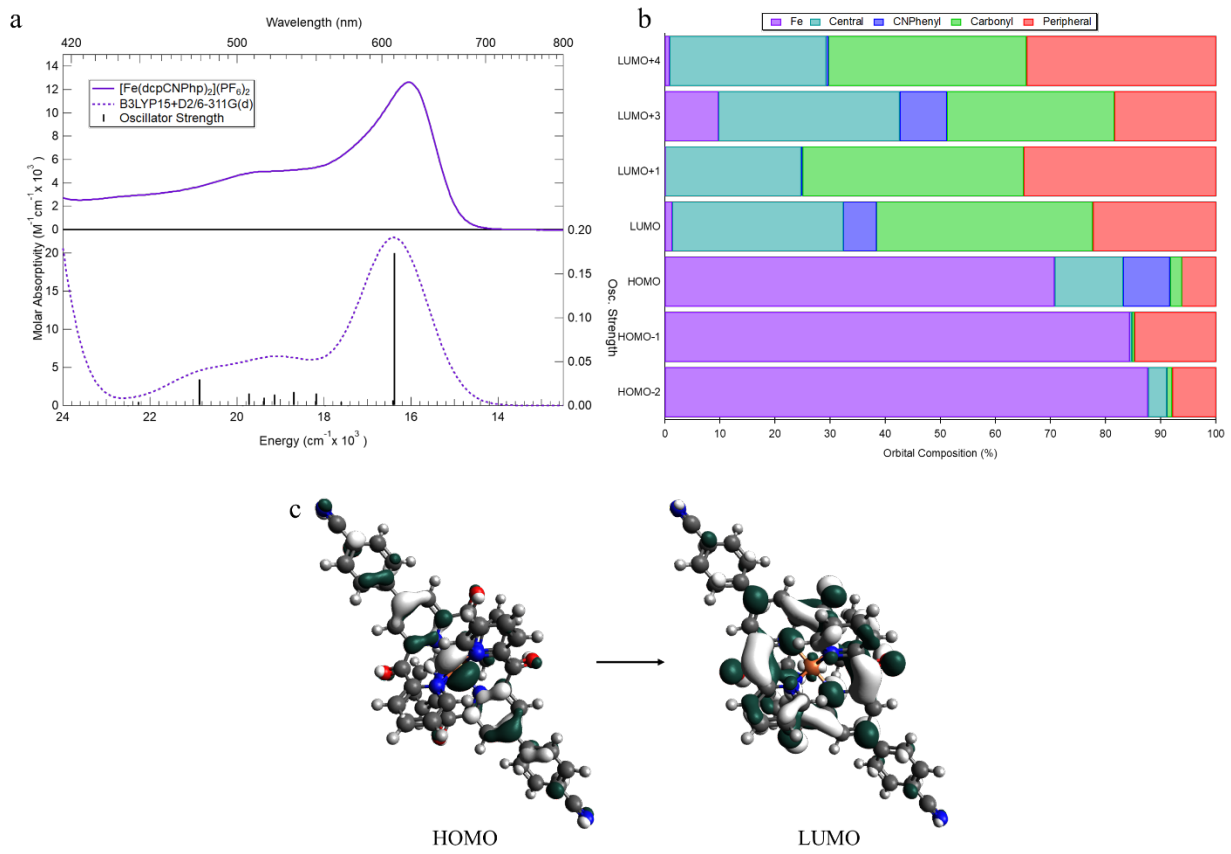

Figure 3.19. (a) (Top) Experimental MLCT spectrum of $[Fe(dcpCNPhp)_2](PF_6)_2$ in MeCN (Bottom) Calculated absorption spectrum (dashed) in MeCN and individual transitions (sticks) (b) Molecular orbital composition determined using AOMix (c) Molecular orbitals associated with the lowest energy transition with a slater coefficient corresponding to 100%.

With this result, we continued the search for more strongly withdrawing functional groups. Again, looking for inspiration from the Ru(II)[46–48] literature as well as work done by Constable and co-workers with Fe(II)[49,50] complexes, we found that alkylated pyridiniums could present a new and interesting avenue for this class of complexes. $[Fe(pyper)_2](PF_6)_2$ was synthesized and modeled with TD-DFT. The comparison of the experimental and calculated spectra is shown in Figure 3.20a. The decomposition of the molecular orbitals is reminiscent to that of $[Fe(dcpCNPhp)_2]^{2+}$ in which there are contributions from the extended π-system in the LUMOs of the complex, but to a slightly lesser extent. This shows that between these two complexes the nitrile

is the stronger withdrawing group as would be expected. But, upon alkylation of $[Fe(pyper)_2]^{2+}$ from a theoretical standpoint, we can begin to tell a new story.

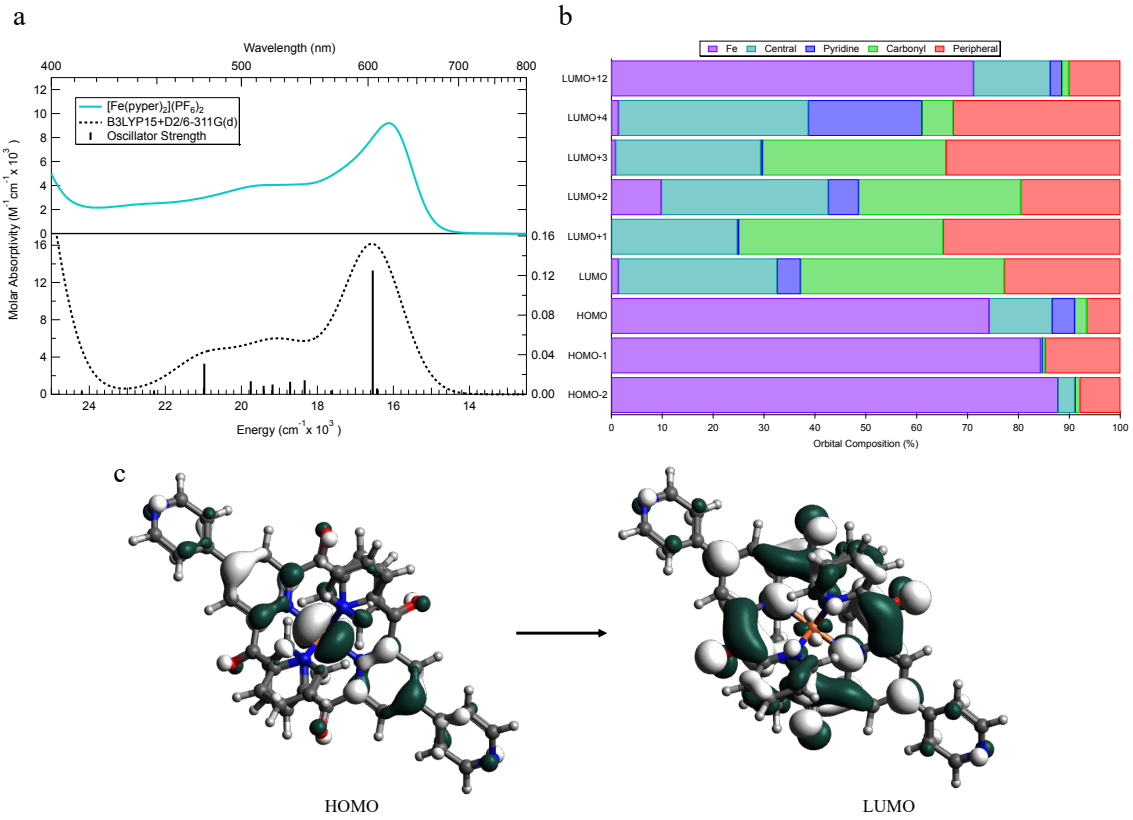

Figure 3.20. (a) (Top) Experimental MLCT spectrum of $[Fe(pyper)_2](PF_6)_2$ in MeCN (Bottom) Calculated absorption spectrum (dashed) in MeCN and individual transitions (sticks) (b) Molecular orbital composition determined using AOMix (c) Molecular orbitals associated with the lowest energy transition with a slater coefficient corresponding to 100%.

The alkylated complex that was modeled was that of $[Fe(^{Me}pyper)_2]^{4+}$ whereas the target complex is $[Fe(^{Et}pyper)_2]^{4+}$. The ethyl derivative is the target complex due to the greater solubility of ethylating starting materials such as $[Et_3O]BF_4$ in organic solvents that are amenable to the complexes. Modelling of methyl groups becomes slightly easier computationally as longer alkyl chains tend to present difficulties in geometry convergence due to the shallow potential surface for rotation of the C-C bond. This should not have any dramatic impacts on the energetics and the

analysis of the complex as the pyridinium is the stronger contributor to the overall energetics of the system.

Looking at the calculated spectrum of $[Fe(^{Me}pyper)_2]^{4+}$ (Figure 3.21a), it shows an intense transition centered at 16,290 cm^{-1} (614 nm) corresponding to a $^1A_1 \rightarrow {}^1$MLCT excitation from HOMO to LUMO. To note for this transition is the extension is unlike the previous complexes studied, the HOMO through HOMO-2 have minimal contributions from the central ring and the pyridine, contrary to what is observed in all other complexes with a substitution on the central ring. What is now observed is orbital contributions into the pyridinium, delocalization of the LUMO.

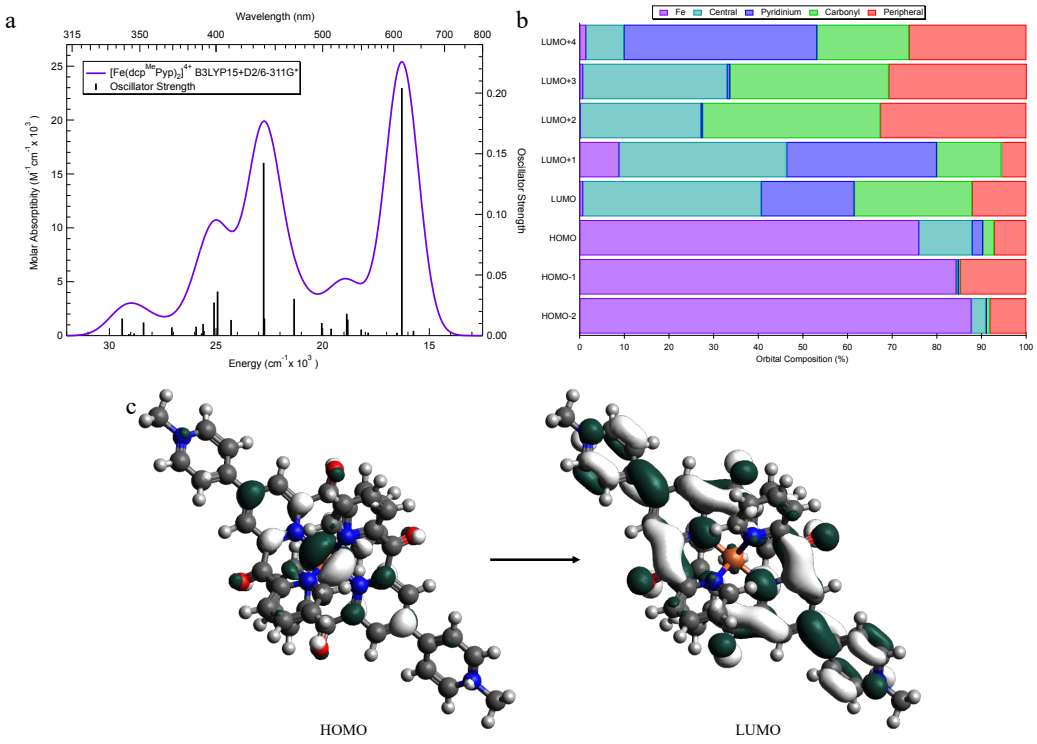

Figure 3.21. (a) Calculated spectrum (purple) and oscillator strength (black sticks) of $[Fe(^{Me}pyper)_2]^{4+}$ (b) Molecular orbital composition determined using AOMix (c) Molecular orbitals associated with the lowest energy transition with a slater coefficient corresponding to 100%.

3.4 Concluding Comments

In this work it has been shown that by functional tuning of B3LYP to incorporate 15% Hartree-Fock exact exchange we can successfully reproduce the experimental spectrum of $[Fe(dcpp)_2]^{2+}$ as well as its derivatives. This allowed for the deconvolution of the charge-transfer spectrum to facilitate the identification of the individual transitions present across the MLCT manifold using aromatic substitutions. Deconvolution of the aromatic substitutions shows a selective increase in the intensity of the lowest energy transition for $[Fe(dcpPhp)_2]^{2+}$ whereas $[Fe(dcPhpp)_2]^{2+}$ shows an increase in the higher energy portion of the manifold. We can correlate the selective increases to the localization of the molecular orbitals associated with the transitions using AOMix and fragmentation the complex.

The orbital compositions of this series in their excited states show minimal extension of the wavefunction into the aromatic groups. This is due to the electron-withdrawing nature of the carbonyl group at the heart of dcpp outcompeting any contributions the phenyl groups could afford. With this knowledge and the optimized functional for the modeling of this class of compounds, we set out to investigate the effects of electron-withdrawing substituents coupled with increased delocalization. This led to the exploration of three new complexes, each with a varying degree of electron-withdrawing ability. The first two complexes, $[Fe(dcpCNPhp)_2]^{2+}$ and $[Fe(pyper)_2]^{2+}$ exhibited similar behavior computationally as $[Fe(dcpPhp)_2]^{2+}$. But, upon alkylation of the pendant nitrogen the preferred behavior of delocalization was observed in the LUMOs of the system, as the positively charged pyridinium is now able to outcompete the carbonyl groups. There is ongoing work in our group in studying the ultrafast processes of these systems, i.e. measuring the MLCT and GSR lifetimes. Computational work also continues on $[Fe(pyper)_2]^{2+}$ as a new ligand motif

wherein the alkylation of the pyridinium could be further leveraged towards the extension of the MLCT lifetime.

REFERENCES

(1) Jamula, L. L.; Brown, A. M.; Guo, D.; McCusker, J. K. Synthesis and Characterization of a High-Symmetry Ferrous Polypyridyl Complex: Approaching the $^5T_2/^3T_1$ Crossing Point for Fe^{II}. *Inorg. Chem.* **2014**, *53* (1), 15–17. DOI: 10.1021/ic402407k.

(2) Brown, A. M. Excited-State Dynamics of Iron(II)-Based Charge-Transfer Chromophores. Ph.D., Michigan State University, East Lansing, 2011.

(3) Britz, A.; Gawelda, W.; Assefa, T. A.; Jamula, L. L.; Yarranton, J. T.; Galler, A.; Khakhulin, D.; Diez, M.; Harder, M.; Doumy, G.; March, A. M.; Bajnóczi, É.; Németh, Z.; Pápai, M.; Rozsályi, E.; Sárosiné Szemes, D.; Cho, H.; Mukherjee, S.; Liu, C.; Kim, T. K.; Schoenlein, R. W.; Southworth, S. H.; Young, L.; Jakubikova, E.; Huse, N.; Vankó, G.; Bressler, C.; McCusker, J. K. Using Ultrafast X-Ray Spectroscopy to Address Questions in Ligand-Field Theory: The Excited State Spin and Structure of $[Fe(dcpp)_2]^{2+}$. *Inorg. Chem.* **2019**, *58* (14), 9341–9350. DOI: 10.1021/acs.inorgchem.9b01063.

(4) Jamula, L. L. Exploring Design Strategies to Tune the Electronic Structure and Ultrafast Dynamics of Iron(II) Polypyridyl Chromophores. Ph. D., Michigan State University, East Lansing, 2013.

(5) Miller, J. N.; McCusker, J. K. Outer-Sphere Effects on Ligand-Field Excited-State Dynamics: Solvent Dependence of High-Spin to Low-Spin Conversion in $[Fe(Bpy)_3]^{2+}$. *Chem. Sci.* **2020**, *11* (20), 5191–5204. DOI: 10.1039/D0SC01506G.

(6) Carey, M. C. Achieving a Long-Lived Charge-Separated Fe(II) Chromophore: Insights into the Role of Reorganization Energy on the Ultrafast Photophysical Processes of d^6 Polypyridyl Complexes, Michigan State University, East Lansing, 2018.

(7) Majewski, M. B.; Tacconi, N. R. D.; MacDonnell, F. M.; Wolf, M. O. Ligand-Triplet-Fueled Long-Lived Charge Separation in Ruthenium(II) Complexes with Bithienyl-Functionalized Ligands. *Inorg. Chem.* **2011**, *50* (20), 9939–9941. DOI: 10.1021/IC201895Y.

(8) Mcclenaghan, N. D.; Leydet, Y.; Maubert, B.; Indelli, M. T.; Campagna, S. Excited-State Equilibration: A Process Leading to Long-Lived Metal-to-Ligand Charge Transfer Luminescence in Supramolecular Systems. *Coord. Chem. Rev.* **2005**, *249*, 1336–1350. DOI: 10.1016/j.ccr.2004.12.017.

(9) Morales, A. F.; Accorsi, G.; Armaroli, N.; Barigelletti, F.; Pope, S. J. A.; Ward, M. D. Interplay of Light Antenna and Excitation "Energy Reservoir" Effects in a Bichromophoric System Based on Ruthenium-Polypyridine and Pyrene Units Linked by a Long and Flexible Poly(Ethylene Glycol) Chain. *Inorg. Chem.* **2002**, *41* (25), 6711–6719. DOI: 10.1021/IC025811D.

(10) Monteiro, J. H. S. K.; Fetto, N. R.; Tucker, M. J.; De Bettencourt-Dias, A. Luminescent Carbazole-Based EuIII and YbIII Complexes with a High Two-Photon Absorption Cross-Section Enable Viscosity Sensing in the Visible and near IR with One- And Two-Photon Excitation. *Inorg. Chem.* **2020**, *59* (5), 3193–3199. DOI: 10.1021/acs.inorgchem.9b03561.

(11) Pietro, S. Di; Imbert, D.; Mazzanti, M. An Efficient Triazole-Pyridine-Bistetrazolate Platform for Highly Luminescent Lanthanide Complexes. *Chem. Comm.* **2014**, *50* (71), 10323–10326. DOI: 10.1039/C4CC04060K.

(12) Chouthaiwale, P. V.; Lapointe, S.; Tanaka, F. Synthesis of 4-Substituted-Pyridine-2,6-Dicarboxylic Acid Derivatives from Pyruvates and Aldehydes in One Pot. *Heterocycles* **2017**, *95* (1), 587–594. DOI: 10.3987/COM-16-S(S)27.

(13) Li, G.; Wolfe, A.; Brooks, J.; Zhu, Z.-Q.; Li, J. Modifying Emission Spectral Bandwidth of Phosphorescent Platinum(II) Complexes Through Synthetic Control. *Inorg. Chem*. **2017**, *56* (14), 8244–8256. DOI: 10.1021/acs.inorgchem.7b00961.

(14) Ohmura, T.; Morimasa, Y.; Suginome, M. Organocatalytic Diboration Involving "Reductive Addition" of a Boron–Boron σ-Bond to 4,4′-Bipyridine. *J. Am. Chem. Soc.* **2015**, *137* (8), 2852–2855. DOI: 10.1021/jacs.5b00546.

(15) Mengel, A. K. C.; Bissinger, C.; Dorn, M.; Back, O.; Förster, C.; Heinze, K. Boosting Vis/NIR Charge-Transfer Absorptions of Iron(II) Complexes by N-Alkylation and N-Deprotonation in the Ligand Backbone. *Chem. Euro. J.* **2017**, *23* (33), 7920–7931. DOI: 10.1002/chem.201700959.

(16) Belanger, D. B.; Siddiqui, M. A.; Curran, P. J.; Hamann, B.; Zhao, L.; Reddy, P. A. P.; Tadikonda, P. K.; Shipps, G. W. JR.; Mansoor, U. F. Novel JNK Inhibitors. US 2010/0179141 A1, 2010.

(17) Pucci, D.; Barberio, G.; Crispini, A.; Ghedini, M.; Francescangeli, O. Induction of Mesomorphism through Supramolecular Association in Coordination Pd (II) Compounds of Dialkyl 2,2′-Bipyridine-4,4′-Dicarboxylates. *Mol. Cryst. Liq. Cryst.* **2003**, *395* (1), 325–335. DOI: 10.1080/15421400390193864.

(18) Worl, L. A.; Duesing, R.; Chen, P.; Ciana, L. Della; Meyer, T. J. Photophysical Properties of Polypyridyl Carbonyl Complexes of Rhenium(I). *J. Chem. Soc., Dalton Trans.* **1991**, No. S, 849. DOI: 10.1039/dt9910000849.

(19) Sheldrick, G. M. SHELXT – Integrated Space-Group and Crystal-Structure Determination. *Acta Crystallogr. A.* **2015**, *71* (1), 3–8. DOI: 10.1107/S2053273314026370.

(20) Dolomanov, O. v.; Bourhis, L. J.; Gildea, R. J.; Howard, J. A. K.; Puschmann, H. OLEX2 : A Complete Structure Solution, Refinement and Analysis Program. *J. Appl. Crystallogr.* **2009**, *42* (2), 339–341. DOI: 10.1107/S0021889808042726.

(21) Sheldrick, G. M. Crystal Structure Refinement with SHELXL. *Acta. Crystallogr. C.* **2015**, *71* (1), 3–8. DOI: 10.1107/S2053229614024218.

(22) Frisch, M. J.; Trucks, G. W.; Schlegel, H. B.; Scuseria, G. E.; Robb, M. A.; Cheeseman, J. R.; Scalmani, G.; Barone, V.; Petersson, G. A.; Nakatsuji, H.; Li, X.; Caricato, M.; Marenich, A. V.; Bloino, J.; Janesko, B. G.; Gomperts, R.; Mennucci, B.; Hratchian, H. P.; Ortiz, J. V.; Izmaylov, A. F.; Sonnenberg. J. L.; Williams-Young, D.; Ding, F.; Lipparini, F.; Egidi, F.;

Goings, J.; Peng, B.; Petrone, A.; Henderson, T.; Ranasinghe, D.; Zakrzewski, G.; Gao, J.; Rega, N.; Zheng, G.; Liang, W.; Hada, M.; Ehara, M.; Toyota, K.; Fukada, R.; Hasegawa, J.; Ishida, M.; Nakajima, T.; Honda, Y.; Kitao, O.; Nakai, H.; Vreven, T.; Throssell, K.; Montgomery Jr., J. A.; Peralta, J. E.; Ogliaro, F.; Bearpark, M. J.; Heyd, J. J.; Brothers, E. N.; Kudin, K. N.; Staroverov., V. N.; Keith, T. A.; Kobayashi, R.; Normand, J.; Raghavachari, K.; Rendell, A. P.; Burant, J. C.; Iyengar, S. S.; Tomasi, .; Cossi, M.; Millam, J. M.; Klene, M.; Adamo, C.; Cammi, R.; Ochterski, J. W.; Martin, R. L.; Morokuma, K.; Farkas, O.; Foresman, J. B.; Fox, D. J. Gaussian 16, Rev B.01. Gaussian Inc.: Wallingford CT 2016.

(23) Becke, A. D. Density-Functional Exchange-Energy Approximation with Correct Asymptotic Behavior. *Phys. Rev. A* **1988**, *38*, 3098–3100.

(24) Reiher, M.; Salomon, O.; Hess, B. A. Reparameterization of Hybrid Functionals Based on Energy Differences of States of Different Multiplicity. *Theor. Chem. Acc.* **2001**, *107* (1), 48–55. DOI: 10.1007/s00214-001-0300-3.

(25) Grimme, S. Semiempirical GGA-Type Density Functional Constructed with a Long-Range Dispersion Correction. *J. Comput. Chem.* **2006**, *27* (15), 1787–1799. DOI: 10.1002/JCC.20495.

(26) Gorelsky, S. I. AOMix Program.

(27) Gorelsky, S. I.; Ghosh, S.; Solomon, E. I. Mechanism of N_2O Reduction by the μ_4-S Tetranuclear Cu_Z Cluster of Nitrous Oxide Reductase. *J. Am. Chem. Soc.* **2006**, *128* (1), 278–290. DOI: 10.1021/ja055856o.

(28) Avogadro: An Open-Source Molecular Builder and Visualization Tool. http://avogadro.cc/.

(29) Hanwell, M. D.; Curtis, D. E.; Lonie, D. C.; Vandermeersch, T.; Zurek, E.; Hutchison, G. R. Avogadro: An Advanced Semantic Chemical Editor, Visualization, and Analysis Platform. *J. Cheminform.* **2012**, *4* (1), 17. DOI: 10.1186/1758-2946-4-17.

(30) Blakemore, D. Suzuki-Miyaura Coupling. In *RSC Drug Discovery Series*; Royal Society of Chemistry, 2016; Vol. 2016-January, pp 1–69. DOI: 10.1039/9781782622086-00001.

(31) Fan, K.; Li, F.; Wang, L.; Daniel, Q.; Gabrielsson, E.; Sun, L. Pt-Free Tandem Molecular Photoelectrochemical Cells for Water Splitting Driven by Visible Light. *Phys. Chem. Chem. Phys.* **2014**, *16* (46), 25234–25240. DOI: 10.1039/c4cp04489d.

(32) Duan, X.-F.; Li, X.-H.; Li, F.-Y.; Huang, C.-H. A Concise Synthesis of 2,4-Disubstituted Pyridines: A Convenient Synthesis of 2-Bromo-4-Iodopyridine via Halogen Dance and Its Successive One-Pot Disubstitutions. *Synthesis* **2004**, 16, 2614–2616. DOI: 10.1055/s-2004-831259.

(33) Krasovskiy, A.; Knochel, P. A LiCl-Mediated Br/Mg Exchange Reaction for the Preparation of Functionalized Aryl- and Heteroarylmagnesium Compounds from Organic Bromides. *Angew. Chem. Int. Ed.* **2004**, *43* (25), 3333–3336. DOI: 10.1002/anie.200454084.

(34) Bowman, D. N.; Bondarev, A.; Mukherjee, S.; Jakubikova, E. Tuning the Electronic Structure of Fe(II) Polypyridines via Donor Atom and Ligand Scaffold Modifications: A Computational Study. *Inorg. Chem.* **2015**, *54* (17), 8786–8793. DOI: 10.1021/acs.inorgchem.5b01409.

(35) Zimmer, P.; Burkhardt, L.; Friedrich, A.; Steube, J.; Neuba, A.; Schepper, R.; Müller, P.; Flörke, U.; Huber, M.; Lochbrunner, S.; Bauer, M. The Connection between NHC Ligand Count and Photophysical Properties in Fe(II) Photosensitizers: An Experimental Study. *Inorg. Chem.* **2018**, *57* (1), 360–373. DOI: 10.1021/acs.inorgchem.7b02624.

(36) Ganzenmüller, G.; Berkaïne, N.; Fouqueau, A.; Casida, M. E.; Reiher, M. Comparison of Density Functionals for Differences between the High-($^5T_{2g}$) and Low-($^1A_{1g}$) Spin States of Iron(II) Compounds. IV. Results for the Ferrous Complexes [Fe(L)('NHS_4')]. *Journal of Chemical Physics* **2005**, *122* (23), 37. DOI: 10.1063/1.1927081.

(37) Reiher, M. Theoretical Study of the $Fe(Phen)_2(NCS)_2$ Spin-Crossover Complex with Reparametrized Density Functionals. *Inorg. Chem.* **2002**, *41* (25), 6928–6935. DOI: 10.1021/IC025891L.

(38) Droghetti, A.; Alfè, D.; Sanvito, S. Assessment of Density Functional Theory for Iron(II) Molecules across the Spin-Crossover Transition. *J. Chem. Phys.* **2012**, *137* (12), 124303. DOI: 10.1063/1.4752411/190854.

(39) Curtin, G. M.; Jakubikova, E. Extended π-Conjugated Ligands Tune Excited-State Energies of Iron(II) Polypyridine Dyes. *Inorg. Chem.* **2022**, *61* (47), 18850–18860. DOI: 10.1021/acs.inorgchem.2c02362.

(40) Damrauer, N. H.; McCusker, J. K. Ultrafast Dynamics in the Metal-to-Ligand Charge Transfer Excited-State Evolution of $[Ru(4,4'\text{-Diphenyl-}2,2'\text{-Bipyridine})_3]^{2+}$. *J. Phys. Chem. A* **1999**, *103* (42), 8440–8446. DOI: 10.1021/jp9927754.

(41) Campagna, S.; Puntoriero, F.; Nastasi, F.; Bergamini, G.; Balzani, V. Photochemistry and Photophysics of Coordination Compounds: Ruthenium. In *Photochemistry and Photophysics of Coordination Compounds I*; Springer Berlin Heidelberg: Berlin, Heidelberg, 2007; Vol. 280, pp 117–214. DOI: 10.1007/128_2007_133.

(42) Juris, A.; Balzani, V.; Barigelletti, F.; Campagna, S.; Belser, P.; von Zelewsky, A. Ru(II) Polypyridine Complexes: Photophysics, Photochemistry, Electrochemistry, and Chemiluminescence. *Coord. Chem. Rev.* **1988**, *84*, 85–277. DOI: 10.1016/0010-8545(88)80032-8.

(43) Fang, Y.-Q.; Taylor, N. J.; Laverdière, F.; Hanan, G. S.; Loiseau, F.; Nastasi, F.; Campagna, S.; Nierengarten, H.; Leize-Wagner, E.; Van Dorsselaer, A. Ruthenium(II) Complexes with Improved Photophysical Properties Based on Planar 4′-(2-Pyrimidinyl)-2,2′:6′,2″-Terpyridine Ligands. *Inorg. Chem.* **2007**, *46* (7), 2854–2863. DOI: 10.1021/ic0622609.

(44) McCusker, C. E.; McCusker, J. K. Synthesis and Spectroscopic Characterization of CN-Substituted Bipyridyl Complexes of Ru(II). *Inorg. Chem.* **2011**, *50* (5), 1656–1669. DOI: 10.1021/ic102085b.

(45) Brown, A. M.; McCusker, C. E.; Carey, M. C.; Blanco-Rodríguez, A. M.; Towrie, M.; Clark, I. P.; Vlček, A.; McCusker, J. K. Vibrational Relaxation and Redistribution Dynamics in Ruthenium(II) Polypyridyl-Based Charge-Transfer Excited States: A Combined Ultrafast Electronic and Infrared Absorption Study. *J. Phys. Chem. A* **2018**, *122* (40), 7941–7953. DOI: 10.1021/acs.jpca.8b06197.

(46) Maestri, M.; Armaroli, N.; Balzani, V.; Constable, E. C.; Thompson, A. M. W. C. Complexes of the Ruthenium(II)-2,2′:6′,2″-Terpyridine Family. Effect of Electron-Accepting and -Donating Substituents on the Photophysical and Electrochemical Properties. *Inorg. Chem.* **1995**, *34* (10), 2759–2767. DOI: 10.1021/ic00114a039.

(47) Sun, S.-S.; Silva, A. S.; Brinn, I. M.; Lees, A. J. Self-Assembly Molecular Squares with Metal Complexes as Bridging Ligands. *J. Chem. Soc., Chem. Commun.* **1992**, *31* (5), 1649. DOI: 10.1021/ic991226+.

(48) Constable, E. C.; Thompson, A. M. W. C. Pendant-Functionalised Ligands for Metallosupramolecular Assemblies; Ruthenium(II) and Osmium(II) Complexes of 4′-(4-Pyridy1)-2,2′ :6′,2″-Terpyridine. *J. Chem. Soc., Dalton Trans.* **1994**, *9*, 1409–1418. DOI: 10.1039/DT9940001409.

(49) Constable, E. C.; Thompson, A. M. W. C. Ligand Reactivity in Iron(II) Complexes of 4′-(4‴-Pyridyl)-2,2′ :6′,2″-Terpyridine. *J. Chem. Soc., Dalton Trans.* **1992**, *20*, 2947–2950. DOI: 10.1039/DT9920002947.

(50) Constable, E. C.; Dunphy, E. L.; Housecroft, C. E.; Kylberg, W.; Neuburger, M.; Schaffner, S.; Schofield, E. R.; Smith, C. B. Structural Development of Free or Coordinated 4′-(4-Pyridyl)-2, 2′:6′,2′-Terpyridine Ligands through N-Alkylation: New Strategies for Metallamacrocycle Formation. *Chem. Euro. J.* **2006**, *12* (17), 4600–4610. DOI: 10.1002/chem.200600069.

APPENDIX

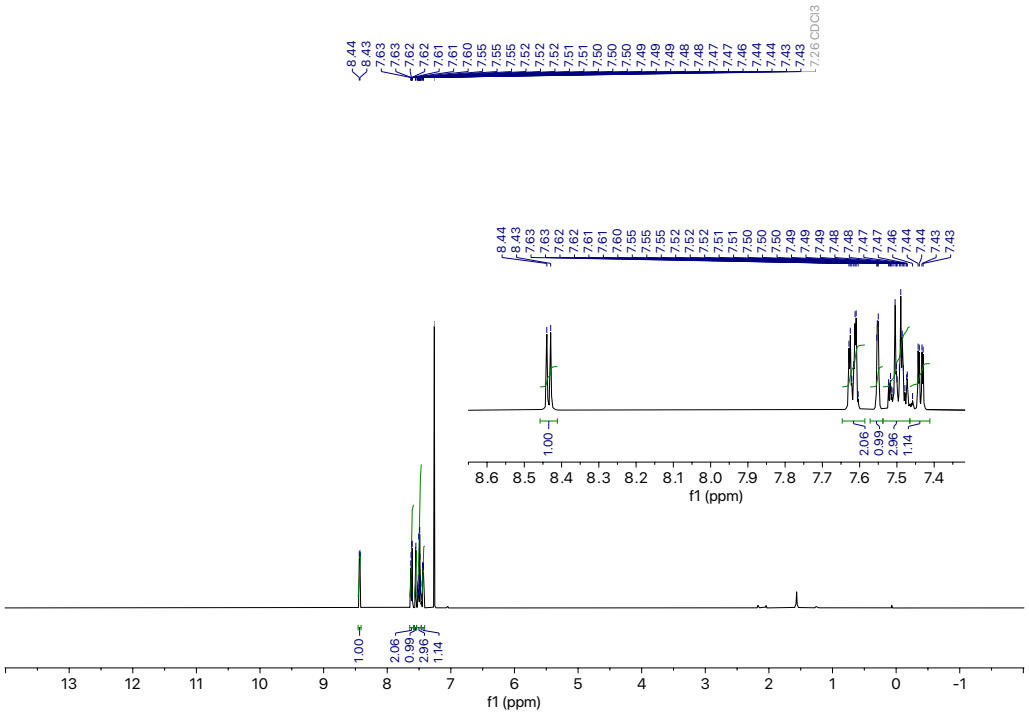

Figure 3.22. ^{1}H NMR of 2-chloro-4-phenylpyridine in $CDCl_3$. Inset is a zoom in of the aromatic region.

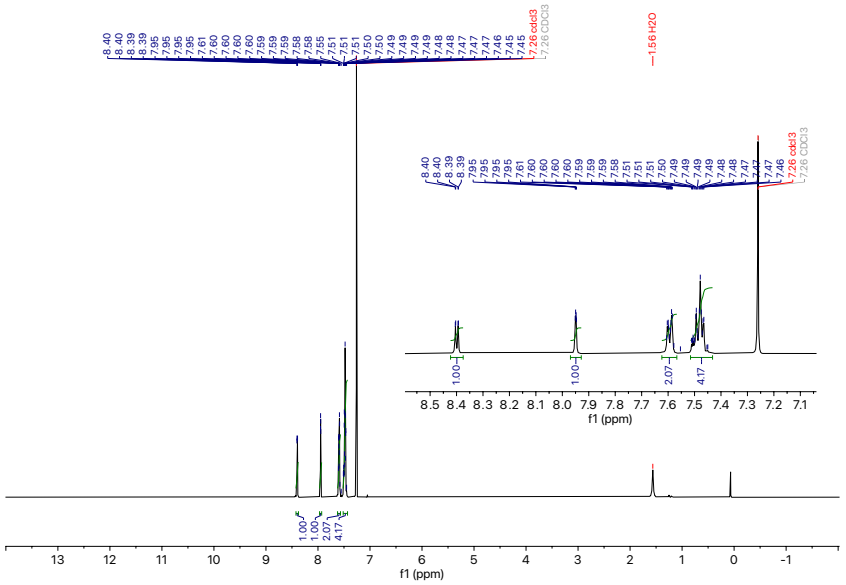

Figure 3.23. ^{1}H NMR of 2-iodo-4-phenylpyridine in $CDCl_3$. Inset is a zoom in of the aromatic region.

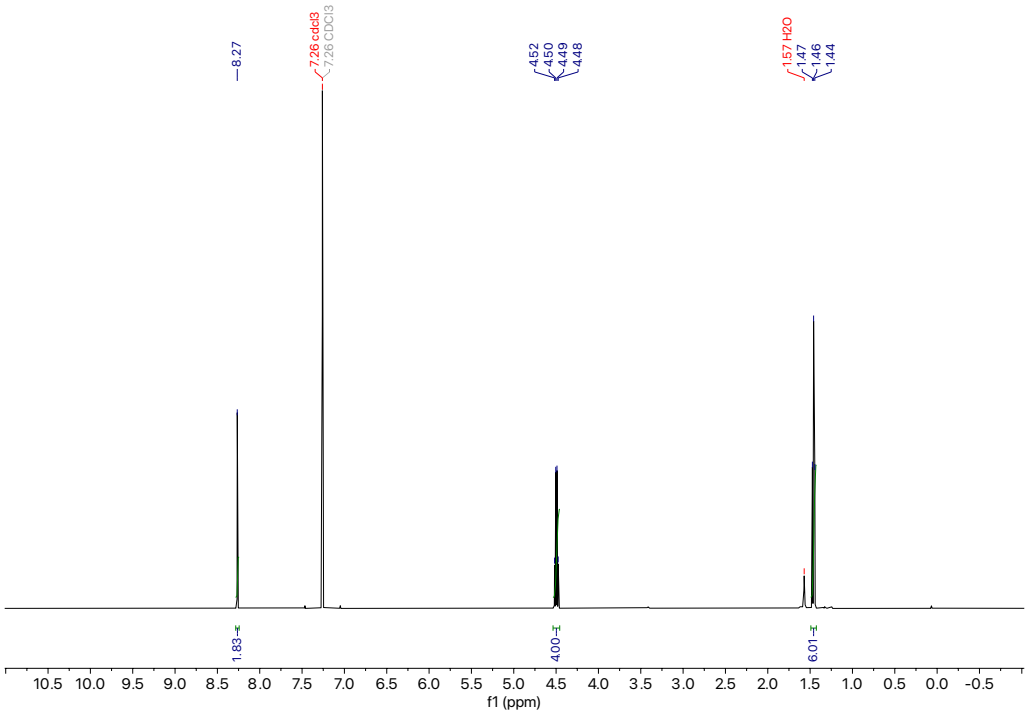

Figure 3.24. ^{1}H NMR of diethyl 4-chloro-2,6-pyridine dicarboxylate in $CDCl_3$.

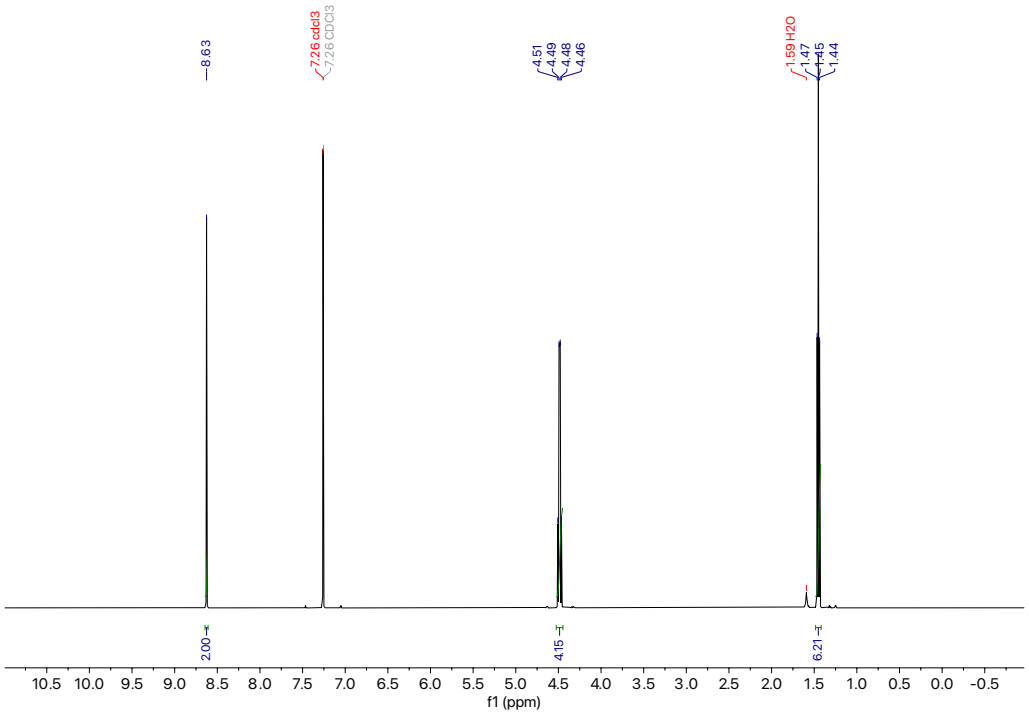

Figure 3.25. 1H NMR of diethyl 4-iodo-2,6-pyridine dicarboxylate in $CDCl_3$.

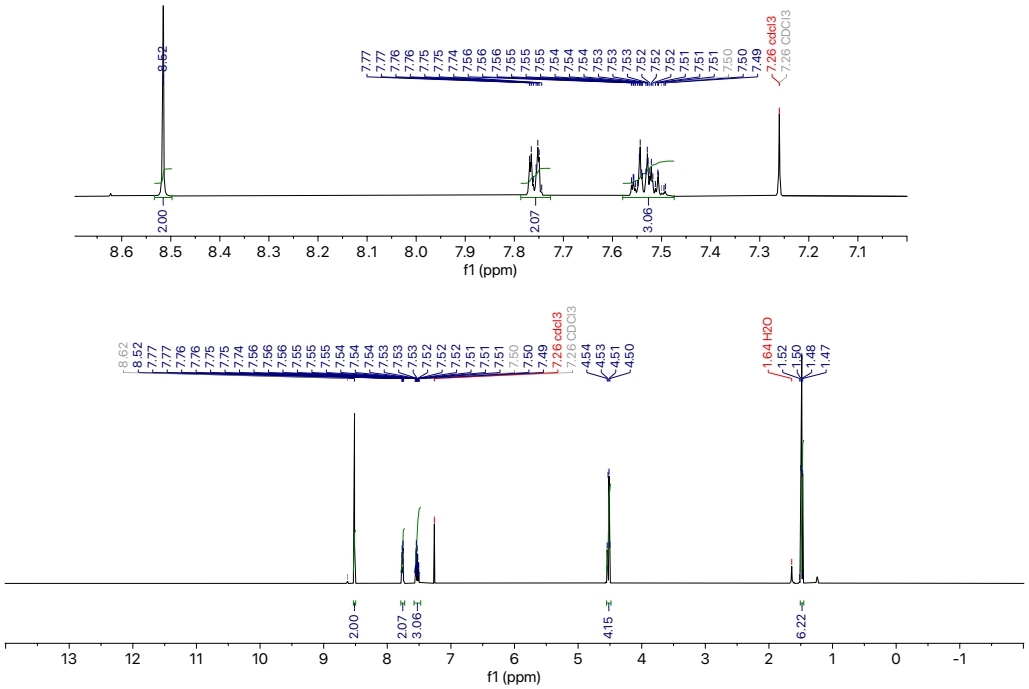

Figure 3.26. ^{1}H NMR of diethyl 4-phenyl-2,6-pyridine dicarboxylate in $CDCl_3$. Inset is an expansion of the aromatic region.

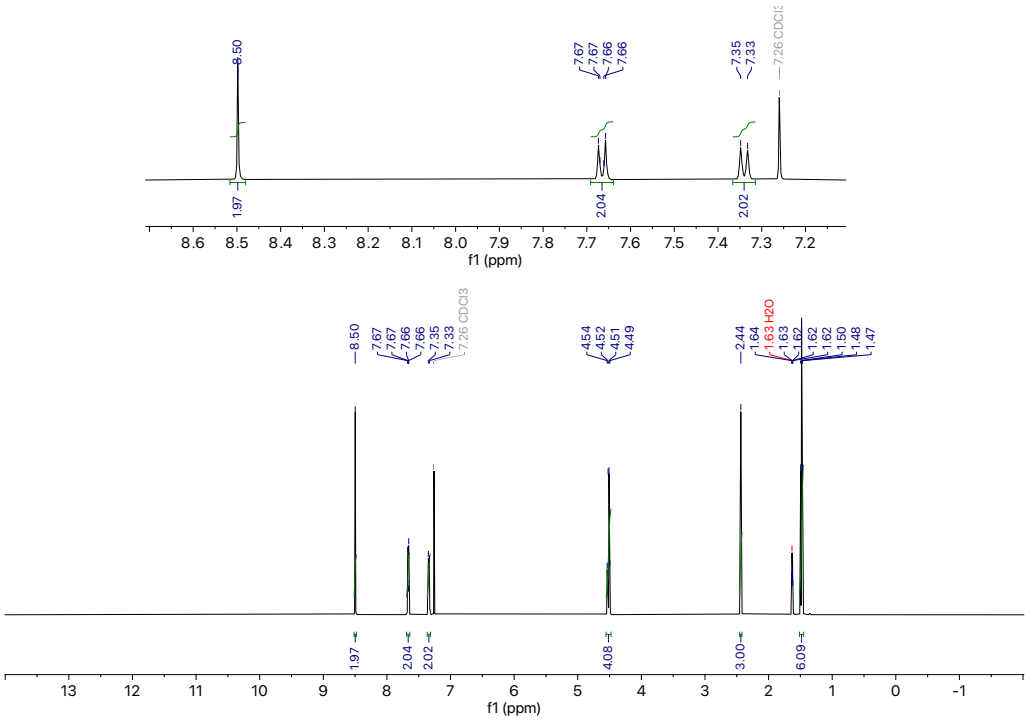

Figure 3.27. ^{1}H NMR of diethyl 4-(*p*-tolyl)-2,6-pyridine dicarboxylate in $CDCl_3$. Inset is an expansion of the aromatic region.

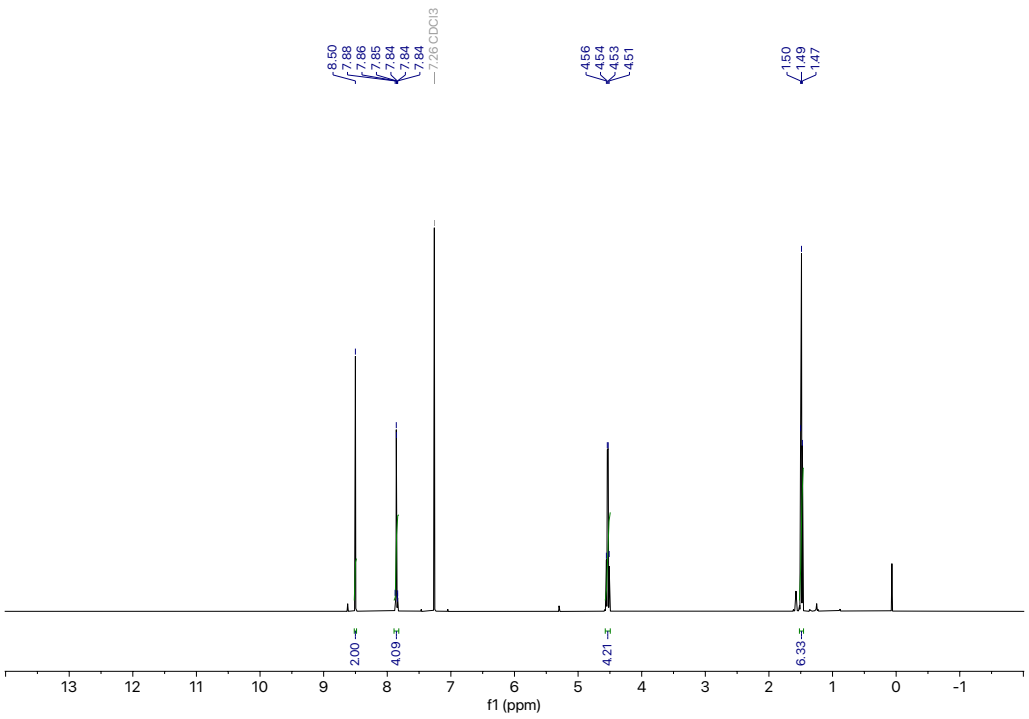

Figure 3.28. ^{1}H NMR of diethyl 4-(4-cyanophenyl)-2,6-pyridine dicarboxylate in $CDCl_3$.

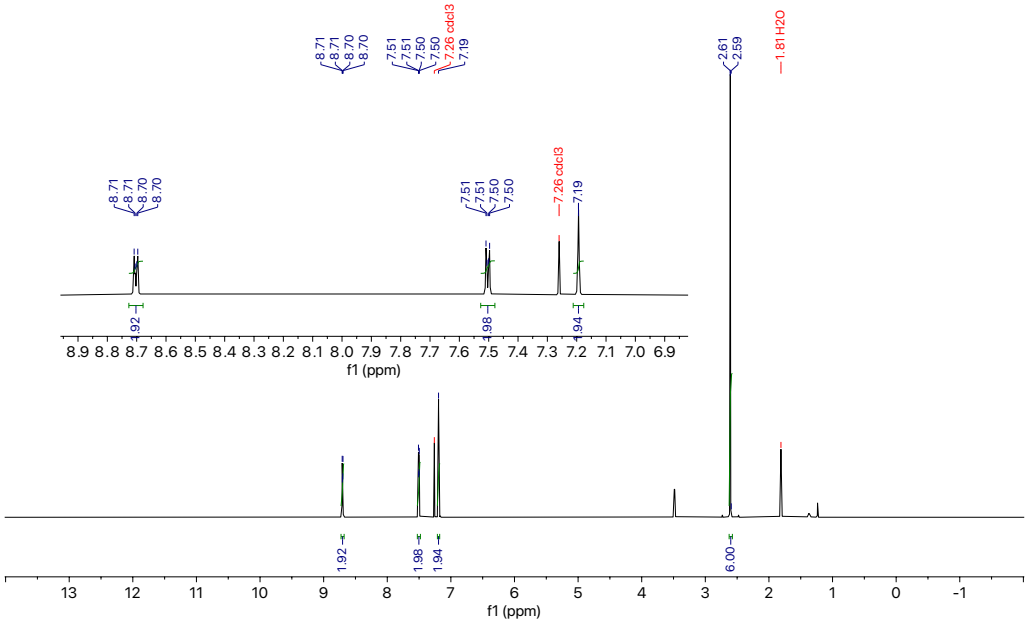

Figure 3.29. ^{1}H NMR of 2,6-dimethyl-4,4′-bipyridine in $CDCl_3$. Inset is an expansion of the aromatic region.

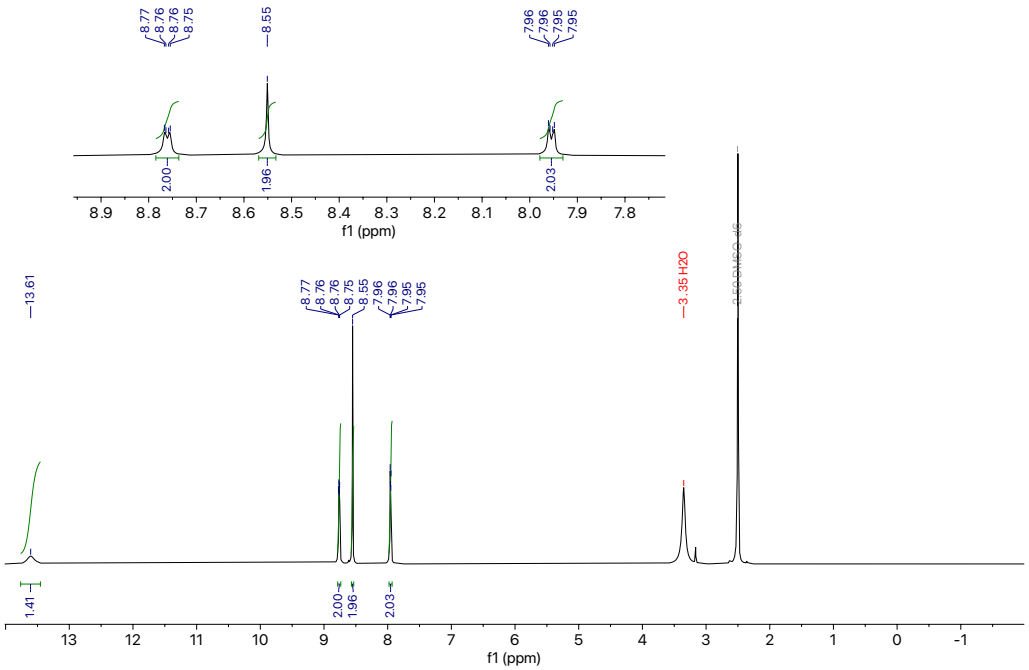

Figure 3.30. ^{1}H NMR of 4,4′-bipyridine-2,6-dicarboxylic acid in DMSO-d_6.

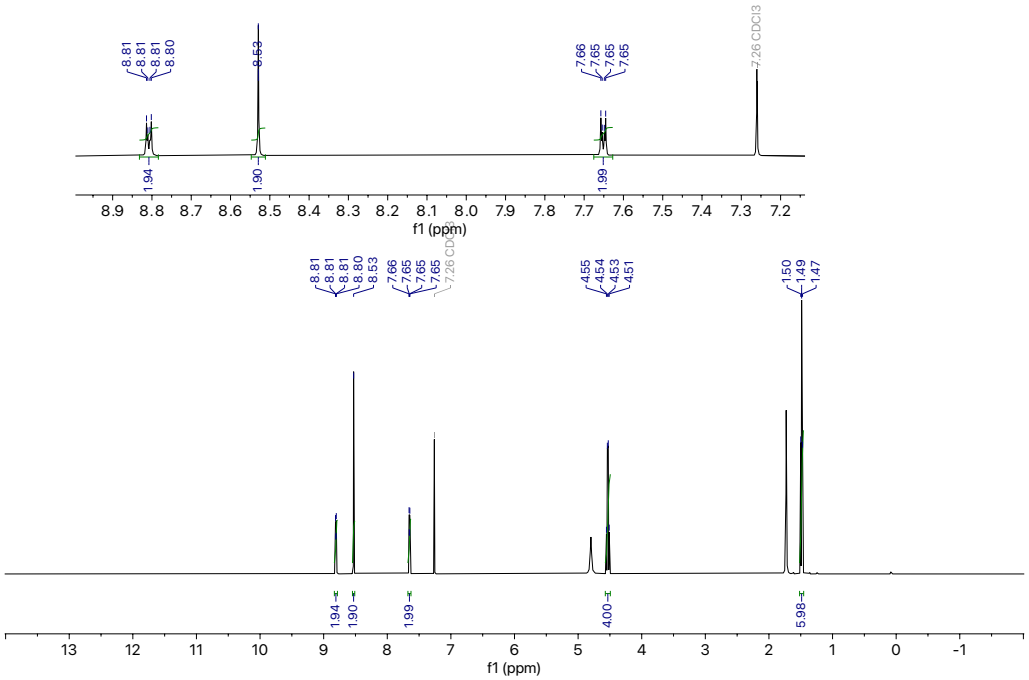

Figure 3.31. ^{1}H NMR of diethyl 4,4′-bipyridine-2,6-dicaroxylate in $CDCl_3$. Inset is an expansion of the aromatic region.

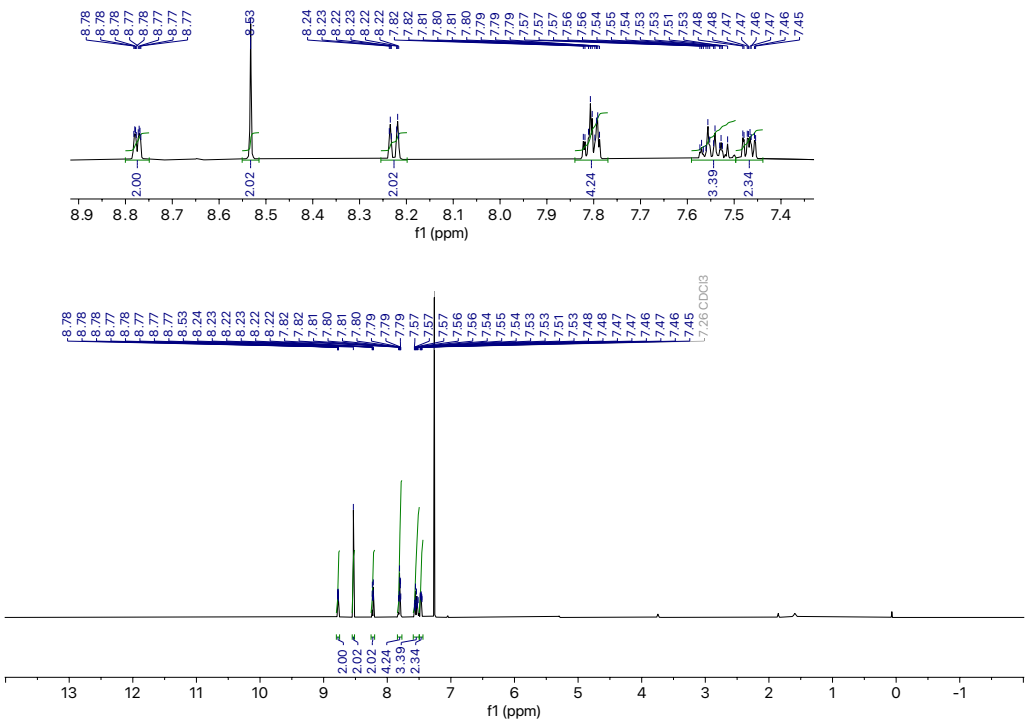

Figure 3.32. ^{1}H NMR of dcpPhp in $CDCl_3$. Inset is an expansion of the aromatic region.

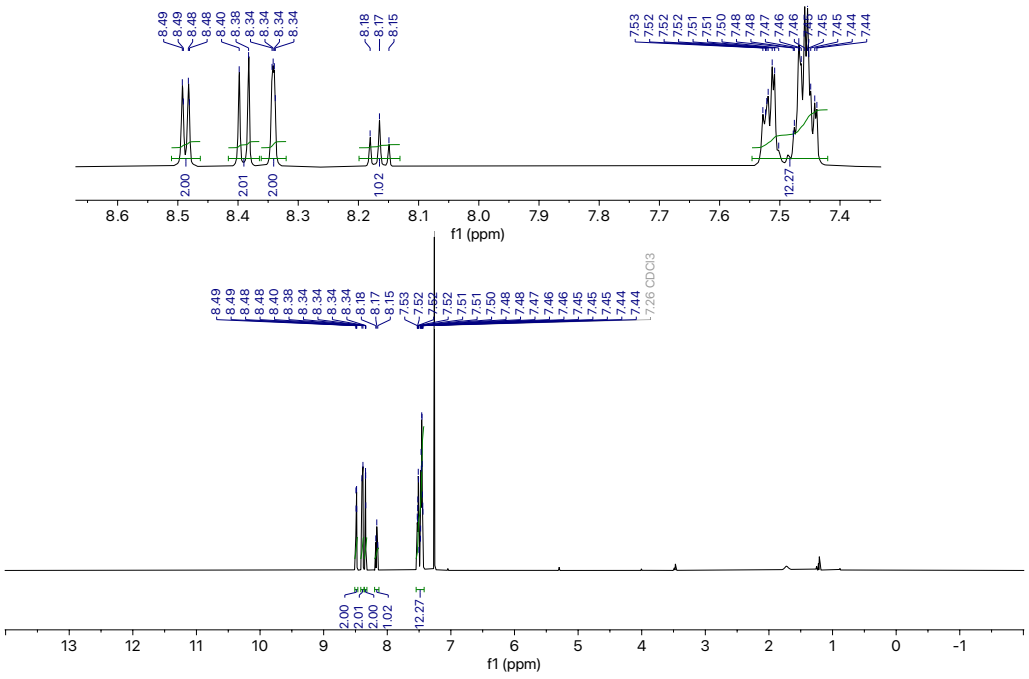

Figure 3.33. ^{1}H NMR of dcPhpp in $CDCl_3$. Inset is an expansion of the aromatic region.

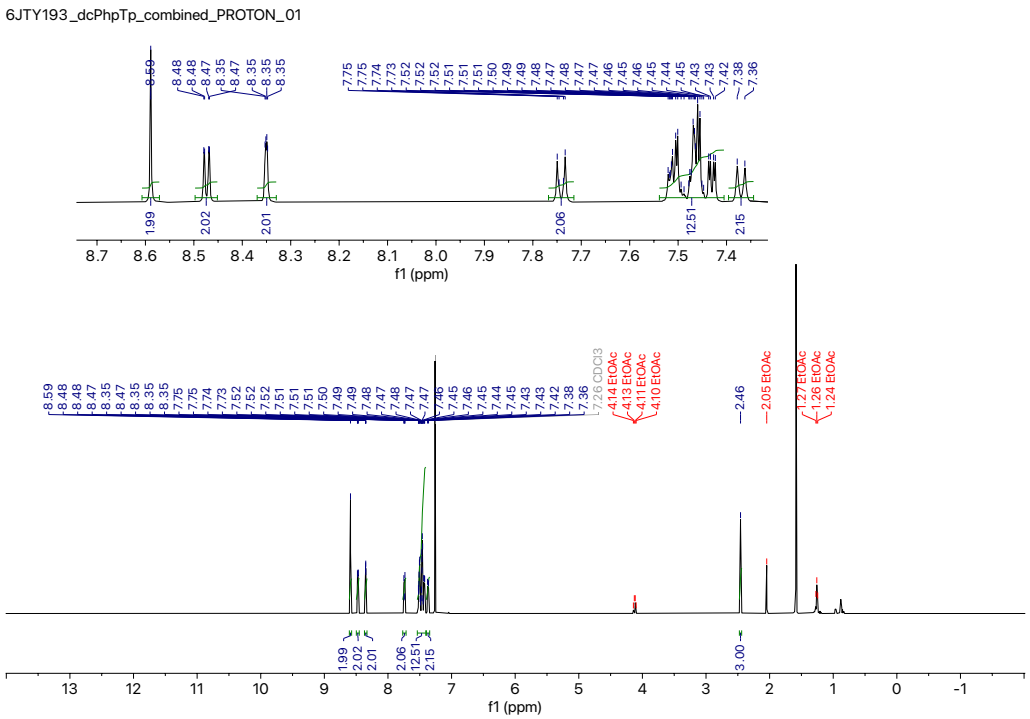

Figure 3.34. ^{1}H NMR of dcPhpTp in $CDCl_3$. Inset is an expansion of the aromatic region.

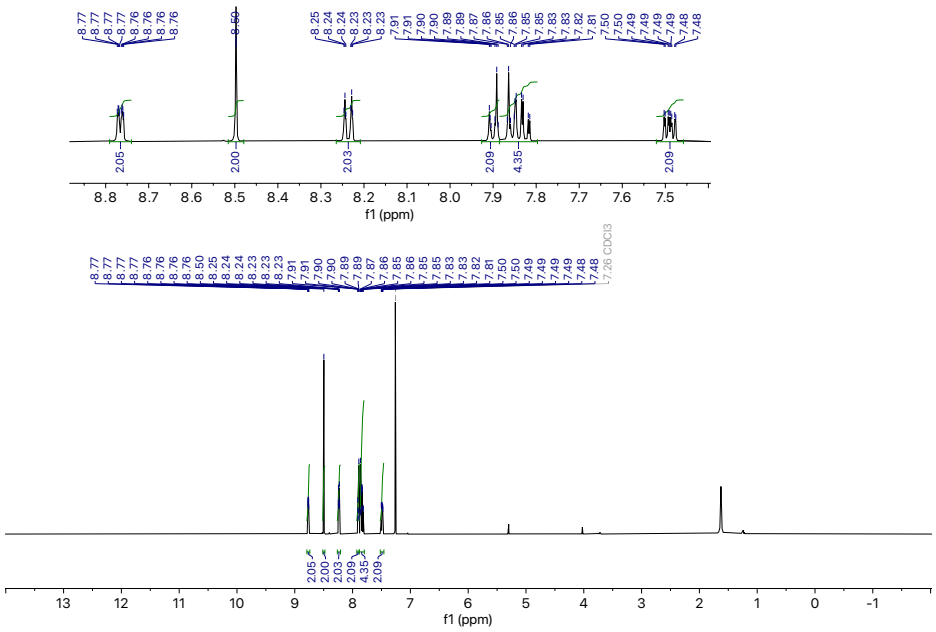

Figure 3.35. ^{1}H NMR of dcpCNPhp in $CDCl_3$. Inset is an expansion of the aromatic region.

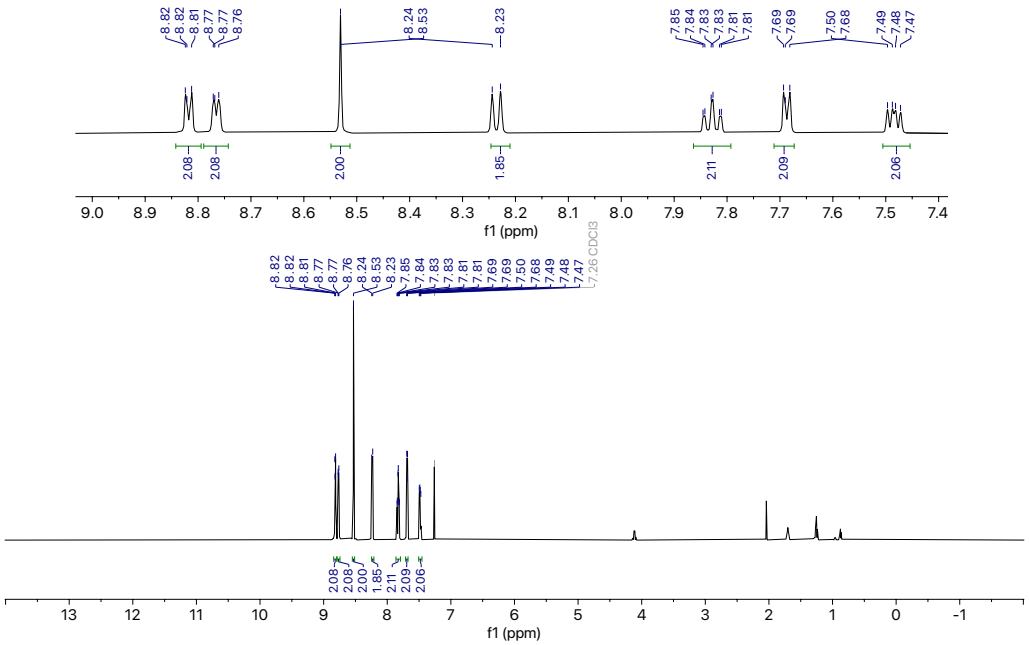

Figure 3.36. ^{1}H NMR of pyper in $CDCl_3$. Inset is an expansion of the aromatic region.

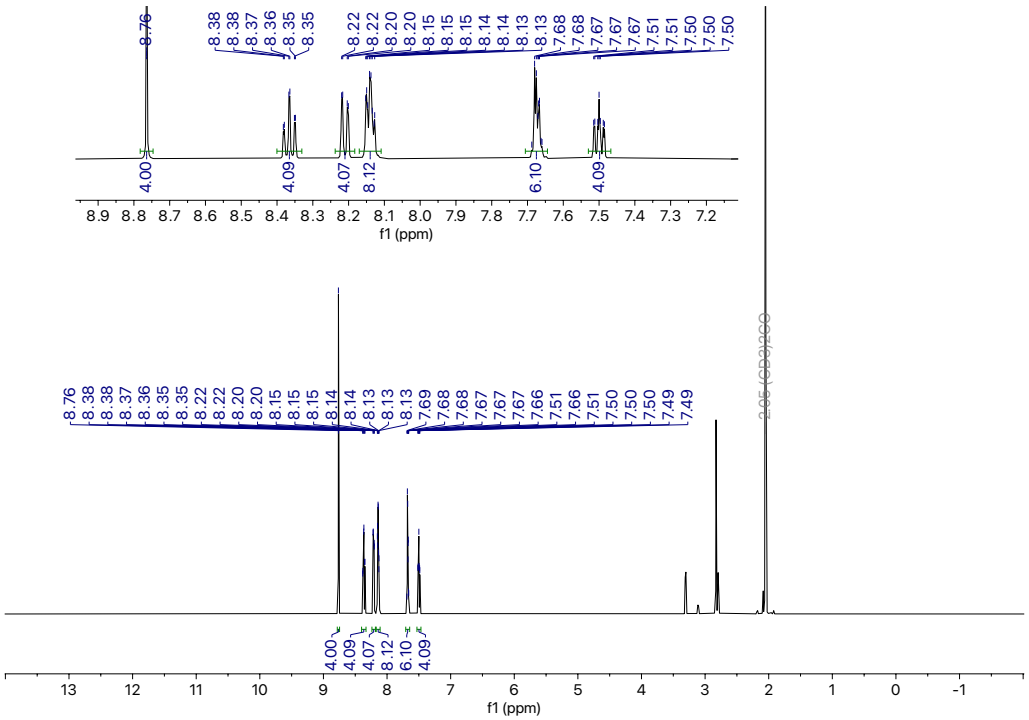

Figure 3.37. ^{1}H NMR of $[Fe(dcpPhp)_2](PF_6)_2$ in acetone-d_6. Inset is an expansion of the aromatic region.

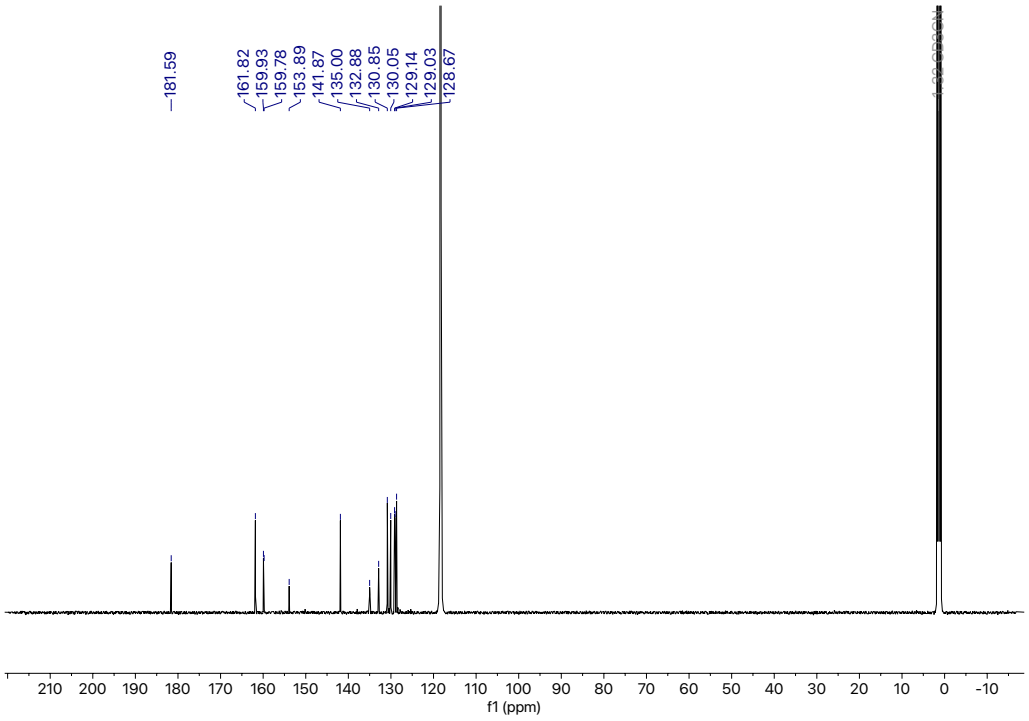

Figure 3.38. ^{13}C NMR of $[Fe(dcpPhp)_2](PF_6)_2$ in CD_3CN.

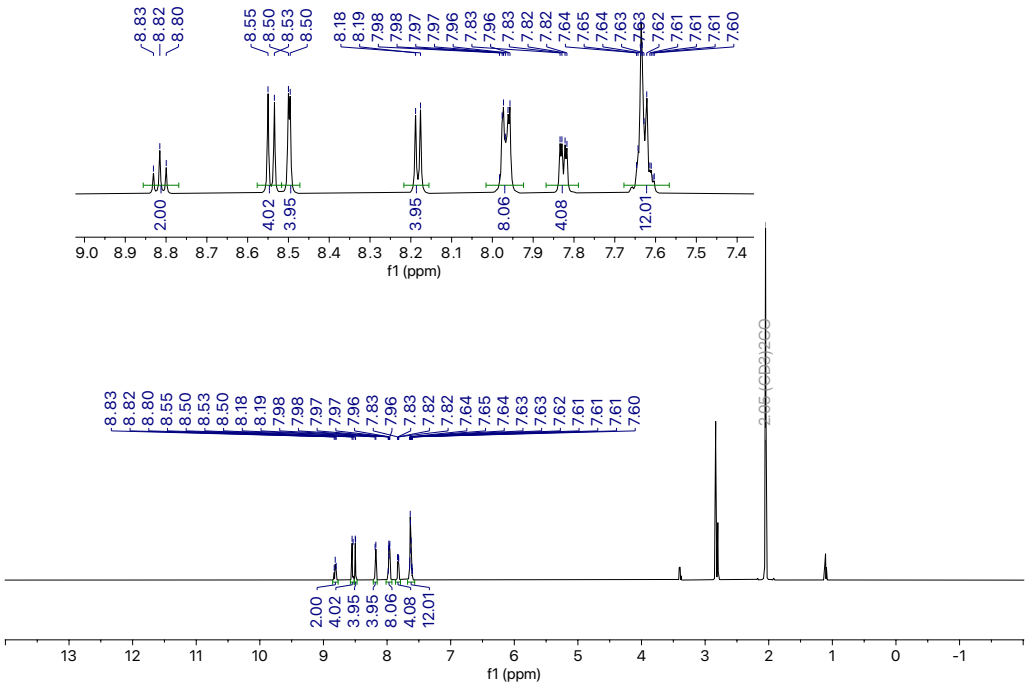

Figure 3.39. ^{1}H NMR of $[Fe(dcPhpp)_2](PF_6)_2$ in acetone-d_6. Inset is an expansion of the aromatic region.

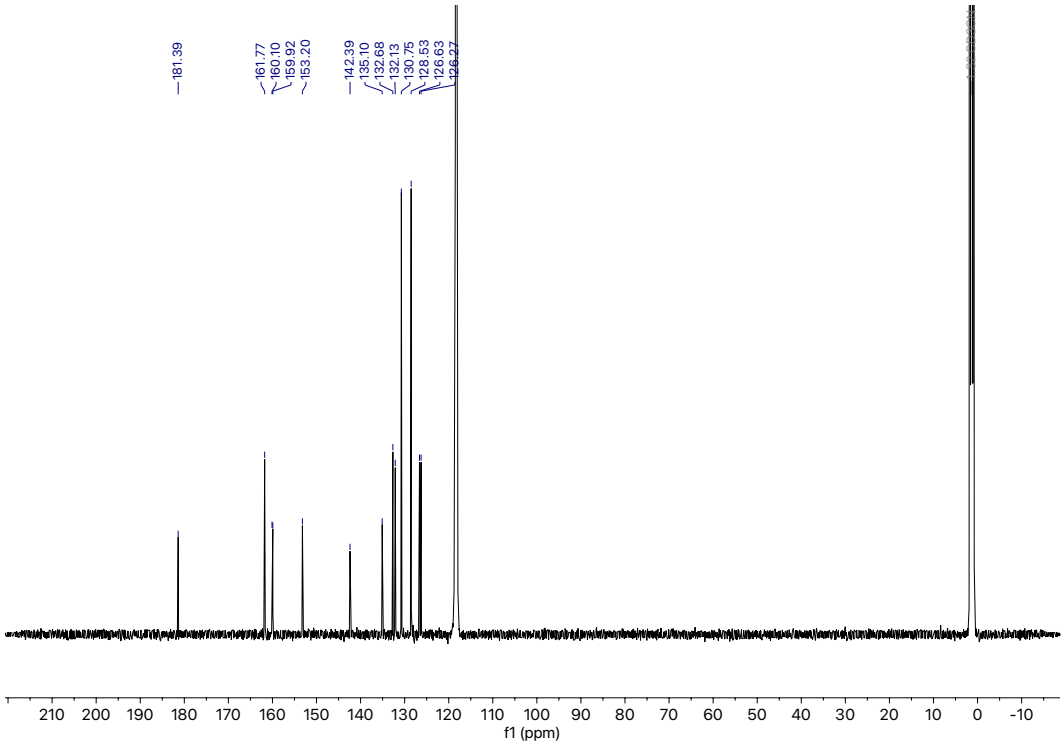

Figure 3.40. ^{13}C NMR of $[Fe(dcPhpp)_2](PF_6)_2$ in CD_3CN.

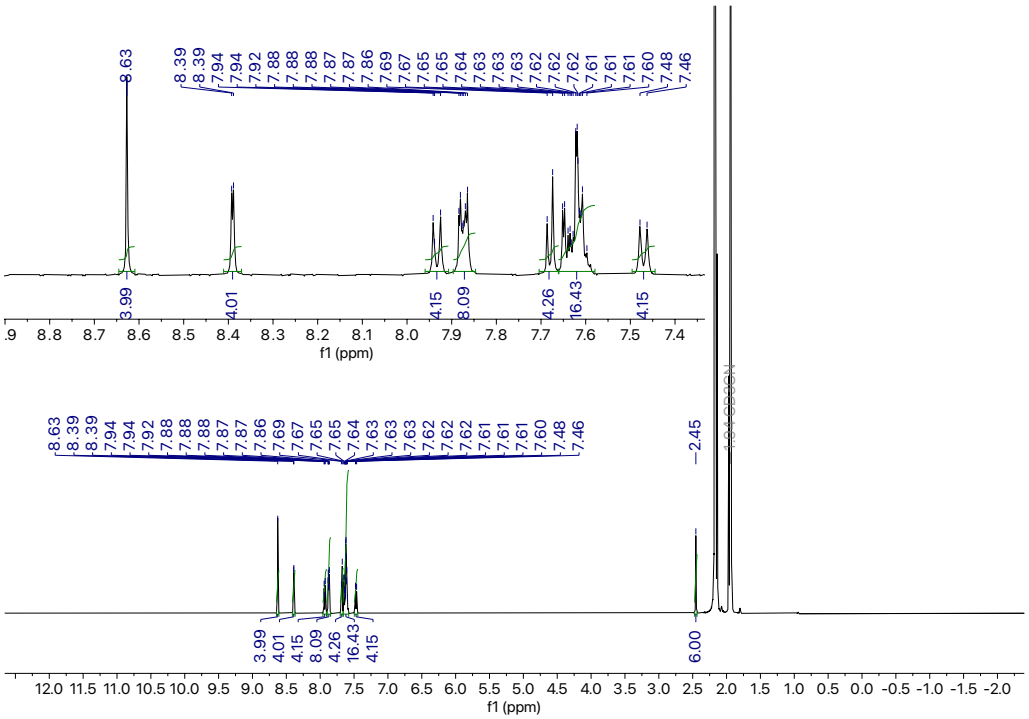

Figure 3.41. ^{1}H NMR of $[Fe(dcPhpTp)_2](PF_6)_2$ in CD_3CN. Inset is an expansion of the aromatic region.

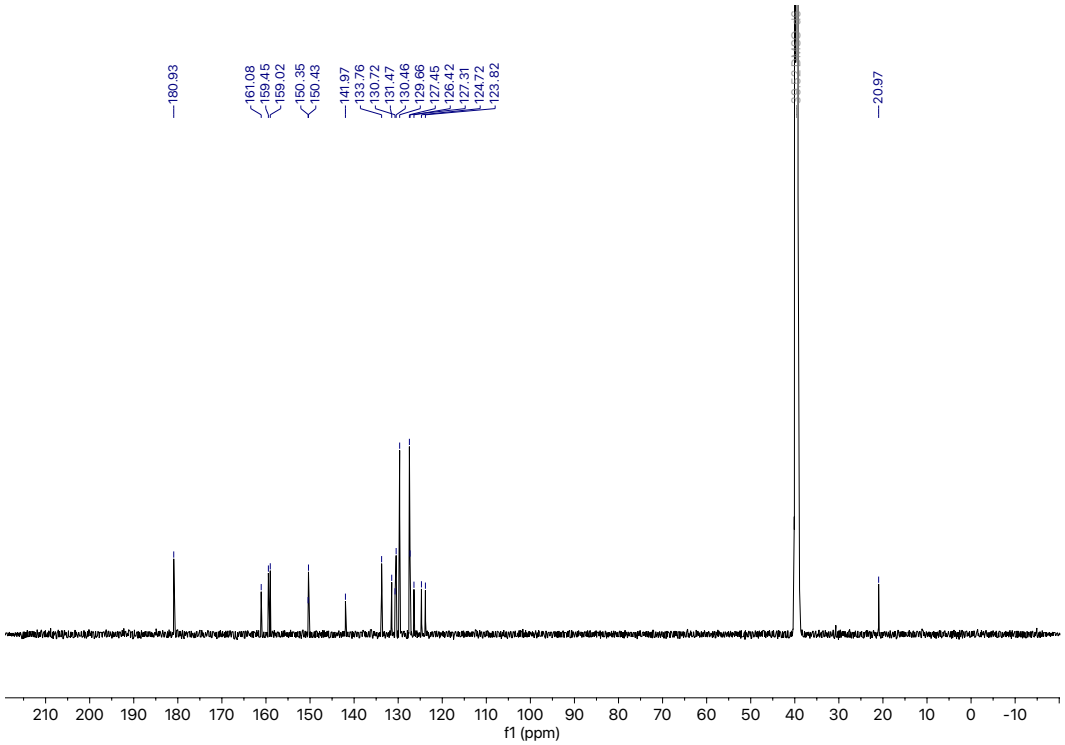

Figure 3.42. ^{13}C NMR of $[Fe(dcPhpTp)_2](PF_6)_2$ in DMSO-d_6.

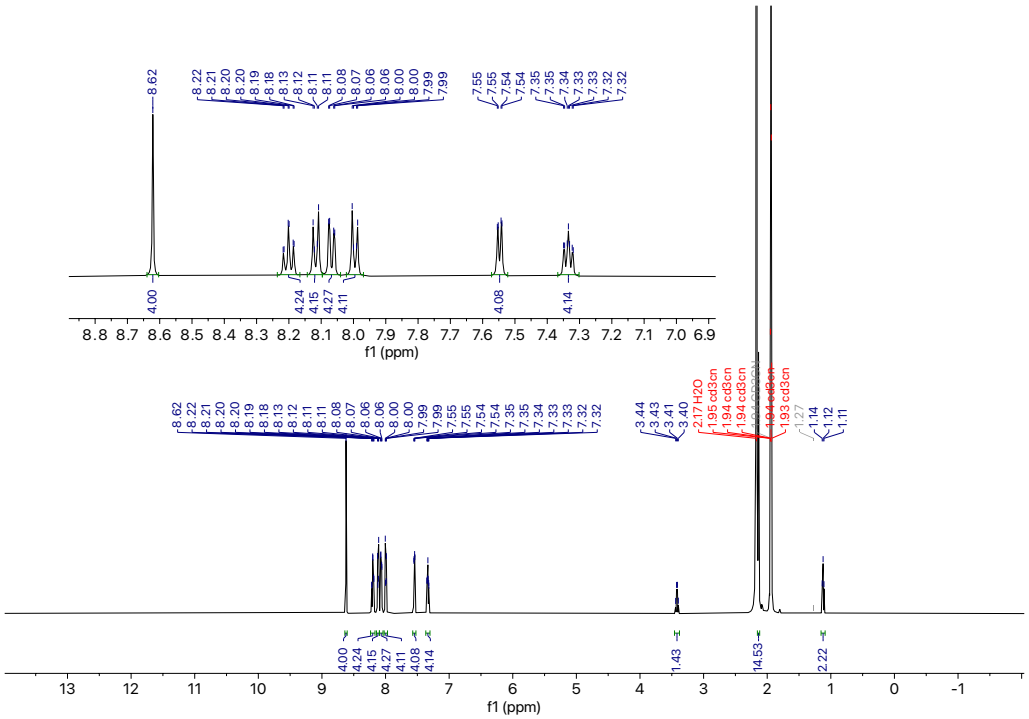

Figure 3.43. ^{1}H NMR of $[Fe(dcpCNPhp)_2](PF_6)_2$ in CD_3CN. Inset is an expansion of the aromatic region.

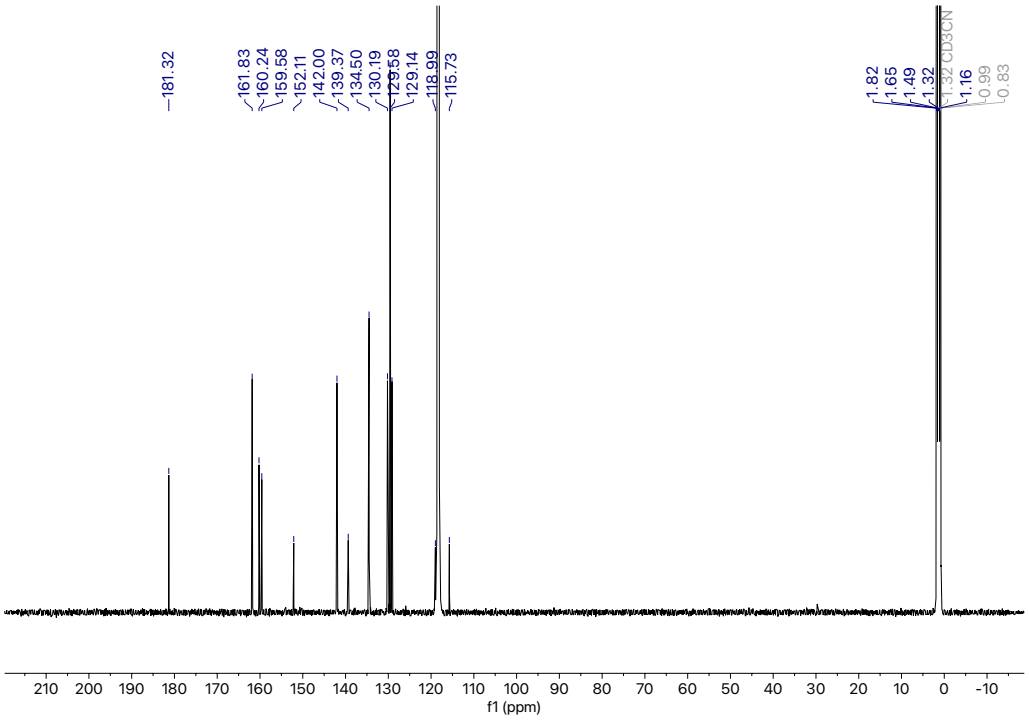

Figure 3.44. ^{13}C NMR of $[Fe(dcpCNPhp)_2](PF_6)_2$ in CD_3CN.

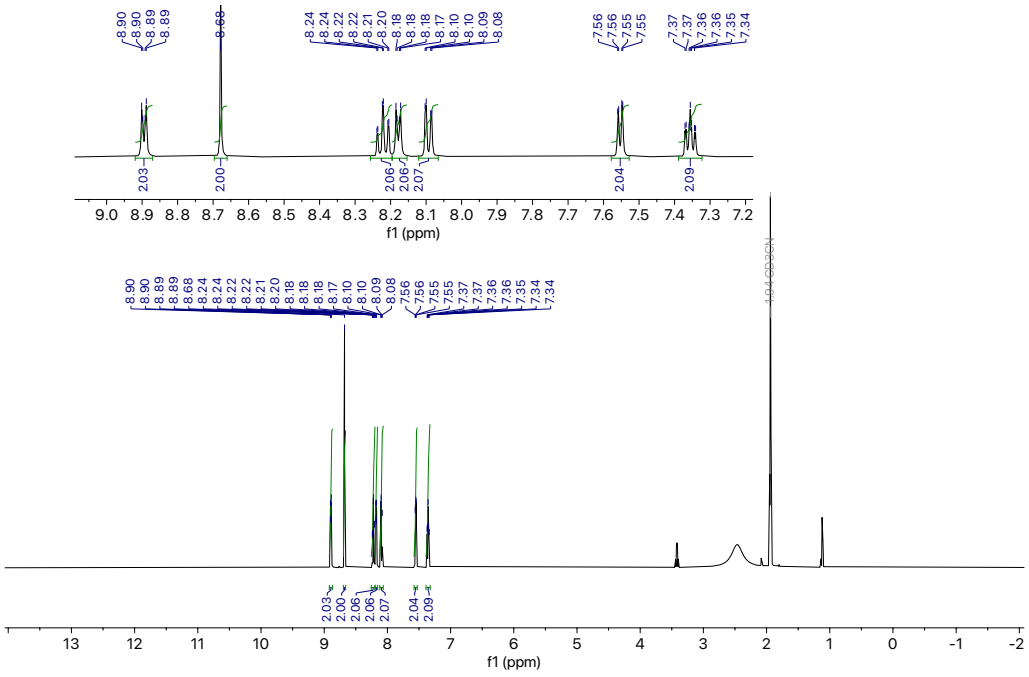

Figure 3.45. ^{1}H NMR of $[Fe(pyper)_2](PF_6)_2$ in CD_3CN. Inset is an expansion of the aromatic region.

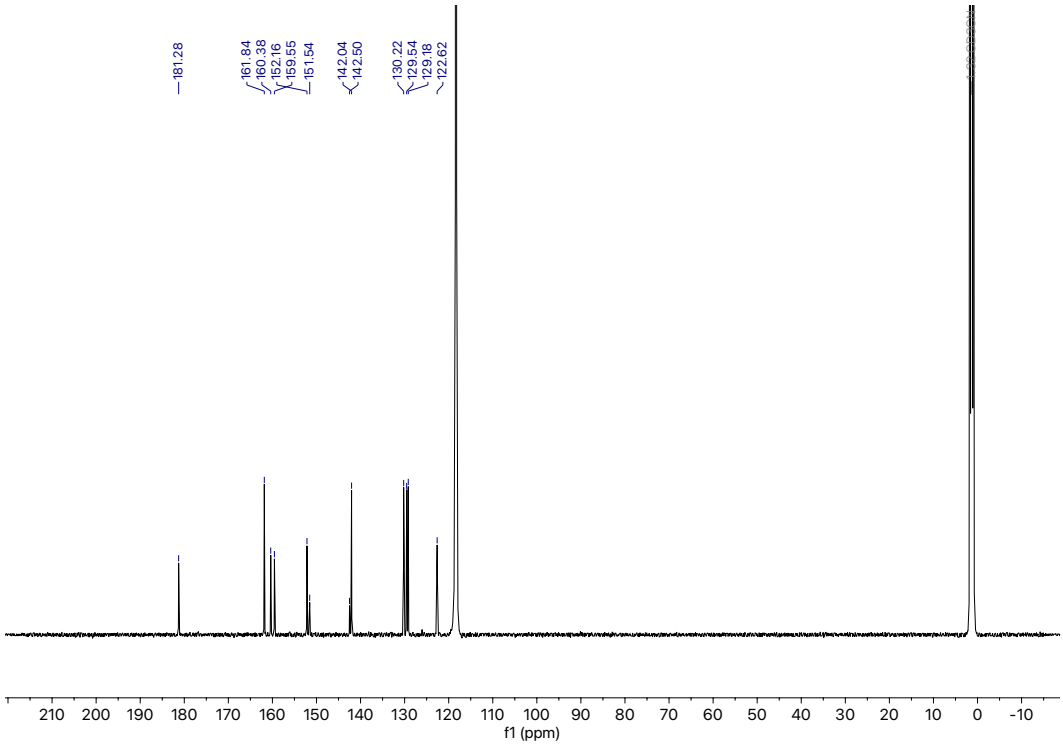

Figure 3.46. ^{13}C NMR of $[Fe(pyper)_2](PF_6)_2$ in CD_3CN.

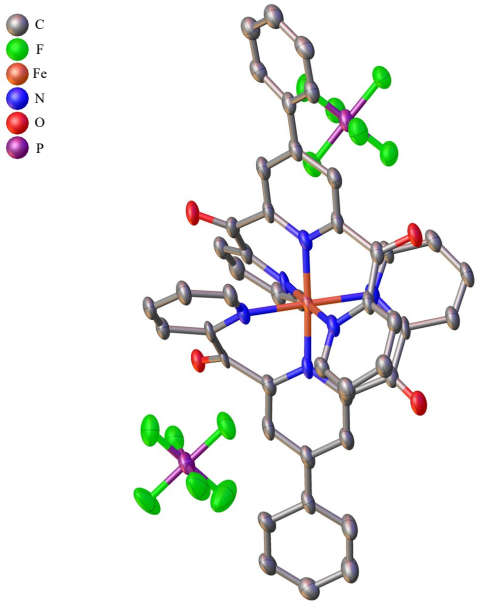

Figure 3.47. X-ray crystal structure of $[Fe(dcpPhp)_2](PF_6)_2$ with solvent and hydrogens removed for clarity.

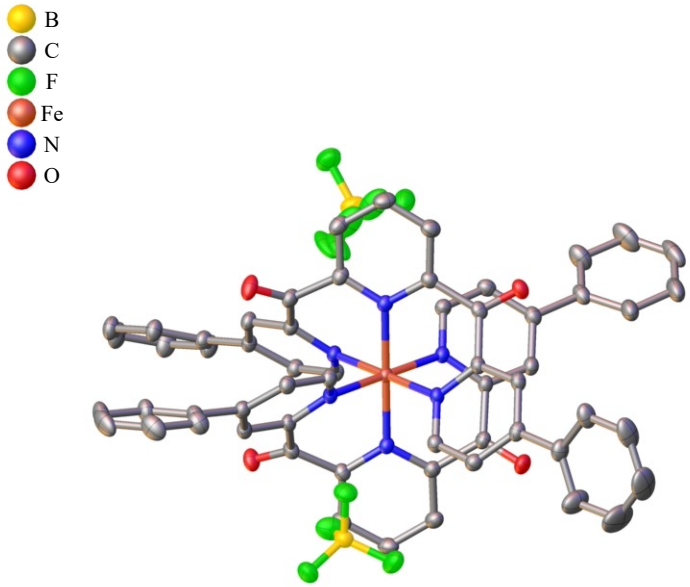

Figure 3.48. X-ray crystal structure of $[Fe(dcPhpp)_2](BF_4)_2$ with solvent and hydrogens removed for clarity.

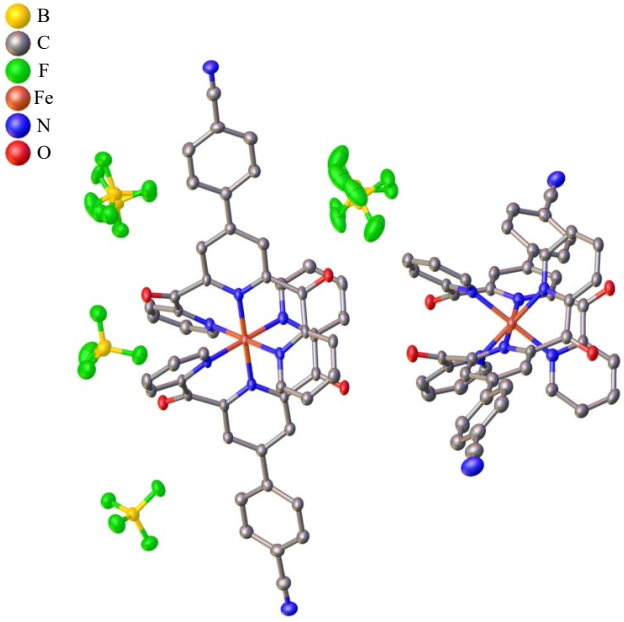

Figure 3.49. X-ray crystal structure of $[Fe(dcpCNPhp)_2](BF_4)_2$ with hydrogens and solvent removed for clarity.

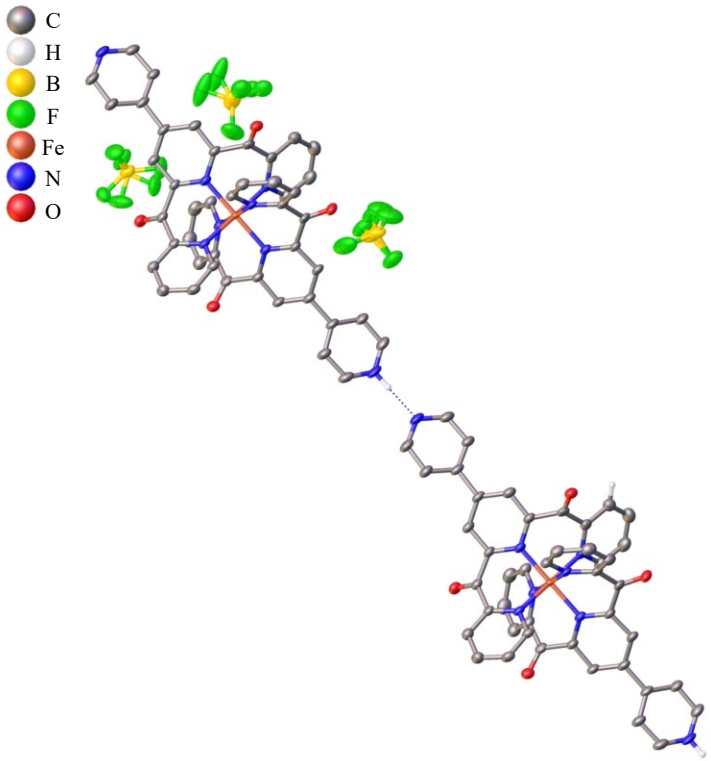

Figure 3.50. X-ray crystal structure of [Fe(pyper)(Hpyper)]$(BF_4)_3$. All hydrogens except for those involved in hydrogen bonding have been removed for clarity.

Table 3.5. Crystallographic data and structure refinement

Identification code	[Fe(dcpPhp)$_2$]$(PF_6)_2$	[Fe(dcPhpp)$_2$]$(PF_6)_2$	[Fe(dcpCNPhp)$_2$]$(PF_6)_2$	[Fe(pyper)(Hpyper)]$(BF_4)_3$
Empirical formula	$C_{46}H_{30}F_{12}FeN_6O_4P_2$•MeCN	$C_{58}H_{48}B_2F_8FeN_6O_4$•MeCN,0.5Acetone	$C_{48}H_{28}B_2F_8FeN_8O_4$•2.5MeCN, 0.3DCM	$C_{44}H_{29}B_3F_{12}FeN_8O_4$•0.5MeCN,0.6toluene
Formula weight	1117.60	1182.50	1140.49	1125.84
Temperature/K	100.00(10)	100.00(10)	100.00(10)	100.00(10)
Crystal system	monoclinic	monoclinic	monoclinic	monoclinic
Space group	$P2_1/c$	$P2_1/c$	$P2_1/c$	$P2_1/n$
a/Å	20.0926(6)	15.65127(14)	11.66290(10)	14.01723(9)
b/Å	10.9426(3)	12.11763(9)	40.6406(5)	16.65200(11)
c/Å	20.6078(4)	29.0528(3)	21.6923(3)	20.67418(11)
α/°	90	90	90	90
β/°	91.024(2)	99.9226(8)	98.0460(10)	104.1438(6)
γ/°	90	90	90	90
Volume/Å^3	4530.2(2)	5427.62(8)	10180.7(2)	4679.37(5)
Z	4	4	8	4
ρ_{calc}g/cm^3	1.639	1.447	1.488	1.598
μ/mm^{-1}	4.282	2.963	3.455	3.525
F(000)	2264	2424.0	4645.0	2284.0
Crystal size/mm^3	0.42 × 0.07 × 0.06	0.334 × 0.185 × 0.132	0.25 × 0.17 × 0.14	0.301 × 0.134 × 0.066
Radiation	Cu Kα (λ = 1.54184)	Cu Kα (λ = 1.54184)	Cu Kα (λ = 1.54184)	Cu Kα (λ = 1.54184)
2Θ range for data collection/°	8.582 to 161.38	5.732 to 160.5	4.654 to 153.836	6.9 to 160.25
Index ranges	$-25 \le h \le 25$, $-13 \le k \le 13$, $-26 \le l \le 26$	$-20 \le h \le 19$, $-15 \le k \le 11$, $-36 \le l \le 37$	$-14 \le h \le 12$, $-50 \le k \le 41$, $-26 \le l \le 27$	$-17 \le h \le 17$, $-20 \le k \le 16$, $-25 \le l \le 25$
Reflections collected	12986	48099	82892	74930
Independent reflections	12986 [R_{int} = 0.0785, R_{sigma} = 0.0420]	11627 [R_{int} = 0.0412, R_{sigma} = 0.0370]	19648 [R_{int} = 0.0581, R_{sigma} = 0.0468]	9977 [R_{int} = 0.0396, R_{sigma} = 0.0207]
Data/restraints/parameters	12986/0/669	11627/0/777	19648/174/1463	9977/14/682
Goodness-of-fit on F^2	1.072	1.043	1.031	1.045
Final R indexes [I>=2σ (I)]	R_1 = 0.0907, wR_2 = 0.2431	R_1 = 0.0464, wR_2 = 0.1193	R_1 = 0.0631, wR_2 = 0.1712	R_1 = 0.0512, wR_2 = 0.1342
Final R indexes [all data]	R_1 = 0.1120, wR_2 = 0.2637	R_1 = 0.0509, wR_2 = 0.1223	R_1 = 0.0807, wR_2 = 0.1844	R_1 = 0.0553, wR_2 = 0.1373
Largest diff. peak/hole / e Å^{-3}	1.46/-0.98	0.85/-0.51	0.91/-0.70	0.74/-0.50

CHAPTER 4: A MODULAR APPROACH TO LIGHT-HARVESTING CHROMOPHORES: POLYPYRIDYL CARBENE SYSTEMS

4.1 Introduction

Photoinduced electron transfer processes are of high interest, especially within the context of photocatalysis,[1–3] artificial photosynthesis,[4] and solar energy conversion and a fundamental perspective.[5–9] As discussed in Chapter 1, the most studied complexes in these contexts are those of Ru(II) and Ir(III). Both chromophores are able to undergo oxidative or reductive electron transfer from long-lived ^{3}MLCT charge transfer excited-states owing to their success in applications in photocatalysis.[10–12] An added benefit to these long-lived states is strongly absorbing properties of these complexes. This obviates the need for large quantities of material for the successful application of catalysis. Though the second- and third-row metal have garnered much success in their light harvesting applications, they are amongst the rarest elements within the Earth's crust. This has created considerable interest in exploring complexes of the first transition series as comparable or complimentary replacements.[13–19]

There has been marked success in the use of molybdenum,[20,21] chromium,[14,22] cobalt,[23,24] and copper[25,26] complexes for participation in electron transfer processes, but the utility of iron complexes has been of particular interest due to its high natural abundance and its valence isoelectronic structure with Ru(II).[27,28] As discussed in Chapter 1, the main limitation for the implementation of Fe(II) chromophores in applications that other metals have found success is related to the endemic ultrafast relaxation from the ^{3}MLCT state to the ligand-field manifold, which is observed for almost all Fe(II) polypyridyl complexes.[29,30] The sub-100 fs deactivation into the $^5T_2$ ligand-field (LF) state stymies any reactivity that could be leveraged from the charge transfer state. This is not to say that a ligand-field excited state is not able to participate in electron

transfer reactions as our group has previously shown, but due to the nature of metal-centered states they are fairly remote and are lower in energy than MLCT states limiting their reactivity for organic transformations.[31]

This limitation by lifetime has been attempted to be remedied by research groups around the world through the introduction of strongly σ-donating carbene ligands which showed potential in destabilizing the LF states such that the ^{3}MLCT has become the lowest energy excited-state.[32–35] The first example of this class of complexes was first published by the Wärnmark group in 2013 by using a tridentate biscarbene ligand which was able to push the ^{3}MLCT lifetime to, at that time, a ground-breaking 9 ps.[32] This record would continue to be broken culminating in a hexacarbene system with a record 528 ps ^{3}MLCT lifetime.[35] Continuing to push the envelope, cyclometallation was employed to synthesize systems reminiscent of Ir(ppy) (where ppy is 2-phenylpyridine) which then approached the 1 ns regime.[36] With MLCT lifetimes approaching the timescale of diffusion we can begin to envision the implementation of these Fe(II) chromophores in photoinduced electron transfer processes without the concern of elemental scarcity. Though now that the problem of energetic ordering has been ameliorated by the use of carbenes destabilizing the LF manifold to near or above the MLCT manifold, the next problem that arises is light-capture. Though carbenes are strong σ-donors, they are poor π-acceptors and are typically electron-rich by virtue. This leads to a convolution of effects in that the chromophores absorptions continue to push further into the bluer wavelengths. Though not a problem as a stand-alone complex, if being used with organic substrates in photocatalysis this can lead to overlapping features and excitation of both chromophore and substrate, which can also reduce the efficiency of the intended reaction. The employed carbene ligands can be modified in such a way to shift and increase the absorptivity of the MLCT, but it is not as facile as the chemistry of 2,2′-bipyridine or 1,10-phenanthroline ligands.

We previously showed that it is possible to break the donor portion and light absorbing portion of the problem into two pieces by the synthesis of a heteroleptic Fe(II) complex which contained 1,10-phenanthroline as the chromophoric region as well as a bis(acyclic diaminocarbene) for LF destabilization with a ^{3}MLCT lifetime of 8 ps.[37] In this chapter, we begin to build on these results as well as explore new motifs towards the extension of MLCT lifetimes as well as delve into the fundamental properties of these new systems.

4.2 Experimental

4.2.1 Synthesis

General. All reaction and spectroscopic solvents were obtained from Sigma Aldrich Chemical Co. and used without further purification unless otherwise stated. Dry THF, MeCN, and DCM were obtained from a Solvtek solvent drying system using neutral alumina. Anhydrous ethanol was obtained from Acros Organics. Unless otherwise noted, all reactions were conducted either using standard Schlenk techniques or in an inert atmosphere glove box (nitrogen-filled, Vacuum Atmospheres). $FeBr_2$ was obtained from Strem Chemicals Inc. 2,2′-bipyridine, 1,10-phenanthroline, 1-methylimidazole, and triflic anhydride (Tf_2O) were obtained from Oakwood Chemicals and used as received. 30% H_2O_2 was obtained from Fisher Scientific. 1.6 M n-BuLi was obtained from Sigma Aldrich Chemical Co. NMR spectra were collected in the Max T. Rogers NMR Facility of Michigan State University on an Agilent 500 MHz or a Bruker 500 MHz spectrometer; spectra were referenced internally to the residual solvent peak of $CDCl_3$, CD_3CN, or $(CD_3)_2CO$ which were obtained from Cambridge Isotopes. Electrospray ionization mass spectra were obtained at the Michigan State University Mass Spectrometry and Metabolomics Core on a Waters G2-XS QToF mass spectrometer interfaced to a Waters Aquity UPLC. Elemental analyses were obtained through the analytical facilities at Michigan State University on samples that had

been ground in a vial and stored under vacuum overnight prior to analysis. 2,2′-bipyridine mono *N*-oxide,[38] 1,10-phenanthroline mono *N*-oxide,[39] and 1-methyl-3-(1,10-phenanthrolin-2-yl)-1H-imidazol-3-ium triflate ([phen^{Me}ImH]OTf)[40] were all prepared by literature methods. The 1,10-phenanthroline mono *N*-oxide was recrystallized from hot toluene before use. ***All reactions for the synthesis of pyridyl N-oxides use excess 30% H_2O_2 and should be worked-up with caution as these reactions can become explosive upon concentration.***

1-methyl-2-(1,10-phenanthrolinyl)-1*H*-imidazol-3-ium hexafluorophosphate ([phen^{Me}ImH]PF$_6$). To a stirred solution of 1.000g of 1,10-phenanthroline mono *N*-oxide (5.1 mmol, 1.0 eq.) in 25 mL of MeCN was added 0.81 mL of 1-methylimidazole (10.2 mmol, 2.0 eq). The reaction was cooled to 0ºC and 1.3 mL of Tf_2O (7.6 mmol, 1.5 eq.) were added dropwise over 20 mins. The orange solution stirred for an additional 15 mins at 0ºC and then warmed to room temperature and stirred for 6 hours. The MeCN was evaporated, and the crude was dissolved in 20 mL of H_2O. To this orange solution was added 1.664 g of NH_4PF_6 (10.2 mmol, 2.0 eq). The precipitate was filtered and washed with H_2O, MeOH, and diethyl ether. Yield: 1.575 g, 76%. ^{1}H NMR (500 MHz, CD_3CN) δ 9.69 (t, J = 1.6 Hz, 1H), 9.16 (dd, J = 4.4, 1.7 Hz, 1H), 8.75 (d, J = 8.6 Hz, 1H), 8.52 (dd, J = 8.1, 1.7 Hz, 1H), 8.34 (t, J = 1.8 Hz, 1H), 8.08 – 8.05 (m, 3H), 7.84 (dd, J = 8.2, 4.4 Hz, 1H), 7.64 (t, J = 1.7 Hz, 1H), 4.04 (s, 3H).

2-(*N*-pyridinium)-1,10-phenanthroline hexafluorophosphate ([phenNPyH]PF$_6$). The compound was prepared using a modification of a literature procedure.[40] To a stirred solution of 1.000 g of 1,10-phenanthroline mono *N*-oxide (5.1 mmol, 1.0 eq.) in 25 mL of MeCN was added 0.82 mL of pyridine (10.2 mmol, 2.0 eq.). This was cooled to 0°C, and 1.3 mL of Tf_2O (7.6 mmol, 1.5 eq.) were added dropwise over 20 min. The resulting mixture was stirred for 15 min at 0°C, and then allowed to warm to room temperature to stir for an additional 10 hours. The MeCN was

evaporated and the crude was dissolved in minimal MeOH. 1.654 g of NH_4PF_6 were added and it stirred for 20 mins. The solid was filtered and washed with H_2O, MeOH, and Et_2O. X-ray quality single crystals were grown from diffusion of diethyl ether into a MeCN solution containing a small amount of MeOH. Yield: 1.582 g, 76%. ^{1}H NMR (500 MHz, CD_3CN) δ 9.61 – 9.56 (m, 2H), 9.19 (dd, J = 4.4, 1.7 Hz, 1H), 8.90 (d, J = 8.6 Hz, 1H), 8.85 – 8.79 (m, 1H), 8.67 (dd, J = 5.0, 1.6 Hz, 2H), 8.60 – 8.55 (m, 1H), 8.41 – 8.31 (m, 3H), 8.26 (d, J = 8.6 Hz, 1H), 8.21 – 8.12 (m, 2H), 7.91 – 7.82 (m, 3H).

6-(*N*-pyridinium)-2,2′-bipyridine hexafluorophosphate ([bpyNPyH]PF_6). The compound was prepared using a modification of a literature procedure.[40] To a stirred solution of 3.000 g of 2,2′-bipyridine mono *N*-oxide (17.4 mmol, 1.0 eq.) in 90 mL of MeCN was added 2.8 mL of pyridine (34.9 mmol, 2.0 eq.). This was cooled to 0°C and 4.4 mL of Tf_2O (26.1mmol, 1.5 eq.) were added dropwise over 15 min. The resulting mixture was stirred for 20 min at 0°C, and then allowed to warm to room temperature to stir overnight. The solvent was evaporated, and the orange reside was redissolved in a minimal volume of methanol. Excess saturated $KPF_{6(aq)}$ was added forming a pale orange solid. It was filtered and washed with H_2O, MeOH, and diethyl ether. It was recrystallized by dissolving in minimal acetonitrile and adding diethyl ether until cloudy. The suspension was placed in the fridge overnight. Yield: 4.863 g, 80%. ^{1}H NMR (500 MHz, CD_3CN) δ 9.51 – 9.45 (m, 2H), 8.94 – 8.87 (m, 2H), 8.84 – 8.79 (m, 2H), 8.68 (dd, *J* = 7.9, 0.7 Hz, 1H), 8.61 (t, *J* = 8.0 Hz, 1H), 8.38 (dddd, *J* = 7.5, 6.4, 1.9, 1.0 Hz, 2H), 8.26 (dd, *J* = 8.1, 0.7 Hz, 1H), 8.22 (ddd, *J* = 7.3, 5.8, 1.8 Hz, 1H).

2,6-di(*N*-pyridinium)pyridine hexafluorophosphate ([$PyNPy_2$]$(PF_6)_2$). This compound was synthesized using a modification of a literature procedure.[41] In a pressure tube was added 2.000 g of 2,6-dibromopyridine (8.4 mmol, 1.0 eq.) and 1.5 mL of sparged pyridine (18.6 mmol, 2.2 eq.).

The pressure tube was sealed and heated to 150°C for 16 hours behind a blast-shield. Upon completion, the original melt had become a dark brown solid. The vessel was cooled to room temperature and the solid was triturated with DCM until a fine powder formed. The powder was filtered, and the crude was dissolved in H_2O and was gravity filtered to remove insoluble impurities. The dark brown solution was treated with excess $KPF_{6(aq)}$ to precipitate a tan solid. The solid was filtered and washed with additional H_2O (4 x 20 mL), MeOH (3 x 10 mL), and diethyl ether to afford a light tan solid. Yield: 3.102 g, 70%. ^{1}H NMR (500 MHz, acetone-d_6) δ 10.00 – 9.95 (m, 4H), 9.12 (tt, J = 7.8, 1.3 Hz, 2H), 8.98 (dd, J = 8.5, 7.7 Hz, 1H), 8.82 (d, J = 8.1 Hz, 2H), 8.63 – 8.57 (m, 4H). ^{13}C NMR (126 MHz, acetone-d_6) δ 206.19, 150.71, 147.24, 144.30, 129.74, 122.19, 30.30, 30.24, 30.15, 29.99, 29.84, 29.69, 29.53, 29.38.

[Fe(phen^{Me}Im)$_2$](PF$_6$)$_2$. In a flame-dried, N_2 purged flask was added 203 mg of [phen^{Me}ImH]PF_6 (0.5 mmol, 2.0 eq.) and 40 mL of THF. The suspension was cooled to -78°C and 0.31 mL of 1.6 M n-BuLi (0.5 mmol, 2.2 eq.) were added dropwise over 15 minutes. The reaction continued to stir for an additional 1 hour. A solution of 53 mg of $FeBr_2$ (0.25 mmol, 1.0 eq.) in 20 mL of THF was added dropwise via a cannula over 15 minutes. The red/brown solution stirred for 1 hour at -78°C and then allowed to warm to room temperature and stir overnight, protected from light. The solvent was evaporated, and residue was dissolved in acetone and filtered to afford a red solution. A saturated solution of $KPF_{6(aq)}$ was added to precipitate a red solid. This was filtered and washed with H_2O and diethyl ether. The crude was purified on Bio-Beads S-X1, eluting with 4:6 MeCN/toluene followed by recrystallization from slow diffusion of diethyl ether into a saturated acetone solution. X-ray quality single crystals were grown from slow diffusion of diethyl ether into a saturated MeCN solution. Yield: 90 mg, 42%. ^{1}H NMR (500 MHz, CD_3CN) δ 8.93 (d, J = 8.8 Hz, 2H), 8.48 (d, J = 8.8 Hz, 2H), 8.40 – 8.34 (m, 4H), 8.24 (d, J = 2.2 Hz, 2H), 8.12 (d, J =

9.0 Hz, 2H), 7.34 (dd, *J* = 5.2, 1.2 Hz, 2H), 7.29 (dd, *J* = 8.1, 5.2 Hz, 2H), 6.93 (d, *J* = 2.2 Hz, 2H), 2.42 (s, 6H).^{13}C NMR (126 MHz, CD_3CN) δ 196.24, 156.15, 153.63, 149.62, 147.47, 137.13, 136.82, 131.39, 128.04, 127.86, 127.71, 127.41, 126.77, 119.10, 112.30, 35.75. Elemental Analysis: Calc'd (%): C, 49.00; H, 2.62; N, 10.39. Found: C, 48.61; H, 2.55; N, 9.28.

[Fe(phenNPy)$_2$](PF$_6$)$_2$. This complex was prepared using a modification of a literature method.[42] In a glove box, 200 mg of [phenNPyH]PF_6•$HPyPF_6$ (0.32 mmol, 2.2 eq.) and 32 mg of $FeBr_2$ (0.14 mmol, 1.0 eq.) were combined in 30 mL of EtOH. The cloudy orange solution stirred for 30 minutes. To this suspension was added 0.1 mL of triethylamine (0.7 mmol, 5.0 eq.) and the suspension instantly turned a brown-green. The reaction was heated to reflux under N_2 overnight. Upon reaching temperature the reaction turned blue. It was then cooled to room temperature and placed in the freezer as a solid began to precipitate. The solid was filtered and washed with cold EtOH. The blue-purple solid was then dissolved in minimal acetone and saturated $KPF_{6(aq)}$ was added and the volume of the reaction was reduced by approximately 50%. The solid was filtered and washed with H_2O and diethyl ether. The crude was purified on silica eluting with 7:1 MeCN/$KNO_{3(aq)}$ followed by size exclusion chromatography on Bio-Beads S-X1 with 4:6 MeCN/toluene. X-ray quality crystals were grown from slow diffusion of diethyl ether into a solution of MeCN/acetone/MeOH. Yield: 20 mg, 18%. ^{1}H NMR (500 MHz, acetone-d_6) δ 10.01 (d, *J* = 6.7 Hz, 2H), 9.39 (d, *J* = 9.0 Hz, 2H), 9.32 (d, *J* = 9.0 Hz, 2H), 8.70 – 8.63 (m, 4H), 8.45 (d, *J* = 8.9 Hz, 2H), 7.92 (dd, *J* = 5.1, 1.2 Hz, 2H), 7.49 (dd, *J* = 8.1, 5.1 Hz, 2H), 7.38 (td, *J* = 6.9, 1.4 Hz, 2H), 7.19 (ddd, *J* = 8.4, 7.0, 1.2 Hz, 2H), 6.56 (d, *J* = 8.4 Hz, 2H). ^{13}C NMR (126 MHz, acetone-d_6) δ 227.07, 159.14, 153.97, 148.95, 141.94, 137.69, 137.31, 136.04, 135.79, 129.38, 129.37, 127.05, 119.76, 114.84.

[Fe(bpyNPy)$_2$](PF$_6$)$_2$. This complex was prepared using a modification of a literature method.[42] In a glove box, 150 mg of [bpyNPyH]PF$_6$ (0.38 mmol, 2.3 eq.) and 35 mg of FeBr$_2$ (0.16 mmol, 1.0 eq.) were combined in 30 mL of EtOH. The cloudy pink solution stirred for 20 minutes. To this suspension was added 0.08 mL of triethylamine (0.49 mmol, 3.0 eq.) and the suspension instantly turned a brown-green. The reaction was heated to reflux under N_2 overnight. Upon reaching temperature the reaction turned blue. It was then cooled to room temperature and saturated KPF$_{6(aq)}$ was added, and the volume of the reaction was reduced by approximately 50%. The solid was filtered and washed with H_2O and diethyl ether. The crude was purified on silica eluting with 7:1 MeCN/KNO$_{3(aq)}$ followed by size exclusion chromatography on Bio-Beads S-X1 with 4:6 MeCN/toluene. X-ray quality crystals were grown from slow diffusion of diethyl ether into a solution of MeCN/acetone/MeOH. Yield: 18 mg, 15%. ^{1}H NMR (500 MHz, CD$_3$CN) δ 9.34 (dt, *J* = 6.8, 1.2 Hz, 1H), 8.77 (dd, *J* = 7.9, 0.8 Hz, 1H), 8.60 (dd, *J* = 8.6, 0.8 Hz, 1H), 8.57 – 8.49 (m, 2H), 7.99 – 7.92 (m, 1H), 7.23 (ddd, *J* = 5.6, 1.6, 0.8 Hz, 1H), 7.20 – 7.08 (m, 3H), 6.34 (ddd, *J* = 8.2, 1.6, 0.9 Hz, 1H), 2.17 – 2.13 (m, 2H). ^{13}C NMR (126 MHz, CD$_3$CN) δ 227.80, 158.52, 154.95, 151.46, 140.96, 139.23, 137.56, 136.74, 136.13, 127.87, 124.73, 122.45, 119.40, 118.34, 114.52.

4.2.2 Physical Characterization

X-ray crystal structure determination. Crystals of appropriate size were selected and mounted on a nylon loop with paratone oil on a XtaLAB Synergy, Dualflex, HyPix diffractometer. The crystals were kept at a steady *T* = 100.0(2) K during data collection. The structures were solved with the ShelXT[43] solution program using intrinsic phasing or direct methods for twinned data and by using Olex2 1.3[44] as the graphical interface. The model was refined with ShelXL 2018/3[45] using full matrix least squares minimization on $\boldsymbol{F^2}$.

Ground-state absorption spectroscopy. All room temperature extinction coefficient measurements were collected in spectrophotometric grade acetonitrile (Sigma Aldrich) in a 1 cm quartz cuvette on a PerkinElmer Lambda 1050 dual-beam spectrophotometer.

Electrochemistry. Electrochemistry was performed using a CH Instruments CH620D potentiostat in a 0.1 M tetrabutylammonium hexafluorophosphate ($TBAPF_6$) acetonitrile solution with a Pt working electrode, Pt counter electrode, and a Ag wire pseudo-reference electrode in an Ar-filled glovebox. Cyclic voltammetry measurements were conducted with a 100 mV/s scan rate to determine the reversibility of redox processes and differential pulse voltammetry (DPV) was used to accurately determine $E_{1/2}$. All potentials were internally referenced to the Fc/Fc^+ redox couple. $TBAPF_6$ was purchased from Oakwood Chemical Company and recrystallized from ethanol twice before use.

Spectroelectrochemistry. Spectroelectrochemistry was performed in a similar manner as previously described[46] with some slight modifications: all measurements were carried out in an Ar-filled glovebox in spectrophotometric grade MeCN (Sigma Aldrich) with 0.1 M $TBAPF_6$ using a Pine Research Pt honeycomb combination working/reference electrode and Ag wire pseudoreference electrode controlled by a CH Instruments CH620D potentiostat. The solutions were prepared so the absorbance of the solution was ~0.6 at the maximum of the MLCT absorption feature as measured with a SSI400 CCD spectrometer. Spectra were collected every 30 s for 10 min with a ~100 mV overpotential applied for the reductive or oxidative process under investigation.

Ultrafast Transient Absorption Spectroscopy. Preliminary ultrafast Transient absorption measurements were performed in acetonitrile by Atanu Ghosh.

4.2.3 Computational Methods

All calculations were performed with Gaussian 16[47] computational package on the Michigan State University High Performance Computing Center servers. Calculations were performed using either B3LYP[48] or B3LYP5, in which the percentage of Hartree-Fock exchange was modified to 5%. Grimme's Empirical dispersion correction, D2, was employed on all functionals.[49] The integral equation formalism variant of the polarizable continuum model (IEFPCM) was used to model acetonitrile. For geometry optimizations and frequency calculations, a split basis was used with 6-311G(d) for C, H, and N and the SDD basis and pseudo-potential for Fe. The frequency calculations were examined for negative frequencies to ensure a minimum had been found. Time-dependent DFT (TD-DFT) was performed using the previous functionals and the 6-311G(d) basis set for all atoms and requesting 40 singlet states. Molecular orbitals were visualized using Avogadro at an isovalue of 0.02.[50,51]

4.3 Results and Discussion

4.3.1 Synthesis

The synthesis of the [phen^{Me}ImH]PF_6 ligand was accomplished using 1,10-phenanthroline mono *N*-oxide and treatment with triflic anhydride in the presence of 1-methylimidazole (Figure 4.1b) in good yield.[40] This is a convenient preparation as opposed to the general 5-step procedure which would require 2-bromo-1,10-phenanthroline starting material and treatment with imidazole in an Ullmann type coupling, followed by alkylation of the free nitrogen (Figure 4.1a).[52,53] Due to the ease of preparation of mono N-oxides and the gentle reaction conditions of the previous procedure this would allow for a wide variety imidazolium-based carbenes to be synthesized.

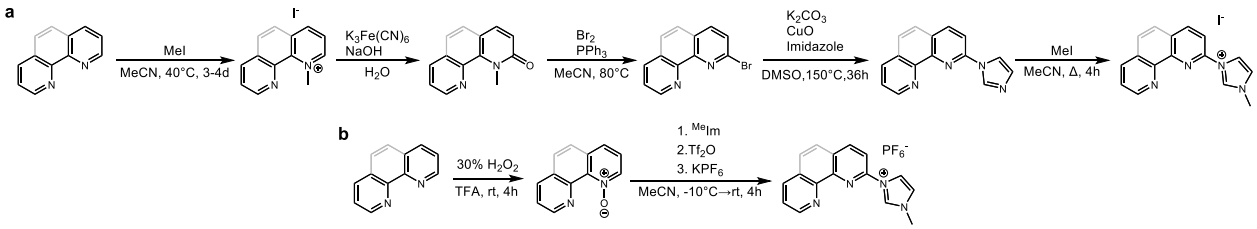

Figure 4.1. (a) Conventional synthetic route and (b) Simplified 2-step synthetic procedure towards 2-substituted-1,10-phenanthroline or 6-substituted-2,2′-bipyridine imidazolium salts.

As with the imidazolium carbene, the pyridinium-based systems were prepared in a similar manner, starting from the mono N-oxide, but treating with pyridine instead of an imidazole derivative to form the corresponding bipyridyl or phenanthroline ligand (Figure 4.2). Interestingly, the [phenNPyH]PF_6 ligand when synthesized and metathesized using NH_4PF_6 forms as the pyridinium hexafluorophosphate adduct in a 1:1 ratio as confirmed by NMR and crystallography. As this adduct was not anticipated to interfere in the coordination of the ligand under basic conditions it was used as isolated. Both pyridinium-based ligands were metathesized to the hexafluorophosphate salts to simplify the cleaning process.

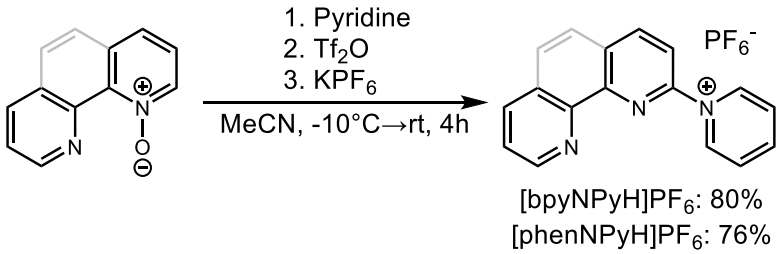

Figure 4.2. General synthetic procedure for the synthesis of 1,10-phenanthroline and 2,2′-bipyridine pyridinium salts.

Complexation of [phenMeImH]PF_6 was originally attempted using literature methods developed by the Bauer group[54,55] using LiHMDS as the base at cryogenic temperatures in THF. In their studies, the ligands were iodide or bromide salts exhibiting increased solubility in THF. As

this ligand was hexafluorophosphate salt, the solubility was diminished in ethereal solvents preventing the full deprotonation of the imidazolium. This limitation was overcome by dropwise addition of n-BuLi, a much stronger base, at cryogenic temperatures leading to full deprotonation and a clear solution of lithiated ligand. Dropwise addition of the Fe(II) source to the lithio-imidiazolium followed by metathesis afforded the target bis-carbene complex, $[Fe(phen^{Me}Im)_2](PF_6)_2$ (Figure 4.3). The complex, once formed, was able to be cleaned using Bio-Beads S-X1 size exclusion chromatography.

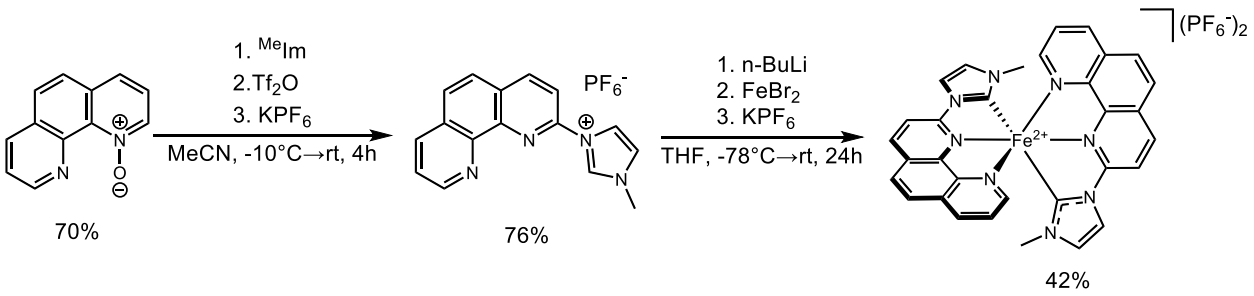

Figure 4.3. General synthetic procedure for the synthesis of $[Fe(phen^{Me}Im)_2](PF_6)_2$ starting from 1,10-phenanthroline mono *N*-oxide.

The next series of complexes to be synthesized were pyridinium-based, creating a pyridine (pyridinylidene) analogue to carbenes. Unlike the imidazolium-based ligand, the pyridinium ligands that were *N*-bound directly to the bipyridine and phenanthroline rings proved more difficult in coordination with Fe(II). Initial attempts at coordination of $[phenNPyH]PF_6$ to Fe(II) followed the procedures by the Bauer group.[54,55] Treatment of the ligand at cryogenic temperatures with LiHMDS followed by addition of $FeBr_2$ and warming to room temperature afforded no product. A review of the literature shows that this class of pyridiniums, though easily isolated, are extremely sensitive to nucleophilic attack. These two ligands resemble a Zinke pyridinium which are known to undergo aminolysis by nucleophilic attack of the 2-position by weak and strong nucleophiles

alike leading to a ring opening of the pyridinium and a resulting aromatic amine.[56–58] Review of the literature for similar classes of compounds led to a new coordination protocol following a procedure for heteroleptic Ru(II) complexes bearing a terpyridine with the peripheral ring being *N*-alkylated.[42,59] These procedures employed a pre-formed [Ru(terpy)Cl_2] complex and were treated with the pyridinium ligand in ethanol at reflux with a large excess of triethylamine as a base as well as a reductant to form a bis(tridentate) heteroleptic complex. The initial reaction conditions for the coordination of [bpyNPyH]PF_6 and [phenNPyH]PF_6 used $FeCl_2$ as the metal source in ethanol and triethylamine. While this procedure did lead to the intended product, the yields were extremely low with only 1-2 mg of isolated complex (~2% yield). The main issue noticed while using $FeCl_2$ was the solubility of the pre-formed complex. The reactions even when refluxed showed a purple precipitate, which is hypothesized to preclude deprotonation by base to form the bis(tridentate) complex. Switching the Fe(II) source to $FeBr_2$ exhibited increased solubility in ethanol at reflux and led to a cleaner, yet still low yielding, formation of the intended pyridinylidene complexes (Figure 4.4). Column chromatography on silica of both complexes eluted the target blue complex along with a pink impurity. Darker purple and brown impurities remained at the top of the column.

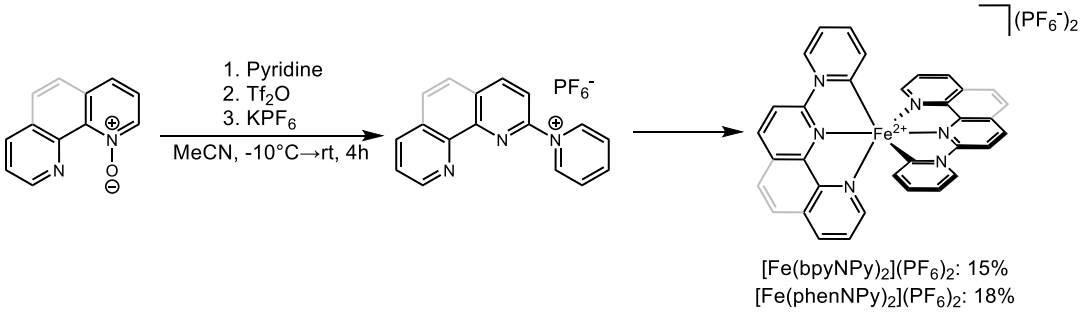

Figure 4.4. General synthetic procedure for the synthesis of [Fe(bpyNPy)$_2$](PF_6)$_2$ and [Fe(phenNPy)$_2$](PF_6)$_2$ starting from the corresponding mono *N*-oxide.

An attempt to complete the series was sought out in the synthesis of $[Fe(PyNPy_2)_2](PF_6)_2$ following the previous synthetic procedures for the other pyridinium complexes. At this moment the target complex has not been isolated nor is there spectroscopic evidence of its formation in its crude ^1H NMR but efforts in its synthesis will be on going.

4.3.2 X-ray Crystallography

[phenNPyH]PF_6•$HPyPF_6$: The ligand crystallizes in the $P\bar{1}$ space group with 1 ligand in the asymmetric unit with no disorder. The free pyridinium is hydrogen bonded to the phenanthroline ligand and the position of the hydrogen on the pyridinium was able to be refined.

[$PyNPy_2$](PF_6)$_2$: This ligand crystallized in the $P\bar{1}$ space group with 1 ligand and two anions in the asymmetric unit with no disorder. The crystal was twinned by 32% with component two rotated by 179.94º about the c-axis in reciprocal space.

[Fe(phen^{Me}Im)$_2$](PF_6)$_2$: The complex crystallizes in the $P2_1/n$ space group with 1 molecule in the asymmetric unit and one acetonitrile solvent molecule present. Due to disordered solvent in the lattice a solvent mask was calculated, and 90 electrons were found in a volume of 416 $Å^3$ in 1 void per unit cell. This is consistent with the presence of 0.5 molecules of diethyl ether per Asymmetric Unit which accounts for 84 electrons per unit cell.

[Fe(phenNPy)$_2$](BF_4)$_2$: This complex crystallizes in the $P2_1/n$ space group with 1 complex and two rotationally disordered BF_4^- anions. A solvent mask was also employed. Due to poor diffraction of the crystal, only low-angle data was collected, but to a completeness of 98.2%. This precludes the determination of structural parameters for the complex but allows for reliable atom connectivity.

[Fe(bpyNPy)$_2$](PF_6)$_2$: The complex crystallizes in the $P2_12_12_1$ chiral space group with 1 complex in the asymmetric unit and two anions. There is one translationally disordered PF_6^- anion in the

lattice with the occupancy refined to 0.62:0.38 such that the total occupancy was unity. The crystal was a pseudo-tetragonal twin with rotation around the c-axis and the refined weighted fractions of 0.91:0.09.

4.3.3 Ground- and Excited-State Characterization of [Fe(phen^{Me}Im)$_2$](PF$_6$)$_2$

The initial complex that was studied was [Fe(phen^{Me}Im)$_2$](PF$_6$)$_2$. This complex takes inspiration from the work of Bauer and co-workers who performed an in-depth study of the effect of *N*-heterocyclic carbene (NHC) count on the photophysical properties of Fe(II) chromophores.[55] In this study, a series of four NHC complexes were synthesized, including the 2,2′-bipyridyl analogue of [Fe(phen^{Me}Im)$_2$](PF$_6$)$_2$, and the corresponding ^{1,3}MLCT and ground-state recovery (GSR) dynamics were measured. For [Fe(bpy^{Me}Im)$_2$](PF$_6$)$_2$, a sub-100 fs deactivation corresponding to depopulation of the ^{3}MLCT manifold to a metal-centered state was observed followed by ground-state recovery on the order of 96 ps. Though these dynamics are not ideal, it lays the ground-work by which we can begin to compare new complexes against while using similar ligand motifs.

[Fe(phen^{Me}Im)$_2$](PF$_6$)$_2$ was synthesized and its ground-state electronic properties were first investigated. The electronic absorption spectrum (Figure 4.5) was collected and compared to the bipyridyl analogue synthesized by the Bauer group as well the parent complexes, [Fe(phen)$_3$](PF$_6$)$_2$ and [Fe(bpy)$_3$](PF$_6$)$_2$.

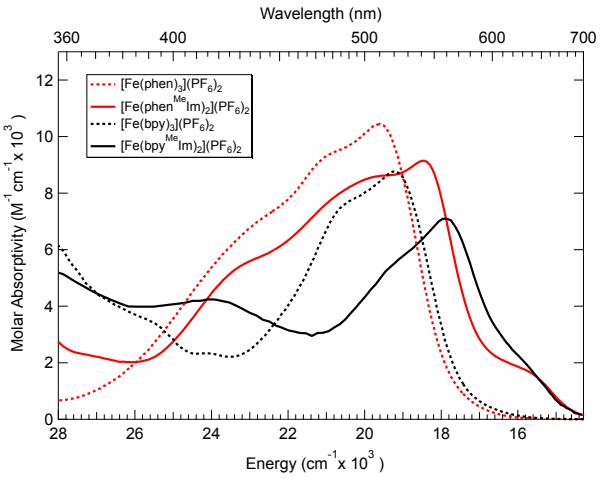

Figure 4.5. Ground-state electronic absorption spectra of $[Fe(bpy)_3](PF_6)_2$ (black dashed), $[Fe(phen)_3](PF_6)_2$ (red dashed), $[Fe(phen^{Me}Im)_2](PF_6)_2$ (red), and $[Fe(bpy^{Me}Im)_2](PF_6)_2$ (black) which was reproduced from reference 55. All spectra were recorded in acetonitrile.

Table 4.1. Spectroscopic data of tris(polypyridyl) and bis(polypyridylcarbene) complexes collected in CH_3CN

Complex	λ_{max} nm	**Molar Absorptivity** $M^{-1}cm^{-1}$
$[Fe(bpy)_3](PF_6)_2$	520	8770
$[Fe(phen)_3](PF_6)_2$	510	10450
$[Fe(bpy^{Me}Im)_2](PF_6)_2$	560	7090
$[Fe(phen^{Me}Im)_2](PF_6)_2$	540	9150

For both carbene complexes, a noticeable bathochromic shift in the $^1A_1 \rightarrow {}^1$MLCT absorption is observed, as well as a decrease in the observed intensity of the absorption. A unique aspect of the $[Fe(phen^{Me}Im)_2]^{2+}$ spectrum is the shoulder that appears at approximately 16,000 cm^{-1}. This pronounced shoulder is not present in either parent complexes nor the bipyridyl analogue but, it is present in terpyridyl Fe(II) complexes and may be an endemic feature to these two classes of compounds.

In addition to the electronic absorption spectra, electrochemical measurements were carried out on $[Fe(phen^{Me}Im)_2]^{2+}$ (Figure 4.6). The oxidation wave corresponding to the $Fe^{II/III}$ couple is

fully reversible under the measurement conditions. The reductive electrochemistry though presents with two reductive events presenting irreversibility on the return waves. This behavior is in agreement with the electrochemistry presented by Bauer and co-workers as well as that of the Wärnmark group.[32,55] Compared to the bipyridyl analogue, the phenanthroline complex exhibits a slightly less positive $Fe^{II/III}$ redox couple at 0.42 V (Table 4.2) as opposed to 0.44 V. Both of these values are substantially more positive than the Wärnmark complex at 0.31 V, but is well within agreement of having fewer NHC donors to create an electron-rich Fe(II) center, facilitating an easier oxidation. The reductive chemistry of the $[Fe(phen^{Me}Im)_2]^{2+}$ complex exhibits two irreversible reductions whereas the bpy complex is reported to have two fully reversible events. Though irreversible we can glean that the less negative first redox event for the phen-based ligand is indicative of the more delocalized π-system leading to an easier reduction. With the ground-state characterization in hand, we can begin to turn towards the excited-state dynamics of the complex.

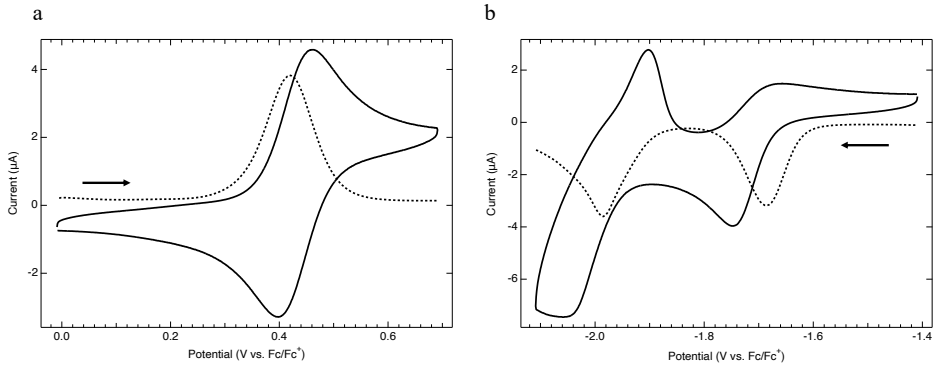

Figure 4.6. Cyclic voltammograms (solid) and DPV (dashed) of $[Fe(phen^{Me}Im)_2](PF_6)_2$ showing (a) The reversible $Fe^{II/III}$ couple and (b) the irreversible reduction of the $phen^{Me}Im^{-\bullet}$ ligand.

Table 4.2. Electrochemical data of imidazolium-based Fe(II) carbene complexes[a]

Complex	$E_{1/2}^{2+/3+}$	$E_{1/2}^{2+/+}$	$E_{1/2}^{+/0}$
$[Fe(B^{Me}ImPy)_2]^{2+}$[c]	0.31	-2.39[b]	-
$[Fe(bpy^{Me}Im)_2]^{2+}$[d]	0.44	-1.74	-2.02
$[Fe(phen^{Me}Im)_2]^{2+}$	0.42	-1.69[b]	-1.99[b]

[a]All electrochemical measurements were performed in CH_3CN [b]Irreversible [c]Taken from reference 32 [d]Taken from reference 55.

Using the electrochemical data presented in Table 4.2, we can now use spectroelectrochemistry to model the behavior of the MLCT absorption for ultrafast transient absorption measurements (Figure 4.7). Due to the irreversibility of the reduction of the complex only spectra for the oxidation were recorded. There is an obvious bleach centered around 500 nm corresponding to the MLCT absorption in addition to a weak positive feature beginning at approximately 690 nm and continuing to 850 nm. This is assigned to be associated with the $phen^{Me}Im$ anion radical absorption. From this data, we can now begin to investigate the excited-state dynamics of this complex.

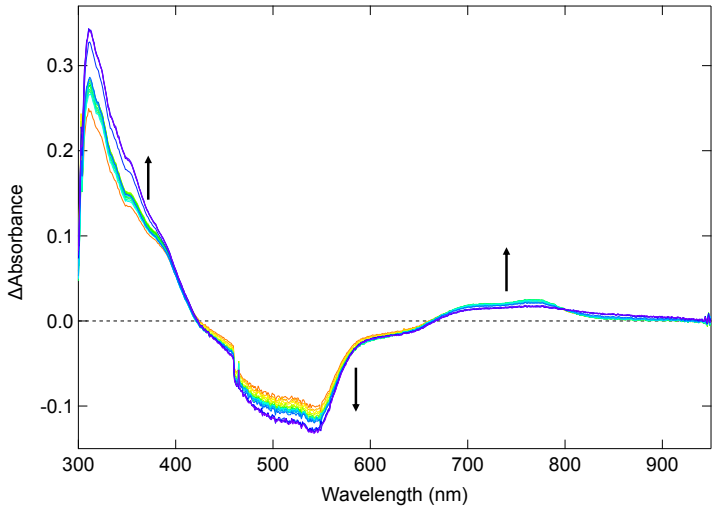

Figure 4.7. Oxidative spectroelectrochemistry of $[Fe(phen^{Me}Im)_2]^{2+}$ in CH_3CN.

Ultrafast transient absorption measurements were undertaken (Figure 4.8) to probe the excited-state properties of this complex. The ground-state recovery (GSR) dynamics of the complex were first investigated, affording a lifetime of 187 ps, fit with a monoexponential decay (Figure 4.8a). This deactivation is attributed to relaxation from a metal-centered state, either ^{3}MC or ^{5}MC, to the $^1A_1$ ground-state. Compared to the bipyridyl analogue of this complex which possessed a GSR lifetime of 96 ps, the kinetics have slowed by almost a factor of 2.

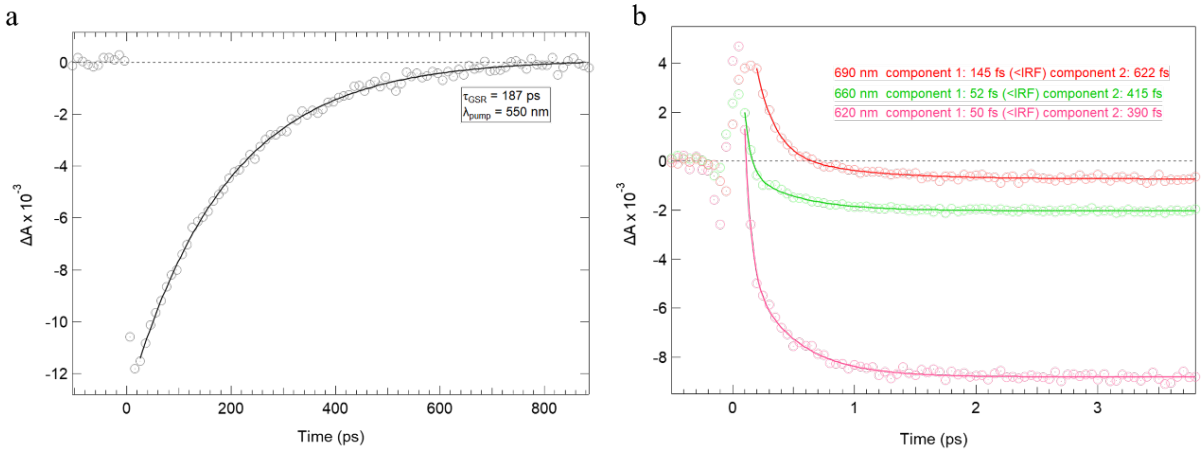

Figure 4.8. Ultrafast transient absorption spectra of $[Fe(phen^{Me}Im)_2](PF_6)_2$ in CH_3CN showing (a) Ground-state recovery dynamics and (b) MLCT deactivation to the ligand-field manifold.

This slower behavior can be explained within the context of ligand-field theory and semi-classical Marcus Theory.[60,61] Within the framework of semi-classical Marcus Theory, there are a multitude of parameters that dictate the nonradiative decay rate constant including (equation 4.1): the electronic coupling matrix element (H_{ab}), the reorganization energy (λ), and the driving force (ΔG^0).

$$k_{nr} = \frac{2\pi}{\hbar}|H_{ab}|^2 \frac{1}{\sqrt{4\pi\lambda k_b T}} exp\left[\frac{-(\lambda+\Delta G^0)^2}{4\lambda k_b T}\right] \quad (4.1)$$

Between these two systems we can reasonably assume that H_{ab} and λ should be fairly similar with the homologous nature of the complexes, leading to the main difference driving the kinetics being the change in ΔG^0. From our previous studies of tris(polypyridyl) Co(III) analogues of Fe(II) chromophores we showed that the effective ligand-field strength of phenanthroline is approximately 540 cm^{-1} lower than that of bipyridine, 23940 cm^{-1} and 24480 cm^{-1}, respectively.[62] We can connect this decrease in ligand-field splitting to a concomitant decrease in the driving force, ΔG^0, for ground-state recovery of the complex. Assuming a similar deactivation pathway between the bpy^{Me}Im and phen^{Me}Im complexes, this decrease in driving force would result in a longer lifetime, in line with what we are observing. Preliminary measurements of the MLCT manifold lifetime were carried out using variable probe wavelengths, guided by the spectroelectrochemical data collected. The data collected were all fit to biexponential decays affording two time constants. The short component of the decay is within the instrument response function (IRF) of the instrument while the longer component can be determined with confidence (Figure 4.8b). The short component could be associated with intersystem crossing between the ^{1}MLCT to the ^{3}MLCT manifolds, which is known to occur on ultrashort timescales, though this typically occurs on sub-50 fs timescales for most polypyridyl complexes.[30,63,64] As the second component is much shorter and the lifetime varies dramatically from the GSR lifetime of the complex, there could be multiple explanations for this. The first is it could be associated with direct deactivation of the ^{3}MLCT state to the ligand-field manifold, ^{3}MLCT$\rightarrow^{3,5}$MC. Of note for this pathway is the probe-dependance of the lifetime. The observed time constant becomes shorter as higher energy probe wavelengths are used, decreasing from 622 fs to 390 fs. On these timescales, vibrational cooling would not be possible as those dynamics typically occur in the picosecond regime though an alternative cooling pathway could be included instead, internal vibrational

redistribution (IVR), which can occur on the femtosecond to picosecond regime. A newly published paper shows that a third alternative for the dynamics is the bifurcation of the relaxation in which there is direct conversion from the ^{1}MLCT corresponding to ^{1}MLCT→^{3,5}MC convolved with deactivation from the ^{3}MLCT state into the ligand field manifold as well (Figure 4.9).[65] These dynamics were observed for $[Fe(bpy)_3]^{2+}$ in which there was direct conversion from the initially populated ^{1}MLCT into the LF manifold as well as from the ^{3}MLCT using 2D electronic absorption spectroscopy.

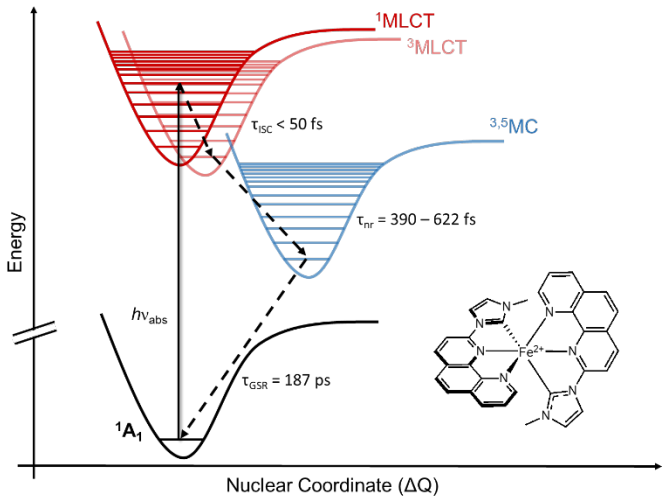

Figure 4.9. Proposed photocycle for $[Fe(phen^{Me}Im)_2]^{2+}$ beginning at population of the ^{1}MLCT followed by ultrafast intersystem crossing to the ^{3}MLCT. There may then be cooling on the ^{3}MLCT surface followed by internal conversion or intersystem crossing to the ligand-field manifold followed by ground-state recovery.

4.3.4 Ground- and Excited-State Characterization of $[Fe(bpyNPy)_2]^{2+}$ and $[Fe(phenNPy)_2]^{2+}$

After reinforcing that thought the imidazolium-based carbene systems have been promising within the context of the studies performed by various groups, it would be beneficial to be able to maintain the light absorption properties associated with polypyridyl ligands while also enforcing a stronger ligand-field strength through strong σ-donors. This initial thrust was undertaken by our

group in the synthesis of a tris(heteroleptic) Fe(II) complex, $[Fe(phen)_2(C_4H_{10}N_4)](BF_4)_2$ (Figure 4.10)[37] By combining the directionality in the charge-transfer with the phenanthroline ligands while concomitantly increasing the ligand-field strength through the use of an acyclic diaminocarbene, a complex with the light absorbing properties of a typical polypyridyl complex was made but with the kinetics observed for strongly donating carbenes.[37] Though this is a promising route for new Fe(II) complexes, there are synthetic drawbacks as the synthesis of the complex requires a large excess of a cyanide source, a strong alkylating reagent, as well as the use of hydrazine.

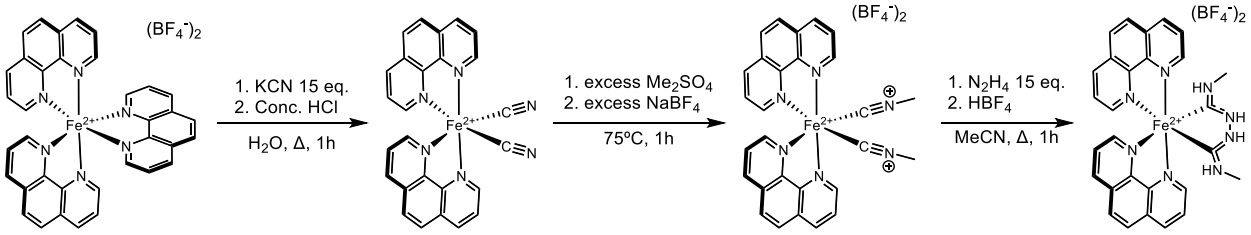

Figure 4.10. Synthetic route for the synthesis of bis(phenanthroline) acyclic diaminocarbene, $[Fe(phen)_2(C_4H_{10}N_4)](BF_4)_2$ starting from $[Fe(phen)_3](BF_4)_2$.

To that end, a new family of complexes were envisioned with simplicity in their synthesis while maintaining a similar motif. Looking at the relative donor strength of carbene-based ligands, there is a correlation between the number of heteroatoms in the coordinating ring and the donor ability. As more heteroatoms are incorporated, the relative donor strength is decreased due to stabilization of the carbene electronic structure via resonance forms (Figure 4.11a). An alternative donor that has been employed in Ru(II), Ir(III), and Pt(II) chemistry is the pyridinium.[42,59,66–69] These systems, unlike the imidazolium-based ligands, lack the stabilization of two heteroatoms in the mesomeric form leading to an increased donor ability comparatively (Figure 4.11b).[70] Two new ligands and

complexes containing this functionality were then synthesized to begin to investigate any new photophysical properties that may arise.

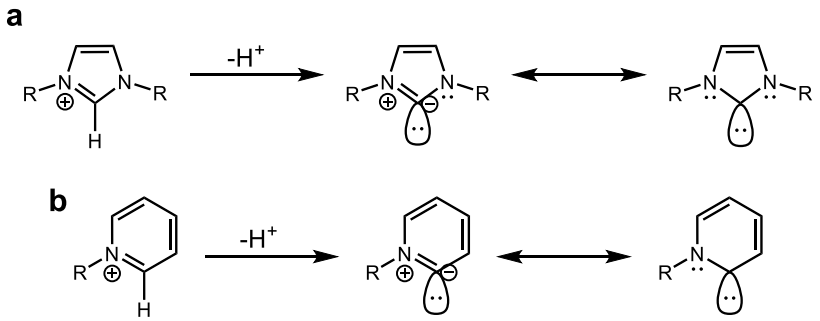

Figure 4.11. Ylidene and mesomeric resonance forms contributing to the stability of (a) 2-imidazolium carbenes and (b) *N*-pyridinium carbenes.

The ground-state electronic absorption of these new complexes, $[Fe(phenNPy)_2](PF_6)_2$ and $[Fe(bpyNPy)_2](PF_6)_2$, are markedly different from the those observed for the imidazolium-based carbenes as well as the parent tris complexes (Figure 4.12). For both the phenNPy and bpyNPy complexes, a bathochromic shift in λ_{max} in the assigned ^{1}MLCT envelope is observed corresponding to 69 nm and 58 nm, respectively, compared to the tris complexes. For the phenNPy complex, the structure of the MLCT manifold is for the most part maintained with multiple obvious transitions contained within as well as a similar molar absorptivity. The bpyNPy complex has a broader absorption than the corresponding tris(bipyridine) complex as well as an increased molar absorptivity. These results are summarized in Table 4.3.

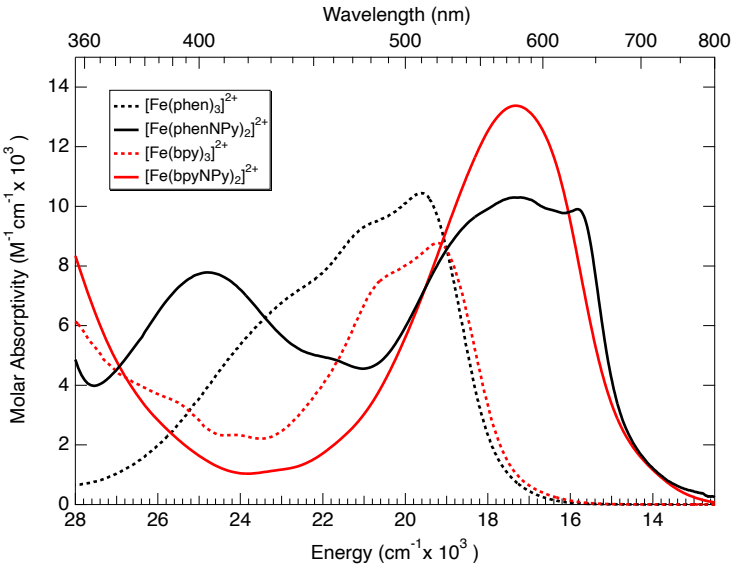

Figure 4.12. Ground-state electronic absorption spectra of $[Fe(phen)_3]^{2+}$ (black dashed), $[Fe(phenNPy)_2]^{2+}$ (solid black), $[Fe(bpy)_3]^{2+}$ (red dashed), and $[Fe(bpyNPy)_2]^{2+}$ (solid red) recorded in CH_3CN.

Table 4.3. Spectroscopic data of tris(polypyridyl) and bis(polypyridyl-*N*-pyridinium) complexes

Complex	λ_{max} nm	**Molar Absorptivity** $M^{-1}cm^{-1}$
$[Fe(bpy)_3](PF_6)_2$	520	8770
$[Fe(phen)_3](PF_6)_2$	510	10450
$[Fe(bpyNPy)_2](PF_6)_2$	578	13370
$[Fe(phenNPy)_2](PF_6)_2$	580	10300

Concluding with the spectroscopic measurements, electrochemical experiments were performed to begin to understand the shifting of the MLCT manifold in both complexes with respect to the parent molecules. Cyclic voltammetry and differential pulse voltammetry were performed to assess the strength of the donation of the two new ligands towards the Fe(II)-center as well as the ease of reduction of the ligand (Figure 4.13). Both $[Fe(phenNPy)_2]^{2+}$ and $[Fe(bpyNPy)_2]^{2+}$ have the same oxidation potential, within the uncertainty of the measurement, of 0.44 V which is assigned as a reversible $Fe^{II/III}$ couple. Unlike in the imidazolium systems which shows a slightly less positive oxidation for the phen-based complex by 20 mV (Table 4.2) these

current complexes are markedly the same. The differences in the electrochemistry arise in the reduction of the ligands. Both present a more positive irreversible reduction compared to the imidazolium-based ligands with potentials determined by DPV to be -1.44 V ($[Fe(bpyNPy)_2]^{2+}$) and -1.34 V ($[Fe(phenNPy)_2]^{2+}$) (Table 4.4). The electrochemical data is in agreement with the observed bathochromic shift in MLCT envelope with the ligand reductions being so facile.

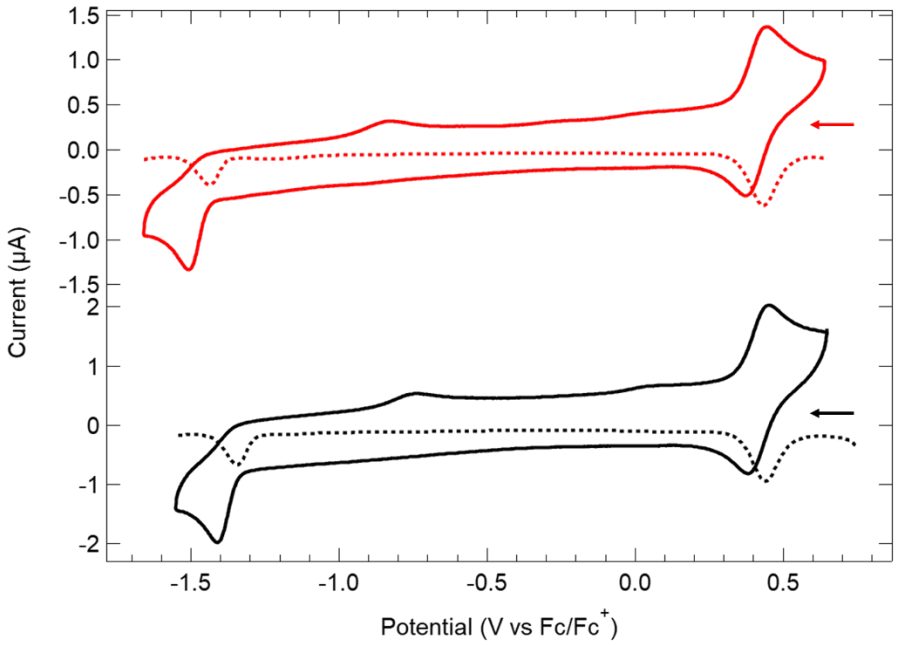

Figure 4.13. Cyclic voltammetry (solid traces) and DPV (dashed traces) of $[Fe(bpyNPy)_2](PF_6)_2$ (red) and $[Fe(phenNPy)_2](PF_6)_2$ (black) in CH_3CN. Reversible positive couples are assigned as FeII/III couple and the negative irreversible reductions are assigned as -formation of the $bpyNPy^{\bullet-}$ or $phenNPy^{\bullet-}$ ions. Arrows indicate scan direction for both CV and DPV.

Table 4.4. Electrochemical data collected for $[Fe(bpyNPy)_2](PF_6)_2$ and $[Fe(phenNPy)_2](PF_6)_2$ in CH_3CN. Potentials reported are from DPV and referenced to Fc/Fc^+

Complex	E_{ox} (V)	E_{red} (V)
$[Fe(bpyNPy)_2](PF_6)_2$	0.44	-1.44
$[Fe(phenNPy)_2](PF_6)_2$	0.44	-1.34

With the electrochemical data in hand, spectroelectrochemistry was performed on $[Fe(bpyNPy)_2]^{2+}$ in CH_3CN (Figure 4.14). The oxidative spectrum shows an increase in absorbance near 430 nm (Figure 4.14a) as well as multiple clean isosbestic points pointing to the reversibility of the oxidation. This increase is also observed in the reductive spectrum in addition to a weak, broad feature beginning around 690 nm and continuing well into the near-IR. This spectrum also exhibits isosbestic points, but due to the irreversibility of the reduction they shift over time. The weak and broad feature is attributed to the $bpyNPy^{\bullet-}$ absorbance and will be diagnostic in ultrafast transient absorption measurements for the presence of charge transfer state. The simulated MLCT transient absorption full spectrum is shown in Figure 4.14c. Using the simulated spectrum we can tailor the pump-probe combinations to begin to dissect the excited-state dynamics of this complex, probing the two cumulative positive absorbances.

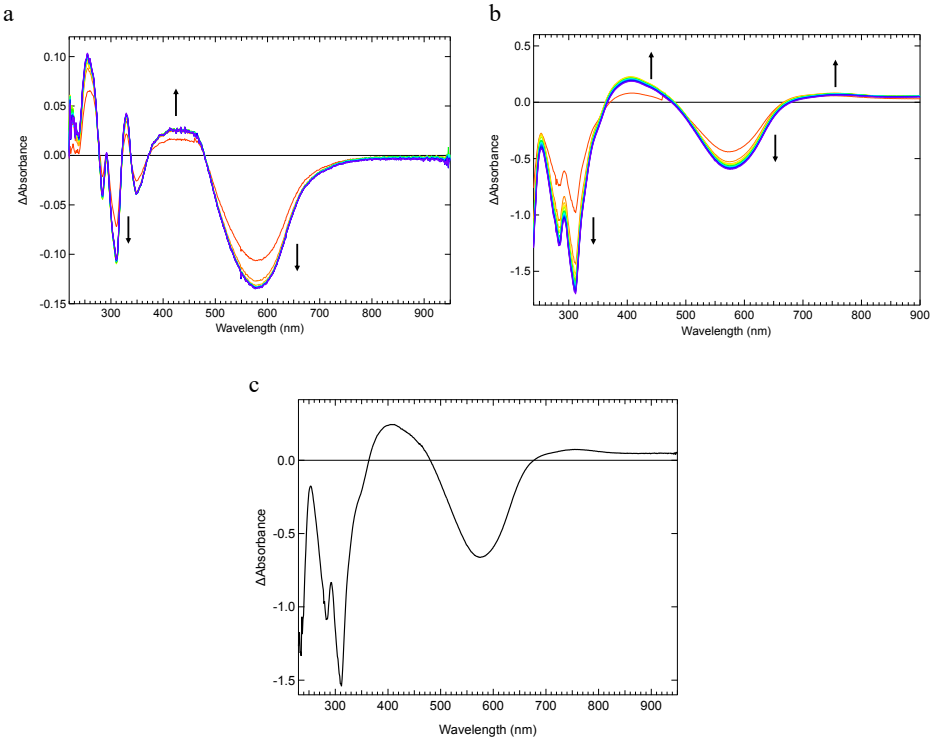

Figure 4.14. Spectroelectrochemical measurements of $[Fe(bpyNPy)_2]^{2+}$ in CH_3CN showing the (a) Oxidative (b) Reductive and (c) Combined simulated full spectrum of the MLCT.

Preliminary ultrafast transient absorption measurements were performed on $[Fe(bpyNPy)_2]^{2+}$ (Figure 4.15) using a pump wavelength of 555 nm and three different probe wavelengths encompassing the two positive features in Figure 4.14c as well as the bleach of the ground-state. The pump-probe combination of 555 nm and 600 nm, respectively, presents a biexponential decay with two time constants, τ_1 = 3 ps and τ_2 = 18 ps. The first time constant is tentatively assigned as vibrational cooling on the excited-state surface and τ_2 representing GSR. To further determine the origin of τ_2, probe wavelengths of 430 nm and 690 nm were chosen. Both decays exhibit biphasic kinetics with the shorter time constants again being assigned as vibrational cooling of the excited-state. The second time constant, specifically using a probe wavelength of 690 nm, presents with the same decay as the ground-state recovery. The concomitant decay of the excited-state absorption coupled with the recovery of the ground-state gives strong evidence to indicate that these kinetics are coming from the same state. In addition, the behavior that the traces using 430 nm and 690 nm do not change sign from positive to negative over the course of the decay as was observed in the $[Fe(phen^{Me}Im)_2]^{2+}$ complex (Figure 4.8) alludes to the state that is being sampled is the ^{3}MLCT and not a ^{3,5}MC state that is typically observed for Fe(II) polypyridyl complexes with only two carbene donors.(carbene references with MC LEES) If the 3MLCT is now the lowest energy excited state for this complex, then it more closely resembles the motifs predicted by Dixon et al. whereby cyclometallation with a N_4C_2 coordination environment could reverse the energetic ordering the ligand-field and MLCT manifolds.[71,72]

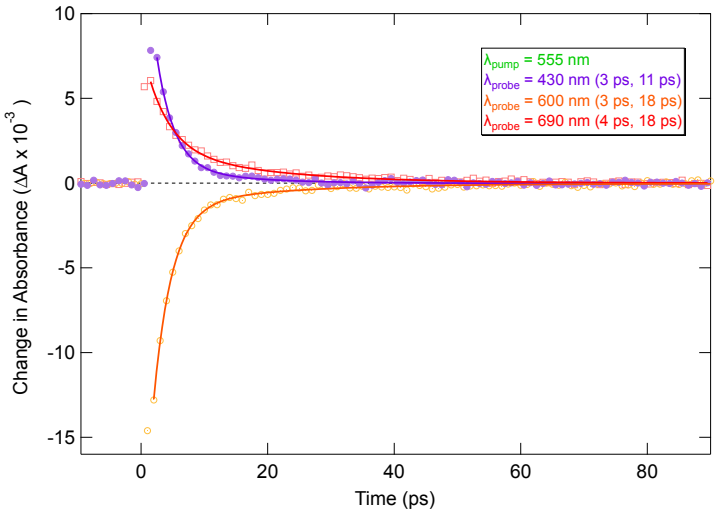

Figure 4.15. Single wavelength ultrafast transient absorption measurements in CH_3CN and biexponential fits using a pump wavelength of 555 nm and probe wavelengths of 430 nm (purple), 600 nm (orange), and 690 nm (red) to probe excited-state dynamics.

A beginning step to give strength to this conclusion, we can measure the donor strength of the imidazolium and pyridinium systems. A typical procedure to ascertain the σ-donor strength of carbene ligands is to use ^{1}H-coupled ^{13}C NMR spectroscopy on a series of carbene ligands on a metal-center.[73,74] The $^{1}J_{CH}$ coupling determined from the spectrum can then be correlated to the σ-donor ability of the ligand using an empirical correlation between the coupling constant and the s-orbital fraction for the hybridization. The lower the $^{1}J_{CH}$ coupling constant is the lower the amount of s-character (where s is the s-character) in the hybrid, the stronger a σ-donor the ligand is (equation 4.2).[73] The downside to this technique is the large amount of sample required due to the insensitivity of ^{13}C NMR as well as the spectrum being coupled. It has been shown that ^{1}H NMR is able to glean the same information but can rely on the sensitivity of the proton and observe the ^{13}C satellites of the carbenic proton.[75] Measuring the distance in Hertz between the satellites and using the equation below allows for the indirect quantification of the strength of donation.

$$^{1}J_{CH} = 500 * s \tag{4.2}$$

From the studies done by Szostak and coworkers, various Arduengo-type carbenes were investigated including cyclic alkylamino carbenes and their $^{1}J_{CH}$ coupling constants reported.[75] We then applied this technique to the protonated [bpyNPyH]PF_6 ligand in CH_3CN (Figure 4.16). From the ^{13}C satellites of the pyridinium 2- and 6-protons a $^{1}J_{CH}$ coupling constant of 194.42 Hz was found or a percent s-character of 38.9% using equation 4.2. Comparing this value to that of the constants determined in the previous study (Table 4.5) we can see that the pyridinium-based systems are closer in donor ability to the extremely strong cyclic alkylamino carbenes than the imidazolium-based systems. This method only determines the σ-donor ability of the ligands and a more in-depth study beginning to measure the π-accepting/donor nature of the ligand would also give more insight into its electronic structure as well as the potential interactions with the metal center utilized. Looking back to the ultrafast TA data collected this would strengthen the argument that we are seeing kinetic most likely associated with the ^{3}MLCT manifold as the imidazolium complex studied in section 4.3.3 is a weaker donor and showed kinetics corresponding to $^{3,5}MC \rightarrow {}^{1}A_1$ with a time constant of 187 ps, and the excited-state absorption transitioned to another electronic state by TA by the single-wavelength kinetics switching from a positive to negative signal. The data presented in this section warrants more in-depth experiments to accurately understand the photocycle of $[Fe(bpyNPy)_2]^{2+}$ but presents as an interesting a new ligand motif for the electronic state inversion of Fe(II) polypyridyl complexes. Ultrafast transient absorption measurements were attempted on the phenNPy analogues complex, but at the moment we believe it undergoes photo-decomposition as the 5,6-bond of the ligand is extremely susceptible to breaking. At this time, we have not collected further data on the complex but the use of a flow cell or modifying the excitation energy could potentially allow us to make comparisons between these two new complexes. Though ultrafast measurements on $[Fe(phenNPy)_2]^{2+}$ have been precluded

due to stability issues, we can still begin to glean more information from the two complexes from a computational perspective.

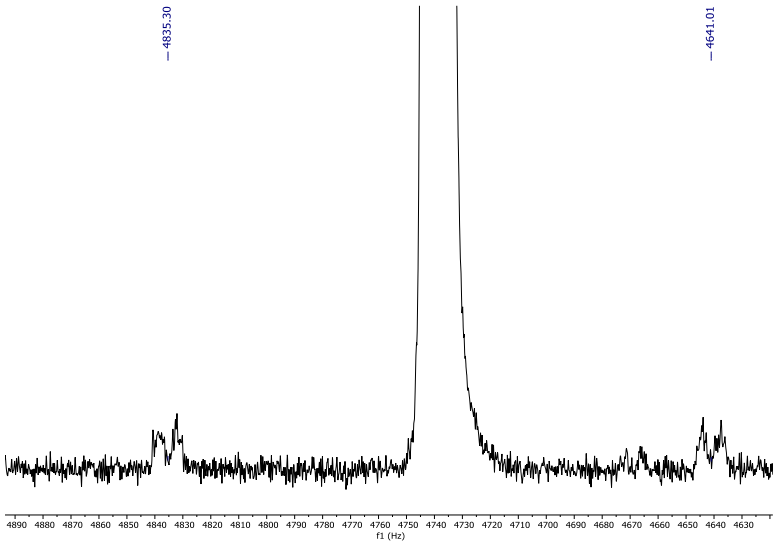

Figure 4.16. Expanded region of the pyridinium 2,6-protons of [bpyNPyH]PF_6 in CH_3CN showing the ^{13}C satellites and their corresponding chemical shifts in Hz for the determination of the $^1J_{CH}$ coupling constant.

Table 4.5. $^1J_{CH}$ coupling constants from ^{13}C satellites of an imidazolium, a cyclic alkylamino, and pyridinium-based carbenes with their corresponding s-character and *sp*-hybridizations

Azolium Salt	$^1J_{CH}$ (Hz)	s-character (%)	Hybridization
[N,N′-$^{t\text{Bu}}$Im]Br[a]	219.35	43.9	$sp^{1.27}$
[CAAC^{Cy}]Cl[a]	188.53	37.7	$sp^{1.65}$
[bpyNPy]PF_6	194.42	38.9	$sp^{1.57}$

Both complexes were modeled using a modified B3LYP* functional with the Hartree-Fock exact exchange lowered to 5% so as to create a better energetic match between the experimental spectra and those simulated by TD-DFT. This in-turn allows for the calculation of an energetic landscape that will more closely match the synthesized complex. Geometry optimizations were performed using B3LYP5+D2/SDD/6-311G(d) (SDD on Fe and 6-311G(d) on all other atoms) as well as single-point energy calculations (B3LYP5+D2/6-311G(d)) were carried out on

$[Fe(bpyNPy)_2]^{2+}$ and $[Fe(phenNPy)_2]^{2+}$. The comparisons of the experimental and simulated spectra are shown below in Figure 4.17 using the modified B3LYP5 functional.

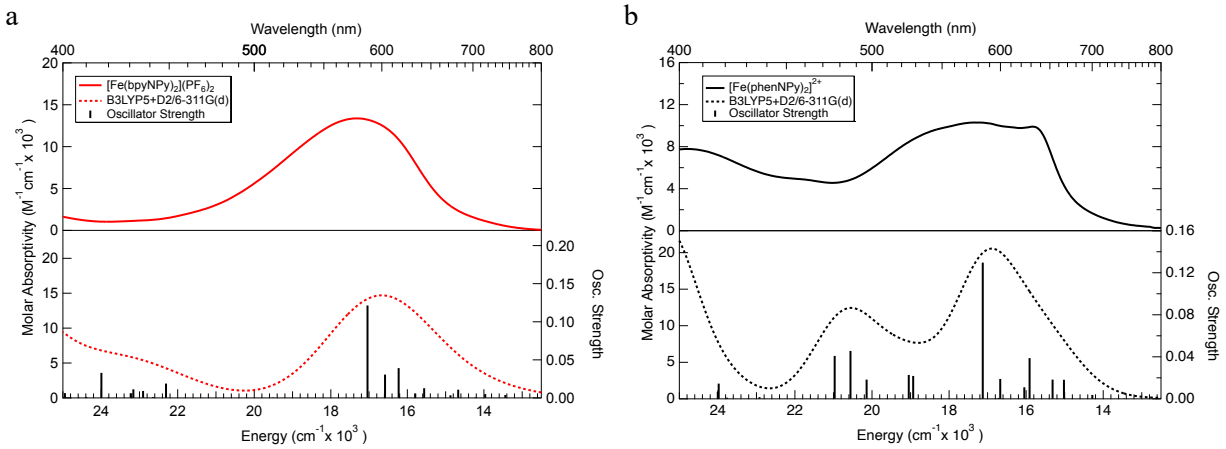

Figure 4.17. Comparison of experimental (solid) and simulated spectra (dashed) of (a) $[Fe(bpyNPy)_2]^{2+}$ and (b) $[Fe(phenNPy)_2]^{2+}$. Simulated spectra are modeled with a FWHM of 1200 cm^{-1}.

Both complexes match satisfactorily with the onset of the MLCT manifold but the phenNPy complex (Figure 4.17a) lacks the structure that is present in the experimental spectrum, likely due to the differences in FWHM needed to model each transition within the $^1A_1 \rightarrow {}^1$MLCT manifold. For each complex there is one transition which accounts for the highest oscillator strength but is of highly mixed character. To disentangle the transitions natural transition orbital (NTO) theory was used.[76] This procedure, which is part of the Gaussian16 package, allows for the density matrix of a transition to be decomposed and create a more compact and easily viewed particle-hole pair to better understand heavily mixed transitions which are listed by percent composition but differ from the use of the Slater Coefficients. The pairs that comprise the highest oscillator strength transition for each complex are shown in Figure 4.18. For both complexes the transition is characterized as MLCT in character. The orbitals from which each transition arises are primarily

localized on the iron-center as well as the rings closest to the pyridinium and the Fe-C bond. The final orbitals are symmetrically delocalized across the entire ligand backbone.

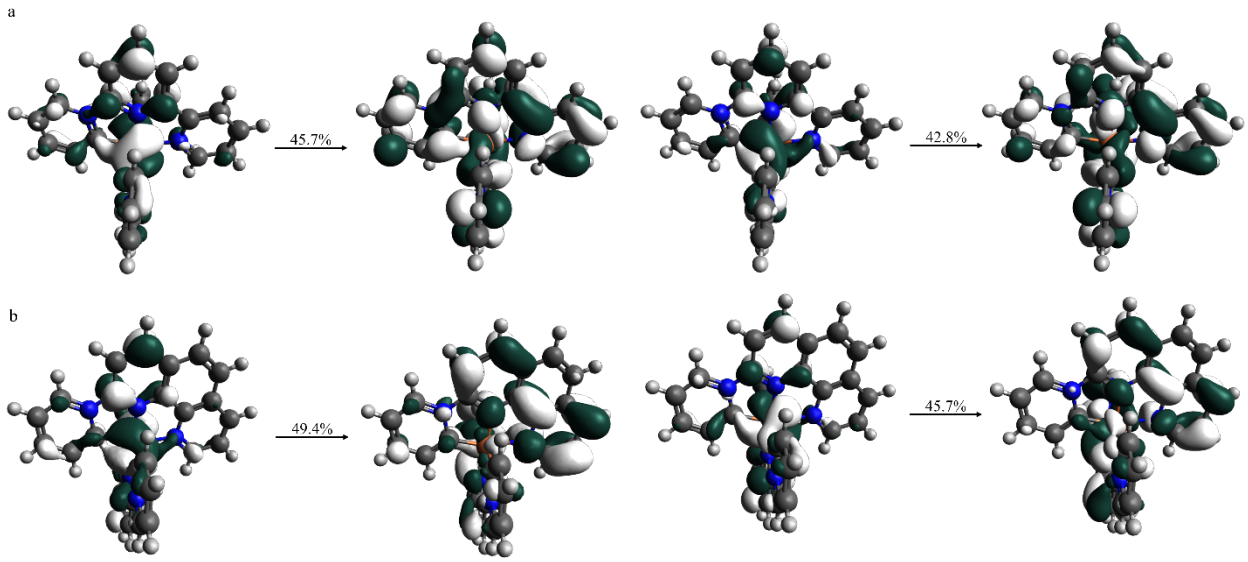

Figure 4.18. NTO decomposition of the highest intensity transition for (a) $[Fe(bpyNPy)_2]^{2+}$ and (b) $[Fe(phenNPy)_2]^{2+}$. Above each arrow is the percent composition of each transition. Each is displayed at an isosurface value of 0.02.

In continuing computational studies to better understand the energetic landscape of the pyridylidene complexes, spin-state energy diagrams as a function of the average Fe-N nuclear coordinate were calculated at the singlet, triplet, and quintet equilibrium geometries (Figure 4.19). The Fe-N coordinate was chosen instead of the Fe-C coordinate as the largest changes in geometry are expected to occur in the expansion of the nitrogen bonds as the carbon bonds will have a higher force constant and therefore a smaller variation. Analyzing the spin-state energetics of both complexes shows a reordering of the LF manifold with the ^{3}MC state now below the ^{5}MC state. The energetics of both complexes are very similar in the LF manifold apart for the average Fe-N bond lengths at the equilibrium geometries. The ^{1}MLCT vertical transition and the relaxed equilibrium geometry are close in energy to the ^{3}MC surface for $[Fe(bpyNPy)_2]^{2+}$ (Figure 4.19a).

Currently, efforts to determine the potential energy surface for the ^{3}MLCT have not been successful. Though, knowing the proximity of the ^{1}MLCT surface to the triplet surface and knowing that the ^{3}MLCT state will be lower in energy than the ^{1}MLCT, the surface could be nested within the ^{3}MC surface or below, assigning the ^{3}MLCT as the lowest energy excited state. The two states could also be close enough in energy in that an equilibrium between the two could be established as what was hypothesized in our previous carbene study.[37] Regardless, the new pyridinium motifs have promise in creating a new family of complexes with low energy MLCT manifolds, ease of modification of the ligand backbone, and picosecond MLCT lifetimes with simple synthetic methodologies.

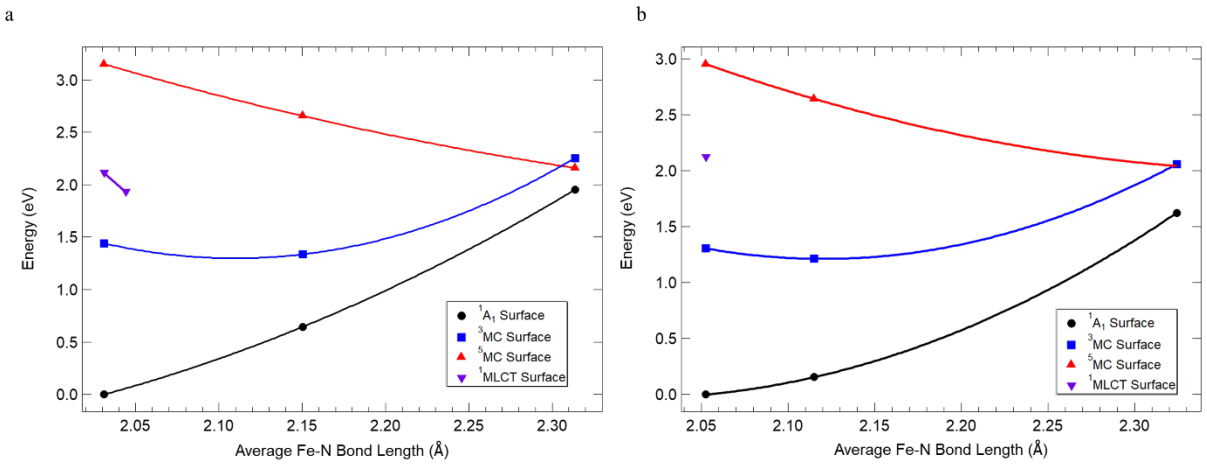

Figure 4.19. Potential energy surface diagrams of the ^{1}A$_1$ ground-state (black), ^{3}MC state (blue), ^{5}MC state, and ^{1}MLCT vertical transition (purple) of (a) $[Fe(bpyNPy)_2]^{2+}$ and (b) $[Fe(phenNPy)_2]^{2+}$. Data points were fit to a 2nd-order polynomial to guide the eye (solid line).

4.4 Concluding Remarks

In this study we have continued on the work of the Bauer group as well as our own carbene systems. The results of the $[Fe(phenMeIm)_2]^{2+}$ agree with the analogous bipyridyl complex in which the lowest energy excited state populated after photoexcitation is a ligand-field state with a

time constant of 187 ps and a prolonged ^{3}MLCT lifetime between 390-600 fs. Building upon the use of Arduengo-type carbenes we investigated the ground- and excited-state electronic structure of pyridinium-based polypyridyl complexes, $[Fe(bpyNPy)_2]^{2+}$ and $[Fe(phenNPy)_2]^{2+}$. These complexes exhibit bathochromically shifted $^1A_1 \rightarrow {}^1$MLCT transitions which are driven by the ease of reduction of the pyridinium ligands. The photophysical measurements of $[Fe(bpyNPy)_2]^{2+}$ exhibits excited-state lifetimes of 4 ps and 18 ps. The shorter time constant was assigned as vibrational cooling on the excited-state surface while the longer time constant was determined to be MLCT in character, ^{3}MLCT. This lifetime is on the same magnitude as our previous system using acyclic diaminocarbenes but presents with a more facile and less hazardous synthesis. Our computational results suggest we have reached the point of LF inversion where the ordering of the $^3T_{1,2}$ states are now below the $^5T_2$. Continuing computational work to determine the energetic ordering of the states more accurately as well as the full ^{1}MLCT and ^{3}MLCT surfaces is ongoing. Further spectroscopic work for this system will be the collection of shorter timescale kinetics as well as solvent studies and full spectra collection. Changing the dielectric constant of the solvent will manifest in the kinetics of the MLCT decay where the more polar solvents will be able to better stabilize the radical anion formed and should allow for a longer persisting signal than with lower dielectric solvents. Full spectrum collection will allow us to assign the shorter time component as vibrational cooling with more confidence as the spectral changes can be more clearly seen. These systems prove promising in their unique photophysics and ground-state properties towards potential applications in photoinduced electron transfer processes and will be an ongoing study.

REFERENCES

(1) Shaw, M. H.; Twilton, J.; MacMillan, D. W. C. Photoredox Catalysis in Organic Chemistry. *J. Org. Chem.* **2016**, *81* (16), 6898–6926. DOI: 10.1021/acs.joc.6b01449.

(2) Prier, C. K.; Rankic, D. A.; MacMillan, D. W. C. Visible Light Photoredox Catalysis with Transition Metal Complexes: Applications in Organic Synthesis. *Chem. Rev.* **2013**, *113* (7), 5322–5363. DOI: 10.1021/cr300503r.

(3) Chan, A. Y.; Perry, I. B.; Bissonnette, N. B.; Buksh, B. F.; Edwards, G. A.; Frye, L. I.; Garry, O. L.; Lavagnino, M. N.; Li, B. X.; Liang, Y.; Mao, E.; Millet, A.; Oakley, J. V.; Reed, N. L.; Sakai, H. A.; Seath, C. P.; MacMillan, D. W. C. Metallaphotoredox: The Merger of Photoredox and Transition Metal Catalysis. *Chem. Rev.* **2022**, *122* (2), 1485–1542. DOI: 10.1021/acs.chemrev.1c00383.

(4) Dogutan, D. K.; Nocera, D. G. Artificial Photosynthesis at Efficiencies Greatly Exceeding That of Natural Photosynthesis. *Acc. Chem. Res.* **2019**, *52* (11), 3143–3148. DOI: 10.1021/acs.accounts.9b00380.

(5) Cebrián, C.; Pastore, M.; Monari, A.; Assfeld, X.; Gros, P. C.; Haacke, S. Ultrafast Spectroscopy of Fe(II) Complexes Designed for Solar-Energy Conversion: Current Status and Open Questions. *ChemPhysChem* **2022**, *23* (7), e202100659. DOI: 10.1002/CPHC.202100659.

(6) Ponseca, C. S.; Chábera, P.; Uhlig, J.; Persson, P.; Sundström, V. Ultrafast Electron Dynamics in Solar Energy Conversion. *Chem. Rev.* **2017**, *117* (16), 10940–11024. DOI: 10.1021/acs.chemrev.6b00807.

(7) Tomar, N.; Agrawal, A.; Dhaka, V. S.; Surolia, P. K. Ruthenium Complexes Based Dye Sensitized Solar Cells: Fundamentals and Research Trends. *Solar Energy* **2020**, *207*, 59–76. DOI: 10.1016/j.solener.2020.06.060.

(8) Brauer, J. C.; Marchioro, A.; Paraecattil, A. A.; Oskouei, A. A.; Moser, J. E. Dynamics of Interfacial Charge Transfer States and Carriers Separation in Dye-Sensitized Solar Cells: A Time-Resolved Terahertz Spectroscopy Study. *J. Phys. Chem. C* **2015**, *119* (47), 26266–26274. DOI: 10.1021/acs.jpcc.5b06911.

(9) Bozic-Weber, B.; Constable, E. C.; Housecroft, C. E. Light Harvesting with Earth Abundant D-Block Metals: Development of Sensitizers in Dye-Sensitized Solar Cells (DSSCs). *Coord. Chem. Rev.* **2013**, *257* (21–22), 3089–3106. DOI: 10.1016/j.ccr.2013.05.019.

(10) Campagna, S.; Puntoriero, F.; Nastasi, F.; Bergamini, G.; Balzani, V. Photochemistry and Photophysics of Coordination Compounds: Ruthenium. In *Photochemistry and Photophysics of Coordination Compounds I*; Springer Berlin Heidelberg: Berlin, Heidelberg, 2007; Vol. 280, pp 117–214. DOI: 10.1007/128_2007_133.

(11) Hofbeck, T.; Yersin, H. The Triplet State of *Fac* -Ir(Ppy)$_3$. *Inorg. Chem.* **2010**, *49* (20), 9290–9299. DOI: 10.1021/ic100872w.

(12) Lee, G. S.; Hong, S. H. Direct C(sp^3)–H Acylation by Mechanistically Controlled Ni/Ir Photoredox Catalysis. *Acc. Chem. Res.* **2023**, *16*, 43. DOI: 10.1021/ACS.ACCOUNTS.3C00252.

(13) Schmidt, J.; Domenianni, L. I.; Leuschner, M.; Gansäuer, A.; Vöhringer, P. Observing the Entry Events of a Titanium-Based Photoredox Catalytic Cycle in Real Time. *Angew. Chem. Int. Ed.* **2023**, *62* (35), e202307178. DOI: 10.1002/ANIE.202307178.

(14) Treiling, S.; Wang, C.; Förster, C.; Reichenauer, F.; Kalmbach, J.; Boden, P.; Harris, J. P.; Carrella, L. M.; Rentschler, E.; Resch-Genger, U.; Reber, C.; Seitz, M.; Gerhards, M.; Heinze, K. Luminescence and Light-Driven Energy and Electron Transfer from an Exceptionally Long-Lived Excited State of a Non-Innocent Chromium(III) Complex. *Angew. Chem. Int. Ed.* **2019**, *131* (50), 18243–18253. DOI: 10.1002/ange.201909325.

(15) Dorn, M.; East, N. R.; Förster, C.; Kitzmann, W. R.; Moll, J.; Reichenauer, F.; Reuter, T.; Stein, L.; Heinze, K. D-d and Charge Transfer Photochemistry of 3d Metal Complexes. In *Comprehensive Inorganic Chemistry III*; Reedijk, J., Poeppelmeier, K. R., Eds.; Elsevier, 2023; pp 707–788. DOI: 10.1016/B978-0-12-823144-9.00063-7.

(16) Reuter, T.; Kruse, A.; Schoch, R.; Lochbrunner, S.; Bauer, M.; Heinze, K. Higher MLCT Lifetime of Carbene Iron(II) Complexes by Chelate Ring Expansion. *Chem. Commun.* **2021**, *57* (61), 7541–7544. DOI: 10.1039/D1CC02173G.

(17) Braun, J. D.; Lozada, I. B.; Kolodziej, C.; Burda, C.; Newman, K. M. E.; van Lierop, J.; Davis, R. L.; Herbert, D. E. Iron(II) Coordination Complexes with Panchromatic Absorption and Nanosecond Charge-Transfer Excited State Lifetimes. *Nat. Chem.* **2019**, *11* (12), 1144–1150. DOI: 10.1038/s41557-019-0357-z.

(18) Rentschler, M.; Schmid, M. A.; Frey, W.; Tschierlei, S.; Karnahl, M. Multidentate Phenanthroline Ligands Containing Additional Donor Moieties and Their Resulting Cu(I) and Ru(II) Photosensitizers: A Comparative Study. *Inorg. Chem.* **2020**, *59* (20), 14762–14771. DOI: 10.1021/acs.inorgchem.9b03687.

(19) Kjær, K. S.; Kaul, N.; Prakash, O.; Chábera, P.; Rosemann, N. W.; Honarfar, A.; Gordivska, O.; Fredin, L. A.; Bergquist, K.-E.; Häggström, L.; Ericsson, T.; Lindh, L.; Yartsev, A.; Styring, S.; Huang, P.; Uhlig, J.; Bendix, J.; Strand, D.; Sundström, V.; Persson, P.; Lomoth, R.; Wärnmark, K. Luminescence and Reactivity of a Charge-Transfer Excited Iron Complex with Nanosecond Lifetime. *Science* **2019**, *363* (6424), 249–253. DOI: 10.1126/science.aau7160.

(20) Büldt, L. A.; Guo, X.; Prescimone, A.; Wenger, O. S. A Molybdenum(0) Isocyanide Analogue of Ru(2,2′-Bipyridine)$_3^{2+}$: A Strong Reductant for Photoredox Catalysis. *Angew. Chem. Int.l Ed.* **2016**, *55* (37), 11247–11250. DOI: 10.1002/anie.201605571.

(21) Büldt, L. A.; Wenger, O. S. Chromium(0), Molybdenum(0), and Tungsten(0) Isocyanide Complexes as Luminophores and Photosensitizers with Long-Lived Excited States. *Angew. Chem. Int. Ed.* **2017**, *56* (21), 5676–5682. DOI: 10.1002/ANIE.201701210.

(22) Wegeberg, C.; Häussinger, D.; Wenger, O. S. Pyrene-Decoration of a Chromium(0) Tris(Diisocyanide) Enhances Excited State Delocalization: A Strategy to Improve the Photoluminescence of $3d^6$ Metal Complexes. *J. Am. Chem. Soc.* **2021**, *143* (38), 15800–15811. DOI: 10.1021/jacs.1c07345.

(23) Kaufhold, S.; Rosemann, N. W.; Chábera, P.; Lindh, L.; Bolaño Losada, I.; Uhlig, J.; Pascher, T.; Strand, D.; Wärnmark, K.; Yartsev, A.; Persson, P. Microsecond Photoluminescence and Photoreactivity of a Metal-Centered Excited State in a Hexacarbene-Co(III) Complex. *J. Am. Chem. Soc.* **2021**, *143* (3), 1307–1312. DOI: 10.1021/jacs.0c12151.

(24) Chan, A. Y.; Ghosh, A.; Yarranton, J. T.; Twilton, J.; Jin, J.; Arias-Rotondo, D. M.; Sakai, H. A.; McCusker, J. K.; MacMillan, D. W. C. Exploiting the Marcus Inverted Region for First-Row Transition Metal–Based Photoredox Catalysis. *Science* **2023**, *382* (6667), 191–197. DOI: 10.1126/SCIENCE.ADJ0612.

(25) Mandal, T.; Katta, N.; Paps, H.; Reiser, O. Merging Cu(I) and Cu(II) Photocatalysis: Development of a Versatile Oxohalogenation Protocol for the Sequential Cu(II)/Cu(I)-Catalyzed Oxoallylation of Vinylarenes. *ACS Org. Inorg. Au* **2023**, *3* (4), 171–176. DOI: 10.1021/ACSORGINORGAU.3C00011.

(26) McCusker, C. E.; Castellano, F. N. Design of a Long-Lifetime, Earth-Abundant, Aqueous Compatible Cu(I) Photosensitizer Using Cooperative Steric Effects. *Inorg. Chem.* **2013**, *52* (14), 8114–8120. DOI: 10.1021/IC401213P.

(27) McCusker, J. K. Electronic Structure in the Transition Metal Block and Its Implications for Light Harvesting. *Science* **2019**, *363* (6426), 484–488. DOI: 10.1126/science.aav9104.

(28) Wenger, O. S. Is Iron the New Ruthenium? *Chem. Euro. J.* **2019**, *25* (24), 6043–6052. DOI: 10.1002/chem.201806148.

(29) Creutz, C.; Chou, M.; Netzel, T. L.; Okumura, M.; Sutin, N. Lifetimes, Spectra, and Quenching of the Excited States of Polypyridine Complexes of Iron(II), Ruthenium(II), and Osmium(II). *J. Am. Chem. Soc.* **1980**, *102* (4), 1309–1319. DOI: 10.1021/ja00524a014.

(30) Monat, J. E.; McCusker, J. K. Femtosecond Excited-State Dynamics of an Iron(II) Polypyridyl Solar Cell Sensitizer Model. *J. Am. Chem. Soc.* **2000**, *122* (17), 4092–4097. DOI: 10.1021/ja992436o.

(31) Woodhouse, M. D.; McCusker, J. K. Mechanistic Origin of Photoredox Catalysis Involving Iron(II) Polypyridyl Chromophores. *J. Am. Chem. Soc.* **2020**, *142* (38), 16229–16233. DOI: 10.1021/jacs.0c08389.

(32) Liu, Y.; Harlang, T.; Canton, S. E.; Chábera, P.; Suárez-Alcántara, K.; Fleckhaus, A.; Vithanage, D. A.; Göransson, E.; Corani, A.; Lomoth, R.; Sundström, V.; Wärnmark, K. Towards Longer-Lived Metal-to-Ligand Charge Transfer States of Iron(II) Complexes: An N-Heterocyclic Carbene Approach. *Chem. Commun.* **2013**, *49* (57), 6412. DOI: 10.1039/c3cc43833c.

(33) Duchanois, T.; Etienne, T.; Cebrián, C.; Liu, L.; Monari, A.; Beley, M.; Assfeld, X.; Haacke, S.; Gros, P. C. An Iron-Based Photosensitizer with Extended Excited-State Lifetime: Photophysical and Photovoltaic Properties. *Eur. J. Inorg. Chem.* **2015**, *2015* (14), 2469–2477. DOI: 10.1002/ejic.201500142.

(34) Liu, L.; Duchanois, T.; Etienne, T.; Monari, A.; Beley, M.; Assfeld, X.; Haacke, S.; Gros, P. C. A New Record Excited State ^{3}MLCT Lifetime for Metalorganic Iron(II) Complexes. *Phys. Chem. Chem. Phys.* **2016**, *18* (18), 12550–12556. DOI: 10.1039/c6cp01418f.

(35) Chábera, P.; Kjaer, K. S.; Prakash, O.; Honarfar, A.; Liu, Y.; Fredin, L. A.; Harlang, T. C. B.; Lidin, S.; Uhlig, J.; Sundström, V.; Lomoth, R.; Persson, P.; Wärnmark, K. FeII Hexa N-Heterocyclic Carbene Complex with a 528 Ps Metal-To-Ligand Charge-Transfer Excited-State Lifetime. *J. Phys. Chem. Lett.* **2018**, *9* (3), 459–463. DOI: 10.1021/acs.jpclett.7b02962.

(36) Leis, W.; Argüello Cordero, M. A.; Lochbrunner, S.; Schubert, H.; Berkefeld, A. A Photoreactive Iron(II) Complex Luminophore. *J. Am. Chem. Soc.* **2022**, *144* (3), 1169–1173. DOI: 10.1021/JACS.1C13083.

(37) Paulus, B. C.; Nielsen, K. C.; Tichnell, C. R.; Carey, M. C.; McCusker, J. K. A Modular Approach to Light Capture and Synthetic Tuning of the Excited-State Properties of Fe(II)-Based Chromophores. *J. Am. Chem. Soc.* **2021**, *143* (21), 8086–8098. DOI: 10.1021/jacs.1c02451.

(38) Zalas, M.; Gierczyk, B.; Klein, M.; Siuzdak, K.; Pędziński, T.; Łuczak, T. Synthesis of a Novel Dinuclear Ruthenium Polypyridine Dye for Dye-Sensitized Solar Cells Application. *Polyhedron* **2014**, *67*, 381–387. DOI: 10.1016/j.poly.2013.09.023.

(39) O'Duill, M. L.; Matsuura, R.; Wang, Y.; Turnbull, J. L.; Gurak, J. A.; Gao, D.-W.; Lu, G.; Liu, P.; Engle, K. M. Tridentate Directing Groups Stabilize 6-Membered Palladacycles in Catalytic Alkene Hydrofunctionalization. *J. Am. Chem. Soc.* **2017**, *139* (44), 15576–15579. DOI: 10.1021/jacs.7b08383.

(40) Bugaenko, D. I.; Yurovskaya, M. A.; Karchava, A. V. Reaction of Pyridine-N-Oxides with Tertiary Sp2-N-Nucleophiles: An Efficient Synthesis of Precursors for N-(Pyrid-2-yl)-Substituted N-Heterocyclic Carbenes. *Adv. Synth. Catal.* **2020**, *362* (24), 5777–5782. DOI: 10.1002/adsc.202001063.

(41) Gründemann, S.; Albrecht, M.; Loch, J. A.; Faller, J. W.; Crabtree, R. H. Tridentate Carbene CCC and CNC Pincer Palladium(II) Complexes: Structure, Fluxionality, and Catalytic Activity. *Organometallics* **2001**, *20* (25), 5485–5488. DOI: 10.1021/om010631h.

(42) Koizumi, T.; Tomon, T.; Tanaka, K. Synthesis and Electrochemical Properties of Bis(Bipyridine)Ruthenium(II) Complexes Bearing Pyridinyl- and Pyridinylidene Ligands Induced by Cyclometallation of N′-Methylated Bipyridinium Analogs. *J. Organomet. Chem.* **2005**, *690* (5), 1258–1264. DOI: 10.1016/j.jorganchem.2004.11.032.

(43) Sheldrick, G. M. SHELXT – Integrated Space-Group and Crystal-Structure Determination. *Acta Crystallogr. A* **2015**, *71* (1), 3–8. DOI: 10.1107/S2053273314026370.

(44) Dolomanov, O. v.; Bourhis, L. J.; Gildea, R. J.; Howard, J. A. K.; Puschmann, H. OLEX2 : A Complete Structure Solution, Refinement and Analysis Program. *J. Appl. Crystallogr.* **2009**, *42* (2), 339–341. DOI: 10.1107/S0021889808042726.

(45) Sheldrick, G. M. Crystal Structure Refinement with SHELXL. *Acta Crystallogr. C* **2015**, *71* (1), 3–8. DOI: 10.1107/S2053229614024218.

(46) Brown, A. M.; McCusker, C. E.; McCusker, J. K. Spectroelectrochemical Identification of Charge-Transfer Excited States in Transition Metal-Based Polypyridyl Complexes. *Dalton Trans.* **2014**, *43* (47), 17635–17646. DOI: 10.1039/c4dt02849j.

(47) Frisch, M. J.; Trucks, G. W.; Schlegel, H. B.; Scuseria, G. E.; Robb, M. A.; Cheeseman, J. R.; Scalmani, G.; Barone, V.; Petersson, G. A.; Nakatsuji, H.; Li, X.; Caricato, M.; Marenich, A. V.; Bloino, J.; Janesko, B. G.; Gomperts, R.; Mennucci, B.; Hratchian, H. P.; Ortiz, J. V.; Izmaylov, A. F.; Sonnenberg. J. L.; Williams-Young, D.; Ding, F.; Lipparini, F.; Egidi, F.; Goings, J.; Peng, B.; Petrone, A.; Henderson, T.; Ranasinghe, D.; Zakrzewski, G.; Gao, J.; Rega, N.; Zheng, G.; Liang, W.; Hada, M.; Ehara, M.; Toyota, K.; Fukada, R.; Hasegawa, J.; Ishida, M.; Nakajima, T.; Honda, Y.; Kitao, O.; Nakai, H.; Vreven, T.; Throssell, K.; Montgomery Jr., J. A.; Peralta, J. E.; Ogliaro, F.; Bearpark, M. J.; Heyd, J. J.; Brothers, E. N.; Kudin, K. N.; Staroverov., V. N.; Keith, T. A.; Kobayashi, R.; Normand, J.; Raghavachari, K.; Rendell, A. P.; Burant, J. C.; Iyengar, S. S.; Tomasi, .; Cossi, M.; Millam, J. M.; Klene, M.; Adamo, C.; Cammi, R.; Ochterski, J. W.; Martin, R. L.; Morokuma, K.; Farkas, O.; Foresman, J. B.; Fox, D. J. Gaussian 16, Rev B.01. Gaussian Inc.: Wallingford CT 2016.

(48) Becke, A. D. Density-Functional Exchange-Energy Approximation with Correct Asymptotic Behavior. *Phys. Rev. A* **1988**, *38*, 3098–3100.

(49) Grimme, S. Semiempirical GGA-Type Density Functional Constructed with a Long-Range Dispersion Correction. *J. Comput. Chem.* **2006**, *27* (15), 1787–1799. DOI: 10.1002/JCC.20495.

(50) Avogadro: An Open-Source Molecular Builder and Visualization Tool. http://avogadro.cc/.

(51) Hanwell, M. D.; Curtis, D. E.; Lonie, D. C.; Vandermeersch, T.; Zurek, E.; Hutchison, G. R. Avogadro: An Advanced Semantic Chemical Editor, Visualization, and Analysis Platform. *J. Cheminform.* **2012**, *4* (1), 17. DOI: 10.1186/1758-2946-4-17.

(52) Kim, H.-M.; Jeong, D.; Noh, H. C.; Kang, Y. K.; Chung, Y. K. Manipulation of Absorption Maxima by Controlling Oxidation Potentials in Bis(Tridentate) Ru(II) N-Heterocyclic Carbene Complexes. *Bull. Korean Chem. Soc.* **2014**, *35* (2), 448–456. DOI: 10.5012/bkcs.2014.35.2.448.

(53) Böttger, M.; Wiegmann, B.; Schaumburg, S.; Jones, P. G.; Kowalsky, W.; Johannes, H.-H. Synthesis of New Pyrrole–Pyridine-Based Ligands Using an in Situ Suzuki Coupling Method. *Beilstein J. Org. Chem.* **2012**, *8*, 1037–1047. DOI: 10.3762/bjoc.8.116.

(54) Vukadinovic, Y.; Burkhardt, L.; Päpcke, A.; Miletic, A.; Fritsch, L.; Altenburger, B.; Schoch, R.; Neuba, A.; Lochbrunner, S.; Bauer, M. When Donors Turn into Acceptors: Ground and

Excited State Properties of Fe^{II} Complexes with Amine-Substituted Tridentate Bis-Imidazole-2-Ylidene Pyridine Ligands. *Inorg. Chem.* **2020**, *59* (13), 8762–8774. DOI: 10.1021/acs.inorgchem.0c00393.

(55) Zimmer, P.; Burkhardt, L.; Friedrich, A.; Steube, J.; Neuba, A.; Schepper, R.; Müller, P.; Flörke, U.; Huber, M.; Lochbrunner, S.; Bauer, M. The Connection between NHC Ligand Count and Photophysical Properties in Fe(II) Photosensitizers: An Experimental Study. *Inorg. Chem.* **2018**, *57* (1), 360–373. DOI: 10.1021/acs.inorgchem.7b02624.

(56) Nguyen, T. M.; Sanchez-Salvatori, M. del R.; Wypych, J.-C.; Marazano, C. Aminopentadiene Imines from Zincke Salts of 3-Alkylpyridines. Application to a Synthesis of Pyridinium Salts from Amino Acids. *J. Org. Chem.* **2007**, *72* (15), 5916–5919. DOI: 10.1021/jo0707582.

(57) Vanderwal, C. D. Reactivity and Synthesis Inspired by the Zincke Ring-Opening of Pyridines. *J. Org. Chem.* **2011**, *76* (23), 9555–9567. DOI: 10.1021/jo201625e.

(58) Cheng, W.-C.; Kurth, M. J. THE ZINCKE REACTION. A REVIEW. *Org. Prep. Proced. Int.* **2002**, *34* (6), 585–608. DOI: 10.1080/00304940209355784.

(59) Koizumi, T.; Tomon, T.; Tanaka, K. Terpyridine-Analogous (N,N,C)-Tridentate Ligands: Synthesis, Structures, and Electrochemical Properties of Ruthenium(II) Complexes Bearing Tridentate Pyridinium and Pyridinylidene Ligands. *Organometallics* **2003**, *22* (5), 970–975. DOI: 10.1021/om020637m.

(60) Ghosh, A.; Yarranton, J. T.; McCusker, J. K. Photophysics of Cobalt(III) Polypyridyl Complexes: Ligand-Field Excited-State Dynamics in the Marcus Inverted Region. *submitted to Nat. Chem.* **2023**.

(61) Carey, M. C.; Adelman, S. L.; Mccusker, J. K. Insights into the Excited State Dynamics of Fe(II) Polypyridyl Complexes from Variable-Temperature Ultrafast Spectroscopy. *Chem. Sci.* **2019**, *10*, 134-144. DOI: 10.1039/c8sc04025g.

(62) Yarranton, J. T.; McCusker, J. K. Ligand-Field Spectroscopy of Co(III) Complexes and the Development of a Spectrochemical Series for Low-Spin d^6 Charge-Transfer Chromophores. *J. Am. Chem. Soc.* **2022**, *144* (27), 12488–12500. DOI: 10.1021/jacs.2c04945.

(63) Auböck, G.; Chergui, M. Sub-50-Fs Photoinduced Spin Crossover in $[Fe(Bpy)_3]^{2+}$. *Nat. Chem.* **2015**, *7* (8), 629–633. DOI: 10.1038/nchem.2305.

(64) Gawelda, W.; Cannizzo, A.; Pham, V.-T.; van Mourik, F.; Bressler, C.; Chergui, M. Ultrafast Nonadiabatic Dynamics of $[Fe^{II}(Bpy)_3]^{2+}$ in Solution. *J. Am. Chem. Soc.* **2007**, *129* (26), 8199–8206. DOI: 10.1021/ja070454x.

(65) Lee, A.; Son, M.; Deegbey, M.; Woodhouse, M. D.; Hart, S. M.; Beissel, H. F.; Cesana, P. T.; Jakubikova, E.; McCusker, J. K.; Schlau-Cohen, G. Observation of Parallel Intersystem Crossing and Charge Transfer-State Dynamics in $[Fe(Bpy)_3]^{2+}$ from Ultrafast 2D Electronic Spectroscopy. *Chem. Sci.* **2023**. DOI: 10.1039/D3SC02613B.

(66) Lam, T. L.; Lai, J.; Annapureddy, R. R.; Xue, M.; Yang, C.; Guan, Y.; Zhou, P.; Chan, S. L. F. Luminescent Iridium(III) Pyridinium-Derived N-Heterocyclic Carbene Complexes as Versatile Photoredox Catalysts. *Inorg. Chem.* **2017**, *56* (18), 10835–10839. DOI: 10.1021/acs.inorgchem.7b00955.

(67) Owen, J. S.; Labinger, J. A.; Bercaw, J. E. Pyridinium-Derived *N*-Heterocyclic Carbene Complexes of Platinum: Synthesis, Structure and Ligand Substitution Kinetics. *J. Am. Chem. Soc.* **2004**, *126* (26), 8247–8255. DOI: 10.1021/ja040075t.

(68) Chen, J. C. C.; Lin, I. J. B. Palladium Complexes Containing a Hemilabile Pyridylcarbene Ligand. *Organometallics* **2000**, *19* (24), 5113–5121. DOI: 10.1021/om000557n.

(69) Stander-Grobler, E.; Schuster, O.; Heydenrych, G.; Cronje, S.; Tosh, E.; Albrecht, M.; Frenking, G.; Raubenheimer, H. G. Pyridine-Derived N-Heterocyclic Carbenes: An Experimental and Theoretical Evaluation of the Bonding in and Reactivity of Selected Normal and Abnormal Complexes of Nickel(II) and Palladium(II). *Organometallics* **2010**, *29* (22), 5821–5833. DOI: 10.1021/om100431u.

(70) Gleiter, R.; Hoffmann, R. Stabilizing a Singlet Methylene. *J. Am. Chem. Soc.* **1968**, *90* (20), 5457–5460. DOI: 10.1021/ja01022a023.

(71) Dixon, I. M.; Alary, F.; Boggio-Pasqua, M.; Heully, J.-L. Reversing the Relative ^{3}MLCT–^{3}MC Order in Fe(II) Complexes Using Cyclometallating Ligands: A Computational Study Aiming at Luminescent Fe(II) Complexes. *Dalton Trans.* **2015**, *44* (30), 13498–13503. DOI: 10.1039/C5DT01214G.

(72) Dixon, I. M.; Boissard, G.; Whyte, H.; Alary, F.; Heully, J. L. Computational Estimate of the Photophysical Capabilities of Four Series of Organometallic Iron(II) Complexes. *Inorg. Chem.* **2016**, *55* (11), 5089–5091. DOI: 10.1021/acs.inorgchem.6b00223.

(73) Tapu, D.; Dixon, D. A.; Roe, C. ^{13}C NMR Spectroscopy of "Arduengo-Type" Carbenes and Their Derivatives. *Chem. Rev.* **2009**, *109* (8), 3385–3407. DOI: 10.1021/cr800521g.

(74) Huynh, H. V.; Han, Y.; Jothibasu, R.; Yang, J. A. ^{13}C NMR Spectroscopic Determination of Ligand Donor Strengths Using N-Heterocyclic Carbene Complexes of Palladium(II). *Organometallics* **2009**, *28* (18), 5395–5404. DOI: 10.1021/om900667d.

(75) Meng, G.; Kakalis, L.; Nolan, S. P.; Szostak, M. A Simple ^{1}H NMR Method for Determining the σ-Donor Properties of N-Heterocyclic Carbenes. *Tetrahedron Lett.* **2019**, *60* (4), 378–381. DOI: 10.1016/j.tetlet.2018.12.059.

(76) Martin, R. L. Natural Transition Orbitals. *J. Chem. Phys.* **2003**, *118* (11), 4775–4777. DOI: 10.1063/1.1558471.

APPENDIX

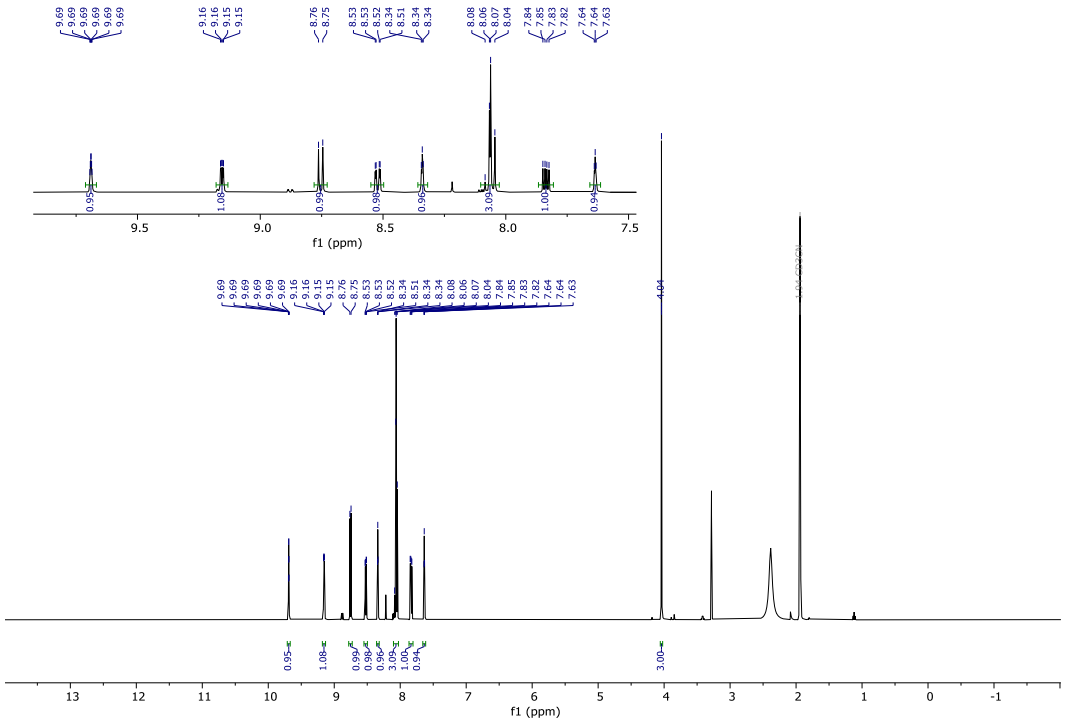

Figure 4.20. ^{1}H NMR of [phen^{Me}Im]PF_6 in CD_3CN. Inset is an expansion of the aromatic region.

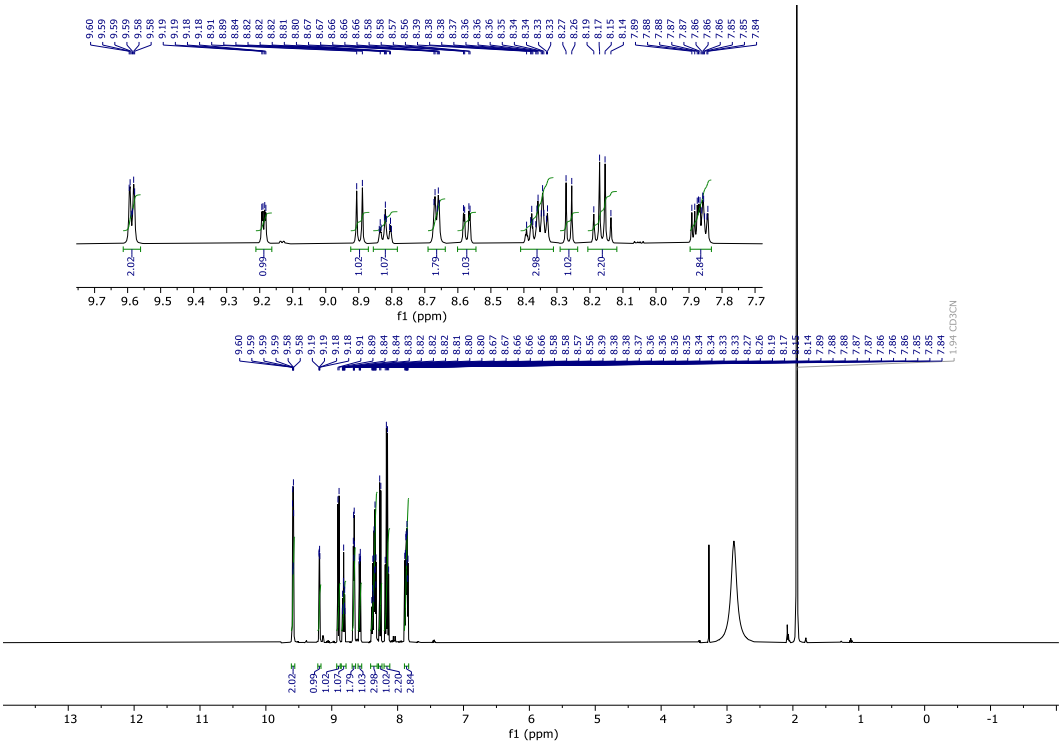

Figure 4.21. ^{1}H NMR of [phenNPyH]PF_6•H$PyPF_6$ in CD_3CN. Inset is an expansion of the aromatic region.

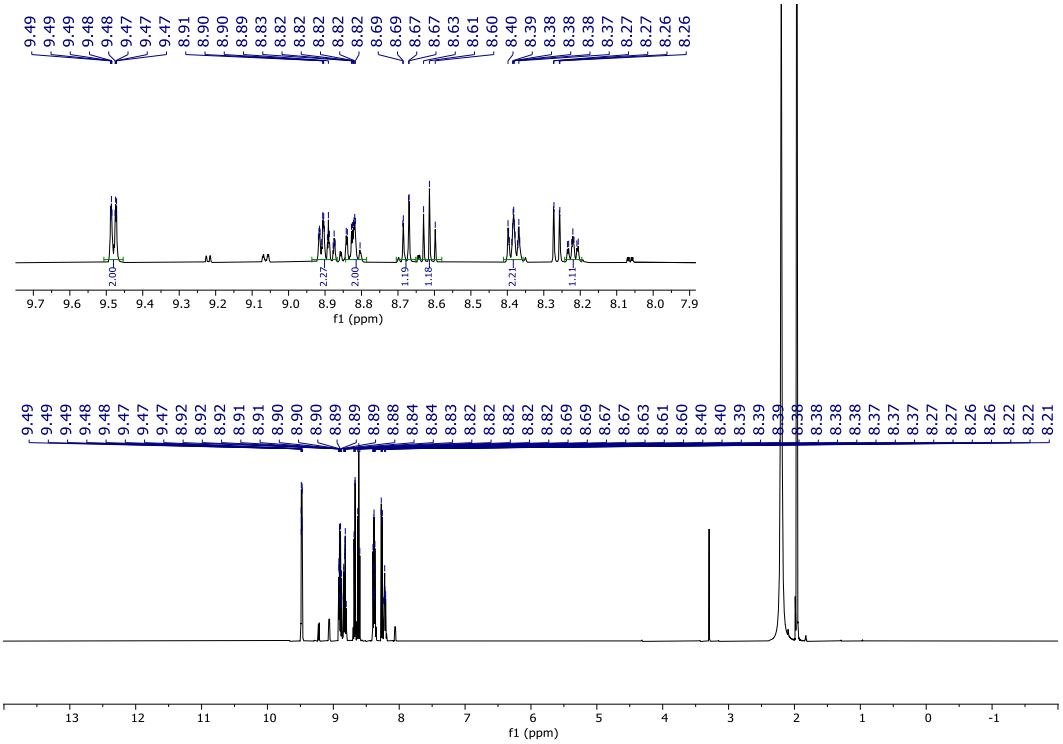

Figure 4.22. ^{1}H NMR of [bpyNPyH]PF_6 in CD_3CN. Inset is an expansion of the aromatic region.

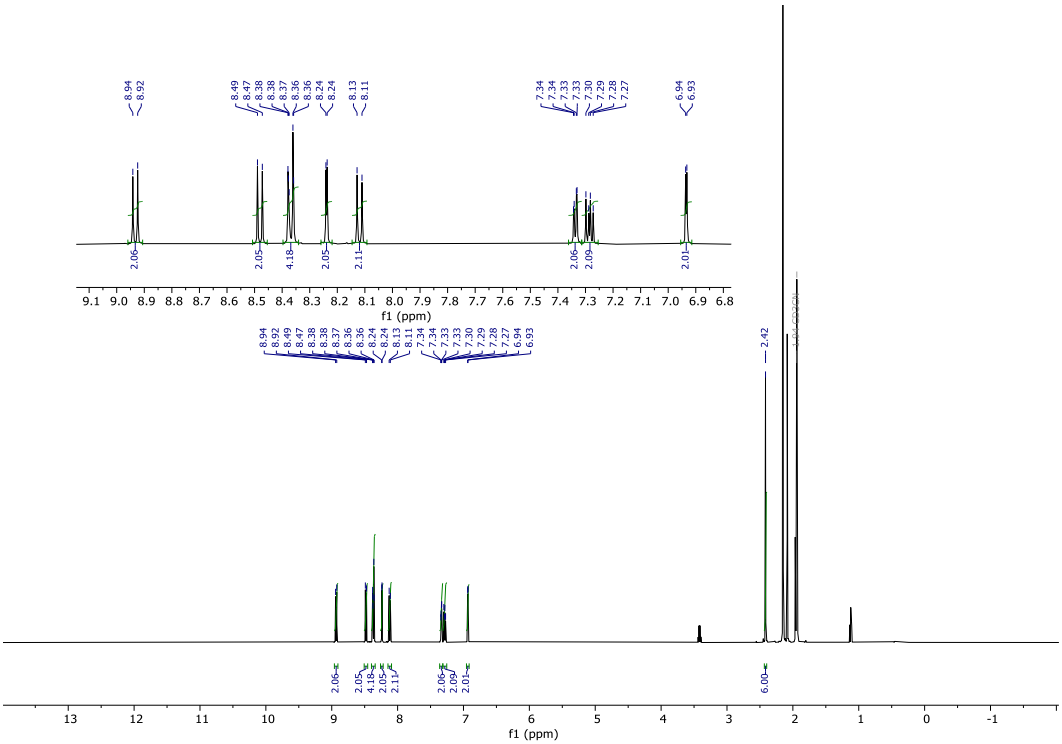

Figure 4.23. ^{1}H NMR of $[Fe(phen^{Me}Im)_2](PF_6)_2$ in CD_3CN. Inset is an expansion of the aromatic region.

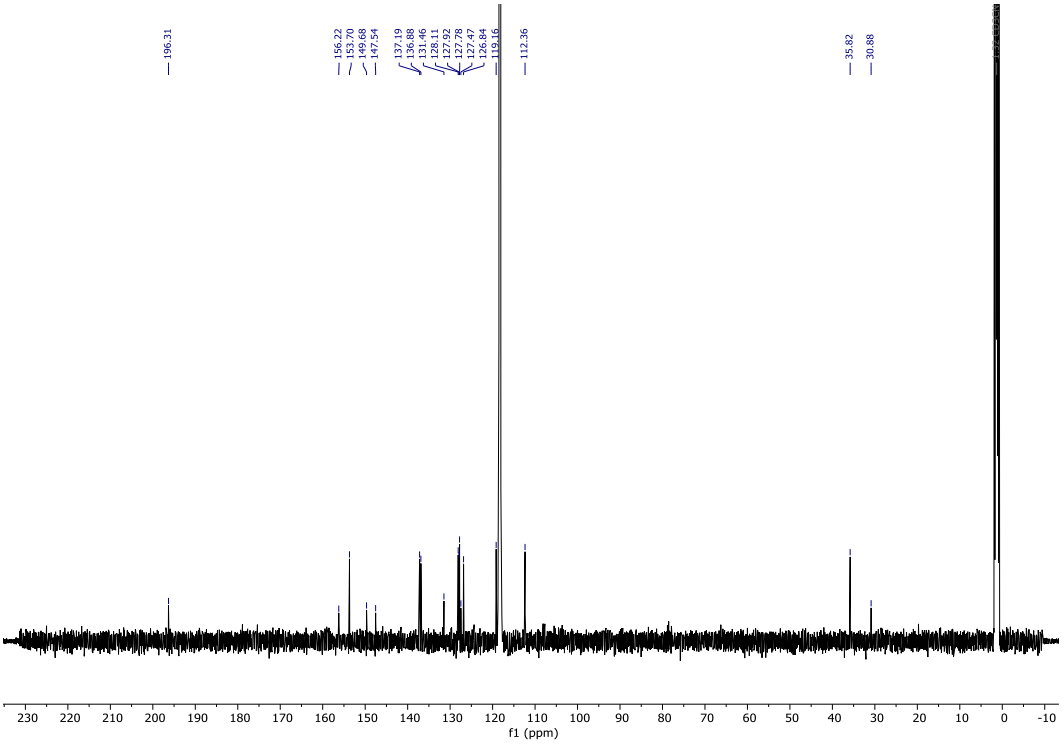

Figure 4.24. ^{13}C NMR of $[Fe(phen^{Me}Im)_2](PF_6)_2$ in CD_3CN.

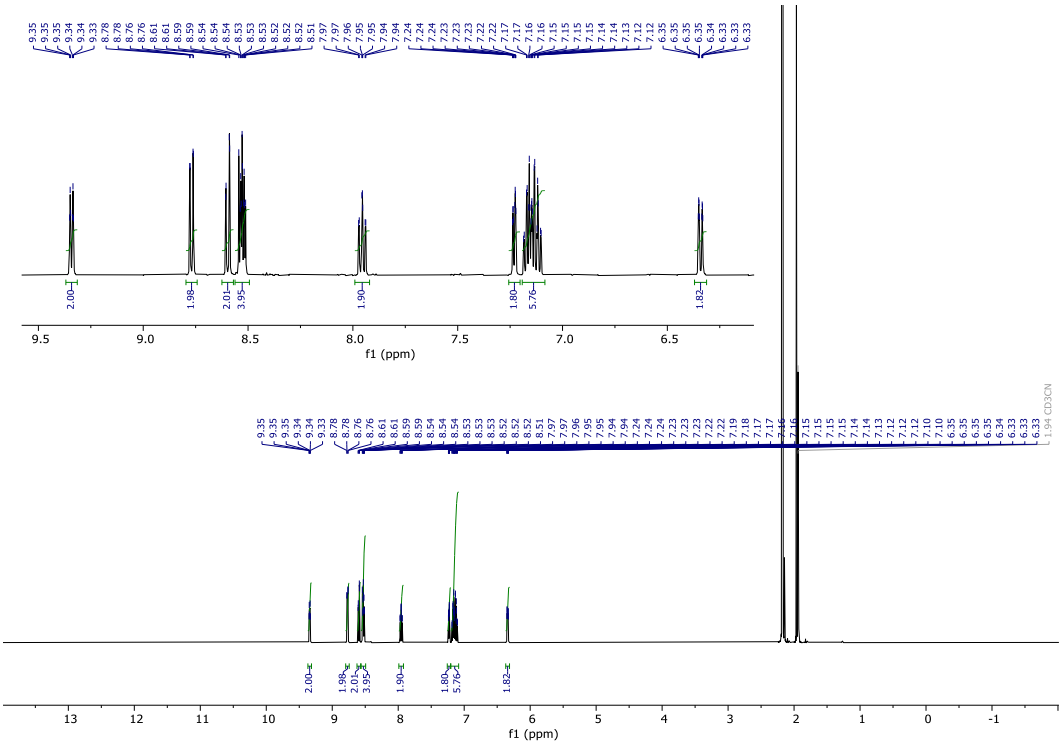

Figure 4.25. ^{1}H NMR of $[Fe(bpyNPy)_2](PF_6)_2$ in CD_3CN. Inset is an expansion of the aromatic region.

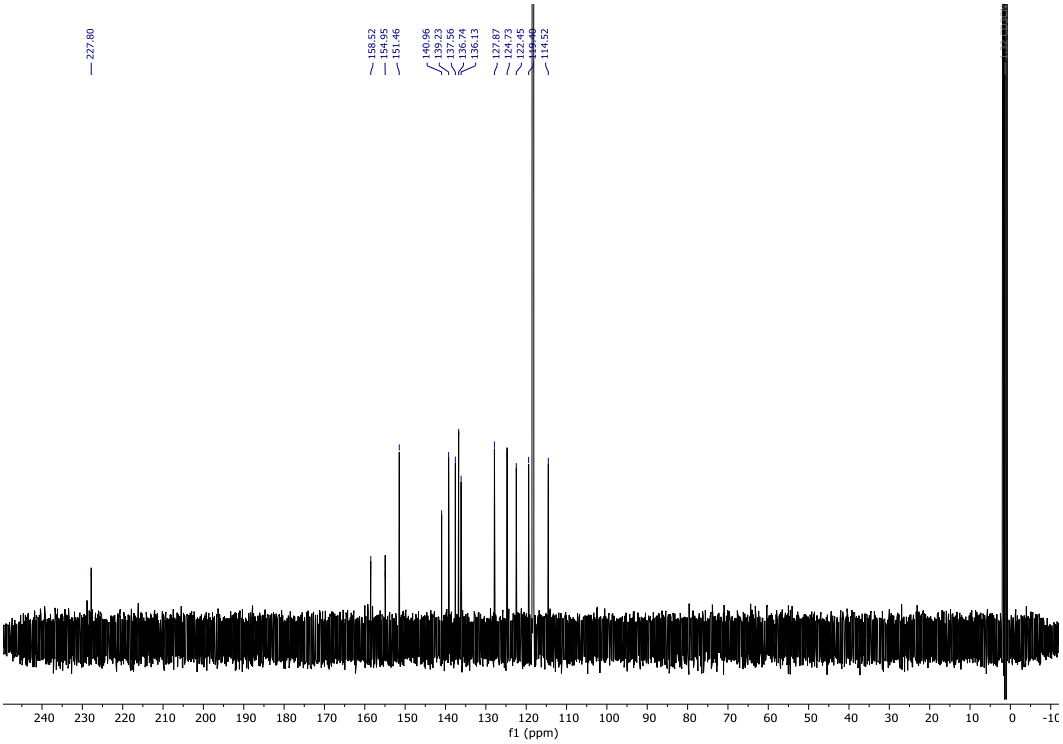

Figure 4.26. ^{13}C NMR of $[Fe(bpyNPy)_2](PF_6)_2$ in CD_3CN.

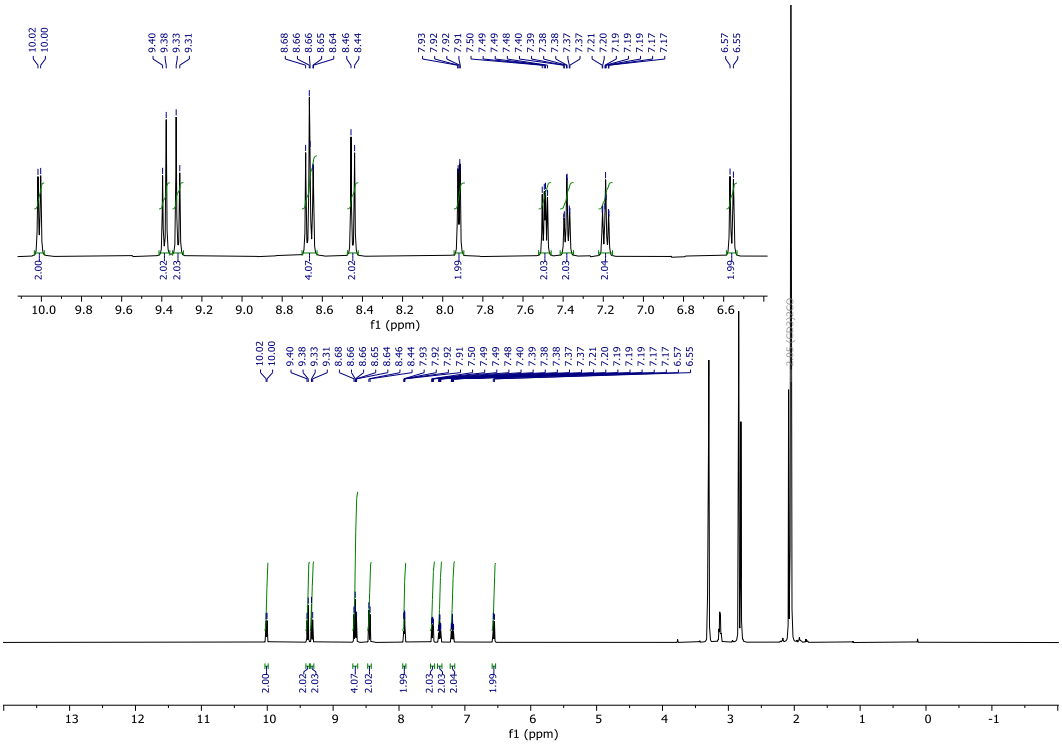

Figure 4.27. ^{1}H NMR of $[Fe(phenNPy)_2](PF_6)_2$ in acetone-d_6. Inset is an expansion of the aromatic region.

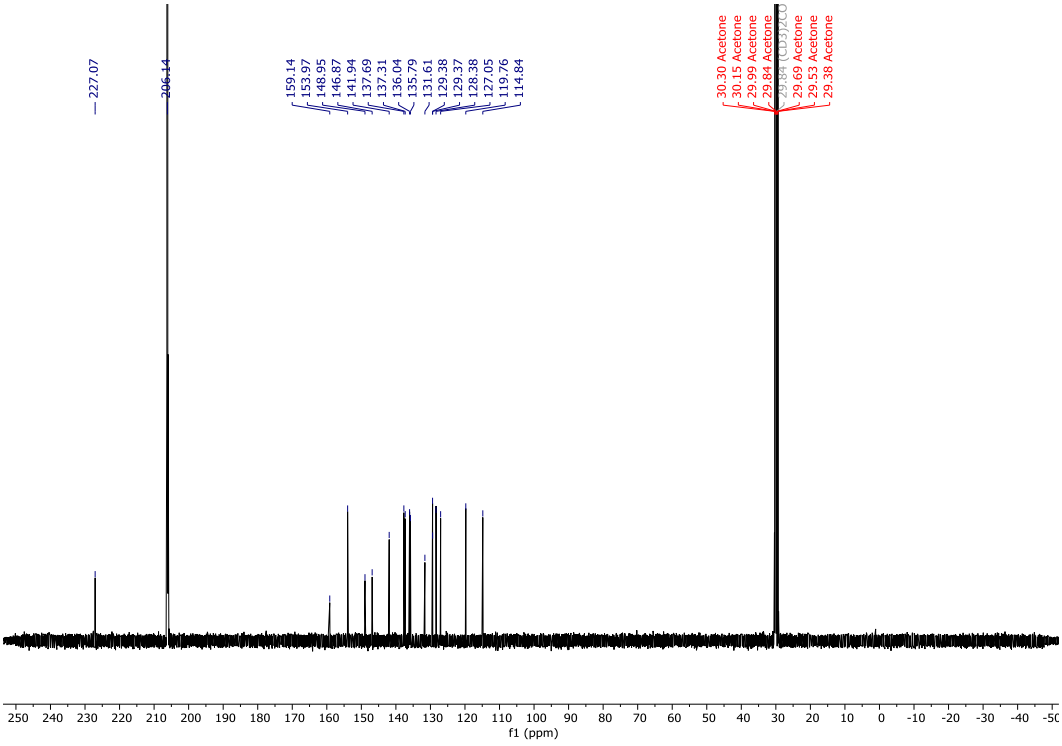

Figure 4.28. ^{13}C NMR of $[Fe(phenNPy)_2](PF_6)_2$ in acetone-d_6.

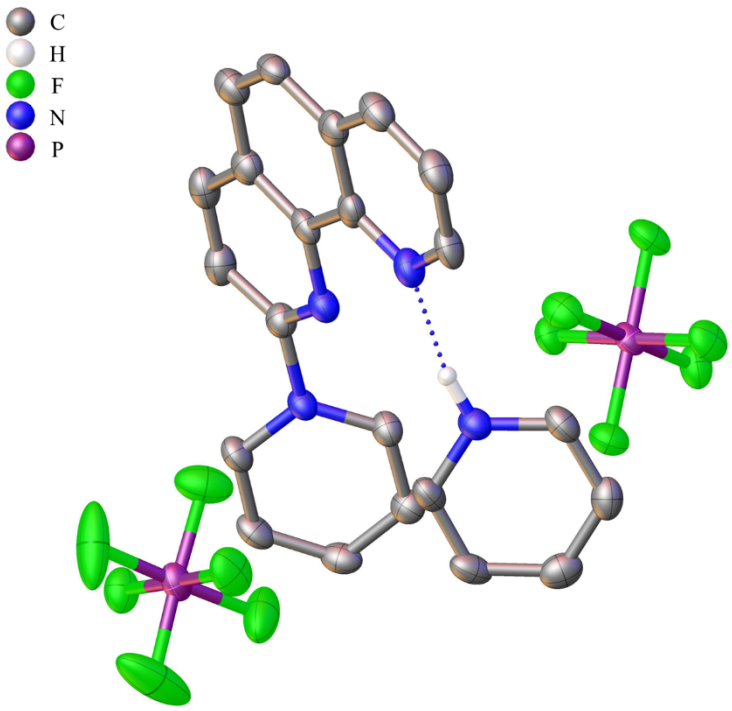

Figure 4.29. Single crystal X-ray structure of [phenNPy]PF_6•HPyPF_6. Hydrogens have been removed for clarity.

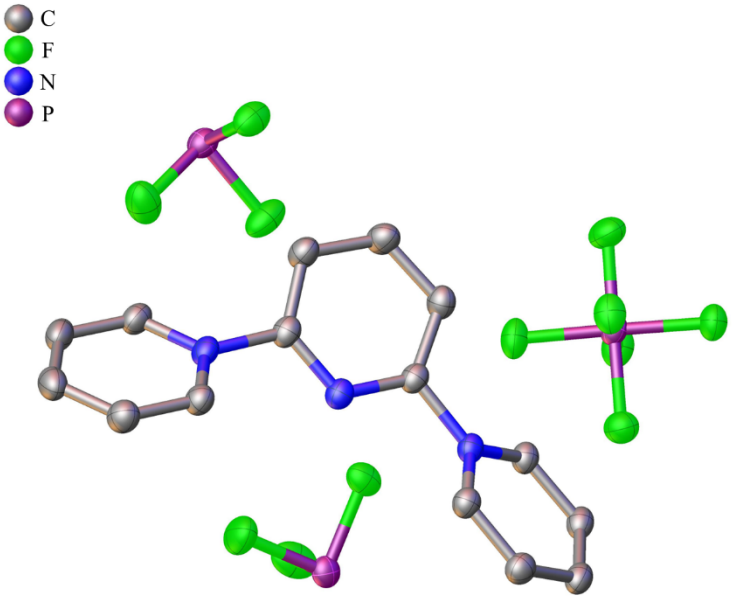

Figure 4.30. Single crystal X-ray structure of [PyNPy_2]PF_6. Hydrogens have been removed for clarity.

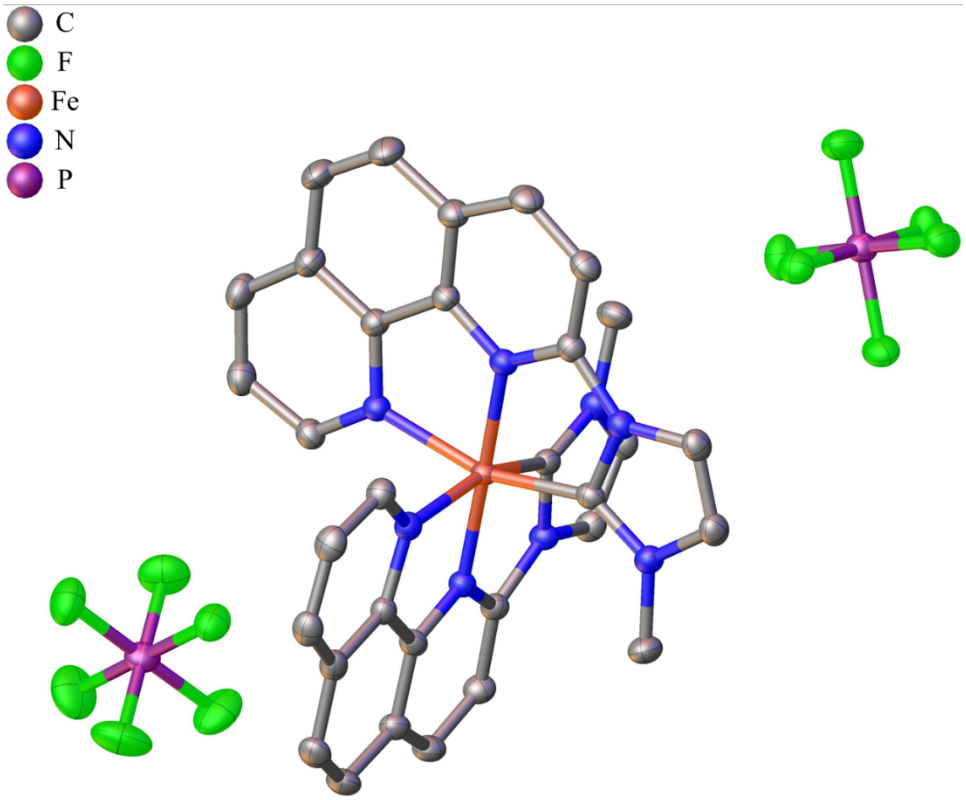

Figure 4.31. Single crystal X-ray structure of $[Fe(phen^{Me}Im)_2](PF_6)_2$. Solvent and hydrogens have been removed for clarity.

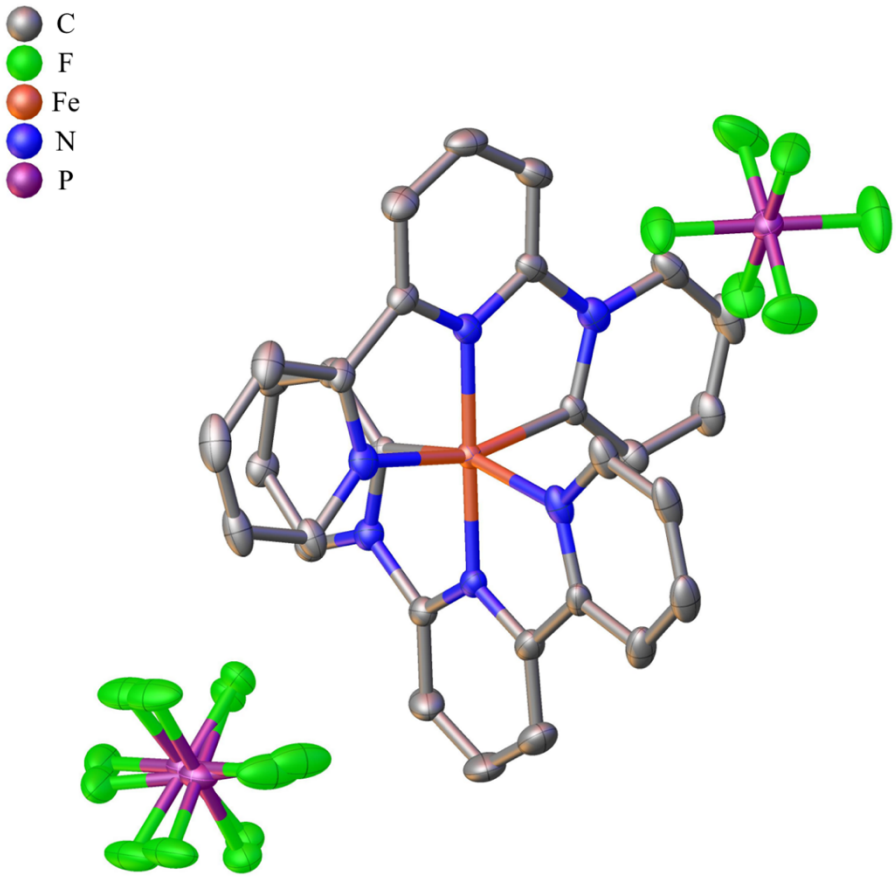

Figure 4.32. Single crystal X-ray structure of $[Fe(bpyNPy)_2](PF_6)_2$. Solvent and hydrogens have been removed for clarity.

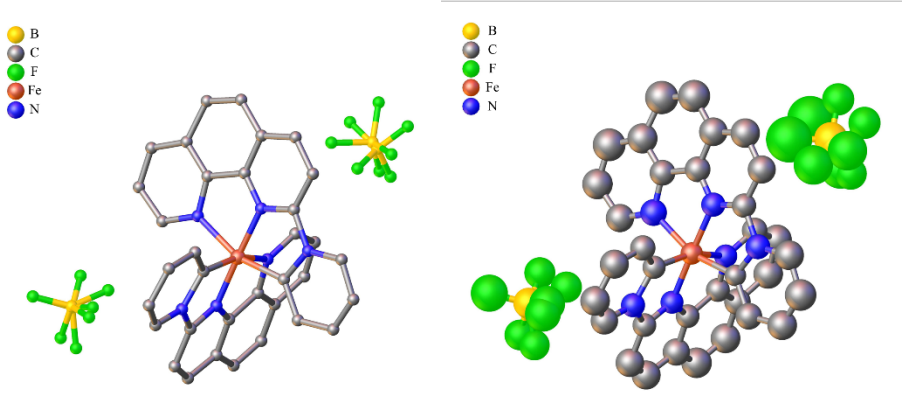

Figure 4.33. Single crystal X-ray structure of $[Fe(phenNPy)_2](PF_6)_2$ (left) ball and stick model and (right) isotropic. Solvent and hydrogens have been removed for clarity.

Table 4.6. Crystallographic data and structure refinement

Identification code	[phenNPy]PF_6•[PyH]PF_6	[$PyNPy_2$]$(PF_6)_2$	[$Fe(phen^{Me}Im)_2$]$(PF_6)_2$	[$Fe(bpyNPy)_2$]$(PF_6)_2$	[$Fe(phenNPy)_2$]$(BF_4)_2$
Empirical formula	$C_{17}H_{12}N_3PF_6$•$C_5H_6PF_6$	$C_{15}H_{13}F_{12}N_5P_2$•CH_3CN	$C_{32}H_{24}F_{12}FeN_6P_2$•$CH_3CN$,0.5 Et_2O	$C_{30}H_{22}F_{12}FeN_6P_2$	$C_{34}H_{22}B_2F_8FeN_6$• Et_2O
Formula weight	628.34	566.28	929.96	812.32	818.16
Temperature/K	100(2)	99.99(10)	100(2)	100(2)	100(2)
Crystal system	triclinic	triclinic	monoclinic	orthorhombic	monoclinic
Space group	P-1	P-1	$P2_1/n$	$P2_12_12_1$	$P2_1/n$
a/Å	8.30561(17)	6.17030(10)	12.01467(8)	8.81189(19)	8.7252(3)
b/Å	10.83636(16)	12.0998(3)	25.5273(2)	8.83473(19)	32.9928(9)
c/Å	13.6426(3)	15.3044(4)	12.47175(7)	39.9523(8)	12.2601(5)
α/°	80.2280(15)	88.027(2)	90	90	90
β/°	82.9465(17)	81.623(2)	91.5548(6)	90	102.620(4)
γ/°	86.9453(15)	76.306(2)	90	90	90
Volume/Å^3	1200.24(4)	1098.29(4)	3823.70(5)	3110.32(12)	3444.0(2)
Z	2	2	4	4	4
ρ_{calc}g/cm^3	1.739	1.712	1.615	1.735	1.578
μ/mm^{-1}	2.736	2.908	4.876	0.695	4.279
F(000)	632.0	568.0	1882.0	1632.0	1672.0
Crystal size/mm^3	0.247 × 0.136 × 0.124	0.311 × 0.211 × 0.186	0.228 × 0.162 × 0.113	0.111 × 0.095 × 0.078	0.12 × 0.05 × 0.036
Radiation	Cu Kα (λ = 1.54184)	Cu Kα (λ = 1.54184)	CuKα (λ = 1.54184)	Mo Kα (λ = 0.71073)	Cu Kα (λ = 1.54184)
2Θ range for data collection/°	6.618 to 160.866	5.838 to 160.296	6.926 to 160.754	4.722 to 70.166	7.86 to 161.768
Index ranges	-10 ≤ h ≤ 10, -9 ≤ k ≤ 13, -17 ≤ l ≤ 17	-7 ≤ h ≤ 7, -15 ≤ k ≤ 15, -19 ≤ l ≤ 19	-15 ≤ h ≤ 15, -32 ≤ k ≤ 30, -9 ≤ l ≤ 15	-14 ≤ h ≤ 13, -13 ≤ k ≤ 14, -64 ≤ l ≤ 63	-11 ≤ h ≤ 9, -33 ≤ k ≤ 42, -15 ≤ l ≤ 15
Reflections collected	15885	8233	36301	69388	22791
Independent reflections	5106 [R_{int} = 0.0339, R_{sigma} = 0.0347]	8233 [R_{int} = 0.0756, R_{sigma} = 0.0199]	8213 [R_{int} = 0.0325, R_{sigma} = 0.0274]	12705 [R_{int} = 0.0736, R_{sigma} = 0.0647]	7131 [R_{int} = 0.0743, R_{sigma} = 0.0629]
Data/restraints/parameters	5106/0/361	8233/0/339	8213/0/526	12705/51/483	7131/16/495
Goodness-of-fit on F^2	1.055	1.045	1.068	1.059	1.060
Final R indexes [I>=2σ (I)]	R_1 = 0.0626, wR_2 = 0.1572	R_1 = 0.0599, wR_2 = 0.1719	R_1 = 0.0344, wR_2 = 0.0857	R_1 = 0.0439, wR_2 = 0.0933	R_1 = 0.1178, wR_2 = 0.3105
Final R indexes [all data]	R_1 = 0.0663, wR_2 = 0.1598	R_1 = 0.0626, wR_2 = 0.1750	R_1 = 0.0362, wR_2 = 0.0867	R_1 = 0.0616, wR_2 = 0.0987	R_1 = 0.1479, wR_2 = 0.3329
Largest diff. peak/hole / e Å^{-3}	1.20/-0.58	0.42/-0.43	0.37/-0.32	0.49/-0.39	0.96/-0.38
Flack Parameter	-	-	-	-0.013(7)	-

CHAPTER 5: FUTURE DIRECTIONS

5.1 Introduction

As was discussed in the previous chapters, we are attempting to understand and controllably modulate the excited-state energetic landscape of low-spin d6 chromophores. In Chapter 2, Co(III) was utilized to understand the ligand-field manifold and the net donor and acceptor ability of bipyridyl ligands. Chapters 3 and 4 focused on Fe(II), where we were able to deconvolve the MLCT spectrum of $[Fe(dcpp)_2]^{2+}$ through aromatic substitutions and synthesize new pyridylidene-based chromophores for the extension of the MLCT lifetime, respectively. In this final chapter, I will provide new thrusts based upon the previous findings on which we can continue to expand our understanding of the photophysical behaviors of these chromophores as well as push towards their applications.

5.2 Experimental

5.2.1 Synthesis

General. All reaction and spectroscopic solvents were obtained from Sigma Aldrich Chemical Co. and used without further purification unless otherwise stated. Dry THF and MeCN were obtained from a Solvtek solvent drying system using neutral alumina. Unless otherwise noted, all reactions were conducted either using standard Schlenk techniques or in an inert atmosphere glove box (nitrogen-filled, Vacuum Atmospheres). $FeBr_2$ was obtained from Strem Chemicals Inc. 2-bromopyridine, TMS-acetylene, and 1.6 M n-BuLi were obtained from Sigma Aldrich Chemical Co. 9-bromoanthracene was obtained from Oakwood Chemicals. NMR spectra were collected in the Max T. Rogers NMR Facility of Michigan State University on an Agilent 500 MHz spectrometer; spectra were referenced internally to the residual solvent peak of $CDCl_3$, CD_3CN, or $(CD_3)_2CO$ which were obtained from Cambridge Isotopes. Diethyl 4-chloro-chelidimate (Cl-

DEP)[1], Diethyl 4-iodo-chelidimate (I-DEP),[2] 9-(TMSethynyl)anthracene (TMSyneAn),[3] 9-ethynylanthracene,[4] 4′-(4‴-pyridyl)-2,2′:6′,2″-terpyridine (pyterpy),[5] and [Fe(terpy)Cl_3][6] were all prepared by literature methods.

diethyl 4-(9-anthracenyl)-2,6-pyridine dicarboxylate (An-DEP). To a N_2 purged round-bottom flask was added 1.000 g of I-DEP (2.9 mmol, 1.0 eq), 0.119 g of Pd(dppf)Cl_2•DCM (5mol%), 3.027 g of Cs_2CO_3 (8.6 mmol, 3.0 eq), 0.766 g of 9-anthracene boronic acid (3.5 mmol, 1.2 eq.), and 10 mL of 1,4-dioxane. The reaction was heated to 80ºC for 15 hours and was monitored by TLC. After completion, the reaction was cooled to room temperature and the dioxane was evaporated. The crude was taken into 120 mL of EtOAc and was washed with H_2O (3 x 50 mL) and twice with brine. The organic layer was dried over $MgSO_4$, filtered, and evaporated. The crude can either be column on silica with 30% EtOAc/Hexanes or recrystallized from 9:1 EtOH/DCM and placed in the freezer to complete purification. Yield: 0.812 g, 71%. ^{1}H NMR (500 MHz, $CDCl_3$) δ 8.60 (s, 1H), 8.38 (s, 2H), 8.09 (dt, *J* = 8.6, 1.1 Hz, 2H), 7.51 (ddd, *J* = 8.4, 4.8, 2.8 Hz, 2H), 7.46 – 7.38 (m, 4H), 4.52 (q, *J* = 7.1 Hz, 4H), 1.46 (t, *J* = 7.1 Hz, 6H).

Diethyl 4-(9-ethynylanthracene)-2,6-pyridine dicarboxylate (AnYne-DEP). In 10 mL of THF were added 461 mg of I-DEP (1.3 mmol, 1.0 eq.), 20 mg of Pd(PPh_3)$_2Cl_2$ (2mol%), 10 mg of CuI (4mol%), and 1.3 mL of TEA (9.5 mmol, 7.2 eq.). The reaction was sparged for 5 minutes after which 321 mg of 9-ethynylanthracene (1.6 mmol, 1.2 eq.) were added. The reaction thickened instantly upon addition. The reaction stirred overnight at room temperature and was monitored by TLC. Upon completion, the solvent was evaporated and the crude was dissolved in DCM and washed with H_2O (2 x 30 mL). The organic layer was dried over $MgSO_4$, filtered, and evaporated to afford a brown residue. The crude was dissolved in minimal DCM, filtered, and EtOH was added until cloudy. This was placed in the freezer to complete crystallization. Yield: 260 mg, 46%.

^{1}H NMR (500 MHz, $CDCl_3$) δ 8.60 (dd, J = 8.7, 1.1 Hz, 2H), 8.55 (s, 3H), 8.07 (dt, J = 8.5, 0.8 Hz, 2H), 7.68 (ddd, J = 8.7, 6.6, 1.2 Hz, 2H), 7.57 (ddd, J = 8.1, 6.6, 1.2 Hz, 2H), 4.56 (q, J = 7.1 Hz, 4H), 1.51 (t, J = 7.1 Hz, 6H).

2,6-di(2-carboxypyridyl)-4-(9-anthracenyl)pyridine (dcpAnp). To a flame-dried flask was added 0.16 mL of 2-bromopyridine (1.7 mmol, 2.2 eq.) and 50 mL of THF. The solution was cooled to -78ºC and 1.1 mL of 1.6 M n-BuLi (1.7 mmol. 2.2 eq.) were added dropwise over 30 minutes. The red-orange solution stirred for an additional 30 minutes. To this was added dropwise a 30 mL THF solution containing 297 mg of An-DEP (0.8 mmol, 1.0 eq.) over 1 hour. It stirred for an additional hour at -78ºC after addition and was then quenched with 3 mL of MeOH. The red solution was allowed to warm to room temperature stirred overnight. The reaction concentrated to by ~80% and was then added to 60 mL of 10% hydrochloric acid. The THF layer was removed the aqueous layer was washed once with 20 mL of DCM. The acidic layer was basified with 5 M NaOH and was then extracted with DCM (3 x 50 mL). The combined organics were dried over $MgSO_4$, filtered, and evaporated to afford a beige powder. Yield: 100 mg, 30 %. ^{1}H NMR (500 MHz, $CDCl_3$) δ 8.58 (dt, J = 4.7, 1.4 Hz, 2H), 8.40 (s, 1H), 8.23 (s, 2H), 8.10 (dt, J = 7.9, 1.1 Hz, 2H), 7.90 (d, J = 8.5 Hz, 2H), 7.65 (td, J = 7.7, 1.7 Hz, 2H), 7.52 (dd, J = 8.8, 1.1 Hz, 2H), 7.36 – 7.23 (m, 6H).

2,6-di(2-carboxypyridl)-4-(9-ethynylanthracenyl)pyridine (dcpAnYnep). To a flame-dried flask was added 0.1 mL of 2-bromopyridine (1.1 mmol, 2.3 eq.) and 15 mL of THF. This was cooled to -78°C and 0.7 mL of 1.6 M n-BuLi (1.1 mmol, 2.3 eq.) were added dropwise over 20 min. It stirred for an additional 15 min at -78°C. A 15 mL THF solution containing 200 mg of 9-AnYne-DEP (0.5 mmol, 1.0 eq.) was added dropwise via 22G cannula over 45 min. The orange solution turned blue upon addition of the ester. The solution stirred for 1.5 hours at -78°C. 1.5 mL

of MeOH were added to quench the reaction and it was allowed to warm to room temperature overnight. The solvent was evaporated, and the residue was sonicated with diethyl ether. The oil solidified. The orange powder was filtered and washed with additional ether. The solid has limited solubility in common solvents. Yield: 95 mg, 41% ^{1}H NMR (500 MHz, $CDCl_3$) δ 8.80 (dt, J = 4.7, 1.5 Hz, 2H), 8.64 (d, J = 8.7 Hz, 2H), 8.56 (d, J = 10.9 Hz, 3H), 8.25 (dd, J = 7.8, 1.1 Hz, 2H), 8.07 (d, J = 8.5 Hz, 3H), 7.83 (td, J = 7.8, 1.7 Hz, 2H), 7.69 (ddd, J = 8.8, 6.4, 1.3 Hz, 2H), 7.60 – 7.54 (m, 2H), 7.50 (ddd, J = 7.7, 4.7, 1.2 Hz, 2H).

Bis(2,6-di(2-carboxypyridyl)-4-(9-anthracenyl)pyridine)iron(II) hexafluorophosphate ($[Fe(dcpAnp)_2](PF_6)_2$). To a N_2 purged flask was added 15 mL of THF and 22 mg of dcpAnp (0.05 mmol, 2.2 eq.). To this solution was added 7 mg of $Fe(BF_4)_2 \cdot 6H_2O$ (0.02 mmol, 1.0 eq.). The solution turned green instantly. The reaction stirred for 24 hours. To the resulting green solution was added saturated KPF6(aq) to precipitate a green solid. The solid was filtered and washed with H_2O and diethyl ether. Due to the green color the complexation did not proceed. Single crystals of the target were able to be grown from the crude reaction mixture by slow diffusion of diethyl ether into a saturated acetonitrile solution. No yield or NMR are reported.

X-ray crystal structure determination. A crystal of $[Fe(dcpAnp)_2](PF_6)_2$ of appropriate size was selected and mounted on a nylon loop with paratone oil on a XtaLAB Synergy, Dualflex, HyPix diffractometer. The crystal was kept at a steady T = 100.0(2) K during data collection. The structure was solved with the ShelXT[7] solution program using intrinsic phasing and by using Olex2 1.3[8] as the graphical interface. The model was refined with ShelXL 2018/3[9] using full matrix least squares minimization on $\boldsymbol{F^2}$.

5.3 Results and Discussion

5.3.1 π-Extension of dcpp and the Potential for Triplet-Triplet Annihilation

From the results of Chapter 3, it was shown that aromatic substitutions on the ligand back bone of dcpp can modulate the absorption spectrum of $[Fe(dcpp)_2]^{2+}$, increasing the low-energy or higher-energy transitions. The increased size of the π-system showed small contributions of the phenyl rings in the excited-states. We looked towards further increasing the delocalization of the excited state so as to decouple the Fe(II)-center from the ligand during excitation. Phenyl substituents with cyano or electron withdrawing groups computationally showed increased delocalization, but increasing the size of the aromatic system from phenyl to anthracene or pyrene could better facilitate the goal. It has been shown for pyrene decorated Cr(0) isocyanide complexes[10] and Fe(II) pyrene and anthracene chromophores[11] there was an observable extension of MLCT lifetimes as well as emission from the linked organic chromophores.

Using anthracene as the beginning aromatic moiety, the complex $[Fe(dcpAnp)_2](PF_6)_2$ was synthesized (Figure 5.1a). The complexation of the ligand was attempted in THF instead of acetonitrile as had been used for previous complexations as the decreased solubility of the complex was thought to push the equilibrium towards product. The resulting solution was green which is hypothesized to be the monoligated complex. Though the reaction was not complete a single crystal X-ray structure was able to be collected (Figure 5.1b). The structure shows that the anthracene dihedral angle is canted to 89.4°. The orthogonality effectively shuts down all communication of the ligand π-system with that of the anthracene's, precluding the delocalization of the excited state.

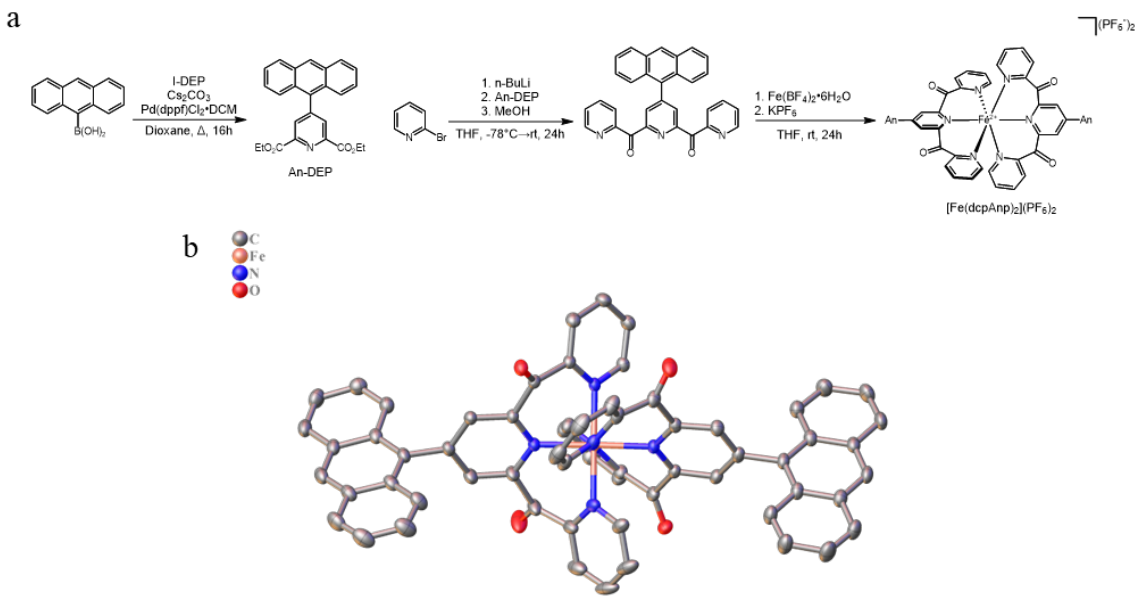

Figure 5.1. (a) Synthetic procedure for the synthesis of An-DEP and $[Fe(dcpAnp)_2](PF_6)_2$ (b) Single crystal X-ray structure of $[Fe(dcpAnp)_2](PF_6)_2$ showing the orthogonality of the anthracene and the dcpp backbone. Solvent, hydrogens, and counter ions have been removed for clarity.

In hopes of alleviating the steric interactions of the 1 and 8 hydrogens of the anthracene with the pyridine extending the distance of the anthracene from the ligand was envisioned. To maintain the electronic communication of the anthracene with MLCT of the complex we chose to use an alkyne spacer. Using successive Sonogashira couplings starting from 9-bromoanthracene, the potential ligand was synthesized (Figure 5.2a). The coupling of 9-ethynylanthracene with I-DEP proceeded in low yield. This is attributed to the instability of 9-ethynylanthracene. After isolation, a red insoluble material slowly begins to appear which is hypothesized to be a Diels-Alder type reaction between the alkyne of one anthracene and the 9- and 10-position of another. To remedy this, a one-pot reaction is proposed whereby 9-(TMSethynyl)anthracene is deprotected in-situ and then undergoes the requisite coupling with I-DEP (Figure 5.2b).[12]

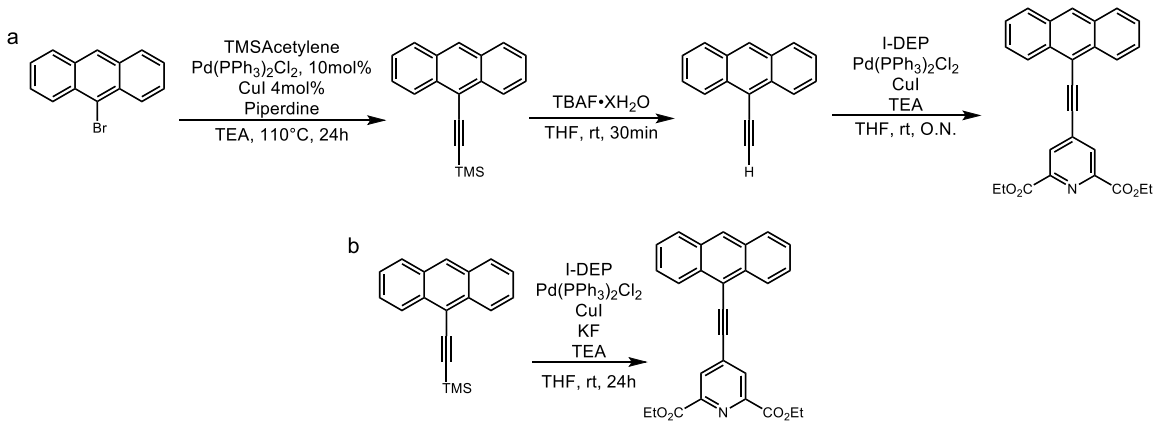

Figure 5.2. (a) Current synthetic route towards AnYne-DEP deprotecting the 9-(TMSethynyl)anthracene followed by a Sonogashira coupling (b) Proposed one-pot deprotection and Sonogashira coupling for the simplified and cleaner synthesis of AnYne-DEP.

Though the main goal of the synthesis of dcpAnYnep complex was initially proposed as further delocalization of the MLCT excited-state, if successful, this could also lead toward applications in triplet-triplet annihilation (TTA).[13,14] Anthracene is a well-known energy transfer acceptor from a photoexcited photosensitizer donor.[15–17] The utility of this is in that low-energy photons can separately excite a chromophore which can transfer its excited-state energy to the anthracene. Once two anthracenes diffuse to each other in solution they then undergo TTA and the original low-energy photon has been converted to a higher-energy photon. This process finds high utility in the realm of solar energy conversion due to a majority of solar cells inefficiently absorbing low-energy light to convert into current.[18] Sensitizing the solar cell with a triplet-triplet annihilators can improve efficiency by converting the red solar irradiance to higher energy photons the solar cell can utilize. With the low-energy $^1A_1 \rightarrow {}^1$MLCT transition in $[Fe(dcpp)_2]^{2+}$ and its derivatives the potential of converting ~600 nm red light into blue light with judicious synthesis of an anthracene or pyrene derivative is extremely promising.

5.3.2 Sensitization of Catalytically Relevant Bimetallic Systems

Sensitization is an important aspect in many catalytically relevant molecular systems. For many of these applications, the 2nd- and 3rd-row transition metals have garnered much attention due to their diffusionally long lifetimes and ease of tailoring their absorptive features.[19] As this dissertation has focused on the implementation of 1st-row metals to supplement or supplant the heavier metals in these applications, focusing on systems that could be realized for this have been envisioned. A widely studied molecular system for catalytic reduction of CO_2 includes Re(I). A typical complex of [Re(bpy)$(CO)_3$X] (where bpy is 2,2′-bipyridine and X is either a halogen or other ligator) is used.[20,21] An endemic problem with Re(I) complexes is the high MLCT energy, typically absorbing well into the blue region of the spectrum. To remedy this, photosensitization has been used to undergo visible-light photoinduced electron transfer between the sensitizer and the Re(I) complex so that it may then enter the catalytic cycle.[21,22] To increase the efficiency of the catalysis, covalently linked photosensitizer-Re(I) dyads have been synthesized so at to not have the kinetics dependent on the diffusion of the two together in solution.

Synthesizing a prototype system, we aim to use 4″-pyridyl-terpyridine coupled with the well-known [Re(bpy)$(CO)_3$OTf] and [Fe(terpy)Cl_3] starting materials (Figure 5.3a). After displacement of the triflate by 4″-pyridyl-terpyridine the resulting complex can be combined with the Fe(III) starting material. Upon bis-complexation, the Fe(III)-center is reduced by one of the terpyridines to Fe(II), affording the target complex.[6] Using this reaction as at test-case and proof-of-concept, we will move to using the pyper ligand system developed in Chapter 3. Unlike, in the pyterpy system, a mono ligated Fe(II) or Fe(III) system will be difficult to isolate due to the poor coordination behavior of dcpp and its pyper derivative. A potential method will be mixing 1 equivalent of pyper and 1 equivalent of dcpp with the Fe(II) starting material. This will result in a

statistical mixture but should be easily isolable from the crude using column chromatography. Isolating the target [Fe(dcpp)(pyper)]$(PF_6)_2$ complex, coordination to the Re(I) center using gentle reaction conditions should then afford the target [Re(bpy)$(CO)_3$(pyterpy)Fe(dcpp)]$(PF_6)_3$ (Figure 5.3b). The question may now be, if the initial Re-pyterpyFe complex can be formed why put in the extra effort for the pyper analogue? $[Fe(dcpp)_2]^{2+}$ and its derivatives all possess an extremely positive oxidation potential, ~1.29 V vs Fc/Fc^+. This potential coupled with the low energy MLCT transition, there is potentially a large driving force in the excited state to push the catalysis from the Re(I)-center.

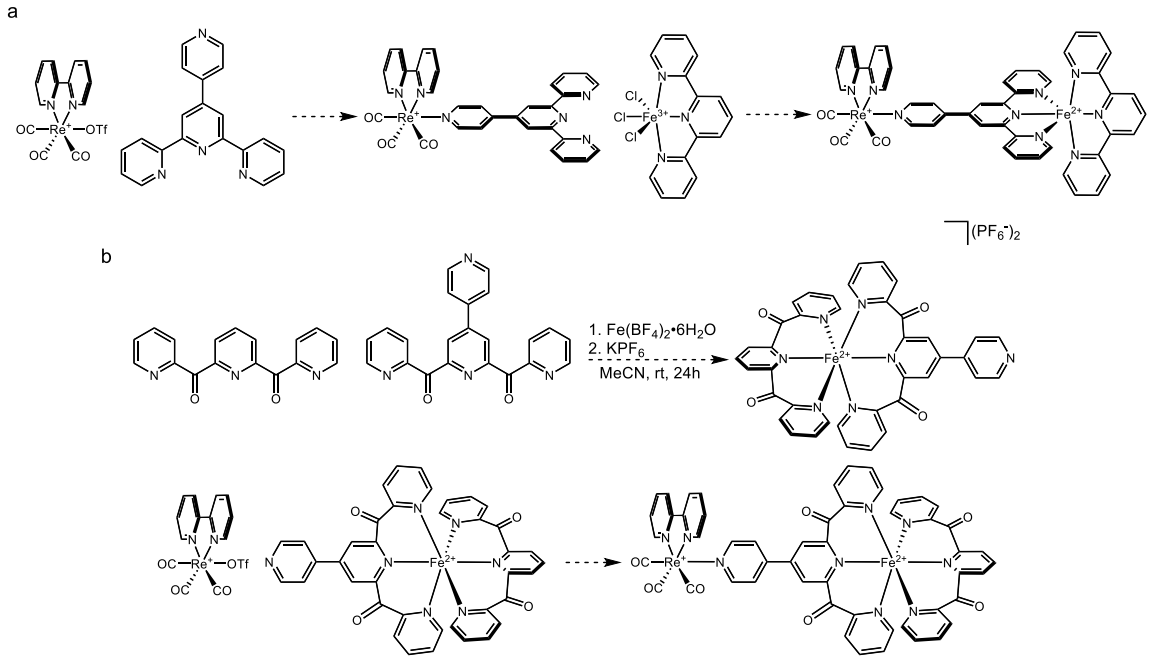

Figure 5.3. (a) Proposed synthetic scheme for prototype system [Re(bpy)$(CO)_3$(pyterpy)Fe(terpy)]$(PF_6)_3$ (b) Proposed synthetic scheme for the heteroleptic synthesis of [Fe(dcpp)(pyper)]$(PF_6)_2$ and complexation to [Re(bpy)$(CO)_3$OTf].

5.3.3 Continuing Exploration of Modular Carbene Systems: Pyridylidenes and Alkylamino Carbenes

In Chapter 4 we explored a new class of Fe(II) chromophores using pyridylidene donors in place of the widely used imidazolium-based systems. The simple substitution of the pyridine afforded an observed inversion of the ^{3}MLCT and LF energetics placing the charge transfer as the lowest energy excited state with a lifetime of 18 ps. This simple yet effective substitution opens the doorway for a multitude of new Fe(II) chromophores with low-energy MLCT transitions but strong donation, ideal if Fe(II) complexes are to be more effectively utilized in the field of photo-redox catalysis.

What can be envisioned for the complexes from Chapter 4, specifically $[Fe(bpyNPy)_2](PF_6)_2$, is a study of the effect of the Fe-C bonding position on the pyridinium on the photophysics of the complex (Figure 5.4). It is known that the position the metal occupies on the pyridinium ring manifests in dramatically different σ-donation from the ring as observed by ^{13}C NMR.[23–26] If binding occurs in the 2- or 4-position of the pyridinium a pyridylidene-type bonding occurs with ^{13}C chemical shifts past 220 ppm, whereas if bonded in the 3-position a shift more in line with cyclometallation is observed, less than 200 ppm.[27] By bonding in the 4-position the complex should find marked increased stability as opposed to the 2-position, which the previous study had been conducted, and higher yields during complexation. The pro-ligands are not as synthetically facile to synthesize as $[bpyNPyH]PF_6$, but none-the-less, completely feasible from literature preparations (Figure 5.4).[28–30]

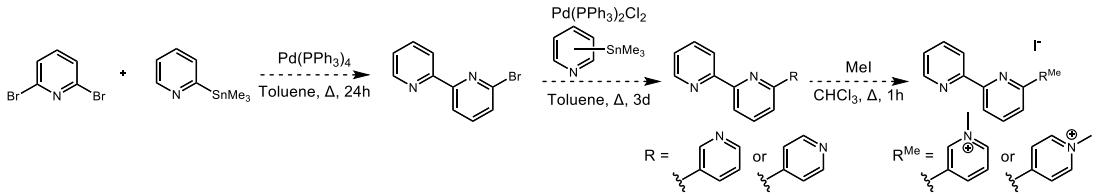

Figure 5.4. Proposed synthetic procedure for the synthesis of 2,2′:6′,3″- and 2,2′:6′,4″-terpyridine and the corresponding alkylation.

In addition to the study of the photophysics as a function of the ligating carbon atom, we can then begin to delve further into this family of complexes and hopefully begin to leverage the longer ^{3}MLCT lifetimes. Using the approach from Chapter 3, phenyl substituents could be installed in the 4- and 4′-positon of the 2,2′-bipyridine core thereby further increasing the absorptive properties as well as allowing for further delocalization of the excited state. It would be of interest to also install anchoring groups on the backbone of the ligand for binding to TiO_2 or another semi-conductor for DSSCs. As the observed lifetime of $[Fe(bpyNPy)_2](PF_6)_2$ is 18 ps, this is on the timescale for interfacial electron transfer in dye-sensitized solar cells.[31–33] Coupling this lifetime with low energy MLCT manifold could be beneficial in capturing the often-missed red-light irradiance from the solar spectrum to increase the efficiency of the cell. A retrosynthetic scheme for the synthesis of the π-extended systems (Figure 5.5a) as well as the anchored ligands are shown below (Figure 5.5b).[34]

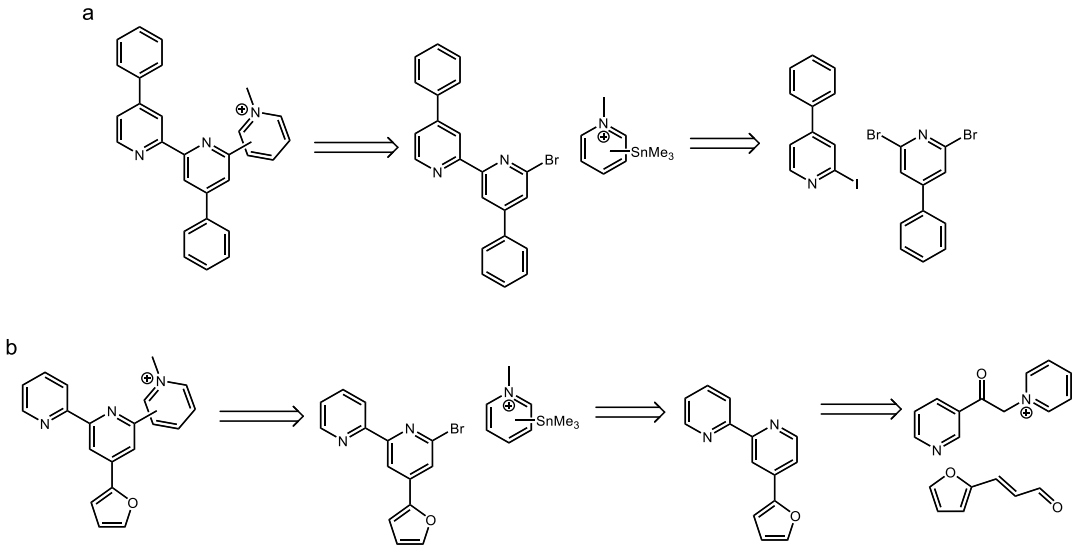

Figure 5.5. Retrosynthetic pathway for the synthesis of (a) π-extended pyridinium ligand and (b) protected carboxylic acid pyridinium pro-ligand for use in DSSCs.

Seeing as the pyridinium systems imposed a strong ligand-field strength than the widely used imidazolium carbenes, we propose further increasing the strength of the σ-donation by implementing one of the strongest carbene donors in the literature, cyclic alkylamino carbenes (CAACs). This class of carbenes was first synthesized by Bertrand et al. and their monodentate derivatives were complexed to noble metals for catalysis.[35–37] We can extend the monodenticity of these ligands into polydentate by judicious choice of starting material. CAACs begin from a typically sterically demanding amine functionality and then through a multistep process led to the cyclic iminium form for carbene generation. I propose that by starting from 2,2′-bipyridine mono *N*-oxide a similar reaction pathway can be created thereby creating a new tridentate system with the chromophoric properties of the bipyridine and donor strength of the CAACs (Figure 5.6).[37,38]

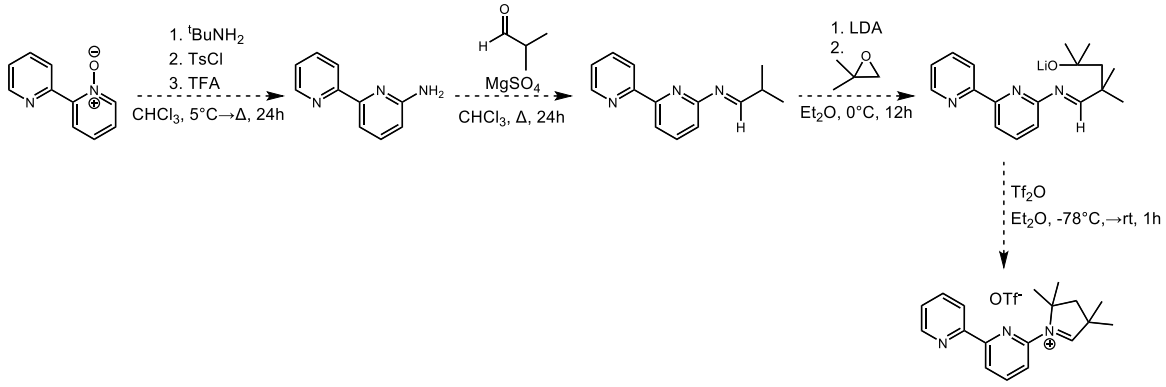

Figure 5.6. Proposed synthetic scheme for the synthesis of 2,2′-bipyridyl cyclic alkylamino carbene starting from 2,2′-bipyridine mono *N*-oxide.

If this chromophore exhibits the longer excited-state lifetime as imagined, we can then begin to look at the effect of the peripheral steric interactions of the CAAC. All CAACs must have at least two non-hydrogen atoms in the 4-position of the ring to preclude deprotonation and reactivity at that carbon. What Bertrand and others have shown is that chirality can be introduced at that carbon through cyclohexyl groups, thereby creating a chiral-at-ligand complex allowing for participation in stereochemical reactions.

5.4 Concluding Remarks

Since 2013, Fe(II) chromophores have found a new life with the implementation of polypyridyl-carbenes and cyclometallation. The energetic landscape of these complexes is drastically different than those that came before. With the ability to now synthesize Fe(II) chromophores with the MLCT as the lowest energy excited state, new avenues in photoinduced electron transfer applications, be it photocatalysis or DSSCs, are now closer than ever. Through this dissertation, the ligand-field energetics of Co(III) were explored to ascertain a more in-depth understanding of low-spin d^6 chromophores as well as the synthesis of new pyridylidene Fe(II) complexes that have inverted the ligand field and MLCT manifolds while maintaining low energy excitation. In addition, a deeper understanding of the MLCT transitions of $[Fe(dcpp)_2]^{2+}$ was found

by using aromatic substitutions, allowing for the selective enhancement of separate regions of the ^{1}MLCT manifold. I hope that the work presented here shows the various methods by which the excited-state manifold, be it ligand field or charge transfer in nature, can be modulated and understood.

REFERENCES

(1) Monteiro, J. H. S. K.; Fetto, N. R.; Tucker, M. J.; De Bettencourt-Dias, A. Luminescent Carbazole-Based Eu^{III} and Yb^{III} Complexes with a High Two-Photon Absorption Cross-Section Enable Viscosity Sensing in the Visible and near IR with One- And Two-Photon Excitation. *Inorg. Chem.* **2020**, *59* (5), 3193–3199. DOI: 10.1021/acs.inorgchem.9b03561.

(2) Pietro, S. Di; Imbert, D.; Mazzanti, M. An Efficient Triazole-Pyridine-Bistetrazolate Platform for Highly Luminescent Lanthanide Complexes. *Chem. Commun.* **2014**, *50* (71), 10323–10326. DOI: 10.1039/C4CC04060K.

(3) Claus, T. K.; Telitel, S.; Welle, A.; Bastmeyer, M.; Vogt, A. P.; Delaittre, G.; Barner-Kowollik, C. Light-Driven Reversible Surface Functionalization with Anthracenes: Visible Light Writing and Mild UV Erasing. *Chem. Commun.* **2017**, *53* (10), 1599–1602. DOI: 10.1039/C6CC09897E.

(4) Keller, S.; Yi, C.; Li, C.; Liu, S. X.; Blum, C.; Frei, G.; Sereda, O.; Neels, A.; Wandlowski, T.; Decurtins, S. Synthesis, Structures, Redox and Photophysical Properties of Benzodifuran-Functionalised Pyrene and Anthracene Fluorophores. *Org. Biomol. Chem.* **2011**, *9* (18), 6410–6416. DOI: 10.1039/c1ob05778b.

(5) Constable, E. C.; Thompson, A. M. W. C. Ligand Reactivity in Iron(II) Complexes of 4′-(4‴-Pyridyl)-2,2′:6′,2″-Terpyridine. *J. Chem. Soc., Dalton Trans.* **1992**, No. 20, 2947–2950. DOI: 10.1039/DT9920002947.

(6) Hathcock, D. J.; Stone, K.; Madden, J.; Slattery, S. J. Electron Donating Substituent Effects on Redox and Spin State Properties of Iron(II) Bis-Terpyridyl Complexes. *Inorganica Chim. Acta* **1998**, *282* (2), 131–135. DOI: 10.1016/S0020-1693(98)00154-6.

(7) Sheldrick, G. M. SHELXT – Integrated Space-Group and Crystal-Structure Determination. *Acta Crystallogr. A* **2015**, *71* (1), 3–8. DOI: 10.1107/S2053273314026370.

(8) Dolomanov, O. v.; Bourhis, L. J.; Gildea, R. J.; Howard, J. A. K.; Puschmann, H. OLEX2 : A Complete Structure Solution, Refinement and Analysis Program. *J. Appl. Crystallogr.* **2009**, *42* (2), 339–341. DOI: 10.1107/S0021889808042726.

(9) Sheldrick, G. M. Crystal Structure Refinement with SHELXL. *Acta Crystallogr. C* **2015**, *71* (1), 3–8. DOI: 10.1107/S2053229614024218.

(10) Wegeberg, C.; Häussinger, D.; Wenger, O. S. Pyrene-Decoration of a Chromium(0) Tris(Diisocyanide) Enhances Excited State Delocalization: A Strategy to Improve the Photoluminescence of $3d^6$ Metal Complexes. *J. Am. Chem. Soc.* **2021**, *143* (38), 15800–15811. DOI: 10.1021/jacs.1c07345.

(11) Dierks, P.; Päpcke, A.; Bokareva, O. S.; Altenburger, B.; Reuter, T.; Heinze, K.; Kühn, O.; Lochbrunner, S.; Bauer, M. Ground- And Excited-State Properties of Iron(II) Complexes Linked to Organic Chromophores. *Inorg. Chem.* **2020**, *59* (20), 14746–14761. DOI: 10.1021/acs.inorgchem.0c02039.

(12) Xu, K.; Sun, S.; Zhang, G.; Yang, F.; Wu, Y. One-Pot Synthesis of Unsymmetrical Diarylacetylenes via Sonogashira/Deacetonation/Sonogashira Cross-Coupling of Two Different Aryl Chlorides with 2-Methyl-3-Butyn-2-Ol. *RSC Adv.* **2014**, *4* (62), 32643–32646. DOI: 10.1039/C4RA02720E.

(13) Murakami, Y.; Kamada, K. Kinetics of Photon Upconversion by Triplet-Triplet Annihilation: A Comprehensive Tutorial. *Phys. Chem. Chem. Phys*. **2021**, *23*,18268–18282. DOI: 10.1039/d1cp02654b.

(14) Castellano, F. N.; McCusker, C. E. MLCT Sensitizers in Photochemical Upconversion: Past, Present, and Potential Future Directions. *Dalton Trans.* **2015**, *44* (41), 17906–17910. DOI: 10.1039/c5dt03212a.

(15) Zhong, F.; Zhao, J. Phenyleneanthracene Derivatives as Triplet Energy Acceptor/Emitter in Red Light Excitable Triplet-Triplet-Annihilation Upconversion. *Dyes and Pigments* **2017**, *136*, 909–918. DOI: 10.1016/J.DYEPIG.2016.09.057.

(16) Wang, C.; Reichenauer, F.; Kitzmann, W. R.; Kerzig, C.; Heinze, K.; Resch-Genger, U. Efficient Triplet-Triplet Annihilation Upconversion Sensitized by a Chromium(III) Complex via an Underexplored Energy Transfer Mechanism. *Angew. Chem. Int. Ed.* **2022**, *61* (27). DOI: 10.1002/anie.202202238.

(17) Ringström, R.; Schroeder, Z. W.; Mencaroni, L.; Chabera, P.; Tykwinski, R. R.; Albinsson, B. Triplet Formation in a 9,10-Bis(Phenylethynyl)Anthracene Dimer and Trimer Occurs by Charge Recombination Rather than Singlet Fission. *J. Phys. Chem. Lett.* **2023**, *14*, 7897–7902. DOI: 10.1021/acs.jpclett.3c02050.

(18) Naimovičius, L.; Bharmoria, P.; Moth-Poulsen, K. Triplet–Triplet Annihilation Mediated Photon Upconversion Solar Energy Systems. *Mater. Chem. Front.* **2023**, *7* (12), 2297–2315. DOI: 10.1039/D3QM00069A.

(19) Kreitner, C.; Mengel, A. K. C.; Lee, T. K.; Cho, W.; Char, K.; Kang, Y. S.; Heinze, K. Strongly Coupled Cyclometalated Ruthenium Triarylamine Chromophores as Sensitizers for DSSCs. *Chem. Euro. J.* **2016**, *22* (26), 8915–8928. DOI: 10.1002/chem.201601001.

(20) Takeda, H.; Koike, K.; Inoue, H.; Ishitani, O. Development of an Efficient Photocatalytic System for CO_2 Reduction Using Rhenium(I) Complexes Based on Mechanistic Studies. *J Am. Chem. Soc.* **2008**, *130* (6), 2023–2031. DOI: 10.1021/JA077752E.

(21) Karlsson, J. K. G.; Cerpentier, F. J. R.; Lalrempuia, R.; Appleby, M. V.; Shipp, J. D.; Chekulaev, D.; Woodford, O.; Weinstein, J. A.; Pryce, M. T.; Gibson, E. A. Ruthenium–Rhenium and Ruthenium–Palladium Supramolecular Photocatalysts for Photoelectrocatalytic CO_2 and H^+ Reduction. *Sustain. Energy Fuels* **2023**, *7* (14), 3284–3293. DOI: 10.1039/D3SE00442B.

(22) Kuramochi, Y.; Sato, R.; Sakuma, H.; Satake, A. Photocatalytic CO_2 Reduction Sensitized by a Special-Pair Mimic Porphyrin Connected with a Rhenium(I) Tricarbonyl Complex. *Chem. Sci.* **2022**, *13* (34), 9861–9879. DOI: 10.1039/D2SC03251A.

(23) Koizumi, T.; Tomon, T.; Tanaka, K. Terpyridine-Analogous (N,N,C)-Tridentate Ligands: Synthesis, Structures, and Electrochemical Properties of Ruthenium(II) Complexes Bearing Tridentate Pyridinium and Pyridinylidene Ligands. *Organometallics* **2003**, *22* (5), 970–975. DOI: 10.1021/om020637m.

(24) Schubert, J.; Mock, S.; Schubert, U. Übergangsmetall-Stannyl-Komplexe, 7. Darstellung von Carben-Komplexen (Π1-Aromat)$(CO)_2CrCR_2$ Durch Umsetzung Der Anionischen Stannyl-Komplexe $[(Π1\text{-Aromat})(CO)_2CrSnPh_3]^-$ Mit R_2CX_2 Oder $[R_2CX]Y$. *Chem. Ber.* **1993**, *126* (3), 657–664. DOI: 10.1002/cber.19931260316.

(25) Constable, E. C.; Cargill Thompson, A. M. W.; Cherryman(in part), J.; Liddiment, T. 2,2′:6′,4″-Terpyridine: A Cyclometallating Analogue of 2,2′:6′2″-Terpyridine for Metallosupramolecular Chemistry. *Inorganica Chim. Acta* **1995**, *235* (1–2), 165–171. DOI: 10.1016/0020-1693(95)90058-E.

(26) Koizumi, T.; Tomon, T.; Tanaka, K. Synthesis and Electrochemical Properties of Bis(Bipyridine)Ruthenium(II) Complexes Bearing Pyridinyl- and Pyridinylidene Ligands Induced by Cyclometallation of N′-Methylated Bipyridinium Analogs. *J Organomet. Chem.* **2005**, *690* (5), 1258–1264. DOI: 10.1016/j.jorganchem.2004.11.032.

(27) Hartwig, J. F.; Bergman, R. G.; Andersen, R. A. Structure, Synthesis, and Chemistry of Ruthenium Complex $(PMe_3)_4Ru(\eta^2\text{-Benzyne})$. Reactions with Arenes, Alkenes, and Heteroatom-Containing Organic Compounds. Synthesis and Structure of a Monomeric Hydroxide Complex. *J. Am. Chem. Soc.* **1991**, *113* (9), 3404–3418. DOI: 10.1021/ja00009a028.

(28) Constable, E. C.; Housecroft, C. E.; Kopecky, P.; Martin, C. J.; Wright, I. A.; Zampese, J. A.; Bolink, H. J.; Pertegas, A. Solution, Structural and Photophysical Aspects of Substituent Effects in the N^N Ligand in $[Ir(C^N)_2(N^N)]^+$ Complexes. *Dalton Trans.* **2013**, *42* (22), 8086. DOI: 10.1039/c3dt50492a.

(29) Beauchamp, D. A.; Loeb, S. J. Silver(I) Complexes of 2,2′;6′,4″-Terpyridine: The Formation of Discrete Dimers versus Helical Polymers Is Anion Dependent. *Supramol. Chem.* **2005**, *17* (8), 617–622. DOI: 10.1080/10610270500127162.

(30) Gaballah, S. T.; Kerr, C. E.; Eaton, B. E.; Netzel, T. L. SYNTHESIS OF 5-(2,2′-BIPYRIDINYL AND 2,2′-BIPYRIDINEDIIUMYL)-2′-DEOXYURIDINE NUCLEOSIDES: PRECURSORS TO METALLO-DNA CONJUGATES. *Nucleosides Nucleotides Nucleic Acids* **2002**, *21*, 547–560. DOI: 10.1081/NCN-120015068.

(31) Bowman, D. N.; Mukherjee, S.; Barnes, L. J.; Jakubikova, E. Linker Dependence of Interfacial Electron Transfer Rates in Fe(II)-Polypyridine Sensitized Solar Cells. *J. Phys. Condens. Matter* **2015**, *27* (13). DOI: 10.1088/0953-8984/27/13/134205.

(32) Tichnell, C. R.; Miller, J. N.; Liu, C.; Mukherjee, S.; Jakubikova, E.; Mccusker, J. K. Influence of Electrolyte Composition on Ultrafast Interfacial Electron Transfer in Fe-Sensitized TiO_2-Based Solar Cells. *J. Phys. Chem. C* **2020**, *124* (3), 1794–1811. DOI: 10.1021/ACS.JPCC.9B09404.

(33) Brauer, J. C.; Marchioro, A.; Paraecattil, A. A.; Oskouei, A. A.; Moser, J.-E. Dynamics of Interfacial Charge Transfer States and Carriers Separation in Dye-Sensitized Solar Cells: A Time-Resolved Terahertz Spectroscopy Study. *J. Phys. Chem. C* **2015**, *119* (47), 26266–26274. DOI: 10.1021/acs.jpcc.5b06911.

(34) Zhao, L.-X.; Moon, Y.-S.; Basnet, A.; Kim, E.; Jahng, Y.; Park, J. G.; Jeong, T. C.; Cho, W.-J.; Choi, S.-U.; Lee, C. O.; Lee, S.-Y.; Lee, C.-S.; Lee, E.-S. Synthesis, Topoisomerase I Inhibition and Structure–Activity Relationship Study of 2,4,6-Trisubstituted Pyridine Derivatives. *Bioorg. Med. Chem. Lett.* **2004**, *14* (5), 1333–1337. DOI: 10.1016/j.bmcl.2003.11.084.

(35) Soleilhavoup, M.; Bertrand, G. Cyclic (Alkyl)(Amino)Carbenes (CAACs): Stable Carbenes on the Rise. *Acc. Chem. Res.* **2015**, *48* (2), 256–266. DOI: 10.1021/ar5003494.

(36) Melaimi, M.; Jazzar, R.; Soleilhavoup, M.; Bertrand, G. Cyclic (Alkyl)(Amino)Carbenes (CAACs): Recent Developments. *Angew. Chem. Int. Ed.* **2017**, *56* (34), 10046–10068. DOI: 10.1002/anie.201702148.

(37) Lavallo, V.; Canac, Y.; Präsang, C.; Donnadieu, B.; Bertrand, G. Stable Cyclic (Alkyl)(Amino)Carbenes as Rigid or Flexible, Bulky, Electron-Rich Ligands for Transition-Metal Catalysts: A Quaternary Carbon Atom Makes the Difference. *Angew. Chem. Int. Ed.* **2005**, *44* (35), 5705–5709. DOI: 10.1002/anie.200501841.

(38) Homberg, L.; Roller, A.; Hultzsch, K. C. A Highly Active PN_3 Manganese Pincer Complex Performing N-Alkylation of Amines under Mild Conditions. *Org. Lett.* **2019**, *21* (9), 3142–3147. DOI: 10.1021/acs.orglett.9b00832.

APPENDIX

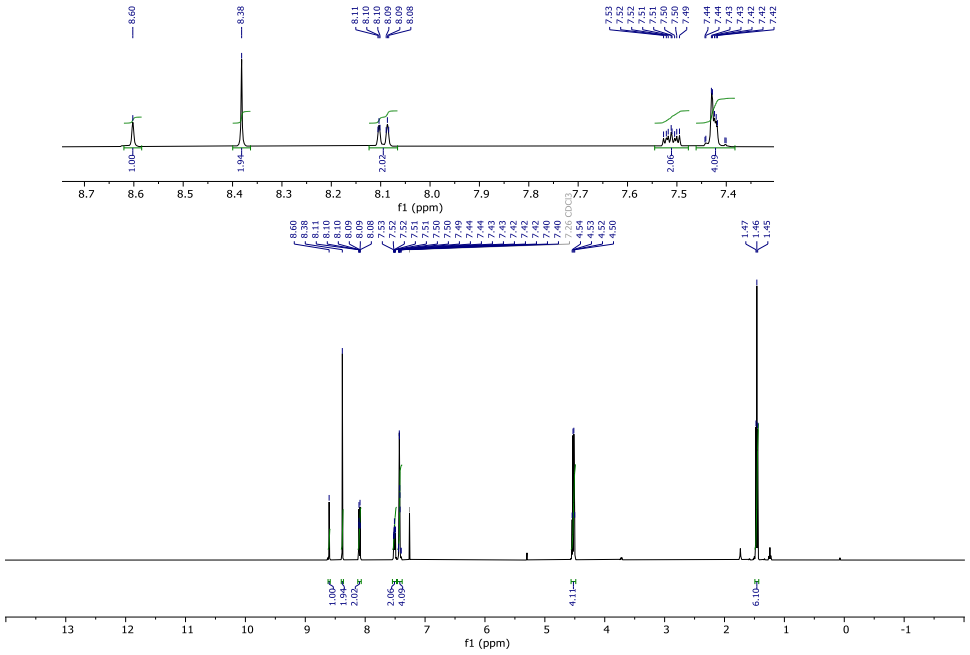

Figure 5.7. ^{1}H NMR of diethyl 4-(9-anthracenyl)-2,6-pyridine dicarboxylate in $CDCl_3$. Inset is an expansion of the aromatic region.

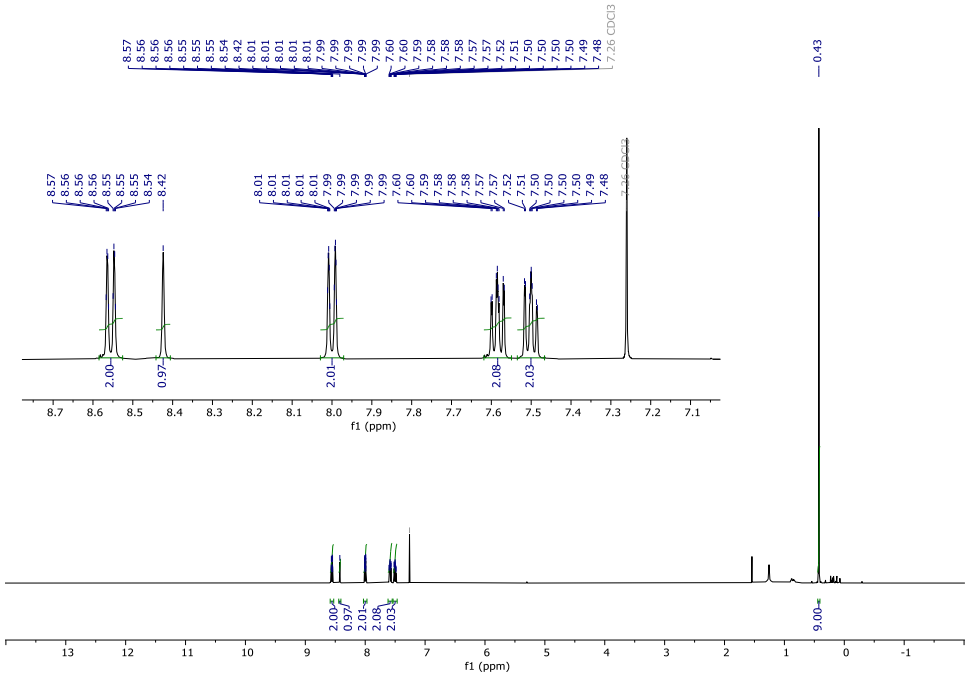

Figure 5.8. ^{1}H NMR of 9-(trimethylsilylethynyl)anthracene in $CDCl_3$. Inset is an expansion of the aromatic region.

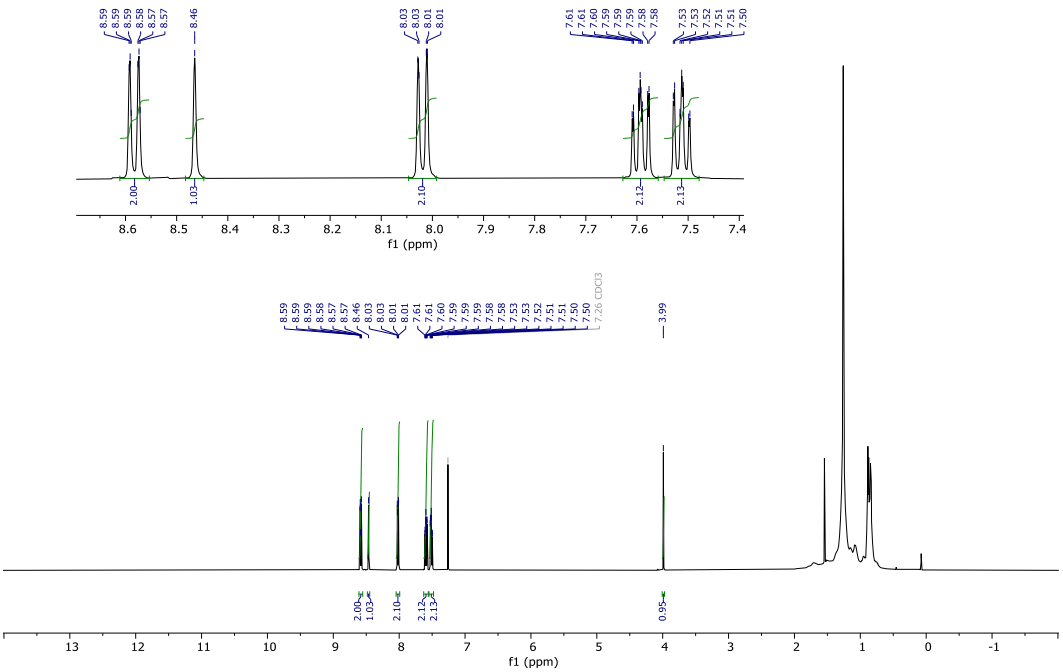

Figure 5.9. ^{1}H NMR of 9-ethynylanthracene in $CDCl_3$. Inset is an expansion of the aromatic region.

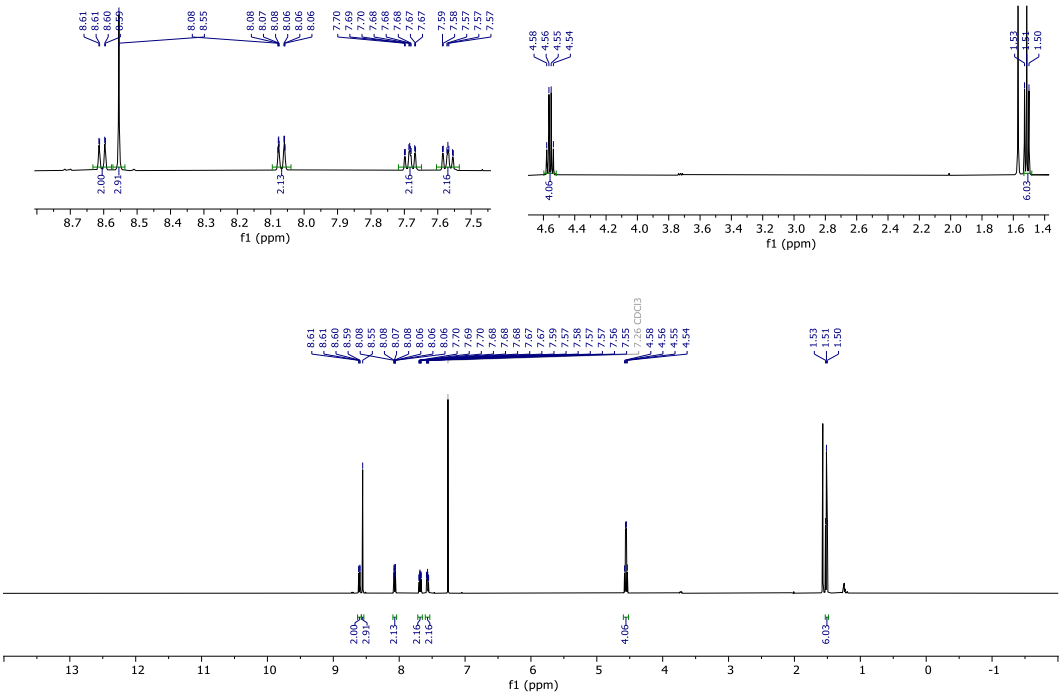

Figure 5.10. ^{1}H NMR of diethyl 4-(9-ethynylanthracenyl)-2,6-pyridine dicarboxylate in $CDCl_3$. Inset Left is an expansion of the aromatic region. Inset Right is an expansion of the aliphatic region.

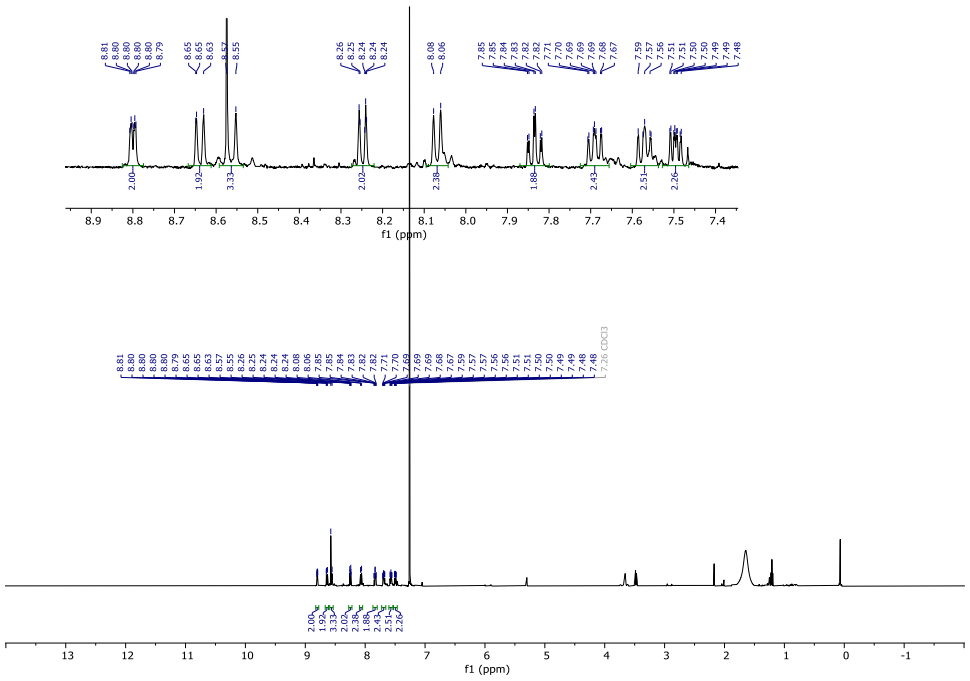

Figure 5.11. Crude ^{1}H NMR of 2,6-di(2-carboxypyridyl)-4-(9-ethynylanthracenyl)pyridine in $CDCl_3$. Inset is an expansion of the aromatic region.

Table 5.1. Crystallographic data and structure refinement

Identification code	$[Fe(dcpAnp)_2](PF_6)_2$
Empirical formula	$C_{62}H_{38}FeN_6O_4P_2F_{12}•2CH_3CN$
Formula weight	1358.88
Temperature/K	100.0(3)
Crystal system	monoclinic
Space group	$P2_1/c$
a/Å	10.00041(9)
b/Å	32.2386(3)
c/Å	20.12551(17)
α/°	90
β/°	97.8225(8)
γ/°	90
Volume/Å^3	6428.07(10)
Z	4
ρ_{calc}g/cm^3	1.404
μ/mm^{-1}	3.130
F(000)	2768.0
Crystal size/mm^3	0.318 × 0.191 × 0.08
Radiation	Cu Kα (λ = 1.54184)
2Θ range for data collection/°	5.212 to 161.216
Index ranges	$-12 \leq h \leq 11$, $-40 \leq k \leq 40$, $-21 \leq l \leq 25$
Reflections collected	69418
Independent reflections	13759 [R_{int} = 0.0402, R_{sigma} = 0.0288]
Data/restraints/parameters	13759/0/837
Goodness-of-fit on F^2	1.045
Final R indexes [I>=2σ (I)]	R_1 = 0.0507, wR_2 = 0.1211
Final R indexes [all data]	R_1 = 0.0569, wR_2 = 0.1246
Largest diff. peak/hole / e Å^{-3}	0.60/-0.62